Optimisation, Design, Development, and Trial of a Low-Cost Solar Oven with Novel Concentrator Geometry

Ian Berryman

Kellogg College



A thesis submitted in partial fulfilment of the requirements

for the degree of Doctor of Philosophy

Department of Engineering Science

University of Oxford

Hilary 2016

Optimisation, Design, Development, and Trial of a Low-Cost Solar Oven with Novel Concentrator Geometry

Ian Berryman
Kellogg College, University of Oxford

DPhil
Department of Engineering Science

A thesis submitted in partial fulfilment of the requirements for the degree of Doctor of Philosophy, Hilary Term 2016

Abstract

A promising and novel solar concentrator design has been thoroughly investigated and optimised. A prototype concentrator based on this novel geometry was validated using ray tracing techniques. This ray tracing demonstrated the comparative performance of this novel concentrator in regards to equivalent parabolic dishes. The effect of mirror surface normal errors on performance was established using Monte-Carlo based ray tracing code, which agreed well with the optical performance of this prototype which was determined experimentally.

A need for low-cost solar cookers to replace bio-mass worldwide was identified, and the concentrator design was then developed as a low-cost solar oven. Despite existing in some number, no current design is able to achieve high performance at low-cost. An industrial partner, Dytecna, was initially involved in the process of this development of the system as a solar cooker.

In support of a field trial for the solar cooker developed with Dytecna, a detailed thermal model of the oven was developed. A low-cost lightmeter was constructed and calibrated in order to measure the direct normal irradiance during the field trial in Italy. Laboratory work provided baseline results for the heating of various thermal masses in the oven.

The Italian field trials provided a wealth of feedback into the design of the system and many valuable results. The solar cooker was able to bring 0.75L of water to the boil in 33 minutes with an average heat throughput of 203W. Important benchmark results and practical experience of several competing receiver materials was obtained; further lab testing provided more accurate measurements of the receivers' performances.

The experiences of the Italian field trial were fed back into the design of a subsequent prototype, intended for a much larger field trial in Tanzania. Improvements in the hotplate, receiver material, and the oven were all incorporated into the design. Additionally, the structure of the solar cooker was redesigned to incorporate a low-cost wooden construction. Supporting work was conducted for the month long trial in which 8 solar cookers would be distributed to families in Tanzania.

The field trial in Tanzania provided a wealth of user feedback into the design. At the same time the new solar cooker exceeded previously established performances in Italy. The new design was able to provide an average of 246W of heat to 1kg of water, which was brought to boiling point in 25 minutes. This represents a heating efficiency of 66% compared to the incident solar flux on the hotplate. In response to findings during the Tanzanian trials, further laboratory work was conducted into establishing the reflectivities of low-cost candidate mirror materials.

Throughout all phases of the project the design of the solar cooker was refined and improved with the goal of a solar cooker design that could reach price-point, performance, and usability standards which would ensure market success.

Acknowledgements

I would firstly like to thank everyone that has been involved with the solar cooker project over the past few years. Considering the multitude of unsuccessful solar cookers that have come before us, it was no small challenge that we set ourselves. Although we may not have arrived at a commercially available product just yet, I hope that my contributions have pushed us ever closer.

From Engineering Science, I would like to thank Paul Bailey, Mike Dadd, and Thom Smith for their initial involvement with the project. I would like to thank Chim Chu from ISIS for putting us in touch with our industrial partner Dytecna, even if this partnership didn't work out in the long term.

Additionally, I owe a large debt of gratitude to Dr Joseph Matiko. It is no exaggeration to say that without his assistance the field trial in Tanzania would not have been possible at all. I would also like to acknowledge and thank the STFC for the funding which made our field trials possible.

For sharing the pain of programming errors, I would like to thank my fellow lab mates Dr Felix Leach, Dr Kun Liang, Dr Joseph Camm and Dr Nathan Hinton. Furthermore, I would like to thank all the other amazing friends I've made in Oxford over the years, for keeping me sane during the long, cold winters. Large thanks are due to Kellogg College for being my home away from home. To my loving and supporting girlfriend Faith, thank you for putting up with me during this last year of my thesis.

I owe a large debt of gratitude to the engineers, scientists, and activists too numerous to name that have dared to dream of a world free of fossil fuels, and have been my sources of inspiration these past few years.

However, I must save the largest acknowledgment for my supervisors Prof Richard Stone and Prof Nick Jelley for their continuous support of my thesis. Their patience, knowledge, and guidance over the past few years made my thesis possible. It hasn't been an easy road for myself, from a knee reconstruction to the passing of my mother. Throughout everything they have been nothing but understanding and supportive.

Finally, I would like to thank my parents. From a very young age they both encouraged my interest in science, nurturing a tiny spark into a great passion. Between my father's love of science and my mother's practical mind (and no small amount of Lego) it's probably no surprise that I became an engineer. Though they are no longer with me, I will hold them both in my heart when I graduate and know that they will be proud of me.

Contents

Abstract i

Acknowledgements ii

Contents iii

1 Introduction 1

1.1 Concentrated Solar Power 2

1.2 CSP in the Developing World 3

1.3 Motivation for Solar Cooking 4

1.4 Solar Cookers 7

1.4.1 Box-type Solar Cookers 7

1.4.2 Concentrating Solar Cookers 9

1.4.3 Panel Solar Cookers 10

1.5 Commercialisation of Solar Cookers 10

1.5.1 Market Potential 10

1.5.2 Barriers to the Success of Solar Cookers 11

1.6 The Reflex Concentrator 12

1.6.1 Industrial Partner 13

1.6.2 Previous Work 14

2 Novel Mirror Geometry 15

2.1 Vector Proof of Mirror Geometry 16

2.1.1 Geometric Description 16

2.1.2 Geometric Variables 18

2.1.3 Vector Proof 19

2.2 Excel Design Aid 23

2.2.1 Indeterminate Solutions to the Parabolic Geometry 24

2.2.2 Defining the Parabolic Mirror Geometry 26

2.2.3 Flattened Mirror Geometry 27

2.2.4 Selection of Mirror Geometry 28

2.2.5 Geometry of Laboratory Prototype 29

3 Optical Modelling and Initial Experimental Results 32

3.1 MATLAB Ray Tracing Program 32

3.1.1 Rationale behind Developing Ray Tracing Code 32

3.1.2 Description of Program 34

3.1.3 Sunshape Profile 36

3.1.4 On-Axis Results 37

3.1.5 Off-Axis Results 39

3.1.6 Summary of Ray Tracing Results 42
3.2 Experimental Optical Results of Prototype 43
3.2.1 Prototype Concentrator 43
3.2.2 Experimental Aims 44
3.2.3 Laser Pointers 45
3.2.4 Experimental Methodology 50
3.2.5 Camera 51
3.3 Experimental Results 58
3.3.1 First Position 59
3.3.2 Repositioning the Camera Sensor 63
3.3.3 Summary of Results from Laser Pointer Data 64
3.4 Modelling of Mirror Errors 65
3.4.1 Description of Program 65
3.4.2 Measurement of Resultant Focal Plane Images 66
3.4.3 Modelling Results 66
3.4.4 Summary of Results 68
3.4.5 Images of Focal Plane with Increasing Mirror Surface Errors 72
3.4.6 Discussion and Implications for Concentrator Design 75
3.5 Conclusion 76
4 Oven 79
4.1 Thermal Model of Oven 80
4.1.1 Description of Heat Flows 80
4.1.2 Mathematical Characterisation of the Oven Model 82
4.2 Relevant Thermal Properties used in Calculations 89
4.3 Measurement of Thermal Contact Resistance 90
4.4 Analytical Solution to Initial Temperature Rise 95
4.5 Investigation of effect of Thermal Contact Resistance on Oven Performance 98
4.6 Sensitivity Analysis of the Oven Model 101
4.6.1 Effect of Oven Wall Insulation on Oven Performance 101
4.6.2 Effect of Convective Losses from the Hotplate on Oven Performance 103
4.6.3 Effect of Contact Conductance on Oven Performance 104
4.6.4 Summary of Sensitivity Analysis 106
4.7 Comparison of Model with Experimental Data 106
4.8 Estimation of Heat Losses 107
5 Dytecna Prototype 109
5.1 Design Features 110
5.1.1 Lab Verification of Optics 112
5.1.2 Construction of Lightmeter 113

5.1.3 Calibration of the Lightmeter 114
5.1.4 Data Acquisition System 123
5.2 Italian Field Trials 123
5.2.1 Preparation for the Trials 124
5.2.2 Calibration of Solar Irradiance in Italy 124
5.2.3 Key Results from the Italian Field Trial 128
5.2.4 Feedback from Trial 132
5.3 Measurement of Receiver Absorptivities 133
5.3.1 Experimental Results 135
5.4 Summary of Dytecna Prototype 137
6 Tanzanian Field Trials 138
6.1 Design Changes for the Tanzanian Prototype 138
6.1.1 Revised Oven 138
6.1.2 Redesign of Hotplate 139
6.2 Preparation for the Field Trial 139
6.3 Notes on the Field Trial 139
6.4 Technical Results 140
6.4.1 Calibrating Solar Irradiance Measurements 140
6.4.2 Boiling Water Test – Saturday the 15th 147
6.4.3 Testing of Vinyl vs. Alanod Mirrors 150
6.4.4 Billet Tests 154
6.5 Technical Feedback 167
6.5.1 Performance of Vinyl Mirror Surface 167
6.5.2 Manufacturing Tolerances 168
6.5.3 Conformity of Mirror Geometry 168
6.5.4 Stability 168
6.5.5 Condensation 169
6.5.6 Mirror Surface Finish 169
6.5.7 Oven Support Material 169
6.6 User Feedback 170
6.6.1 General Feedback 170
6.6.2 Ease of Assembly 170
6.6.3 Ease of 'Track-ability' 170
6.6.4 Ergonomic considerations 171
6.6.5 Mobility 171
6.6.6 Safety – Glare 171
6.6.7 Ease of Cleaning 172
6.6.8 Initial Orientation 172

6.6.9 Switching between cooking modes 172
6.6.10 Latitudinal Adjustments 173
6.6.11 Hemisphere Adjustments 173
6.6.12 Physical Exertion 173
6.6.13 Affordability 173
6.6.14 Safety – Fire Hazard 173
6.6.15 Performance 174
6.7 Summary of Field Trials 174
6.8 Reflectivity Measurements of Proposed Mirror Materials 177
6.8.1 Proposed Mirror Materials 177
6.8.2 Spectrophotometer 178
6.8.3 Calibration of the Spectrophotometer 181
6.8.4 Expected Reflectance Results 182
6.8.5 Reflectance Results 183
6.8.6 Solar-Weighting 186
6.8.7 Errors 189
6.8.7 Other Considerations in Mirror Selection 192
7 Conclusions and Future Work 194
7.1 Conclusions 194
7.2 Future Work 197
Bibliography 200

1 Introduction

The current pattern of global energy consumption is inherently unsustainable, with the continued exploitation of fossil fuels the primary factor driving anthropogenic climate change. Unchecked, this global warming will one day pose an existential threat to civilization as we know it. The problem of global warming is further exacerbated by the justifiable lifestyle aspirations of the developing world. Satisfying the ever-growing energy demands of the developing world, whilst tackling climate change, will be perhaps one of the single greatest issues of equity and justice in our lifetime.

Compared to pre-industrial levels, average global temperatures are predicted to rise by as much as 4K by the end of the century, driven primarily by CO_2 emissions. Worryingly, much of this temperature rise may already be locked in. Climate models call for a drastic reduction in CO_2 emissions if the worst aspects of climate change are to be avoided. The EU goal of 80-90% reduction in CO_2 emissions from 1990 levels by mid-century necessitates a drastic move away from fossil fuels towards renewable energy technologies.

Currently, renewable resources supply about 18.6% of total world energy demand. However, this figure may be misleading due to its inclusion of both traditional biomass (predominantly firewood) and legacy hydropower which represent, respectively, 10.2% and 2.4% of the total. Current unsustainable wood burning coupled with increased climate variability is pushing many areas of the globe to land degradation and deforestation, whilst most major hydropower resources have already been exploited. Therefore, new renewable technologies such as wind and solar are required to not only meet existing demand but match increasing demand as global populations grow and industrialise.

Globally, solar and wind energy potential trump all other sources of renewable energy by orders of magnitude; whilst the potential of tidal, wave, geothermal, and hydro all fall

significantly short of the global energy demand currently imposed by civilization. Of solar and wind, solar potential is by far the greatest; the Earth receives more energy in one hour from the Sun than the whole of human civilization consumes in one year. Expressed more accurately; 60% of sunlight incident on the atmosphere reaches the Earth's surface, only 0.1% of this energy converted at 15% efficiency would provide the entire world's current average energy consumption of ~18 TW. Solar holds the greatest absolute potential of any renewable energy source, and indeed non-renewable energy source, currently available to mankind.

1.1 Concentrated Solar Power

The exploitation of solar resources is not just limited to photovoltaics (PV), concentrated solar power (CSP), or solar thermal, holds great potential in meeting worldwide energy demand. In general CSP functions by concentrating the rays of the sun, normally with mirrors, to either a point or line focus at which an absorber is placed. Thermal energy may then be utilised at this absorber or carried away via a heat transfer medium. This makes CSP perfectly suited for thermal applications where no more energy conversions are required, whilst a CSP system generating electricity will generally be limited by Carnot efficiencies in its power block.

Although the concentrating optics of CSP are generally dependent on the availability of direct sunlight, the key advantage in CSP systems is that both mirrors and absorbers are generally 90-95% efficient. Therefore, CSP thermal efficiencies greatly exceed even the most promising PV cell efficiencies. For heating and industrial process applications CSP therefore holds great potential.

Despite higher capital costs for equivalent grid-connected capacity than PV in recent years, another key advantage of CSP lies in its ability to store thermal energy much more cheaply than current battery technology allows. The Crescent Dunes project is a solar power tower system, located in Nevada, which has a capacity of 110MW with 10 hours or 1.1GWhs of storage, see Figure 1.1. The molten-salt thermal storage module was estimated to cost 8% of the US $975 million total, resulting in an exceptionally low $88/kWh$_e$ price for storage.



Figure 1.1 The 110MW$_e$ SolarReserve© Crescent Dunes project features a solar power tower surrounded by a heliostat (mirror) field [1]**.**

1.2 CSP in the Developing World

In contrast to the industrialised world, the majority of the energy demand in developing countries is in the form of heat and not electricity. Whilst it may take as little 10-20kJ to fully charge a mobile phone, preparing a meal for a family will use several MJ of heat energy. Furthermore, the heating of water for purification, desalination, doing laundry, or bathing requires large amounts of energy. The relatively high specific heat capacity of water coupled with its centrality to our lives demands large energy inputs.

The contribution of solar thermal to the global energy supply is already significant. In 2014 there was 406 GW$_{th}$ of solar thermal hot water heating capacity in the global energy supply, which compares worldwide with installed capacities of 117 GW for solar PV and 370 GW for wind [2]. The vast majority of the contribution to solar thermal capacity is roof based solar hot water heaters. It is estimated that more than 30 million households in China alone have these systems, see Figure 1.2. Mass investment has driven down the price of these units where the Chinese market accounts for 80% of worldwide sales [3].



Figure 1.2 Solar water heaters on rooftops in China [4].

The same properties that suit solar thermal to hot water usage also hold great promise for its use for solar cooking. The high optical and thermal efficiencies of CSP means that surface area requirements and therefore structural supports can be relatively modest. Heating may be achieved via direct contact with the absorber without the need for auxiliary systems or energy conversions. Thermal storage is possible with sensible or even latent heat. Whilst the success of CSP in the electricity markets of developed economies is by no means guaranteed, the clear advantage of CSP in thermal efficiency holds great potential as an energy source in the developing world, particularly in regards to cooking.

1.3 Motivation for Solar Cooking

Cooking fuels remain a large proportion of primary energy consumption in the developing world, approximately 3 billion people use fuels such as wood, charcoal, and dung every day for cooking [5]. Wood remains the primary energy source for much of the world's population leading to serious environmental problems such as deforestation and desertification [6]. Deforestation itself is responsible for as much as 25% of cumulative CO_2 emissions since the beginning of the industrial era [7], whilst much of this is due to changing land use, a significant amount of it can be attributed to demand for fuel, see Figure 1.3.



Figure 1.3 Border between Haiti and the Dominican Republic, the Haitian deforestation is partly due to demand for cooking charcoal, coupled with poor government regulation [8]**.**

Furthermore, rural families expend much time in harvesting wood and many poor urban families spend a large proportion of their income purchasing such fuels. Additionally, the use of bio-mass poses several health concerns including burns, eye disorders and lung diseases [6]. In 2006 the World Health Organisation (WHO) estimated that 1.6 million deaths per year were attributable to indoor air pollution [9] caused by toxic gases from improper or incomplete combustion of solid bio-fuels and fossil fuels. This number has grown to 2.44 million deaths in recent years [10].

These issues often affect the rural poor most severely. Across the Indian population 36% of primary energy consumption is used in cooking. However, rural Indians use 80% of their total household energy budget on cooking [11]. Approximately 95% of the urban Indian population has access to liquefied petroleum gas (LPG) at subsidised rates, whilst 80% of the rural Indian population is entirely dependent on unprocessed solid fuels; firewood, cow dung and crop residue [12]. To put this in perspective, about 70% of India's population live in rural areas, including the majority of the ~44% of the population who still have no access to

electricity. The time and money spent by the rural poor obtaining energy to cook is a severe obstacle to their own economic empowerment, the growth of India and more generally that of the entire developing world.

Currently the use of clean fuel in India's rural areas is practicably negligible. Rural areas will not only continue to depend on solid bio-fuels but this dependence is widely believed to be growing in pace with India's expanding population. The International Energy Agency (IEA), estimated that the 585 million Indians dependent on bio-fuels for cooking and heating in 2000 will grow to 632 million by 2030 [13].

This problem is not just unique to India; in the 50 poorest nations 79% of people lack access to electricity and 1.5 billion people are without electricity worldwide. Although this figure has improved in recent years, the IEA fears that this is the result of a net migration to urban areas rather than an increase or improvement of the electrical infrastructure in rural areas. In sub-Saharan Africa 11 countries still have 90% of their populations without access to electricity [14].

Nevertheless, the developing world has some advantages not available to the industrialised world in tackling climate change. Firstly, the developing world has not already invested in capital intensive, yet environmentally damaging, fossil-fuelled power plants with projected lifespans running decades into the future. Additionally, large parts of the developing world have not invested in the transmission networks necessary for this type of electricity generation. There is no reason why they cannot leap frog this phase of development to a more localised network of distributed renewable generation; analogous to how many of these countries have foregone copper-wire telephone networks and have embraced mobile phone usage. Secondly, and most importantly, is that much of the developing world lies in regions of abundant solar resources, see Figure 1.4. In particular, India has on average 275 sunny days a year with mean daily illumination of 5-7 kWh/m^2 [15] [16].

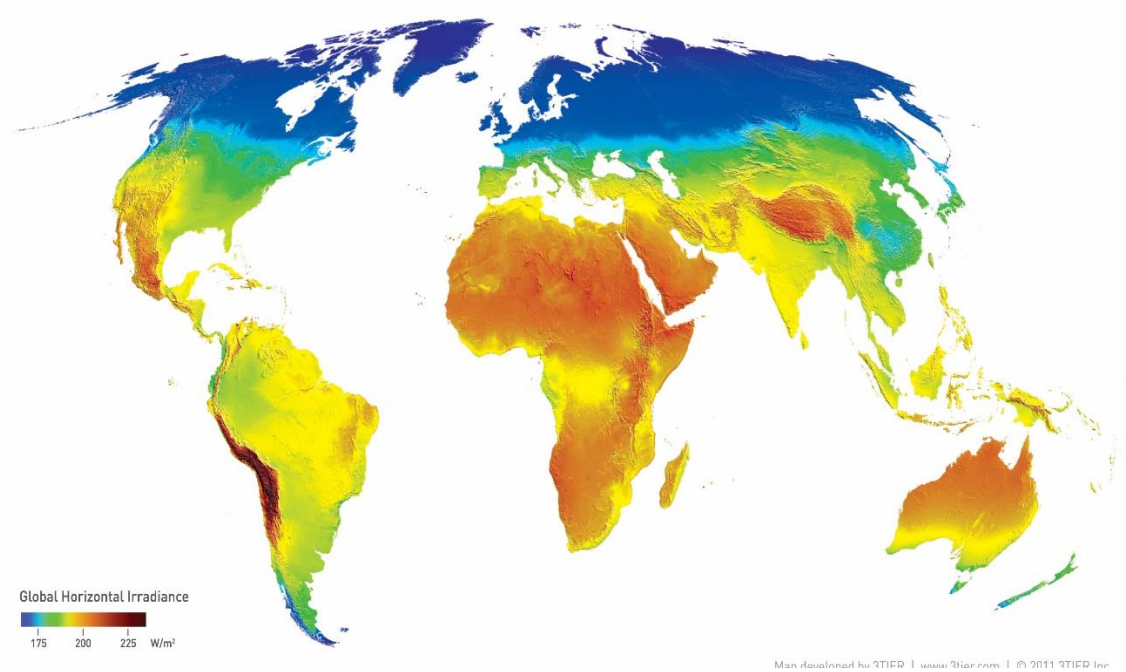


Figure 1.4 Map of global irradiance [17]**.**

The Oxford reflex concentrator has been envisioned as a means of helping to provide energy security for the world's poor. Its developable mirror surfaces will be cheap to manufacture whilst ensuring high concentration factors. In turn this will lead to higher cooking temperatures, better performance, and methods of cooking unavailable to competing designs.

1.4 Solar Cookers

A solar cooker utilises solar energy to heat and cook food. Designs are varied and go back many years to the first reported experiments by Tschirnihausen (1651-1708) [18]. Solar cookers can be broadly categorised into four types; concentrating, indirect, panel, and box. This review concerns the panel, concentrating and box types which heat food directly like the reflex concentrator, and not the indirect type which cook via a heated fluid loop. These indirect cookers are often more complex and expensive, therefore they are generally only utilised on larger-scale community projects rather than being produced for use by individual families.

1.4.1 Box-type Solar Cookers

Box type solar cookers are simply insulated containers with glass covers. They function like a greenhouse in which the glazing is transparent to the shorter wavelengths of solar radiation but are mostly opaque to the longer radiation from the heated objects inside. The glass cover can be dual layered and the box itself is generally well insulated. In some designs several pots can be accommodated simultaneously. Flat mirrors are often attached to the sides of the box to reflect more sunlight inwards and therefore reduce cooking times; however the mirrors require movement to track the sun. More than 600,000 of these cookers have been sold already in India [19].

Box type cookers can be slow to heat up but may function satisfactorily where there is diffuse sunlight or intermittent cloud cover. Due to their insulation they work well in low ambient temperatures or in windy conditions. Box type cookers can only be used for boiling and to a degree baking owing to their limited temperature ranges. Drawbacks include steam condensation on the interior of the cooker resulting in reduced transmission of sunlight and corrosion of absorber surfaces and long cooking times. Box-type stagnation temperatures at the absorber plate of 138°C, and a boiling time of 60 min for 1kg of water were reported for a cooker with a 0.49m^2 glass window and single 0.49m^2 reflector [20].

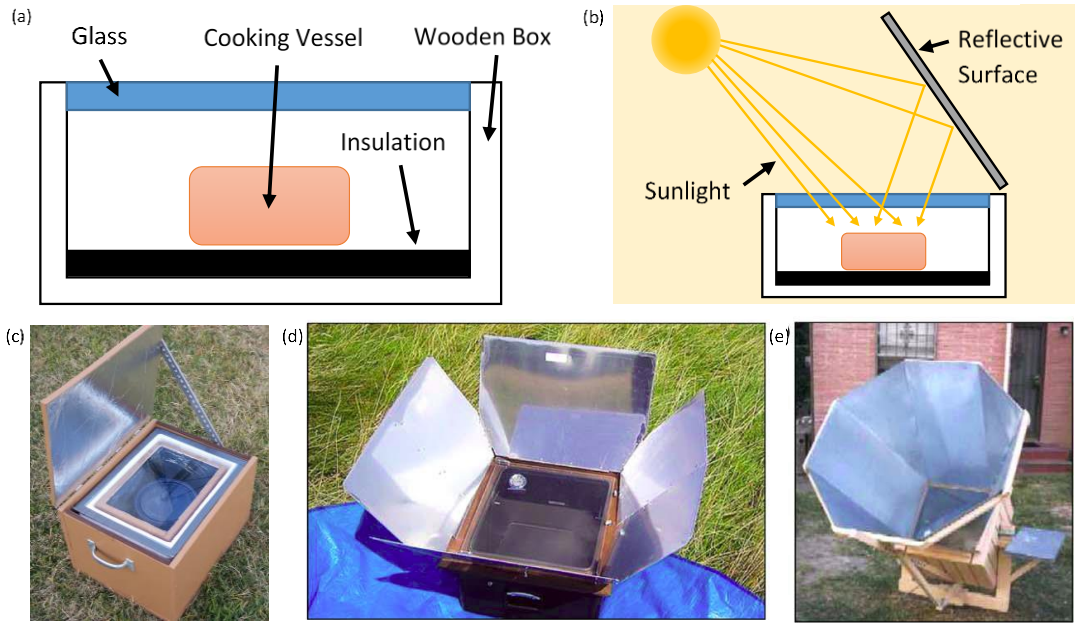


Figure 1.5 Box-type cookers: (a) diagram without reflector, (b) diagram demonstrating single reflector function, (c) with single reflectors, (d) with four reflectors, (e) and with eight reflectors [15].

1.4.2 Concentrating Solar Cookers

In a concentrating solar cooker the cooking is placed at the focal point of a concentrating mirror assembly. The system may concentrate light to either a point or line focus. Non-imaging systems may increase the concentration of light to the absorber without producing a focus. Due to the high concentration factors obtained, concentrating cookers typically reach much higher temperatures than other types of cookers, up to 300°C [15]. However, this is dependent upon the alignment of the optical axis of the concentrator with the sun, which must be maintained. The mirror assembly can be a single parabolic or spherical mirror, or alternatively made up of any compound assembly that produces a focus.

In addition to the tracking requirement other drawbacks include the intense light at the focal point being a fire and safety hazard. Generally they reach cooking temperatures much faster than other types of cookers and can fry foods as well as bake and boil them; roti, an Indian staple, requires cooking temperatures of 170° C. Despite their inherent advantages the complex mirror surfaces utilised in these designs can be quite expensive and concentrating cookers have so far not been as commercially successful as box or panel types.

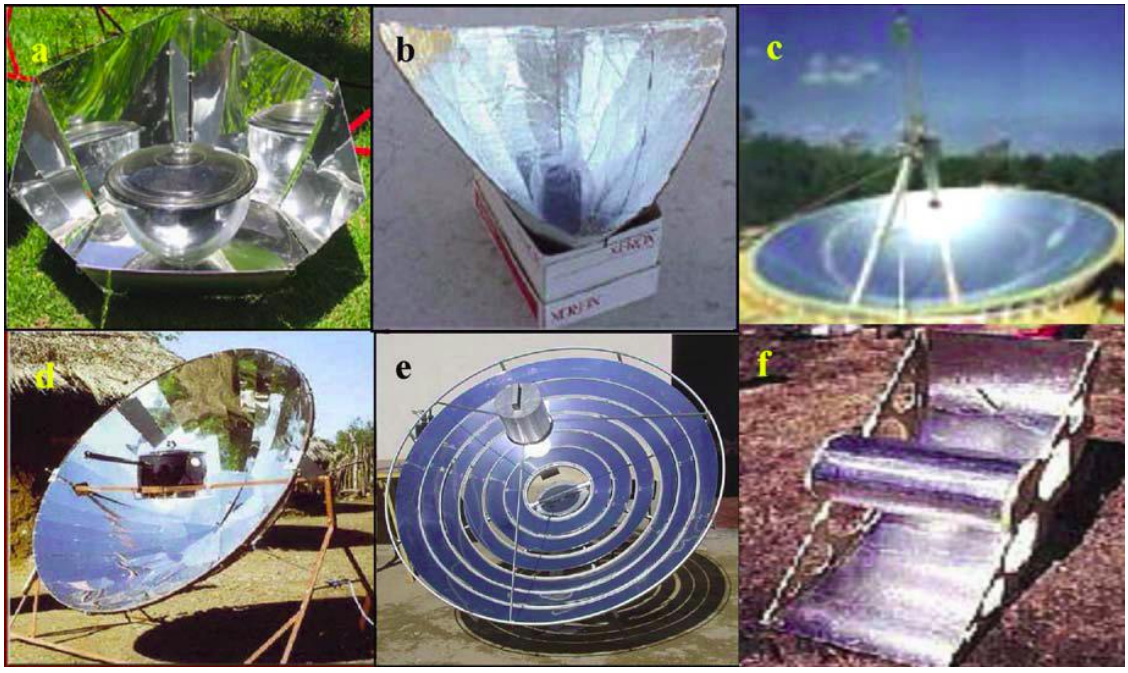


Figure 1.6 Concentrating type cookers; (a) panel cooker, (b) panel cooker, (c) spherical reflector, (d) parabolic reflector, (e) Fresnel concentrator and (f) cylindrical-parabolic concentrator [15].

1.4.3 Panel Solar Cookers

Panel type solar cookers can be considered a hybrid of box and concentrating type cookers. They generally consist of a cardboard reflector that concentrates sunlight onto a pot enclosed in a transparent plastic bag, see Figure 1.6(b). They are relatively common owing to their ease of assembly, portability and low-cost. However, they provide a limited cooking power and can suffer from poor durability.

1.5 Commercialisation of Solar Cookers

Whilst box-type cookers have made some modest inroads into the Indian market there are still few success stories in the commercialisation of solar cookers. The 600,000 cookers estimated in the Indian market account for less than 0.06% of the population. The commercialisation of solar cookers is subject to many of the same factors that prevent large scale commercialisation of enhanced wood stoves; chief among these are pricing and financing concerns. However, like many technologies intended for developing markets other factors, including cultural differences, cannot be ignored. Despite the limited commercialisation of solar cookers to date there clearly remains a huge market potential.

1.5.1 Market Potential

Clearly there is a huge potential market with the nearly 3 billion people who cook everyday with firewood or biomass. However, this potential will only be as strong as the solar cooker is affordable. Charcoal is often cheap, especially in the countryside, and the payback period for any cooker must be competitive. Available figures suggest that in some areas of Africa people spend as much as 240 euros a year on charcoal [21]. Additionally, there will be a strong correlation between the availability of local firewood and its market price.

Furthermore, even with minimal costings there will be financing issues for any rollout of solar cookers. Even if the cooker has a payback period of only a few months, people may not have the capital available to purchase a cooker outright. Microfinance options will need to

be investigated during any product development. To be affordable any labour costs in producing solar cookers will most likely have to borne in their intended markets.

1.5.2 Barriers to the Success of Solar Cookers

Lessons must be learnt from previous incarnations of solar cookers and from other renewable technologies. Some key barriers to the wider dissemination of renewable technologies include the lack of pressure for people to move to renewable technologies, the lack of appropriate technological solutions, the associated financial risks, and lack of access to finance [22]. In particular the high capital costs and subsequent lengthy payback periods combined with the low purchasing power of the intended users poses a major barrier. An analysis by Agrawal and Singh [23] investigated the optimum allocation of energy resources for cooking in the households of Uttar Pradesh, India. Solar cookers were found to be cost prohibitive whilst LPG, biogas and fuel wood provided the optimal allocation of resources, despite their attendant drawbacks. Notably the income of a household is the main determinant for their selection of cooking fuel [24].

Additional barriers include the lack of manpower for maintenance coupled with immature or inappropriate technologies and socio-cultural barriers including difficulties in changes to life style and disharmony with prevailing values [25]. These barriers have existed and have been recognised for some time. With these in mind the design of a successful solar cooker must emphasize its low-cost, simplicity of construction, ease of maintenance and versatility in method of use and availability of usage.

In addition to obvious financial obstacles to the success of a solar cooker there will always be considerations on the limits it poses on cooking methods. Cooking is a deep-rooted part of every culture, and it remains an integral and important part of our daily lives. Therefore, any cooker that necessitates a large deviation in cooking methods is unlikely to succeed. This versatility in cooking will not only be key in the cultural accommodation of a solar cooker but will be a key financial consideration. Clearly it cannot be sunny every day, a

successful solar cooker should be versatile enough to accommodate (or at a minimum not prohibit) cooking with alternative fuels on cloudy days.

A field test of solar cookers conducted in South Africa resulted in solar cookers being used to prepare 35% of all cooked meals during the trial [26] and they were used on 38% of all days. This resulted in an estimated payback period of only 8 months and up to 5 years depending on the type of cooker and the region for this particular cooker. Important to note is that in this study families still continued to use, on average, 2.5 different fuel sources for cooking; often mixing these sources in preparing a single meal. Clearly a solar cooker does not have to provide cooking of every single meal to be of use. Promisingly, many families requested to purchase their preferred solar cookers at the end of the trial.

1.6 The Reflex Concentrator

The Oxford reflex concentrator was designed to achieve high concentration factors, which enables high cooking temperatures as a solar cooker. However, unlike other concentrating cookers, the developable mirrors of the reflex concentrator will be cheap to manufacture. It will therefore be possible for a solar cooker based on the reflex concentrator to compete with box or panel type cookers for value for money. The key advantage of the Oxford reflex concentrator lies in the use of ingenious geometry that enables cheap flat mirrors to produce very high concentration factors.

Preliminary design work highlighted several other areas where the Oxford reflex concentrator will have advantages over competing solar cookers. Firstly, by virtue of its mirror's geometry, it will place the food to be cooked at a comfortable working height, easily accessible from the edge of the concentrator. Competing designs place the food at ground level where it can be contaminated with dust or at hard-to-reach locations in the centre of large mirrors. Furthermore, the high concentrations factors, and therefore high temperatures, obtainable should make many types of thermal storage open to the cooker, including phase

change thermal storage which relies of achieving particular melting (or boiling) temperatures. Phase change thermal storage can generally achieve much higher energy densities than sensible heat storage, whilst avoiding most of the added complexities associated with thermochemical storage. If the Oxford reflex concentrator were able to achieve sufficiently high temperatures to utilise some of these phase change thermal storages, it would represent a significant advantage over competing cooker designs. A cooker with thermal storage may then be able to provide heat for the evening meal.

Additionally, the developable mirrors will allow a system do be designed to be flat-packable, which increases portability and reduces transportation costs. An overview of the potential advantages of a solar cooker designed on the Oxford reflex concentrator, in comparison to existing solar cookers, are highlighted in Table 1.1.

Table 1.1 A broad overview of solar cookers in comparison to the expected performance of the reflex concentrator.

Type	Panel	Box	Dish	Reflex
Cost	Low	Moderate	High	Moderate
Weight	Light	Heavy	Moderate	Moderate
Durability	Poor	Moderate	Good	Good
Portability	High	Low	Low	High
Cooking Temperature	Low	Moderate	High	High

1.6.1 Industrial Partner

The inherent advantages of the reflex concentrator attracted interest from an industrial partner; Dytecna Ltd., a design engineering company which was expanding its areas of expertise to the clean tech sector. From early 2013, Dytecna had been designing a solar cooker dubbed ‘Albedo’ based on the reflex concentrator. In addition to the inherent advantages of the reflex concentrator design, Albedo was designed to be flat-packable and to contain an absolute minimum of parts or components to aid in ease of assembly. Work in collaboration with Dytecna led to the development of the first prototype cooker.

1.6.2 Previous Work

The Oxford reflex concentrator was originally envisaged as forming part of a Dish-Stirling system. These systems have long held records for the highest efficiency conversion of direct-normal sunlight into electricity from nearly 23% in 1986 [27] to 31% in recent years [28]. However, recent drops in the cost of silicon PV have led the solar market to move away from Dish-Stirling and other mirror-based technologies, such as concentrated photovoltaic (CPV). Large-scale PV farms continue to enjoy great commercial success, whilst efforts in grid-scale solar thermal power have centred on parabolic trough and solar power-tower designs.

However, Dish-Stirling systems still hold promise for small scale off-grid installations. A key advantage in using Stirling engines is that the heat source is external which lends its design to hybridisation in which heat can be provided from other sources in times of low insolation; in particular biomass and other low-quality fuels. However, any advantages that Dish-Stirling may still have are unlikely to be of any use to low-cost applications of the Oxford reflex concentrator.

2 Novel Mirror Geometry

The Oxford Reflex Concentrator is a uniquely configured solar concentrating system that achieves a point focus using two mirrors formed from developable surfaces. The advantage of the design lies in the fact that each of its mirrors can be formed from the in-situ bending of flat sheets. This eliminates the requirement for expensive 3-dimensional surfaces used in other concentrators, such as parabolic dishes.

The system utilises segments of a conical mirror and a linear parabolic trough. Independently each mirror forms a line focus given parallel light along their respective optical axes. When both mirrors are used correctly in conjunction these two line foci are in effect superimposed, and a point focus is thusly obtained, see Figure 2.1.

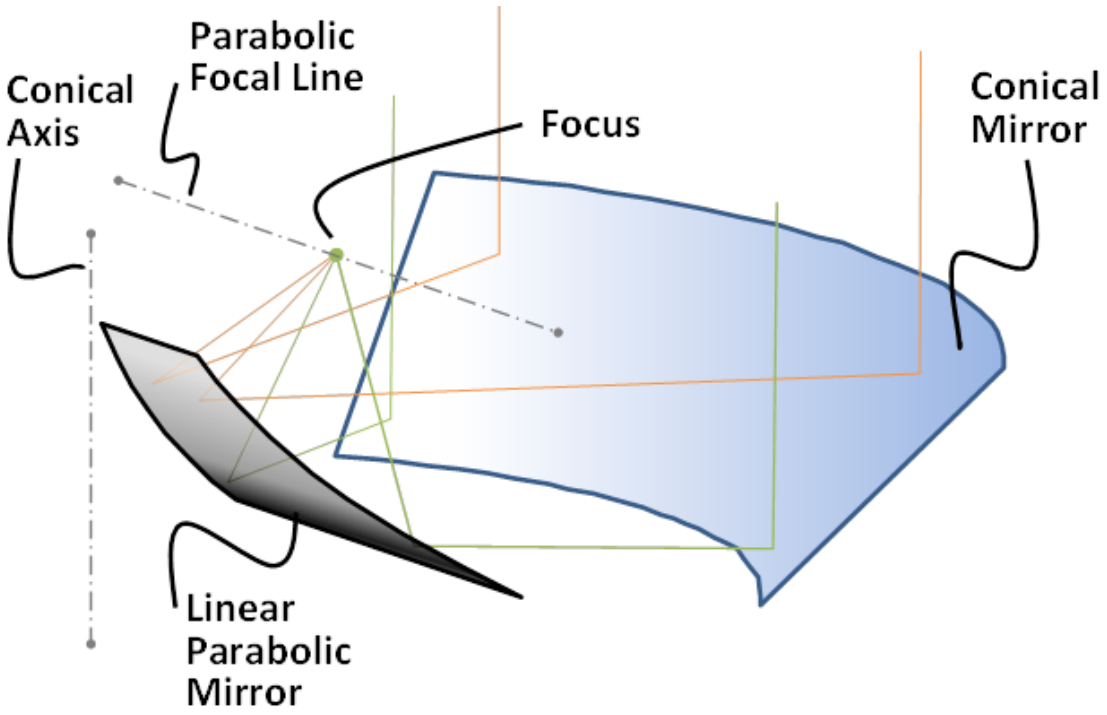


Figure 2.1 Mirror arrangement for the beam-up configuration of the Oxford reflex concentrator. The incident rays of light are parallel to the optical axis of the system, which as seen is vertical.

The use of developable surfaces for the system mirrors enables the solar cooker to be flat-packable for ease of transportation. Although there will be some trade-off in increased

reflectance losses, and increased mirror surface area requirements, compared to a single mirror system, these will be compensated for in the high solar concentrations obtainable and reduced manufacturing, transport, and assembly costs for the flat mirrors.

The mirror's exact arrangement is customisable with several variables remaining free. Furthermore, the parabolic mirror may be positioned in either a beam-up or beam-down configuration depending on usage requirements. However, beam-up configurations will generally hold an advantage in reduced convection losses from the absorber, and are therefore generally more useful in solar cooker applications.

The original idea for this configuration of mirrors came from discussions between Prof. Nick Jelley and Mike Dadd, with regards to an appropriate low-cost mirror system for use with Stirling engines.

2.1 Vector Proof of Mirror Geometry

The ability of the system to produce a point focus is of critical performance. The solving of this problem will express the geometric variables of the mirrors which allow for a valid point-focusing solution to the system. This may be done with a trigonometric solution, however a vector-based approach is considered here. This vector-based approach is both more elegant than the trigonometric solution and will also contribute to the basis for further work on ray tracing of the system.

2.1.1 Geometric Description

The basic geometry of the concentrator is shown in Figure 2.1. The cordinate system of the concentrator is chosen such that the parabolic mirror will be defined by a quadratic equation of the form $y = mx^2 + c$. Therefore the *y*-axis will be horizontal and the *x*-axis vertical, parallel rays of sunlight are incident onto the concentrator along the positive *x*-direction, i.e. downwards. The direction of the *z*-axis is then chosen to keep the coordinate system right-handed, see Figure 2.2.

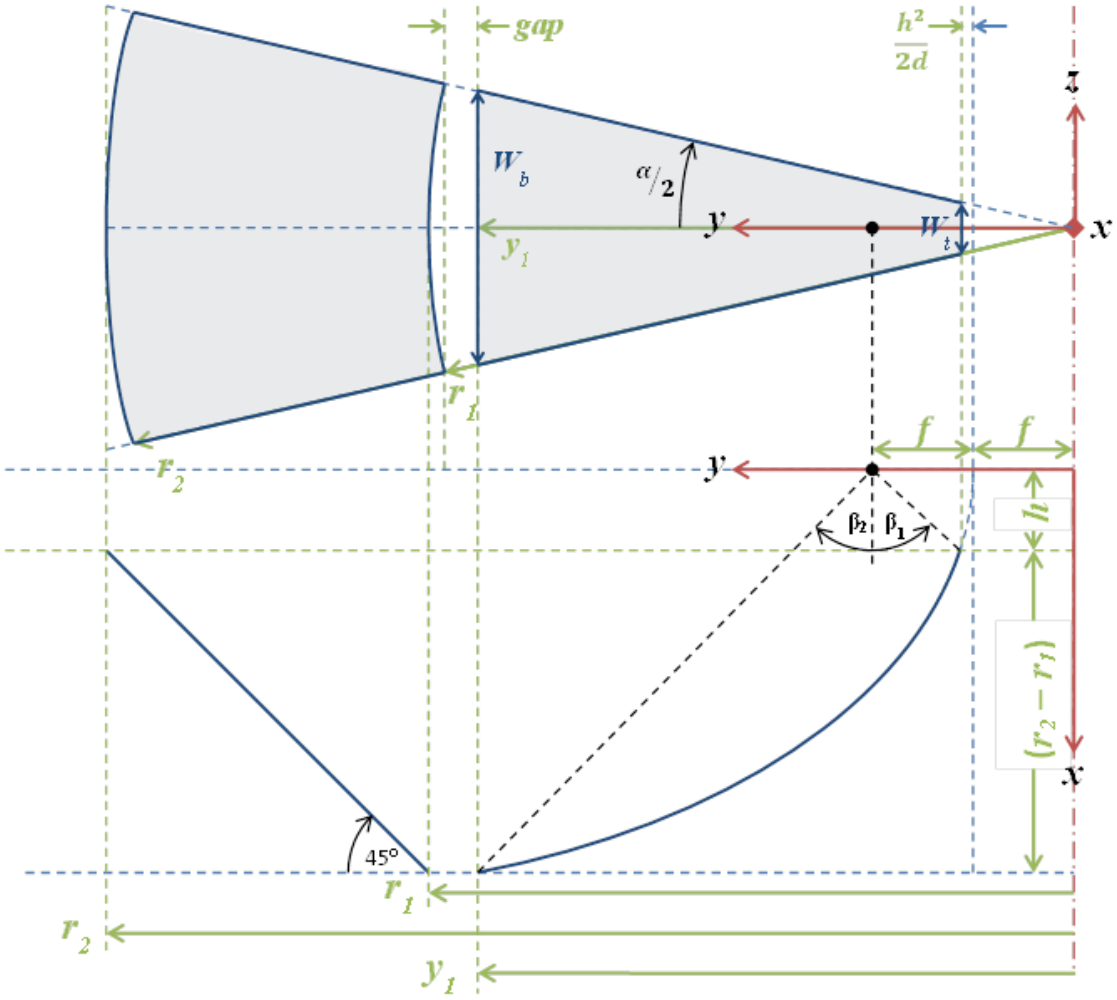


Figure 2.2 **Top and side views of reflex concentrator showing defined geometric variables. The side view is taken through the centre-line, i.e. z=0 , of the concentrator.**

The conical mirror's surface is at an angle of 45° to its centreline, the x-axis. When aligned correctly, vertical incident light will therefore be reflected through 90° from the conical mirror and form a horizontally-parallel wedge with a line-focus along the *x*-axis. The parabolic mirror must be positioned correctly to intercept this light.

A parabolic curve is by definition equidistant from its directrix and its focal point. The parabolic mirror is placed such that its directrix is collinear with the centreline of the conical mirror, the x-axis. Therefore, light incident on the parabolic mirror will travel the same distance to reach the focus of the parabolic mirror as it would have travelled to reach the line focus of the conical mirror. A point focus is therefore obtained following Fermat's principle; in which equidistant light paths will result in a point focus.

2.1.2 Geometric Variables

The exact configuration of the Reflex Concentrator is dependent on several variables and many possible configurations and optimisations are possible. The geometry of the reflex concentrator is fully defined by the variables in Table 2.1.

Table 2.1 Parameters required to fully define the geometry of the system.

Parameter	Description
r_1	Inner conical radius
r_2	Outer conical radius
α	Sector angle of the conical and parabolic mirrors
gap	Gap distance between the parabolic and the conical mirrors
	and one of:
f	Focal length of the parabolic mirror
d	Horizontal distance from *x*-axis to focal point
h	Height of focal point above the mirror top edge
s	Ratio of *h* to *f*

The horizontal distance from the x-axis to the focal point is defined as *d*, where

$$d = 2f \tag{2.1}$$

The focal length can be defined directly; however, from a design perspective it can be useful to define either the height of the focal point above the top of the mirror edges, *h*, or the ratio, *s*, of this height to the focal length.

$$s = \frac{h}{f} = 2\frac{h}{d} \tag{2.2}$$

The equation for a parabola with focal length *f* is given by

$$y = \frac{1}{4f}.x^2 \tag{2.3}$$

The equation of the parabolic mirror in the defined coordinate system is therefore

$$y = \frac{1}{4f}.x^2 + f = \frac{1}{2d}.x^2 + \frac{d}{2} \tag{2.4}$$

2.1.3 Vector Proof

A proof that the mirror system produces a point focus is obtained by propagating a general, vertical, incident vector off the conical mirror and then the parabolic mirror to a point in the focal plane, $x = 0$. In the defined coordinate system the position of an incident light ray on the conical mirror has the following parametric equations, see Figure 2.3:

$$x_c(\theta, r) = -r + (h + r_2) \tag{2.5}$$

$$y_c(\theta, r) = r\cos(\theta) \tag{2.6}$$

$$z_c(\theta, r) = r\sin(\theta) \tag{2.7}$$

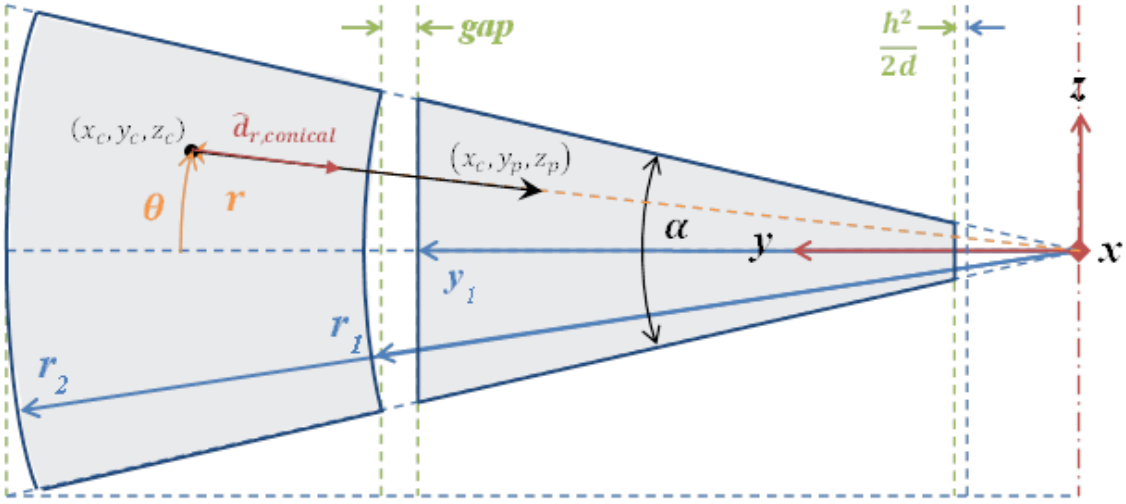


Figure 2.3 Top view of the reflected light ray off the conical mirror and incident upon the parabolic mirror. Here x_p, y_p and z_p are the respective *x*, *y* and *z* coordinates of the reflected light ray on the parabolic mirror.

If x_c, y_c and z_c are the respective *x*, *y* and *z* coordinates of the incident light ray on the conical mirror then we can define

$$\theta = \tan^{-1}\left(z_c/y_c\right), \quad \frac{-\alpha}{2} \leq \theta \leq \frac{\alpha}{2} \tag{2.8}$$

$$r = \sqrt{{y_c}^2 + {z_c}^2}, \quad r_1 \leq r \leq r_2 \tag{2.9}$$

The surface normal of the conical mirror may then be given by

$$\hat{d}_{n.conical} = \langle \frac{\partial x}{\partial \theta}, \frac{\partial y}{\partial \theta}, \frac{\partial z}{\partial \theta} \rangle \times \langle \frac{\partial x}{\partial r}, \frac{\partial y}{\partial r}, \frac{\partial z}{\partial r} \rangle = \frac{1}{\sqrt{2}} \langle -1, -\cos(\theta), -\sin(\theta) \rangle \tag{2.10}$$

The reflected ray is calculated using the vector form of Snell's Law.

$$\hat{d}_r = 2(\hat{d}_n.\hat{d}_i)\hat{d}_n - \hat{d}_i \quad \textbf{(2.11)}$$

Where $\hat{d}_r$ is the reflected unit vector and $\hat{d}_i$ is the unit vector of the incident light ray in the direction of the light source. Therefore:

$$\hat{d}_{i,conical} = \langle -1,0,0 \rangle \quad \textbf{(2.12)}$$

$$\hat{d}_{r,conical} = \langle 0, -\cos(\theta), -\sin(\theta) \rangle \quad \textbf{(2.13)}$$

The reflected ray can now be traced to the parabolic mirror. As there is no *x*-component to the reflected vector it will propagate horizontally from the conical mirror to the parabolic mirror, as in Figure 2.3, and

$$x_p = x_c \quad \textbf{(2.14)}$$

y_p is obtained by solving Equation 2.4 for x_p

$$y_p = \frac{1}{2d}{x_p}^2 + \frac{d}{2} = \frac{1}{2d}{x_c}^2 + \frac{d}{2} \quad \textbf{(2.15)}$$

The *z*-coordinate of the reflected light ray on the parabolic mirror is obtained by similarity.

$$z_p = z_c.\frac{y_p}{y_c} \quad \textbf{(2.16)}$$

The surface normal of the parabolic is now solved at this incident point. The parabolic mirror is constant in the z-direction thus the *z*-component of its surface normal will be zero. The surface normal is perpendicular to the gradient of the parabola, *m*, obtained by calculating the derivative of Equation 2.4.

$$m = \frac{dy}{dx} = \frac{x_p}{d} \quad \textbf{(2.17)}$$

Therefore the parabolic mirror surface normal is given by

$$\hat{d}_{n,parabolic} = \langle -\cos(\beta), -\sin(\beta), 0 \rangle \quad \textbf{(2.18)}$$

where:

$$\beta = \tan^{-1}\left(\frac{-1}{m}\right) = \tan^{-1}\left(\frac{-d}{x_p}\right) \quad \textbf{(2.19)}$$

The incident unit vector on the parabolic mirror, in the direction of the light source (in this case the conical mirror) is:

$$\hat{d}_{i,parabolic} = \langle 0, \cos(\theta), \sin(\theta) \rangle \quad \textbf{(2.20)}$$

The reflected unit vector is therefore given by Snell's Law as:

$$\hat{d}_{r,parabolic} = \langle -\cos(\theta)\sin(2\beta), -\cos(\theta)\cos(2\beta), \sin(\theta) \rangle \quad \textbf{(2.21)}$$

This vector is now propagated to the focal plane of the system, $x = 0$, as in Figure 2.4.

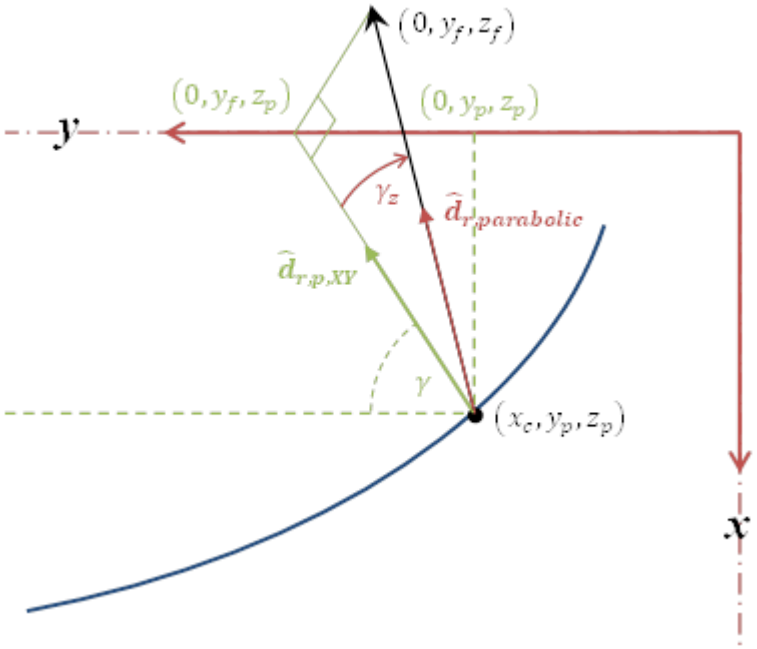


Figure 2.4 Side view of the reflected light ray from the parabolic mirror to the focal plane. Here $\hat{d}_{r,p,XY}$ is the projection of $\hat{d}_{r,parabolic}$ in the *x*-*y* plane.

The *y*-coordinate of the ray in the focal plane is calculated by solving

$$y_f = y_p + \frac{x_p}{\tan(\gamma)} \quad \textbf{(2.22)}$$

γ is obtained from the vector dot product of $\hat{d}_{r,p,XY}$ with the positive direction of the *y*-axis.

$$\cos(\gamma) = \hat{d}_{r,p,XY} . \langle 0,1,0 \rangle \quad \textbf{(2.23)}$$

From Equation 2.21, $\hat{d}_{r,XY}$ is therefore

$$\hat{d}_{r,XY} = \langle -\sin(2\beta), -\cos(2\beta), 0 \rangle \quad \textbf{(2.24)}$$

$$\therefore \gamma = \cos^{-1}(-\cos(2\beta)) \quad \textbf{(2.25)}$$

Following trigonometric identities:

$$\frac{1}{\tan(\gamma)} = \frac{1}{\tan(\cos^{-1}(-\cos(2\beta)))} =$$

$$\frac{-\cos(2\beta)}{\sqrt{1+\cos^2(2\beta)}} = \frac{\frac{\left({}^{d}/_{x_c}\right)^2 - 1}{1+\left({}^{d}/_{x_c}\right)^2}}{\sqrt{1-\left(\frac{\left({}^{d}/_{x_c}\right)^2 - 1}{1+\left({}^{d}/_{x_c}\right)^2}\right)^2}} = \frac{\left({}^{d}/_{x_c}\right)^2 - 1}{2\left({}^{d}/_{x_c}\right)} \quad \textbf{(2.26)}$$

Equation (2.22) can now be solved to find

$$y_f = \frac{1}{2d}{x_c}^2 + \frac{d}{2} + x_c.\left(\frac{\left({}^{d}/_{x_c}\right)^2 - 1}{2\left({}^{d}/_{x_c}\right)}\right) = d \quad \textbf{(2.27)}$$

The *y*-coordinate of the focal point, for a general incident ray, is therefore at *d*. To find the *z*-coordinate we must solve from Figure 2.4:

$$\tan(\gamma_Z) = \frac{z_p - z_f}{\sqrt{\left(y_p - y_f\right)^2 + {x_c}^2}} \quad \textbf{(2.28)}$$

where γ_Z is the angle between $\hat{d}_{r,parabolic}$ and the *x*-*y* plane. γ_Z is found from the dot product of $\hat{d}_{r,p,XY}$ and $\hat{d}_{r,parabolic}$.

$$\cos(\gamma_Z) = \hat{d}_r.\hat{d}_{r,XY} = \cos(\theta)\sin^2(2\beta) + \cos(\theta)\cos^2(2\beta) = \cos(\theta) \quad \textbf{(2.29)}$$

Therefore, using Equation 2.8

$$\tan(\gamma_Z) = \tan(\theta) = \tan\left(\tan^{-1}\left({}^{z_c}/_{y_c}\right)\right) = {}^{z_c}/_{y_c} \quad \textbf{(2.30)}$$

Equation 2.28 now becomes:

$$z_f = z_p - \frac{z_c}{y_c}\sqrt{\left(y_p - y_f\right)^2 + {x_c}^2} = z_c.\frac{y_p}{y_c} - \frac{z_c}{y_c}\sqrt{\left(\frac{1}{2d}{x_c}^2 + \frac{d}{2} - d\right)^2 + {x_c}^2} \quad \textbf{(2.31)}$$

$$\therefore\ z_f = 0 \tag{2.32}$$

The coordinates of the focal point are therefore given by

$$(x_f, y_f, z_f) = (0, d, 0) \tag{2.33}$$

This result is valid for all incident rays on the conical mirror that are vertical, and at any incident point on the conical mirror; a point focus is therefore obtained.

A similar treatment of non-vertical rays will give their final location in the focal plane. However, these off-axis rays will not form a point focus. Furthermore, in this case not all rays reflected from the conical mirror will intersect with the parabolic mirror. The ray tracing program developed utilises logic checks to ensure that propagated rays are indeed incident within the defined mirror geometries. The program then applies Snell's law for the calculation of reflected light rays.

2.2 Excel Design Aid

To assist in the design of a concentrator an Excel based design tool was developed to investigate different configurations for the mirrors. Although there are 5 variables available to define the system geometry completely, see Table 2.1, the selection of values for these 5 variables are not completely independent and restrictions are imposed on ranges of acceptable values, e.g. the outer conical radius must be larger than the inner conical radius.

In general most of these restrictions will be placed on the focal length of the parabolic mirror, after having defined other mirror geometries. From a design perspective it often makes more sense to define the conical mirror geometry first as this determines the surface area available for insolation and therefore the power of the system.

Therefore, given the selection of other variables the Excel design tool identifies and quantifies restrictions on the focal length of the parabolic mirror. The limits imposed on the selection of *f* are analogous to defining limits on *d*, *h*, or *s*. Firstly, the horizontal distance from

the centreline to the bottom edge of the parabolic mirror, y_1, is defined by the following relation:

$$y_1 = r_1.\cos\left(\frac{\alpha}{2}\right) - gap \quad \textbf{(2.34)}$$

This distance, y_1, may also be found by solving the quadratic equation at the bottom edge of the parabola:

$$y_1 = \frac{1}{2d}.\left(h + (r_2 - r_1)\right)^2 + \frac{d}{2} \quad \textbf{(2.35)}$$

Therefore:

$$r_1.\cos\left(\frac{\alpha}{2}\right) - gap = \frac{1}{2d}.\left(h + (r_2 - r_1)\right)^2 + \frac{d}{2} \quad \textbf{(2.36)}$$

If r_1, r_2, α and *gap* are defined then (2.36) becomes a function of *d* and *h* which can be solved as a quadratic in either *d* or *h*.

$$h^2 + 2h(r_2 - r_1) + (r_2 - r_1)^2 + d^2 - 2dy_1 = 0 \quad \textbf{(2.37)}$$

Equation 2.2 may also be substituted into 2.36, which may then be expressed equally as a function of *d* and *s* or *s* and *h.* Assigning a value to either *d*, *s* or *h* will then permit solving the quadratic for one of the other variables. The third variable will then be given by Equation 2.2.

2.2.1 Indeterminate Solutions to the Parabolic Geometry

However, in every case solving for the quadratic given by Equation 2.37 will result in two solutions. This indeterminate solution can lead to confusion as to which solution is desirable, or indeed if they both are. For example, if *h* is defined and the quadratic is solved for *d* (or *s*) two solutions are obtained. In many instances both of these solutions are valid and produce valid mirror geometries. Equivalently, if *s* is defined and the quadratic is solved for *d* (or *s*) there will now exist two solutions for *d*, see Figure 2.5; it is not clear which of these solutions holds most merit.

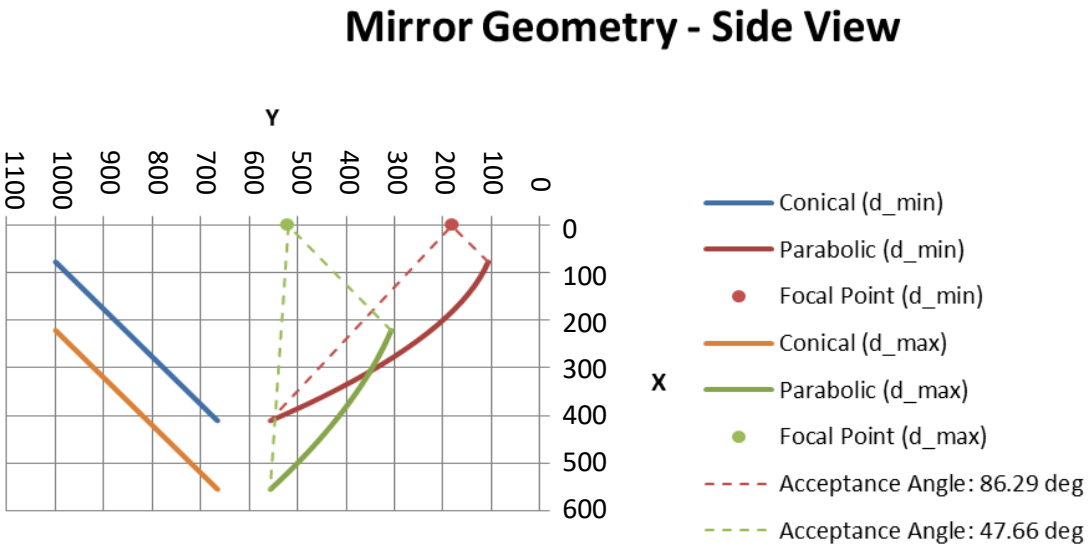


Figure 2.5 **Two real, valid solutions exist for the mirror configuration may exist after defining mirror variables, including *s*.**

However, this confusion may be avoided if *d* is chosen as the variable to set first. Although solving the quadratic produces two solutions for *h*, one of these solutions will always result in a negative value of *h*. As the geometry is defined, this negative value of *h* will never result in a valid mirror configuration, and can therefore be dismissed, see Figure 2.6.

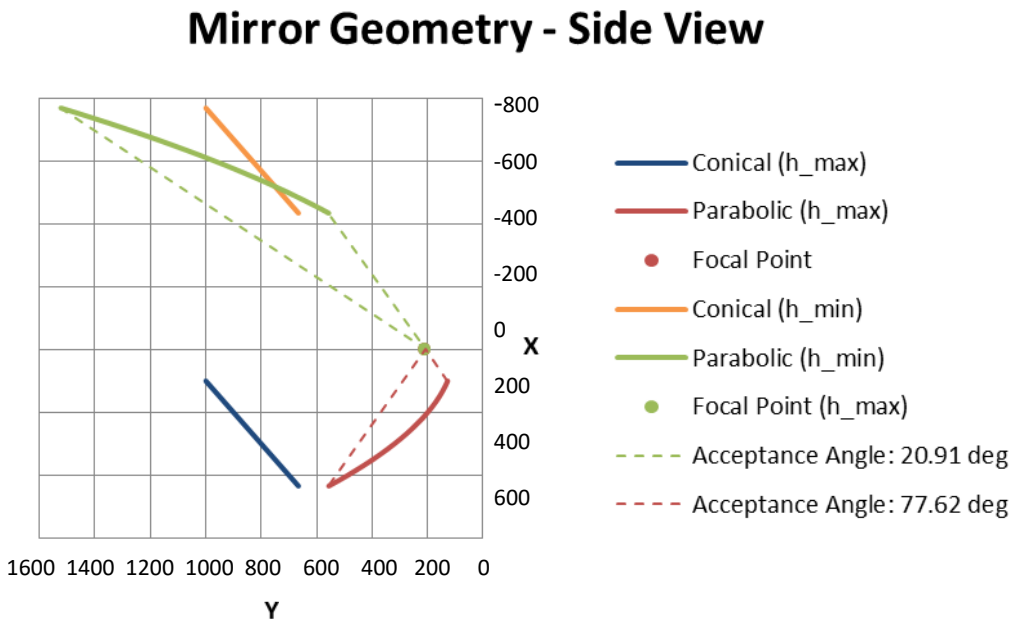


Figure 2.6 **The *h_min* solution obtained from the quadratic results in invalid mirror geometries which intersect. Only *h_max* results in an optically valid solution.**

In effect, setting *d* determines the shape of the parabolic mirror to consider. Solving for *h* will then select points along this defined parabolic. However, one of these points will always

result in invalid mirror geometries and can always be rejected. Therefore, the most instructive way of solving the quadratic equation is to set the value of *d* and solve for either *s* or *h*. If the invalid solution of *h* is dismissed in all cases then this quadratic becomes an analytical function, which aids in coding the geometry for optimisation.

However, although there will always be one invalid solution for *h* this does not ensure that the other solution for *h* is always valid. The second solution to *h* will only be valid over certain domains, which places some limits on the selection of variables for valid mirror geometry.

2.2.2 Defining the Parabolic Mirror Geometry

Setting *d* will define the curvature of the parabola and solving for *s* or *h* will then find two points on this parabola. Solving Equation 2.37 for *h* yields

$$h = -(r_2 - r_1) \pm \sqrt{2dy_1 - d^2} \tag{2.38}$$

The vertex of this quadratic will always lie in the negative plane, i.e. at $-(r_2 - r_1)$.The point focus, and indeed the receiver is required to be positioned above the top edge of the mirrors, therefore the value of *h* must be greater than zero. Therefore, only the positive solution to Equation 2.38 is valid, as in Figure 2.6. Furthermore this solution is only valid over a limited domain, i.e. when:

$$h = -(r_2 - r_1) + \sqrt{2dy_1 - d^2} > 0 \tag{2.39}$$

Equation 2.39 imposes the following restrictions on the domain of *d*:

$$\sqrt{2dy_1 - d^2} > (r_2 - r_1) \tag{2.40}$$

As $d > 0$ and $r_2 > r_1$:

$$0 > d^2 - 2dy_1 + (r_2 - r_1)^2 \tag{2.41}$$

Solving for *d*:

$$d < y_1 + \sqrt{{y_1}^2 - (r_2 - r_1)^2} \tag{2.42}$$

$$d > y_1 - \sqrt{{y_1}^2 - (r_2 - r_1)^2} \quad \textbf{(2.43)}$$

Furthermore, there is the restriction on the maximum value of *d* such that the receiver is not placed above the conical mirror, therefore:

$$d < r_1 \quad \textbf{(2.44)}$$

Lastly the determinant of the quadratic should be positive to ensure real solutions, which imposes:

$$d < 2y_1 \quad \textbf{(2.45)}$$

Therefore by selecting a value of *d* that satisfies Equations 2.42, 2.43, 2.44, and 2.45 a function is obtained to solve for *h*. An analogous solution exists for solving Equation 2.37 for *s*. As $d > 0$ we require that $s > 0$ when solving for *h*. All inequalities still hold with the simple substitution of Equation 2.2.

An Excel spread sheet was created to give a graphical representation of the proposed solutions and to aid in selection of the appropriate configuration. Once the parabolic and conical geometry has been defined the remaining physical dimensions of the concentrator can be calculated, such as the mirror support structures.

2.2.3 Flattened Mirror Geometry

The Excel spread sheet also calculates the required flat mirror geometries to produce the curved mirror profiles. The parabolic mirror, when flattened, is approximated by an isosceles trapezoid with bottom and top widths given by:

$$w_b = 2.y_1.\tan\left(\frac{\alpha}{2}\right) \quad \textbf{(2.46)}$$

$$w_t = \mathrm{d}\left(1 + \frac{\mathrm{s}^2}{4}\right).\tan\left(\frac{\alpha}{2}\right) \quad \textbf{(2.47)}$$

The height of the trapezoid is obtained from the arc length of the parabolic along its centreline. The trapezoidal approximation results in a slight excess of material; see Figure 2. 7.

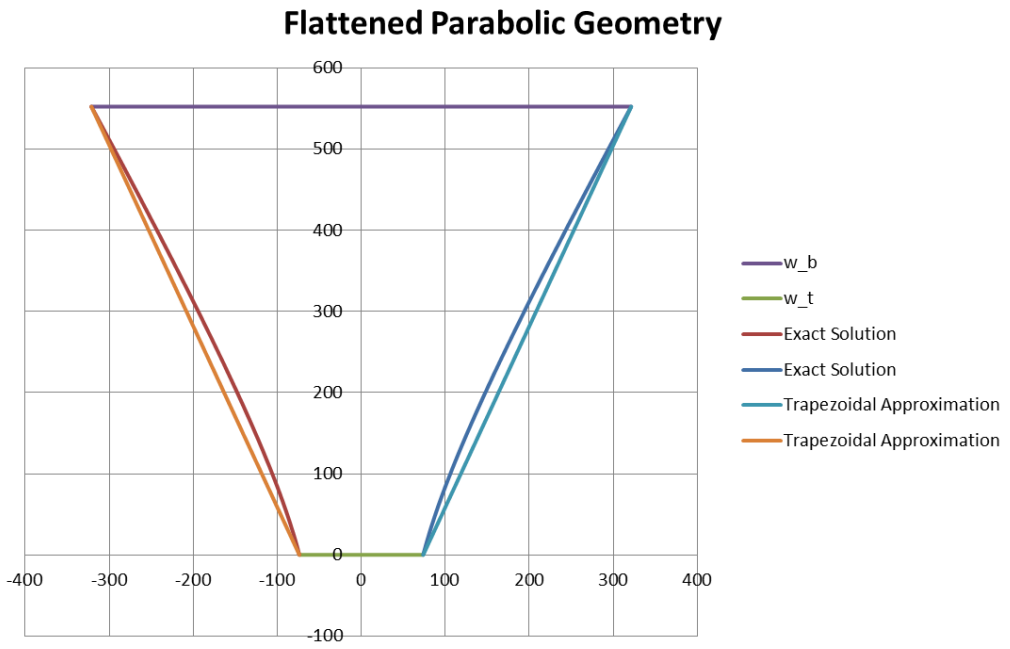


Figure 2.7 **Trapezoidal approximation of flattened parabolic mirror. The dimensions given are in mm for the parabolic mirror of the lab prototype.**

The geometry of the flattened conical mirror is given by an arc with inner radius $r_{1,flat}$, an outer radius $r_{2,flat}$, and sector angle α_{flat}, which are given by:

$$r_{1,flat} = r_1\sqrt{2} \quad \textbf{(2.48)}$$

$$r_{2,flat} = r_2\sqrt{2} \quad \textbf{(2.49)}$$

$$\alpha_{flat} = \frac{\alpha}{\sqrt{2}} \quad \textbf{(2.50)}$$

2.2.4 Selection of Mirror Geometry

In general, r_1, r_2 and α are chosen to maximise the conical mirror surface area or to define the maximum power of the system. Maximum mirror size is limited by the available size of reflective material from which the mirror is cut. Furthermore, pairs of conical and parabolic mirrors must be cut from this reflective sheet whilst minimising wastage from off-cuts. The selection of r_1, r_2 and α imposes some limits on the dimensions of the parabolic mirror.

The value of *gap* is then chosen to be as small as possible whilst leaving space for supporting structures between the mirrors. This distance will be non-zero but should be minimised. At large values, *gap* imposes severe restrictions on the selection of *d* and the positioning of the focal point of the system. Minimising *gap* for a given conical geometry will

maximise the domain of *d*, permitting a larger range of possible parabolic geometries. Additionally, when the system has a tracking error, larger *gap* distances will result in lower optical efficiencies. However, this effect is small and not a major consideration.

The choice of *d* (or *f*, *s*, *h*) will define the parabolic mirror; the optimisation of which will combine the following factors:

- *Acceptance angle*: the angle through which reflected light reaches the focal point from the parabolic mirror, see dashed lines in Figure 2. 5
- *Mean angle*: the mean angle through which reflected light reaches the focal point, measured as difference from vertical
- *Material constraints*: Material cost and limitation of wastage from off-cuts
- *Focal point position*: practical engineering considerations in placing the receiver at the focal point of the system.

Generally, a narrow cone of light incident normal to the receiver will tolerate manufacturing or tracking errors much better than a dispersed beam set at a glancing angle. The acceptance angle should therefore be minimised, whilst the mean angle should be as close to 0° as practicable. Conversely, the concentration factor of the system is maximised when the cone of light incident at the receiver is maximised. However, design considerations, including the possibility of using cavity receivers at the focal plane will influence this decision. Furthermore, limits on maximum concentrations may be desirable given limitations in absorber material properties. Finally, the combination of all these variables in defining the system will influence the performance with regards to off-axis rays.

2.2.5 Geometry of Laboratory Prototype

Given the development of the Excel design tool the geometry of a lab prototype concentrator was confirmed. This concentrator was already in the design phase during the development of the Excel tool. The dimensions of the prototype concentrator are given in Table 2.2.

Table 2.2 Key geometric variables for the lab prototype concentrator.

Variable	Value	Units
r_1	666	mm
r_2	1000	mm
α	60	degrees
gap	20.0	mm
y_1	557	mm
s	0.958	(ratio)
d	208	mm
h	99.5	mm

The conical dimensions had been selected to give an appropriately sized lab-scale demonstration device. The nominal power rating of the device would be 236 W under insolation of 1 sun or 1000 W/m^2 assuming mirror reflectivity's of 90%. The parabolic dimensions were selected to give a mean centreline acceptance angle close to zero.

The mean centreline angle is defined as the average of the angles taken by light from both the bottom and the top of the parabolic mirror to the focal point, refer to angles β_1 and β_2 in Figure 2.2. A mean acceptance angle of zero would therefore mean that the cone of light incident on an absorber placed at the focal point would be approximately vertical. However, the mean angle is only an approximate metric, it only accounts for the maximum extent of rays (at the bottom and top edges of the parabolic mirror) and not their relative density across this cone.

A Matlab code was developed to give greater understanding of the relationship between the determination of the parabolic mirror's geometry and the shape of the cone of light which would be incident at the focal point of the concentrator. Other acceptance and centreline angles were defined, as per Figure 2.8, to investigate the cone of light incident at

the focal point; top, bottom, and side refer to the edges of the parabolic whilst diagonal refers to the angle from the top-left of the parabolic to the bottom-right (and vice versa).

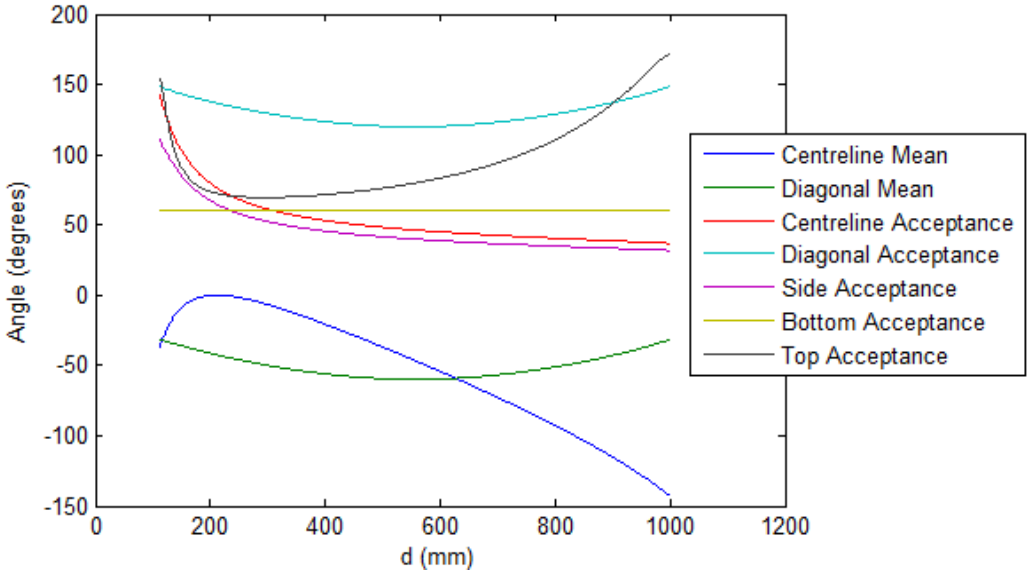


Figure 2.8 **Various centreline and acceptance angles across all possible values of *d* for the laboratory prototype concentrator.**

It can be clearly seen in Figure 2.8 why the value of 208 mm was chosen for *d*, at this value the centreline mean angle is approximately zero. The cone of light incident at the focal point will be approximately vertical in this case. Note that the bottom acceptance angle will not change given that varying the focal length of the parabolic will not change the bottom edge, which is defined by *gap*.

The behaviour of centreline acceptance indicates that a much larger acceptance angle is possible at low values of *d*. However, the acceptance angle cannot be reduced much from the chosen geometry, and could do so only given a proportionally much larger deviation in centreline mean.

3 Optical Modelling and Initial Experimental Results

The Oxford reflex concentrator is easily expected to outperform any non-concentrating optics such as box-type solar cookers. However, its performance compared to parabolic dish type concentrators is less certain. Although, there is a strong case for a cost advantage for the reflex concentrator this must be made with regards to its comparative optical performance.

Although the Excel design tool for the concentrator geometry illustrates the compromises to be made between choices in the geometric variables of the mirrors, it cannot provide a detailed analysis of the optical performance of the system. It was therefore necessary to develop the tools to properly investigate and determine how the system would perform in practice.

3.1 MATLAB Ray Tracing Program

A ray tracing code was developed in MATLAB to provide estimates of the optical performance of the Oxford reflex concentrator under varying conditions. These estimates were used to compare the reflex concentrator's performance with comparable parabolic dish designs and also to provide dimensions of the receiver area required under various tracking regimes.

3.1.1 Rationale behind Developing Ray Tracing Code

The decision was made to develop specific code for modelling of the Oxford reflex concentrator rather than to rely solely on existing ray tracing software. There were various reasons for this decision, primarily though the choice to develop specific code enabled a greater degree of customisation to be built into the ray tracing than was available in other software programs.

The relatively simple geometry of the mirrors meant that all geometric variables could be changed easily within the program. This enabled the effects of changing various mirror

properties to be investigated with relative ease. Other ray tracing software allows the user to define the mirror geometries, however this is always more difficult than simply changing the 5 variables in the MATLAB code which completely define the mirror geometry. Additionally, conical mirrors are not always part of ray tracing software's suite of included geometries.

Additionally, MATLAB enabled the code to be able to follow varying tracking regimes with greater ease. For example, when used as a solar cooker there will generally be manual adjustments to the mirrors in order to track the Sun through the sky, which all imaging point-focus systems must perform. In an automated system this tracking may be performed automatically using an electric motor, which is easily defined. However, in the case of low-cost solar cookers this tracking is likely to be performed manually, and is unlikely to be constant. One would expect tracking adjustments to be made manually on 5-10 minute intervals. Coding for this type of tracking in MATLAB is much easier, where one has complete control over the respective orientations of the Sun, the concentrator, and the receiver; which may all vary independently of one another.

In contrast to this, ray tracing software such as Zemax or SolTrace has much more difficulty in coping with constant and varying changes of orientation between the solar axis, optical axis of the system and the receiver. They can offer great results when studying static systems, but had more difficulty investigating dynamic tracking regimes than the MATLAB code that was developed.

Lastly, there has been relatively little interest in ray-tracing for small scale solar concentrating applications. Ray-tracing generally falls into two categories; 1) Ray-tracing for optical systems such as microscopes, 2) Ray-tracing for industrial scale solar thermal power plants of many hundreds of MW. Evidently, neither of these methods is greatly suited to the needs of the project. However, Zemax was used to verify specific ray tracing results from the MATLAB code. Dimensions of caustic regions and relative fluxes were all in good agreement.

3.1.2 Description of Program

There were many iterations of the MATLAB code, beginning with simple geometric models of the mirror assembly up to the final version which utilised Monte Carlo techniques, had accurate time-dependent sunshape profiles, included statistical approximations of mirror surface defects, was optimised for parallelization, and enabled a user-defined receiver profile and had the ability to include various tracking regimes for the concentrator.

At a basic level the program functions by manipulating large arrays of vectors, which represent rays of light. The simple geometry of the system removes any complicated calculations and all operations become simple matrix multiplication with elementary arithmetic.

The program randomly selects rays of light from the Sun, which are then given random locations on the conical mirror. These randomisations are uniform over the solid angle of the sun and over the conical mirror surface. Where these rays of light are incident on the conical mirror surface, a matrix of surface normal vectors is calculated. Snell's law then enables the reflected vectors to be calculated, which are then propagated to the parabolic mirror. Logic checks remove rays which do not intersect with mirror surfaces. The process is then repeated at the parabolic mirror surface and the reflected rays are propagated to the use-defined focal plane. The incident rays of light are sorted into bins which enable the calculation of fluxes over the receiver surface.

Mirror surface defects are modelled as a normal distribution away from the calculated surface normal vectors of the mirrors. This is implemented as a rotational matrix applied to the matrix of surface normals. This is implemented with a Monte Carlo technique which ensures that the rotations are done both uniformly about the surface normal, and by a normal distribution away from the surface normal. Different values for this surface defect can be applied to both the parabolic and conical mirrors.

In general the simple arithmetic means that the code is limited by the amount of available RAM rather than processor speed or number of cores. However, the sorting algorithm for the binning of incident rays on the receiver was by far the slowest process and received the largest performance gain when parallelised. After several improvements the program was able to run with approximately 40 million rays of light per run, using double-precision floating point numbers on a computer with 16 GB of RAM. Each matrix operation would in general take less than a second or so whilst the sorting algorithm could take several minutes depending on the fineness of the sorting mesh. For graphing purposes only a small subset of rays is selected, see Figure 3.1.

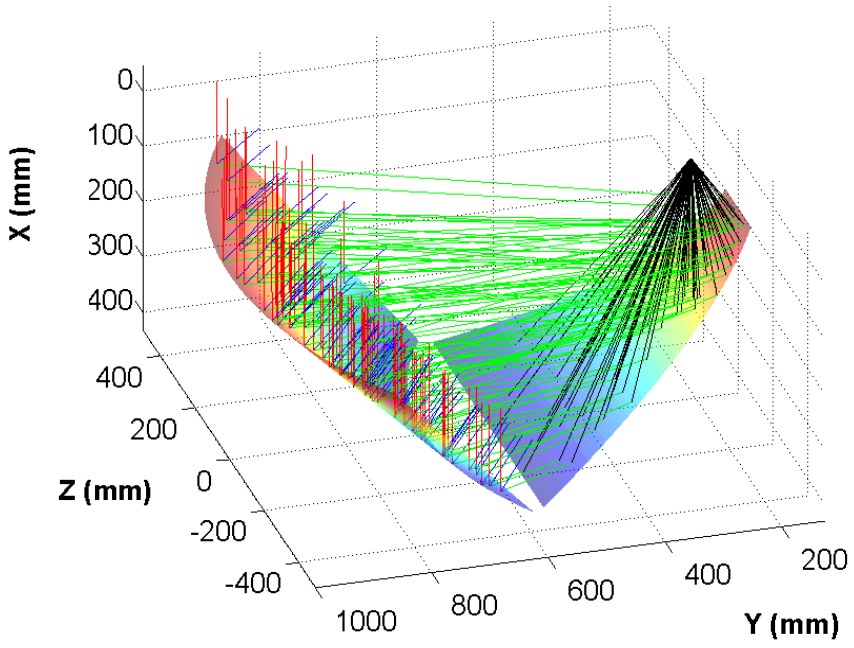


Figure 3.1 **Graphic representation of ray tracing. Incident vectors on the conical mirror are in red, conical surface normal are in blue, and reflected rays are in green and then black.**

As the rays from the Sun are distributed across its solid angle, rather than coming from a point source, the system never produces a point focus. Instead an image of the sun is produced in the focal plane. This is the case in Figure 3.1 where the black rays terminating in the focal plane do not meet at a point. However, the rays from the Sun also have varying relative intensities depending on their location on the solar disk.

3.1.3 Sunshape Profile

The flux profile of the Sun is not uniform over its surface. Additionally, due to atmospheric interaction not all light from the Sun will be within the solar disk and some light will be scattered into the aureole. However, a model exists for the intensity profile of light over the solar disk. Whilst the radiant flux profile in the aureole is dependent on atmospheric and climatic conditions, the radiant flux profile over the solar disk is not. Furthermore, whilst the total radiant flux over the solar disk is dependent on atmospheric conditions the relative profile intensity over the solar disk is not. This relative intensity profile is referred to as the sunshape. As defined by Biue et al [29] this sunshape profile is given by

$$\phi(\theta) = \frac{cos(0.326\theta)}{cos(0.308\theta)} \quad \text{for} \quad \{\theta \in \mathcal{R} | 0 \leq \theta \leq 4.65\, mrad\} \tag{3.1}$$

where the units of θ are in mrads. In general around 95% of the radiant flux will be measured within the solar disk, whilst the remainder falls with the circumsolar region, see Figure 3.2.

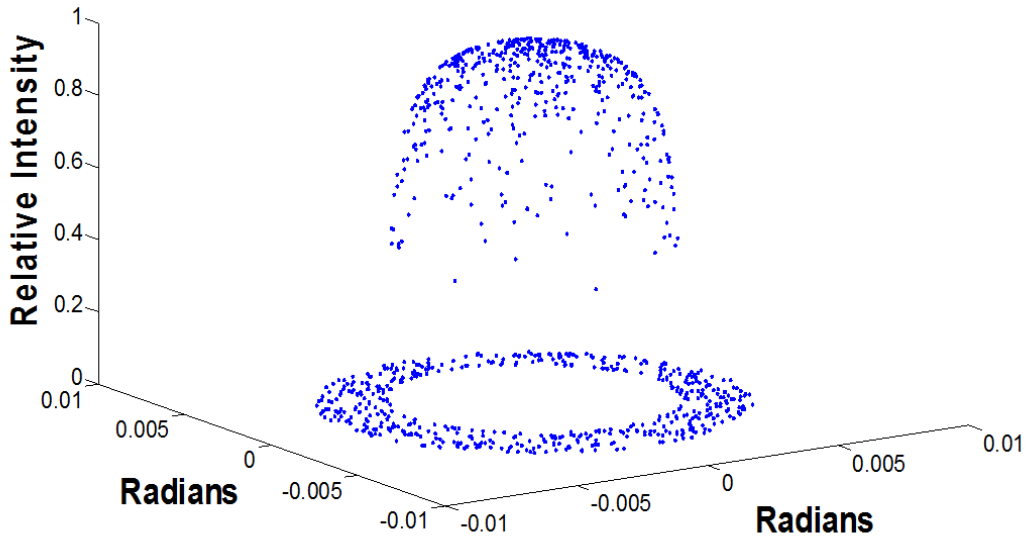


Figure 3.2 Sunshape profile demonstrating the relative radiant flux over the solar disk and aureole. Given the negligible energy contribution of radiant flux from the aureole, rays are only selected from the solar disk during flux calculations.

When selecting incident solar rays the program creates rays using a uniform distribution over the solid angle of the Sun. If the solid angle were to be increased to include the circumsolar region this would result in a drastic increase in computational effort for relatively little gain. Therefore, the MATLAB program restricts ray selection to the solar disk.

Once these rays are selected they are given a relative intensity given their location on the solar disk according to Equation 3.1. The relative solar weighting is then used to calculate the intensity of each ray given the number of rays, the direct normal irradiance, the surface area of the mirrors, and the cosine losses due to mirror orientation. During each subsequent reflection in the program the mirror's reflectivity will decrease this value. These values are then used to calculate the flux incident on the receiver.

3.1.4 On-Axis Results

The first results were a comparison of fluxes on the receivers of both the Oxford reflex concentrator and an equivalent parabolic dish. The comparison parabolic dish was chosen with the same aperture area, 0.291 m^2, as the prototype. A focal length of 438 mm was defined for the comparison parabolic dish such that both systems' mirrors have the same solid angle as measured from their focal points, 1.35 sr, which ensures a fair comparison of concentration factors. Comparisons were first made with both systems properly aligned with the Sun.

For both systems, one of which has two reflections, a mirror reflectivity of 95% is assumed when calculating losses before measuring irradiance in the focal plane. Plots were produced for the flux incident on the focal plane given a direct normal solar irradiance of 1000 W/m^2, see Figures 3.3a and 3.3b. The influence of using an actual sunshape profile can be seen in Figures 3.3a and 3.3b with the drop in incident flux near the edges of the caustic regions in both cases.

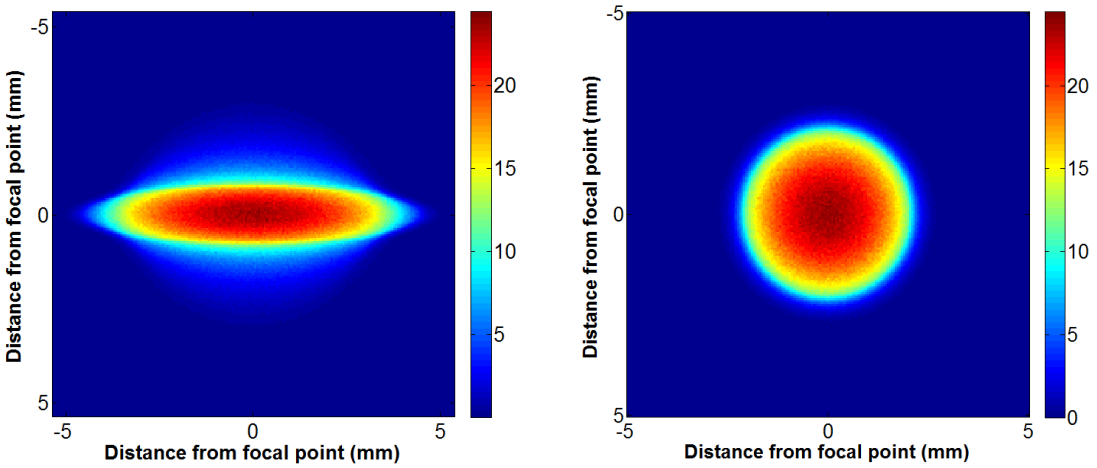


Figure 3.3 **Incident flux (MW/m²) on focal plane for (a) prototype concentrator geometry; (b) equivalent parabolic dish. Dimensions in mm.**

Both systems produced peak irradiance of around 24 MW/m^2 in the focal plane. These idealized cases have concentration factors of around 5,400 for the prototype reflex concentrator system and 10,000 for the parabolic dish. The sizes of the caustic regions are around 53 mm^2 and 27 mm^2 respectively. The theoretical maximum concentration factor for an axially symmetric system, subtending a solid angle of the 1.35 sr is 17,700 for a uniform solar disc of extent 4.65 mrad.

The discrepancy in concentration factors between the systems is due to the asymmetry of the prototype reflex concentrator system. Although, the vast majority of the incident flux in the focal plane falls within a narrow caustic region, there exists a small region of low flux. This region contributes little to the total incident flux, yet it impacts on the calculation of the concentration factor, which includes the region of all extreme rays. These extreme rays are excluded when looking at just the highest 90% of the incident flux on the focal plane, which falls in an area of 19 mm^2 for the proposed system and 14 mm^2 for the parabolic dish.

When comparing Figure 3.3a & 3.3b to the sunshape in Figure 3.2 it becomes clear that both systems use imaging optics. The flux profiles on their receivers are simply images on the sunshape, albeit stretched in the case of the prototype concentrator.

3.1.5 Off-Axis Results

Low-cost solar cookers are unlikely to have accurate tracking systems; therefore the performance of the two systems when subjected to tracking errors was investigated. The behaviour of the prototype system subject to a zenith tracking error of +2.5° was compared to the equivalent parabolic dish with the same tracking error. Zenith tracking errors are defined as rotations around the parabolic focal line and this error therefore corresponds to the Sun being +2.5° higher in the sky than the correct alignment for the concentrator.

With the +2.5° zenith tracking error, the prototype system's peak irradiance in the focal plane has fallen by an order of magnitude to 2.3 MW/m^2 and the 90% caustic region increases to around 900 mm^2 from 19 mm^2, see Figure 3.4.

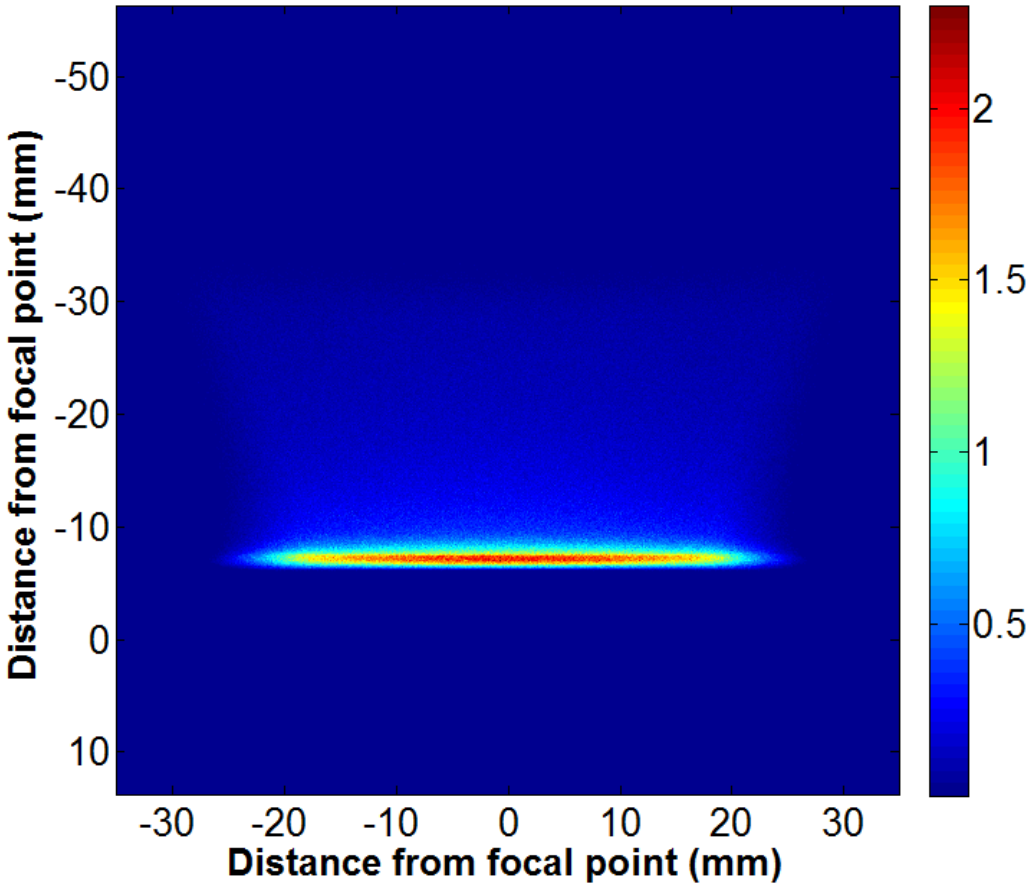


Figure 3.4 Incident flux (MW/m^2) on focal plane with a zenith tracking error of +2.5° for the prototype Oxford reflex concentrator geometry.

In comparison to the prototype system, the equivalent parabolic dish's peak irradiance in the focal plane has fallen but is comparatively much higher at 16 MW/m^2. Correspondingly its 90% caustic region is also much smaller at approximately 46 mm^2, see Figure 3.5.

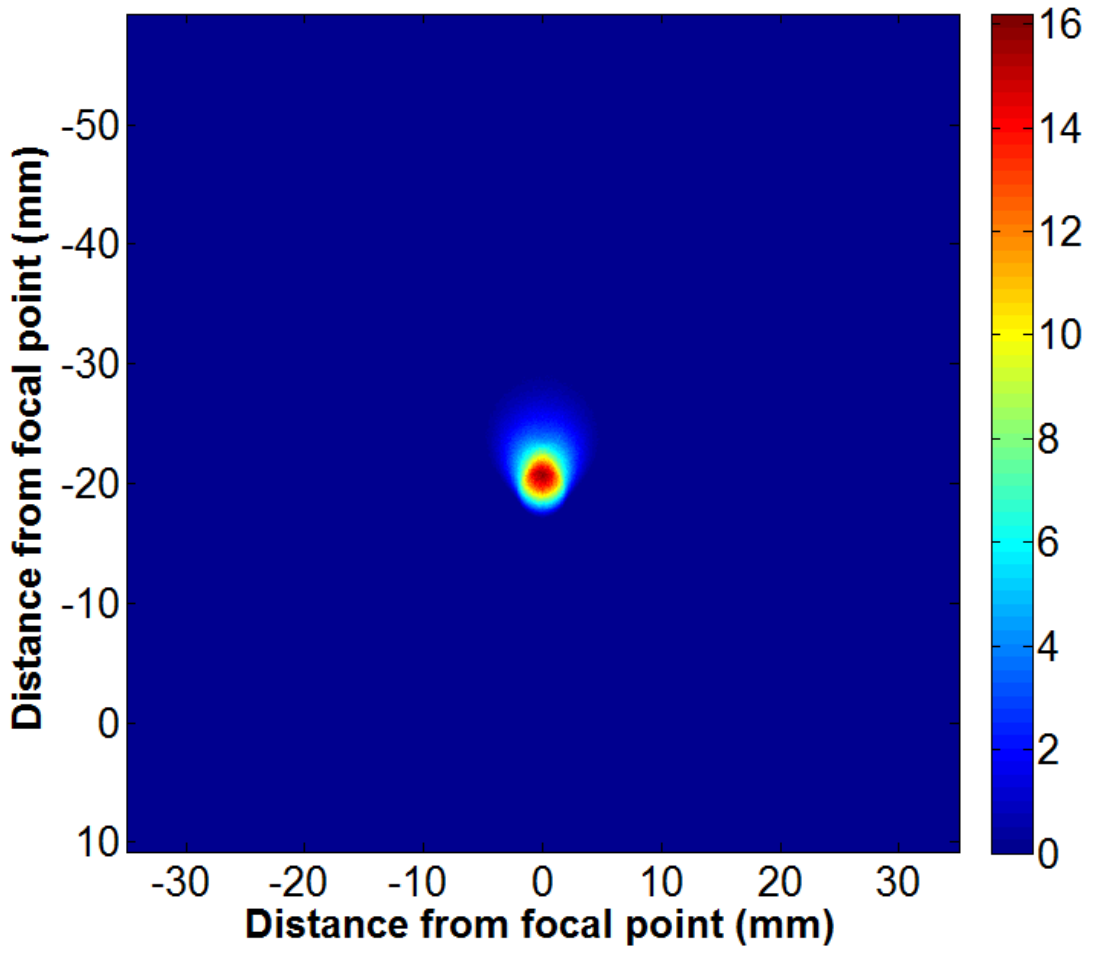


Figure 3.5 Incident flux (MW/m^2) on focal plane with a zenith tracking error of +2.5° for an equivalently parabolic dish.

In the proposed system the edge of the caustic region has translated about 7 mm from the original focal point and has broadened to 40 mm wide; in comparison the centre of the caustic region of the parabolic dish has translated 22 mm from the original focal point and has only broadened slightly.

The direction of the tracking error is important for the prototype system, but has no effect on the parabolic dish, due to its axial symmetry. Azimuthal errors are defined as solar movement when the system is aligned east-west along the parabolic focal line and therefore +2.5° azimuthal error corresponds to approximately 10 minutes of solar movement from alignment. Conversely, the rate that solar Zenith angles vary throughout the year is not constant; 2.5° is therefore only taken as an approximation for 10 days of solar movement.

For the Oxford reflex concentrator prototype, the zenith tracking error of +2.5° from Figure 3.4 should be compared to a zenith tracking error of -2.5° and an azimuthal tracking error of +2.5° as in Figures 3.6a & 3.6b.

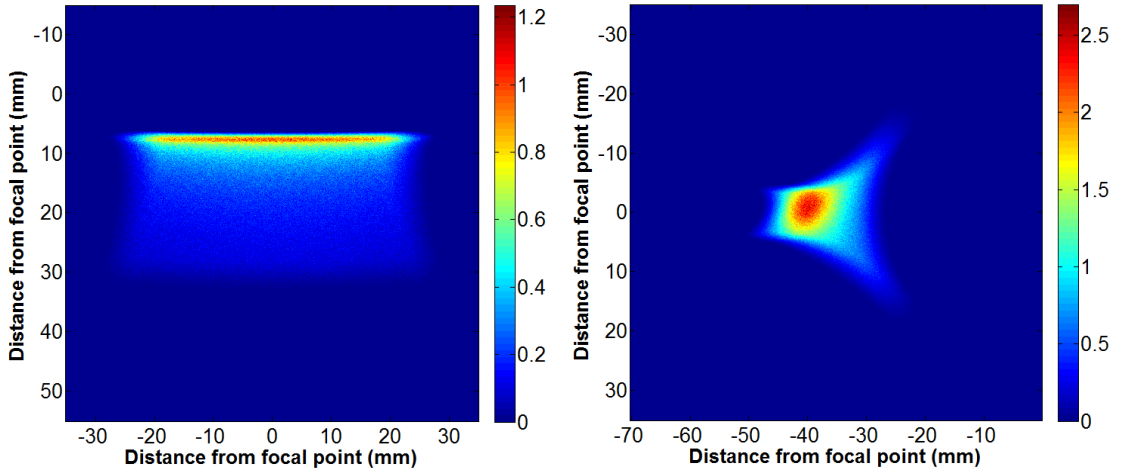


Figure 3.6 Incident flux (MW/m²) on focal plane of prototype concentrator with; (a) zenith tracking error of -2.5° (b) and an azimuthal tracking error of 2.5° for the Oxford reflex concentrator prototype. Dimensions in mm with scale in W/m².

For the proposed system the results are symmetrical with respect to azimuthal errors. Otherwise the direction of the tracking error has a significant effect on the flux measured in the focal plane. Whilst peak irradiances are similar, the displacement of the caustic region from the original position can be up to 40mm, but is generally less. These factors will affect the construction and placement of the receiver, as well as the maximum achievable temperature.

3.1.6 Summary of Ray Tracing Results

The prototype system based on the Oxford reflex concentrator compares favourably with the performance of an idealized parabolic dish when correctly aligned with the Sun. The translation of the caustic region is different with respect to the zenith and azimuthal tracking errors; compared with the parabolic dish these translations are less for zenith angle errors and more for azimuthal, see Table 3.1.

Table 3.1 Summary of results of flux measurements for the prototype system and an equivalent parabolic dish.

System	Tracking Error	Peak Irradiance (W/m^2)	Size of 90% Flux Caustic (mm^2)	Flux-Weighted Translation (mm)
Prototype	**0°**	24	19	0
Prototype	**Zenith +2.5°**	2.3	900	13
Prototype	**Zenith -2.5°**	1.2	930	15
Prototype	**Azimuth ±2.5°**	2.7	270	36
Parabolic Dish	**0°**	24	14	0
Parabolic Dish	**2.5°**	16	46	22

It has been demonstrated that using only single curvature surfaces the proposed system can match the desired properties of an analogous parabolic dish for certain applications under correct solar alignment. The peak irradiance measured in the focal plane of the proposed system is more sensitive to tracking errors than that of a comparable parabolic dish. However, the smaller translation of this caustic region, when misaligned in the zenith, could be advantageous. In the context of a solar cooker the reduction in flux concentration for off-axis rays is not significant provided all the flux is captured, which is easily achievable when the base of a cooking pot has an area of ~400 cm^2. Moreover, the reduced sensitivity to zenith angle error means less frequent zenith angle adjustment in a simple single-axis tracking system.

3.2 Experimental Optical Results of Prototype

The need to take lab measurements of the geometry of the concentrator, and its mirrors, is important for two reasons. Firstly, modelling performed in MATLAB needs to be verified experimentally. Additionally, the performance of the concentrator will be dependent not only on the geometry of the mirrors but ultimately on how accurately this mirror geometry can be assembled in practice. Factors that will affect how well the mirrors conform to the desired geometry are: tolerances in the manufacture and assembly of the support structure, rigidity of the supporting structure under loads, conformity of the mirrors to the supporting structure and the quality of the mirror's reflective surface.

These errors may not be able to be isolated and quantified individually; however, a quantitative measure of their cumulative effect on the concentrator's performance would greatly inform the concentrator's design. This cumulative effect will be quantified as a deviation of mirror surfaces from their geometrically defined surface normals. The magnitude of this deviation will be measured, based on experimental data in the lab, and fed back into performance models for the concentrator.

3.2.1 Prototype Concentrator

A SolidWorks model based on the previously defined mirror geometry was developed. Most of the supporting ribs of the structure were laser cut from aluminium sheet, whilst the brackets and remaining parts were machined, see Figures 3.7a & 3.7b.

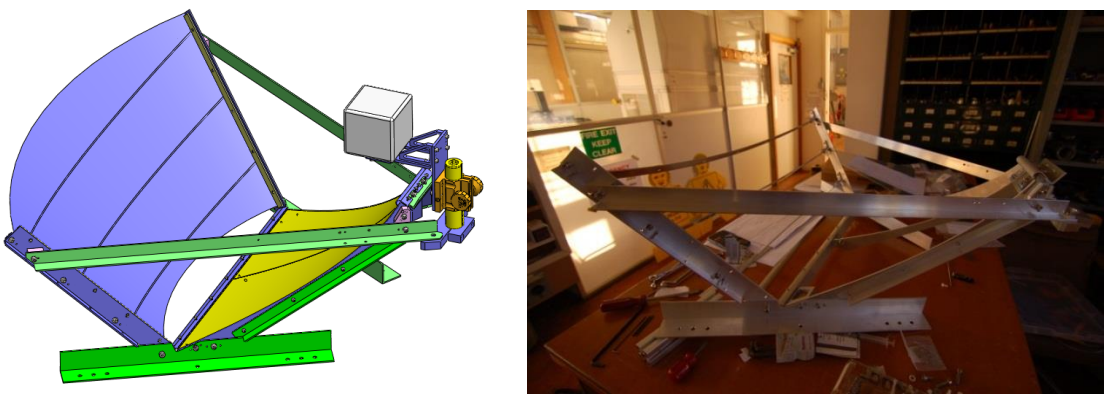


Figure 3.7 (a) Complete SolidWorks model and (b) assembled prototype without mirrors.

The parts were supplied by various companies whilst the only pieces produced in the Engineering Department were the mirrors, cut from a sheet of Alanod Miro-Sun© Weatherproof Reflective 90. This material comes with a 10 year warranty and is designed for long-term outdoor use with a weather resistant coating and a protective layer of epoxy on its back. Any corrosion of the aluminium mirrors is therefore unexpected over the time-scale of this project. The prototype was assembled in the cryogenics lab.

3.2.2 Experimental Aims

The purpose of the experiment was to quantify the cumulative effect of errors in the mirror surfaces. This was accomplished by using a known, parallel and correctly aligned laser beam to scan across the mirrors. This was achieved with the use of a test rig in which a laser pointer could be held in various parallel positions, see Figure 3.8.



Figure 3.8 Test rig with 4 laser pointers and grid paper in focal plane.

The prototype was attached to the test rig such that an exact positioning of the laser points, with respect to the concentrator, was possible. The test rig was made from Rexroth

extruded aluminium section, and a perforated plate was used to give well defined locations in which laser pointers could be placed. The test rig was assembled with a set square and spirit level to ensure that it was horizontal. Fully assembled this arrangement kept the horizontal planes of the perforated plate and the concentrator parallel, and when laser pointers were placed in the perforated plate not only would parallel light be obtained but this light would also be parallel with respect to the optical axis of the concentrator.

With the concentrator correctly aligned within the test rig, and in the absence of any errors in the mirror surfaces, the final position of a laser beam should be at the focal point of the concentrator. Any deviation from this position, in the focal plane, would therefore be due to errors in the mirror surfaces.

To measure the final position of the laser beam a Nikon D50 was placed, without a lens, such that its CCD sensor was coplanar with the focal plane of the concentrator. Therefore, the camera output would give a direct measurement of where the laser beam was incident in the focal plane. The quality of the mirror surfaces can consequently be quantified by a statistical analysis of the final laser point positions in the focal plane.

3.2.3 Laser Pointers

Several sub mW laser pointers were obtained in order to perform the scanning of the mirror surfaces. It was necessary to house these lasers inside brass fitting to ensure that they were positioned correctly with regards to the test rig.

3.2.3.1 Laser Pointer Characteristics

The laser pointers, Velleman model MP1000s, emit at 650nm. To keep them well within Class 1 specifications they were fitted with filters. The filters were obtained from Lee Filters and are '140 Summer Blue,' which transmit approximately 25% of light at 650nm, see Figure 3.9a for the transmittance data for this particular filter. These filters were cut and placed in the bottom of the brass fittings, see Figure 3.9b.

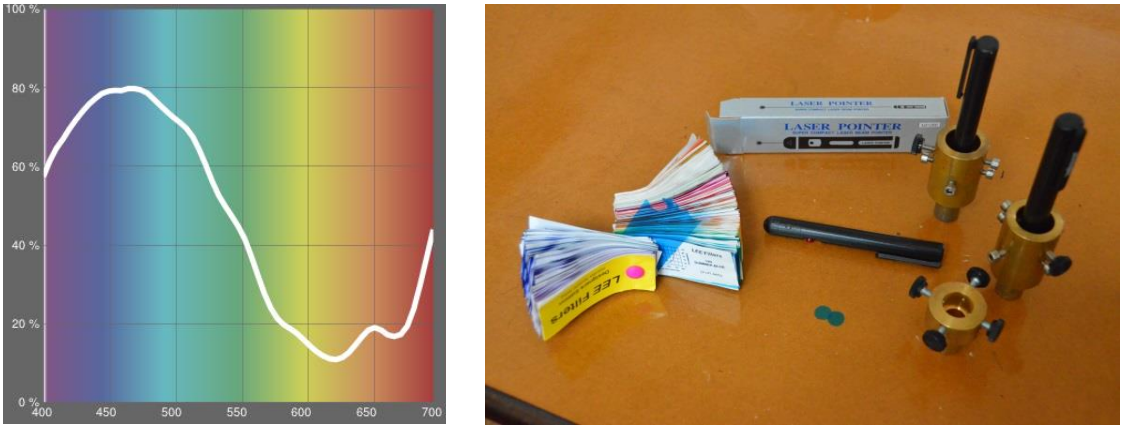


Figure 3.9 (a) Transmission curve for 140 Summer Blue filter. (b) Assembly of filters inside brass mounts.

Despite using the filter, it was later found that very often the intensity of the incident laser beam on the CCD in the Nikon D50 would saturate the sensor. However, the filters were still useful as a further safety measure. During testing, the same laser was used for each set of results and for all trials. The batteries of this laser were replaced periodically to ensure that the output was relatively constant. The manufacturer's data sheet indicated that they would have a battery lifetime of 2 hours of continuous use. However, most of the data taken for the mirrors does not require information regarding the intensity of the laser.

3.2.3.2 Physical Positioning of the Laser Pointer

The brass fittings used to hold the laser pointers in position and to locate them with respect to the holes in the test rig's perforated plate are shown in Figure 3.10. Four adjusting screws enabled the laser pointer to be aligned with the axis of the brass holder.



Figure 3.10 Brass fittings designs, from left to right, 1) original, 2) final, 3) intermediate.

The original configuration was able to produce a beam of light that was parallel with respect to the optical axis of the concentrator. However, there were a few drawbacks with the design. Primarily, the laser pointer extended some distance from the top of the brass fitting and could be accidentally bumped out of alignment when handled. Additionally, the on button of the laser pointer had to be secured with a modified clothes peg which would often fall off. Pressing the button manually for each measurement was deemed not ideal as pressing with too much force against the laser pointer could move it out of position.

To improve on this design the brass fitting was extended so as to incorporate two additional bolts; one of these would press the laser pointer's button the other would provide reactive force on the opposite side of the laser pointer to keep it in place. These two bolts allowed the laser pointer to be moved over the test rig without risk of bumping the pointer out of alignment. The intermediate design in Figure 3.10 was used with the perforated plate on the test rig. The final design featured a square flange for use in later testing.

3.2.3.3 Calibration of Laser Pointer Alignment

To ensure the laser pointer was indeed parallel with the optical axis of the concentrator a calibration target was used. The target was placed on the floor and the laser pointer was centred onto the target axis, see Figure 3.11.



Figure 3.11 Laser pointer with target ensuring beam was parallel with optical axis of the concentrator.

The laser pointer was then rotated in place; if it is parallel to the optical axis of the system then the laser beam should be perpendicular to the floor and the laser point incident on the target should not move. In practice the alignment of the laser pointer was adjusted, by turning the bolts in the brass fitting, in an iterative process until the laser point no longer moved on the target. In Figures 3.12a & 3.12b the correctly aligned beam has been rotated by 90° with no deviation of the laser point from the centre of the target.

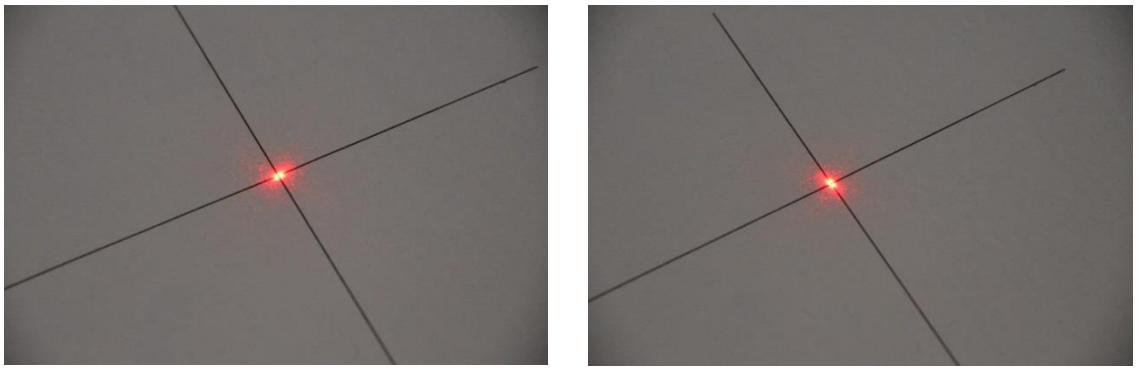


Figure 3.12 (a) Laser point incident on target (b) Laser point rotated by 90° from previous figure.

3.2.3.4 Laser Pointer Beam Spread

Beam spread should not have an effect on the localisation of the peak intensity measure for the incident laser point on the CCD. However, beam spread from the lasers was measured to ensure it did not have an effect on the results. The angular spread of the laser beam was estimated to be low so measurements of the size of the laser pointer spot size were taken at greatly different distances and then compared, see Figures 3.13a & 3.13b.

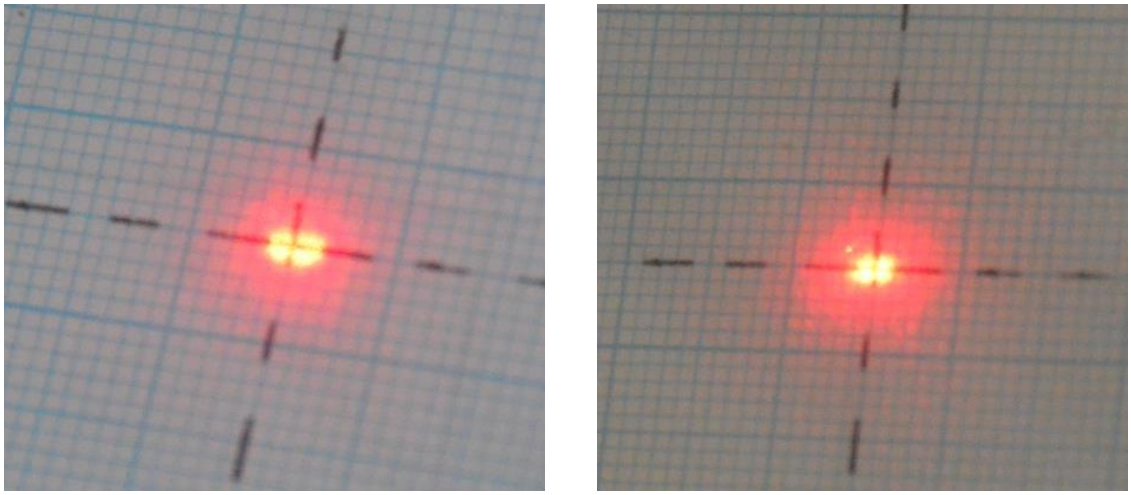


Figure 3.13 Image of the laser beam incident on grid paper from (a) 15cm and (b) 118cm distance.

In Figures 3.13a & 3.13b the peak intensity region of the laser, which appears yellow, does not seem to change much in size and is approximately 5mm^2 throughout. However, the overall size of the laser spot changes slightly and is summarised below in Table 3.2. The total spot size is calculated by summation of the illuminated grid squares in each figure, with both photos taken at the same exposure settings.

Table 3.2 Laser spot size with increased beam path length.

Laser path length	15 cm	118 cm
Total Spot Size	28 mm^2	50 mm^2

For the test rig, the laser beam path length from the perforated plate to the focal plane of the concentrator is 140cm, which is uniform over the entire concentrator. The final laser spot, without reflections, should therefore be similar to that of Figure 3.13b at 118 cm. Given that from 15 cm to 118 cm path length there was an increase in the radius of the total beam from 3 mm to 4 mm a measurement of the beam spread can be made. The angular size of the beam spread is measured to be only 0.08 mrad and the beam should therefore be considered parallel to the degrees of accuracy used elsewhere. For the central spot of peak intensity there seems to be no spread in this region from Figure 3.13a to Figure 3.13b.

The beam profile is not symmetrical and appears elliptical. The orientation of the laser beam between measurements was kept uniform to minimise any effect this may have had on the data. However, given that the laser is almost parallel with very little beam spread, any effect due to its orientation would be negligible.

With the laser calibrated some quick measurements were taken with a sheet of grid paper placed in the focal plane. This was done to double check the alignment of the system before placing the camera at the focal point. Grid paper was attached to a traversing mechanism to enable it to be placed at the height of the focal plane. Measurements confirmed that there was low enough spread of the resultant laser points on the gird paper in

the focal plane to enable the use of more accurate measurements with a CCD Sensor in a Nikon D50, see Figure 3.14b.

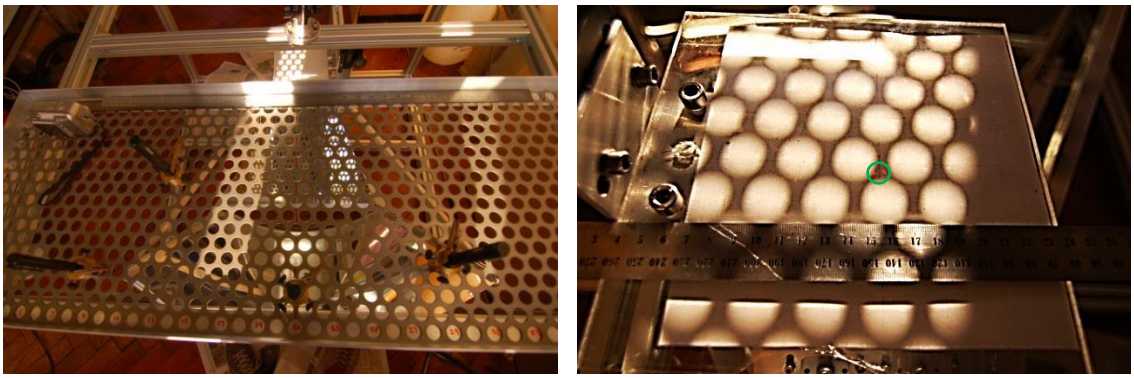


Figure 3.14 Laser pointers in various positions (b) Resultant laser point in the focal plane.

The spread of the resultant laser points in the focal plane initially measured was as, at maximum, of the order of 20mm for all locations across the conical mirror. The physical size of the CCD sensor in a Nikon D50 is 15.5mm by 23.7mm.

3.2.4 Experimental Methodology

For each data set the laser pointer was placed in every perforated plate position that resulted in a laser point being visible in the sensor of the Nikon D50. The first data sets were taken with 160 such positions, which are labelled in Figure 3.15.



Figure 3.15 Perforated plate with regular spacing for placement of laser pointer, holes are numbered left to right, bottom to top as outlined in green. The red line is the axis of symmetry of the concentrator.

Not all laser points incident on the mirrors would reflect onto the camera's sensor; the lens mount of the camera acts as an aperture, blocking incident light at wide angles from reaching

the sensor. Owing to errors in the mirror surfaces and tolerancing in the placement of the concentrator assembly the location of these valid plate positions were not always symmetric about the centreline of the concentrator, as per the green outline in Figure 3.15.

3.2.5 Camera

The camera used for all measurements is a Nikon D50 digital SLR. The CCD sensor in this camera has 2000 x 3008 pixels with physical dimensions of 15.5 mm x 23.7 mm. The sensor is an 8-bit sensor with a Bayer filter. For all measurements the shutter speed was set at 1/4000 seconds and the ISO at 200. No lens was attached for measurements projecting the laser beams directly onto the sensor placed in the focal plane. However, incident light onto the camera's sensor was somewhat limited by the aperture of the camera's lens mount. This lens mount has the dimensions of a standard Nikon F-mount, consisting of an inner diameter of 35 mm with a flange to focal plane distance of 46.5 mm. Some incident laser light would not fall within this aperture and results where therefore limited to the central grouping of laser positions outlined in green in Figure 3.15, and not the entire conical surface area outlined in black in Figure 3.15.

3.2.5.1 The CCD Sensor

The structure of the RGGB sensor, or Bayer filter, is as shown in Figures 3.16a & 3.16b. In practice the Bayer filter may not necessarily line up exactly with the pixels underneath.

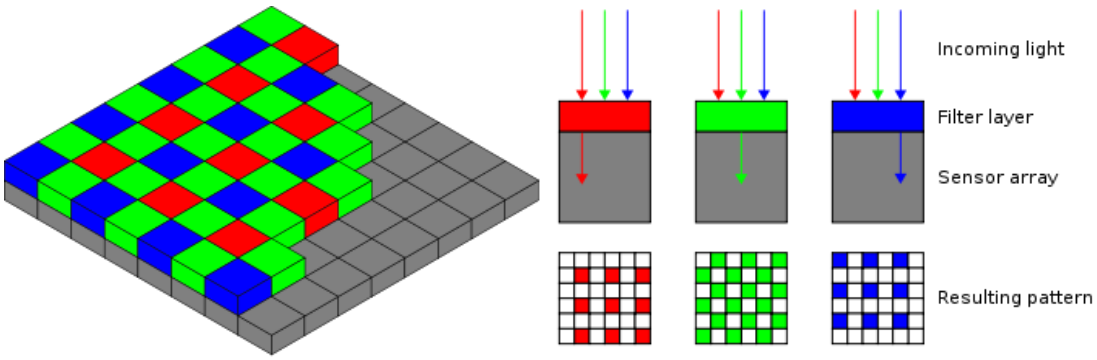


Figure 3.16 (a) General layout of a RGGB sensor (b) Generalised output for separate colour channels [30]**.**

3.2.5.2 File Output Type

Raw data is available from the camera in the form of a NEF file which contains 8-bit intensity data for each pixel, i.e. a 2000 x 3008 matrix. The colour of the filter at each pixel, from the Bayer pattern of the sensor, is then inferred from the data. Alternatively, the camera can output data in the form of a 12-bit jpeg file. This is achieved by simple scaling of the 8-bit data into 12-bits. The camera will then interpolate data for every pixel such that there is a red, green and blue intensity value given at each pixel location, i.e. a 2000 x 3008 x 3 matrix. The values used for the interpolation depend on the make and firmware edition of the camera and are proprietary. Furthermore, they will vary depending on settings within the camera; the white balance, colour saturation, colour vividness, sharpness and contrast.

Intensity measurements were taken using this raw data with some limited success. However, for the localisation data for the laser beam positions it was much easier to simply use jpeg as the file output type for the camera. Firstly, intensity information was not necessarily required to find the laser beam spot. Secondly, the file size for the RAW data was prohibitive when only information for a small laser spot was required.

Both jpeg and raw output from the camera was processed in MATLAB with the files firstly being converted into their equivalent size matrices before data manipulation.

3.2.5.3 Saturation of Pixel Data

The CCD sensor would often saturate under the laser beam. This occurred not only for red pixels, as expected with the 650nm laser, but also for blue and green pixels. This was evident from the values recorded in the blue and green channels of the raw camera files. This could be due to misalignment of the Bayer filter with the underlying pixel structure, the laser beam being so intense that even the low transmittance of the blue and green filters at 650nm would saturate these pixels, or due to charge overflow from the adjacent ‘red’ pixels in the CCD sensor. For the purposes of measuring the beam centre the cause was not important and the saturated blue and green pixels gave valuable information on the beam centroid.

3.2.5.4 Defining Beam Centre from Saturated Data

The following data was obtained from the jpeg image file DSC_1155. The first image, Figure 3.17, is the file output in jpeg format and should therefore be considered a photo. This image was taken for a laser pointer placed at position 26 on the perforated plate, which is relatively central, see Figure 3.15.

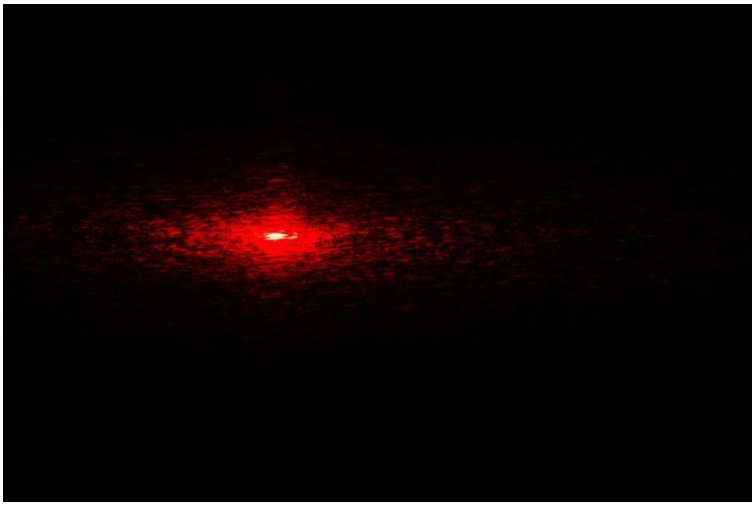


Figure 3.17 Photo output in jpeg format, file DSC_1155, sensor size 15.5 x 23.7 mm.

This jpeg file can then be decomposed into the red, green and blue colour channels. In Figure 3.18 we see the Red Channel, which is clearly saturated over a large region. The image was scaled back to 8-bit and the maximum value is therefore 255, which occurs over a large region of the red channel.

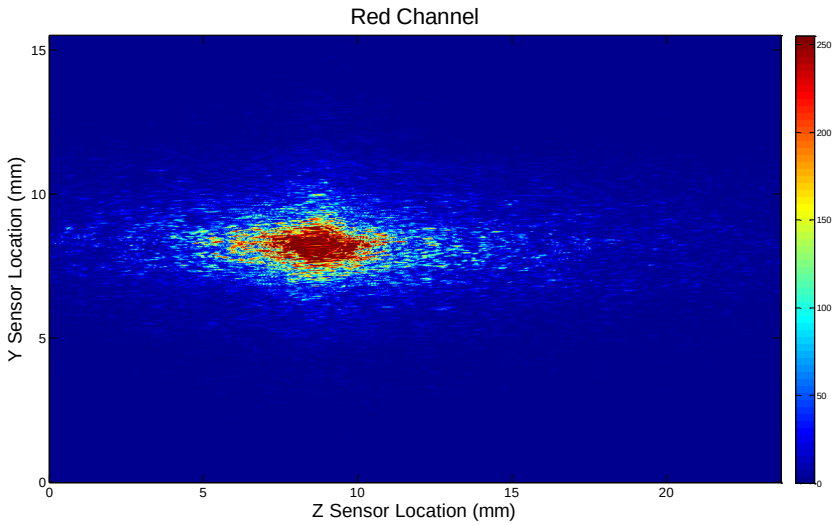


Figure 3.18 Saturated red channel output from the Nikon D50, file DSC_1155, sensor size 15.5 x 23.7 mm.

Where the red channel is saturated there is no useful information to be gained about the light intensity. Furthermore, it makes measuring and predicting the actual beam centre more difficult by effectively cropping off the very peak that one is trying to measure. However, if the blue and green channels are considered this task becomes much easier, see Figures 3.19 & 3.20.

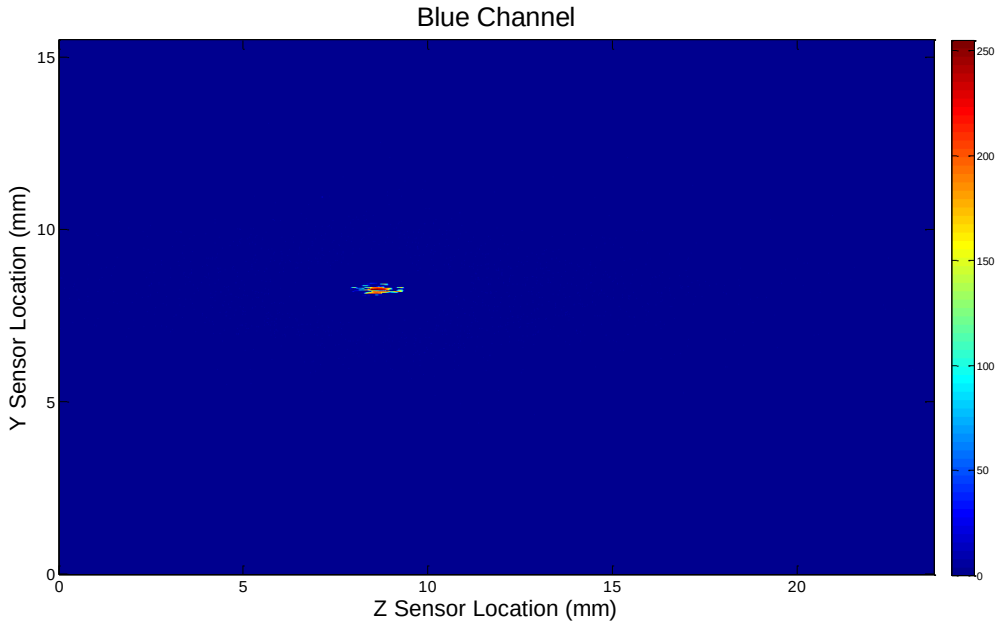


Figure 3.19 Blue channel data for DSC_1155, sensor size 15.5 x 23.7 mm.

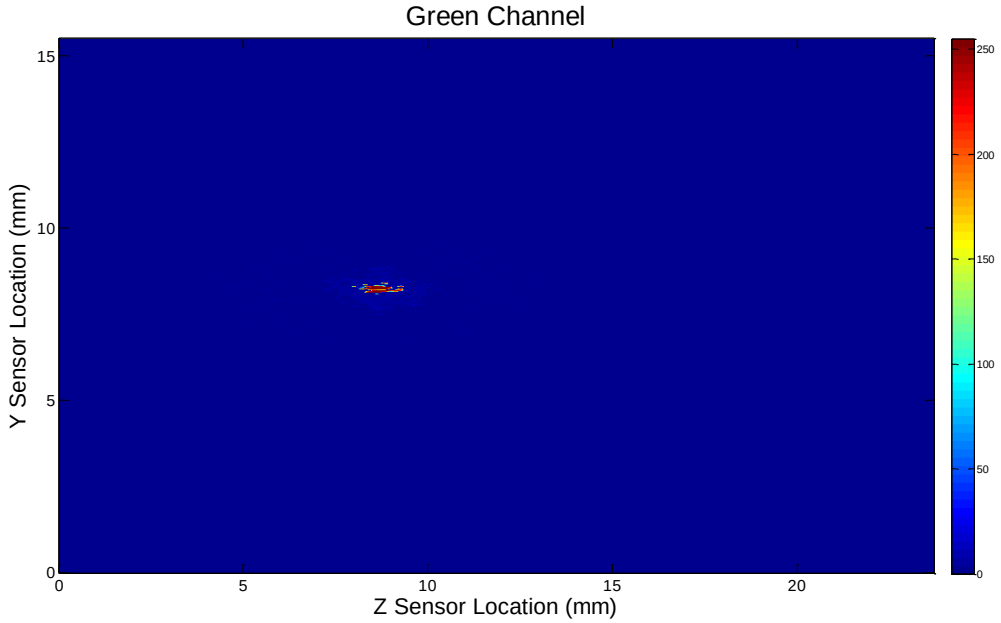


Figure 3.20 Green channel data for DSC_1155, sensor size 15.5 x 23.7 mm.

The saturated regions in the blue and green channels are much smaller than the corresponding region in the red channel. These saturated regions are therefore used to define the beam centre when locating the beam position on the camera sensor.

3.2.5.5 Background Noise

Preliminary data was rejected due to large amounts of background noise in the images. All data was therefore taken at night with the lab lights off. The only light was therefore owing to a small amount of ambient light entering the windows from the street lamps, which was analysed to give background data for the red, green and blue channels.

Additionally, there is a 'hot' or 'stuck' pixel at pixels coordinates (586,904) or 10.96 mm from the bottom edge and 7.12mm from the left. This blue pixel was present at the same value, approx. 46, in the RAW data for every photo. Occasionally it would vary slightly in value in the jpeg output owing to interpolation of values from the surrounding pixels. This stuck pixel produces a line below it of irregularly high values. This is due to the manner in which the CCD data is read by scanning across the sensor. Otherwise there is some non-zero noise but the values are all relatively low, around 10-15. These values correspond to the background noise seen in the green channel in Figure 3.21.

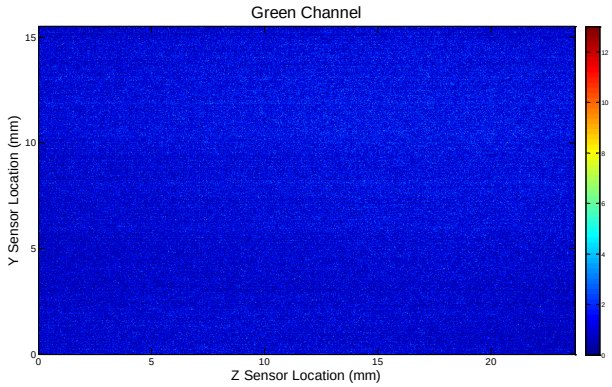


Figure 3.21 Image of background or ambient light taken at night in the cryogenics lab, green channel, file number DSC_1244, sensor size 15.5 x 23.7 mm.

As opposed to the blue and green channels there is somewhat of an image present in the red channel. The most likely explanation for this image is that the street lights present outside the windows to cryogenics are sodium vapour lamps, and emit strongly in the red. Furthermore,

the rounded edge to the intensity profile is most likely an image of the f-mount aperture on the camera body. Regardless the overall intensity for this background is still relatively low at a maximum value of 17, see Figure 3.22.

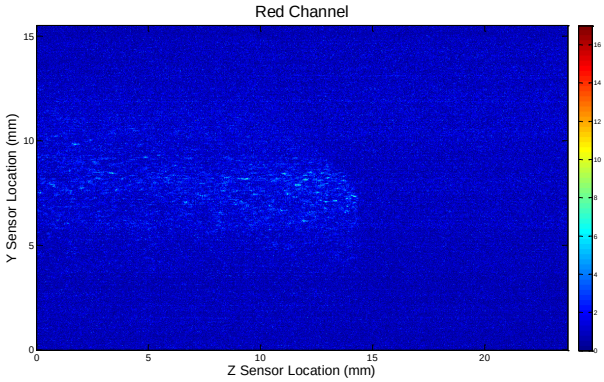


Figure 3.22 Image of background or ambient light taken at night in the cryogenics lab, red channel, file number DSC_1244, sensor size 15.5 x 23.7 mm.

Given the image present in the red data it can be concluded that sensor noise, if present, occurs at a lower level than the effect of ambient light. To remove the effects of this ambient light it was therefore decided to add data processing that would reject values for each channel below certain thresholds, as per Table 3.3.

Table 3.3 Cut-off values for each colour channel in image processing.

Channel	Red	Green	Blue
Threshold Value	20	20	80

The values for the red and green channels are rejected below 20. This cut-off value is much higher for the blue channel owing to the elevated value in the stuck pixel. However, this elevated cut-off value loses very little relevant information from the data; most blue data is either saturated or at background levels, see Figure 3.19.

3.2.5.6 Image Processing

For data processing the cut-off values in Table 3.3 were used to ensure that ambient light was not taken into consideration in the results. For the purpose of finding the beam centre, where the maximum intensities occurred, this did not have much of an effect. However, for the processing of off-axis and mirror reflection data later this would make a noticeable difference.

Image DSC_1155 is given as an example of this data processing. Figure 3.23 is a binary image with no filtering and displays white where non-zero intensities are recorded.

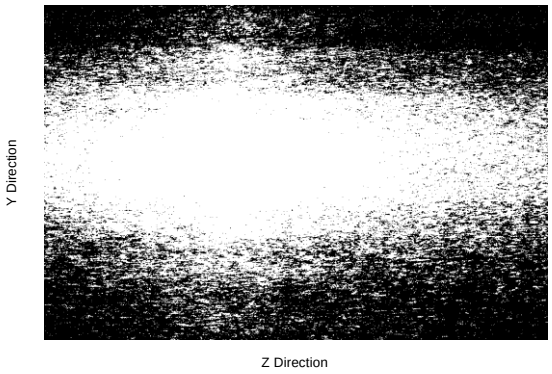


Figure 3.23 Non-zero red pixels, image DSC_1155, sensor size 15.5 x 23.7 mm.

There is background noise present in the image but most of the data is clustered around the laser spot. The filter value for the red channel was then increased to 5, 10, 15 and 20 respectively in Figures 3.25a, 3.25b, 3.26a & 3.26b.

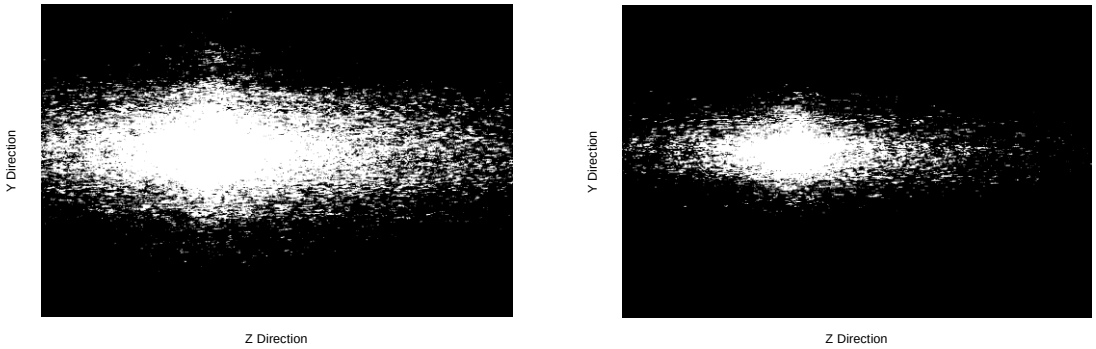


Figure 3.24 Red pixels with intensity above (a) 5 and (b) 20, image DSC_1155, sensor size 15.5 x 23.7 mm.

The filter applied to the data appears to remove some of the data around the beam spot but it also removes the background noise, as seen in Figure 3.22. Applied to the blue or green channels the same filters have a similar effect.

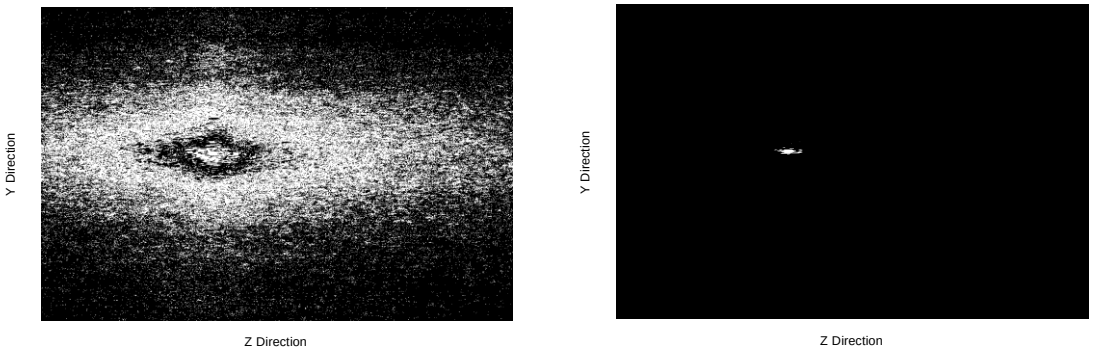


Figure 3.25 No filter & 20 applied to the green channel of image DSC_1155, sensor size 15.5 x 23.7 mm.

3.2.5.7 Measurement Resolution

The CCD sensor of the camera gives a resolution of 7.9µm, which for the 1m focal length of the system is equivalent to 0.0079 mrad. However, the central spot size of the laser pointers is much larger than the resolution of the CCD. This increases the practicable resolution to approximately 0.25mm, which is equivalent to the height of the laser pointer central spot after being focused by the mirrors, see Figures 3.19 & 3.20. Therefore the effect of surface normal errors in the mirrors should be measureable to 0.25-0.38 mad for the conical mirror and 0.38-2 mrad for the parabolic mirror.

3.3 Experimental Results

160 measurements were taken, as per the perforated plate diagram in Figure 3.15, for each data set. At each of the 160 positions 5 values were taken from each photo. Three of these values correspond to the average weighted position of the red, blue and green channels. Another value was recorded, the overall value, which is the average weighted position of the grayscale image, where the grayscale intensity values are given by

$$\text{Greyscale} = 0.299 \times Red + 0.587 \times Green + 0.114 \times Blue \quad \textbf{(3.1)}$$

The final channel, max, is the average position of every saturated pixel; that is the average position of all pixels reading their maximum value. An example of this data is presented in Figure 3.26.

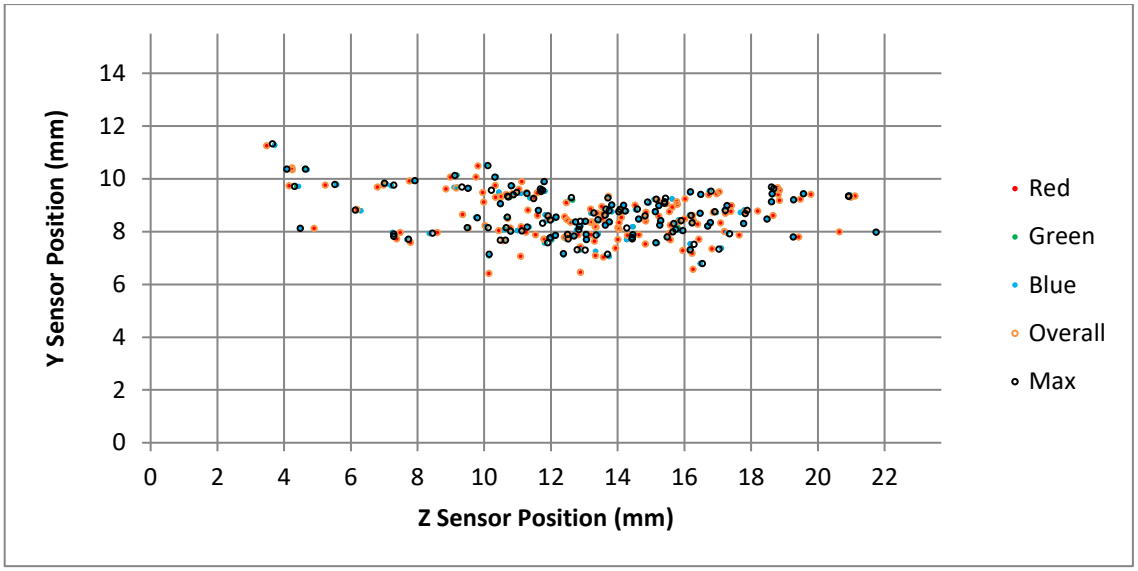


Figure 3.26 Example of 5 channels of data for laser beam position in focal plane.

Given the cropping effect on intensity information due to the saturation of the red channel, and its subsequent effect on the grayscale image, the most accurate results are expected from the blue and green channels. Position data confirms what was already known from the photos; most of the measured light is in the red channel and therefore positions of the weighted centres for the (grayscale) and red channels correlate well. The max channel correlates well with blue and green, however, it does so more closely with green. This is likely due to the fact that saturated pixels are mostly green, simply due to the fact that half the pixels in the sensor are green whilst only a quarter are blue or red respectively.

As demonstrated in Figure 3.26 there is good correlation between the Blue and Green channels, and given they do not have any of the inherent limitations of the other channels they will therefore be the only channels used in the subsequent analysis.

3.3.1 First Position

For the first position the camera was positioned so that the CCD sensor would be centred on the focal point of the system, as measured with respect to known coordinates on the concentrator. To test the reproducibility of the measurements 3 data sets of 160 images were taken at this first camera position. The laser pointer was orientated in the same direction for

each measurement. There was some slight bowing of the perforated plate, which increased the farther the laser pointer was positioned from its edges. This rarely resulted in the laser beam being blocked by the camera's aperture and the laser spot no longer being incident on the sensor; if it did, these results were omitted.

3.3.1.1 First Position – 1st Data Set

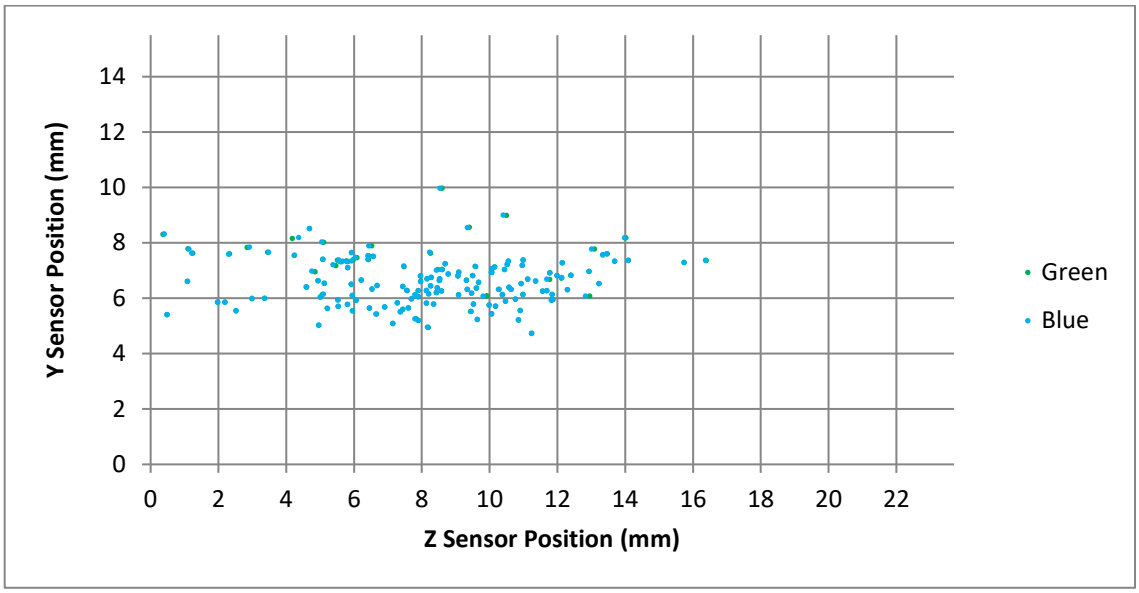


Figure 3.27 **Laser spot centroids in the focal plane, sensor size 15.5 x 23.7 mm.**

3.3.1.2 First Position – 2nd Data Set

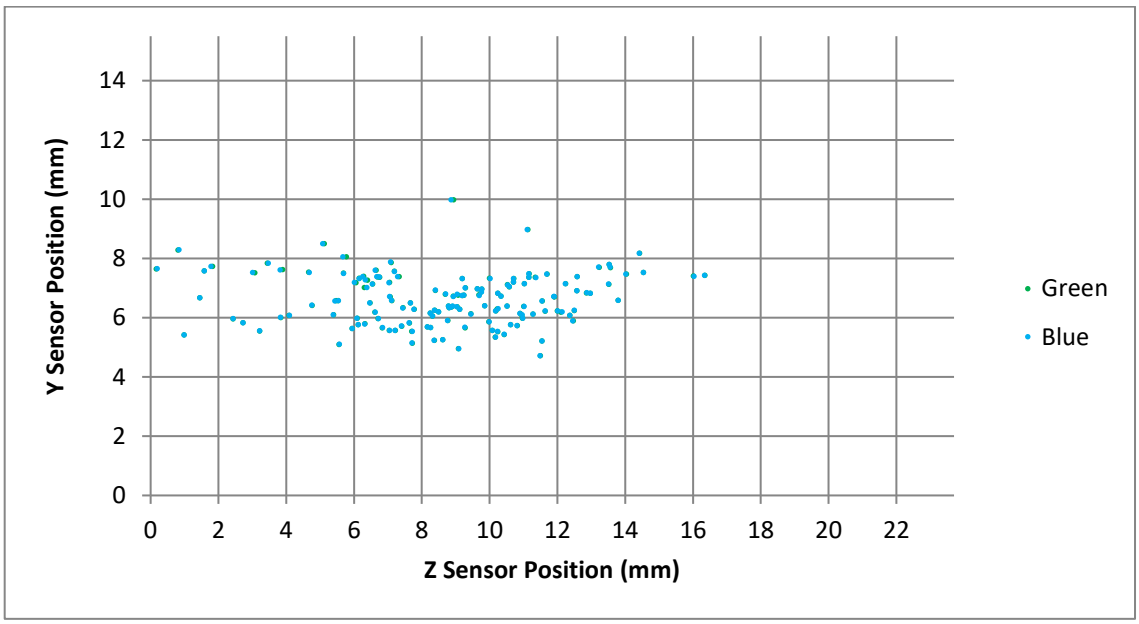


Figure 3.28 **Laser spot centroids in the focal plane, sensor size 15.5 x 23.7 mm.**

3.3.1.3 First Position – 3rd Data Set

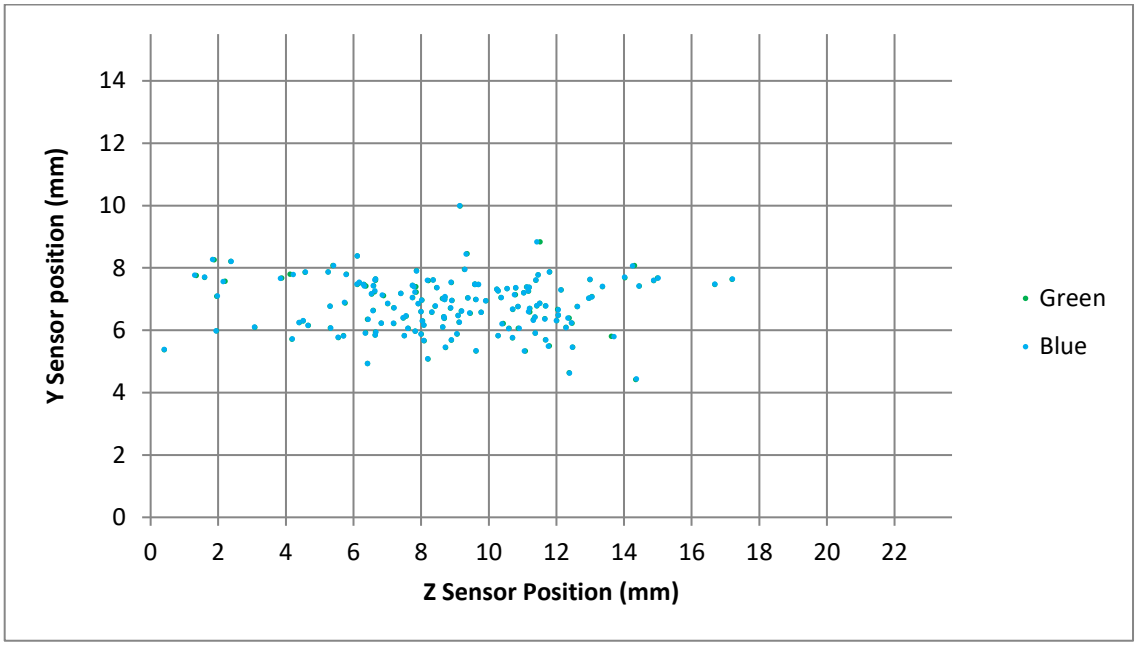


Figure 3.29 **Laser spot centroids in the focal plane, sensor size 15.5 x 23.7 mm.**

3.3.1.4 Reproducibility of Results

The first 3 sets of results were taken from the same CCD sensor position in the focal plane. The laser beams are incident on the CCD and nothing was changed between data sets. Despite this there is some movement in where the same lasers are incident in the focal plane. This is most likely due to some small amount of movement in the perforated plate supporting the laser beam apparatus. The changes in the measured values are summarised in Table 3.4.

Table 3.4 **Summary of data for first 3 data sets at the first camera position.**

	Mean Y Position (mm)	Mean Z Position (mm)	St.Dev Y (mm)	St.Dev Z (mm)
1st Position - 1st Set	6.62	8.21	0.861	3.18
1st Position - 2nd Set	6.66	8.66	0.866	3.21
1st Position - 3rd Set	6.83	8.80	0.856	3.19

Despite small changes in the mean Z position the data sets are quite similar and the standard deviation of points in both directions remains almost constant. Although there are some outliers in the data, these outliers tend to agree in position between data sets and are therefore likely to be systematic. This was investigated in the following graph, Figure 3.30, which gives the absolute distance, in mm, between laser spot locations for corresponding

perforated plate positions between the data sets for the max channel. The max channel was used here to ensure that differences in the red channel data were not overlooked.

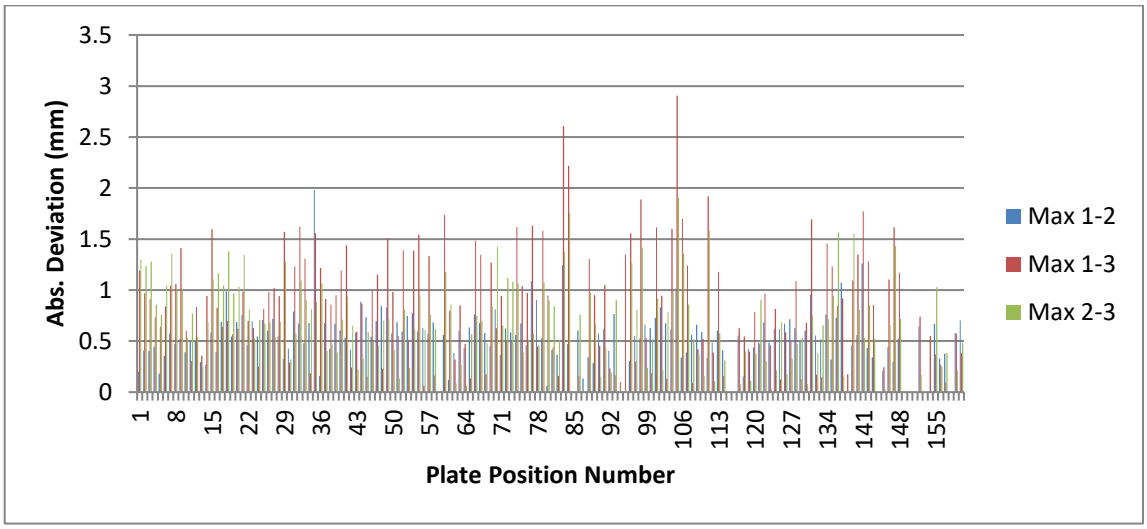


Figure 3.30 Absolute distances between spot locations, over the three data sets, at each perforated plate position.

There was a larger disagreement between the third and first data sets. Possible reasons for this greater disagreement may be equipment being moved slightly or the laser pointer no longer being correctly aligned with the vertical. Where there is no data, in the graph, it is due to photos being rejected from those perforated plate positions. In general, the similarity of these results suggests that laser beam point grouping is qualitatively the same between measurements. Values for the mean differences in laser beam locations are summarised in Table 3.5.

Table 3.5 Average mean distances between subsequent points over the three data sets at position 1.

Compared Data Sets	1-2	1-3	2-3
Average Mean Distance between individual points of Data Sets (mm)	0.642	0.828	0.663

In general, there is only a small difference in subsequent measurements. As most factors to do with laser pointer alignment and orientation have been mitigated, it is therefore possible that these small deviations are partially due to flexing in the perforated plate, in addition to mirror surface errors. Given the geometry of the perforated plate, a flexure of 1mm vertically could result in an angular deviation of 6 mrad in the laser beam from normal,

which could be up to 0.8 mm difference in the focal plane. Whilst this cannot be fully discounted from the errors, care was taken to avoid flexure of the plate whilst taking data. It also seems unlikely that flexure in the plate could explain the relatively large standard deviation in the z position of subsequent data points.

These initial data sets provided a quantified precision for the results but also confirmed that the CCD sensor was not accurately centred at the focal point of the system. The camera was therefore moved in the focal plane to better align the centre of mass of the incident laser pointers with the centre of the CCD. This alignment would minimise the effect of the camera's aperture blocking some incident laser points, as mentioned in section 3.2.4.

3.3.2 Repositioning the Camera Sensor

The camera was repositioned along the positive z-direction by 2mm with the use of a set of callipers. When the 160 subsequent laser points were measured it was determined that the mean z-position has increased by 2.05mm from 8.56mm previously to 10.6mm. However, the mean y-position decreased by 0.59mm. The grouping of the beam spots became slightly more central but it was decided to move the camera again.

For the third position the camera was moved along the positive z-direction by another 2mm and along the positive y-direction by 2mm, using a set of callipers, see Figure 3.31.

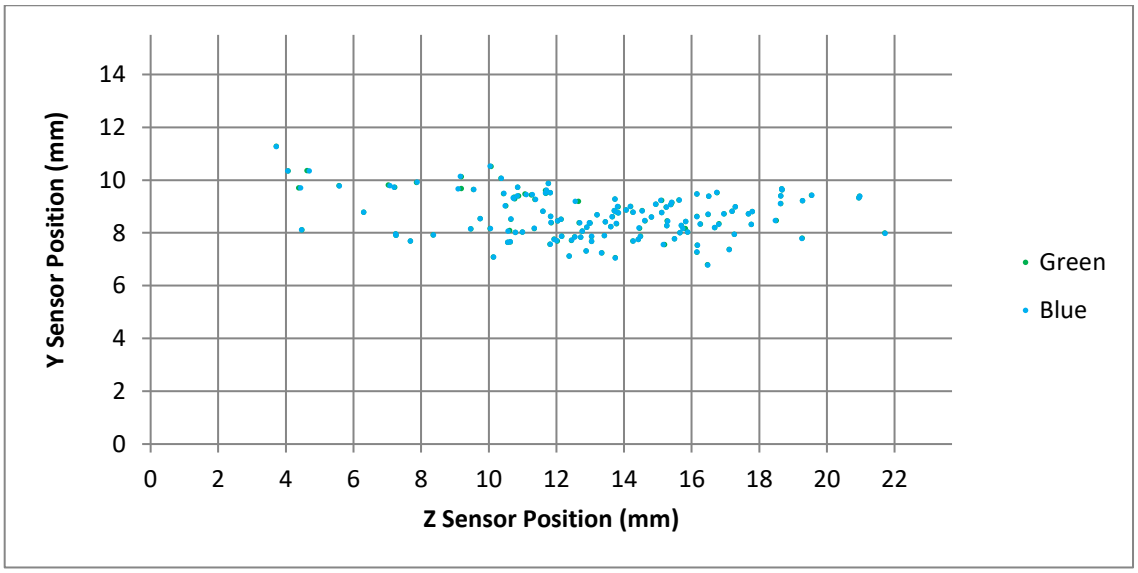


Figure 3.31 Laser spot centroids in the focal plane, 3rd position.

The mean y-position increased by 2.5mm, whilst the mean z-position was increased by 2.6mm. The final mean position (8.64mm,13.2mm) was deemed close enough to the centroid of the CCD sensor at (7.75mm, 11.85mm). This data is summarised below in Table 5.

3.3.3 Summary of Results from Laser Pointer Data

The most meaningful data from the first laser pointer experiments are the mean position for each data set and the standard deviation of each data set from this mean, see Table 3.6.

Table 3.6 Summary of mean positions and standard deviations of laser pointer data.

	Movement	Mean Y Position (mm)	Mean Z Position (mm)	St. Dev in Y (mm)	St. Dev in Z (mm)
1st Position		6.62	8.21	0.861	3.18
1st Position		6.66	8.66	0.866	3.21
1st Position		6.83	8.80	0.856	3.19
2nd Position	Z: 2mm	6.11	10.6	0.925	3.47
3rd Position	Z: 4mm & Y: 2mm	8.65	13.2	0.826	3.65

This data seems to indicate a high degree of reproducibility in the results. It can be clearly seen that moving the camera in the focal plane for the 2nd and 3rd positions had the desired effect of locating the focal point closer to the centre of the CCD sensor at , Y = 7.75mm and Z = 11.85mm. The standard deviations from the average in both Y and Z barely changed during the experiment, which seems to indicate that the same population of points was simply being translated across the CCD sensor. As other sources of error have been dismissed, these results will therefore provide a good estimate of the mirror surface errors remaining.

The standard deviation in the resultant positions is greater in the z-direction than the y-direction due to the intrinsic nature of the system. Reflected errors in the x and z directions of the laser points from the conical mirror will be propagated entirely from the parabolic mirror to the focal plane. However, as the parabolic mirror is focusing along the y-axis, any incident errors in the y-direction will be compressed along this axis. The system will therefore tend to focus more strongly along the y-axis than the z-axis in the focal plane, resulting in

higher standard deviations in the z-direction than the y-direction; this is borne out by the previous optical modelling, see Figure 3.3a.

3.4 Modelling of Mirror Errors

The next step in the process is feeding this data back into models of the concentrator in order to predict the errors present in the concentrator, and their effect on the performance of the system. To gain information about the mirrors a MATLAB model was developed which has the ability to vary the surface normal errors of the mirrors. The standard deviation of the mirror's surface normal will therefore be increased until the distribution of laser points in the focal plane matches that of the lab measurements.

The surface normal of both the conical and parabolic mirrors are calculated at the incident point of each ray. Following Snell's equation for specular reflection, see Equation 3.2, the reflected rays are then calculated.

$$\hat{d}_s = 2(\hat{d}_n \,.\, \hat{d}_i)\hat{d}_n + \hat{d}_i \qquad \textbf{(3.2)}$$

Where $\hat{d}_i$ is the incident light direction, $\hat{d}_n$ is the surface normal, and $\hat{d}_s$ is the specularly reflected direction.

3.4.1 Description of Program

To add errors to the surface normals of the mirrors two rotation matrices are calculated. When the surface normal is calculated for an incident ray (according to the exact mirror geometry) it is transformed with these rotation matrices. The first rotation corresponds to an error magnitude, defined by a normal distribution with a chosen standard deviation. For ease of calculation, and program speed, this rotation is not in a randomised direction. The magnitude of the rotation will however follow the normal distribution desired. The second rotation then rotates this resulting vector about the original surface normal to randomise its orientation, following a uniform distribution from 0 to 2π. Additionally, the starting position for an incident ray is randomly and evenly chosen over the surface of the conical mirror.

3.4.2 Measurement of Resultant Focal Plane Images

Mean and standard deviations of the resultant rays in the focal plane are calculated in the program for all rays incident in the focal plane. The images of the focal plane, however, are limited to a 30mm by 30mm square centred on the focal point of the system. For this image the bin size is at 0.095mm on each side and therefore 0.0090mm^2 for each pixel. There are originally 10^7 rays in the system. However, some of these rays will not reach the parabolic after being reflected from the conic.

3.4.3 Modelling Results

The program was used to calculate the distribution of points in the focal plane, given a parallel light source, for various deviations of mirror surface normal error. The bin values in the focal plane image represent the number of incident rays in each bin, from the total population of 10^7. With no surface normal errors the image would be a single pixel of value 10^7, located at the centre. The surface normal error was gradually increased through a series of tests.

3.4.3.1 Surface Normal Standard Deviation of 0.001 Radians

The first result was taken with a minor error in the mirror surfaces of only 1mrad. In the context of the solar cooker, the sun's radius has an average angular size of 4.65mrad at the Earth's distance.

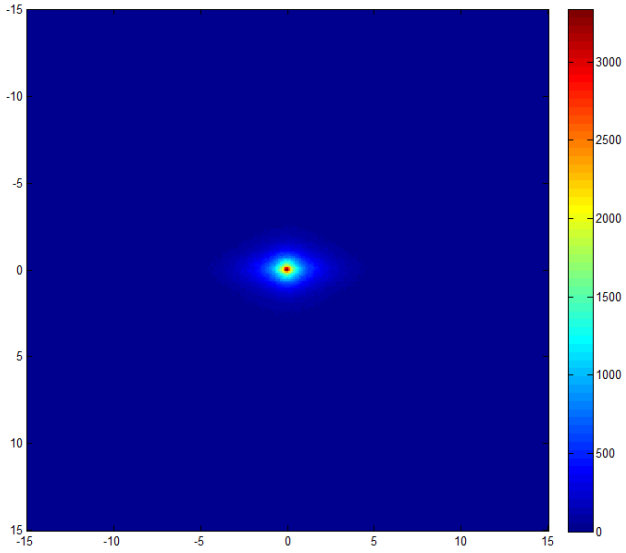


Figure 3.32 Focal plane image of parallel light with 1mrad standard deviation in the mirror normal, axes in mm.

As the error in the mirror surfaces is small, 99.7% of the incident light was reflected off the conic onto the parabolic mirror.

3.4.3.2 Surface Normal Standard Deviation of 0.005 Radians

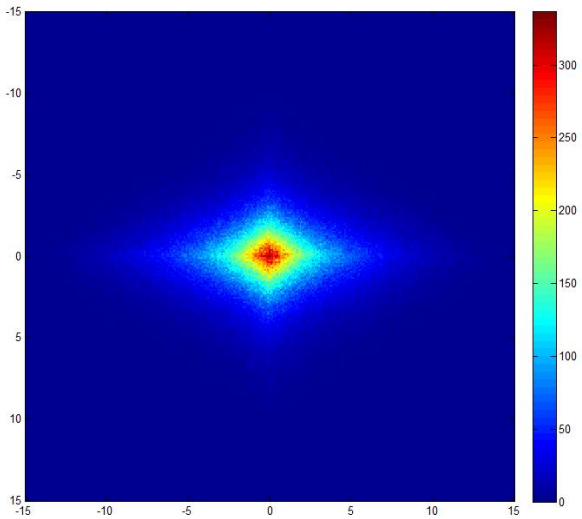


Figure 3.33 Focal plane image of parallel light with 5 mrad standard deviation in the mirror normal, axes in mm.

98.5% of the rays were captured; as expected the maximum concentrations have decreased as well as raising the standard deviation of final points from the mean.

3.4.3.3 Surface Normal Standard Deviation of 0.01 Radians

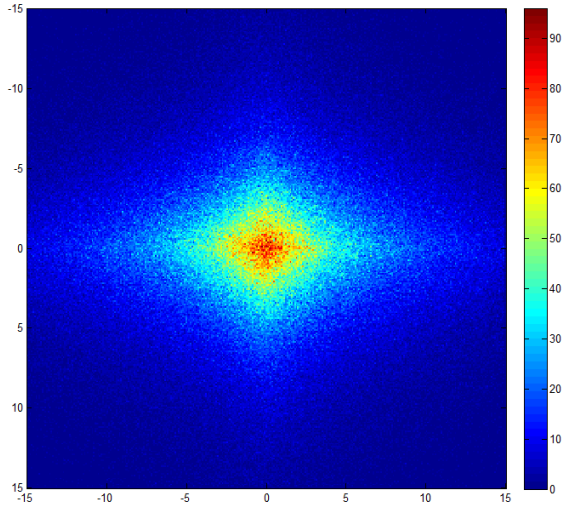


Figure 3.34 Standard deviation of 10mrad to both mirror's surface normal, axes in mm.

At a standard deviation of 10mrad to both mirror's surface normal, the resultant image is much more spread than previously, only 97% of the rays were reflected off the conic mirror such that they intercepted the parabolic mirror and arrived at the focal plane.

3.4.4 Summary of Results

The standard deviations from the normal of the mirrors surfaces were varied to produce the results in Table 3.7. The bold values compare most similarly to those produced in the laser pointer experiment.

Table 3.7 Results of varying the standard deviaiton of mirror surface normals for a parallel beam.

St Dev	Avg Y Pos	Avg Z Pos	St Dev Y Pos	St Dev Z Pos	Area 90% Caustic
Radians	mm	mm	mm	mm	mm^2
0.001	0.00108	0.00131	0.583	0.889	8.21
0.0015	0.00317	0.000383	**0.875**	1.33	18.4
0.002	0.00547	-0.00238	1.17	1.77	32.6
0.003	0.00970	-0.00226	1.75	2.66	69.4
0.004	0.0153	0.0000543	2.35	**3.54**	121
0.005	0.0317	0.000919	2.92	4.41	181
0.01	0.128	0.0178	5.84	8.71	419

Quantitatively, the overal effect of laser alignment, mirror, structural and assembly errors on the geometry of the laboratory prototype have the same effect as adding a standard deviation surface normal error of the order 1.5-4mrad to the mirrors. That is a minimum error of 1.5mrad gives the required deviation of the resultant point in the y direction. However, an error of 4mrad is require to produce the desired deviation in the results in the z direction.

The fact that the standard deviation of the final laser point positions cannot be modelled with a single standard deviation applied to the mirrors hints at systematic errors in the concentrator.

The most likely reason for this is that it was much more difficult to conform the conical mirror to the frame of the concentrator than it was to conform the parabolic. Residual stresses from the manufacture of the Alanod sheet result in a curvature along the direction it was rolled. It is possible to cut the parabolic mirror to take advantage of this fact, in aligning this curvature along the direction of the mirrors intended curvature. However, it is not possible to match the cylindrical curvature of the Alanod with the conical curvature of the primary mirror. Therefore, curvature from residual stresses in the Alanod will tend to improve the conformity of the parabolic mirror whilst hindering the conformity of the conical mirror.

It should therefore not be expected that an overal estimate of concentrator errors can be estimated by applying the same surface normal error to both mirrors equally. A combination of varying magnitude conical compared to parabolic surface normal errors was therefore studied.

3.4.4.1 Conic Deviation at 0.004 Radian with Parabolic Deviation at 0.0015 Radian

It has always been easier to conform the parabolic mirror more closely to the supporting structure than the conical mirror. The first test therefore was to reduce the standard deviation in the parabolic whilst increasing that in the conical, see Table 3.8. The values chosen were

1.5mrad and 4mrad, the two limits of possible global surface errors standard deviations previously found.

Table 3.8 Repeated test with Conical Deviations at 4 mrad and Parabolic at 1.5 mrad.

Avg Y Pos	Avg Z Pos	St Dev Y Pos	St Dev Z Pos	Area 90% Caustic
mm	mm	mm	mm	mm^2
0.0237	0.000126	2.09	3.48	106
0.0247	0.00287	2.09	3.47	105
0.0243	0.00124	2.09	3.47	105

The standard deviaiton of final points in the z-direction remains approximately the same whilst the y-direction standard deviation is too high at 2.09mm compared to 0.857mm from the lab data. As a final example the error was removed from the parabolic mirror to produce the results in Table 3.9.

Table 3.9 Conic standard deviation of 4 mrad with no parabolic surface errors.

Avg Y Pos	Avg Z Pos	St Dev Y Pos	St Dev Z Pos	Area 90% Caustic	Total Area
mm	mm	mm	mm	mm^2	mm^2
0.0272	0.00205	2.05	3.47	103	360

This change did not have the desired effect. The standard deviaiton in the y direction is still too large. It is therefore deduced that the conical surface error has a much greater signifance on the results than that of the parabolic surface error.

Firstly, the path length from the conic to the focal plane is always longer than that of the parabolic mirror. It should therefore be expected that conical errors would have a larger influence on the final results as any angular deviation in the rays direction will propagate a further distance. Furthermore, light reflected at erroneous angles from the conic mirror will not fall on the intended point on the parabolic mirror, further compounding surface errors in the conic mirror.

Additionally, it should be anticipated that given these errors are not equivalent over the two mirrors, they will also not be evenly distibuted for a given mirror. That is, an even distribution of the errors over a 2π rotation is unlikely to be true. Firstly, the direction the

Alanod aluminium mirrors are rolled during manufacture gives them a natural curvature. This was aligned with the desired direction of curvature for the parabolic mirror and good conformity to the concentrator's structure was observed. However, this was not possible for the conical mirror owing the the direction of its curvature. Therefore, it should be anticipated that a systematic error in surface normals is present that would not follow a uniform rotational distribution in 2π.

In practice the conformity of the conical mirror to the structure was not as good as that for the parabolic mirror. Given the geometry of the conical mirror this would give rise to more surface normal errors in the z direction rather than the y direction. In practice, a 1mm gap between the rear of the conical mirror to the structure in the middle of the miror with the edges conforming would lead to surface normal errors of up to 3.7 mrad.

In theory, these systematic errors may be accurately predicted given the geometry of the conical mirror. However, small deviations in conical geomtry are difficult to notice and even more difficult to measure. Care must be taken to ensure good mirror conformity of the conical mirror to the correct geomtry, as small deviations may account for a significant fraction of the observed errors.

The surface normal standard deviation of between 1.5-4mrad was then fed back into the Matlab program. However, this time solar data were used as the light source instead of parallel light. The program therefore gave an indication of fluxes expected on the focal plane and it was possible to anticipate the effect on concentration factors and maximum flux in the focal plane. These results are summarised in Table 3.10, with comparison to the expected output without mirror defects.

3.4.5 Images of Focal Plane with Increasing Mirror Surface Errors

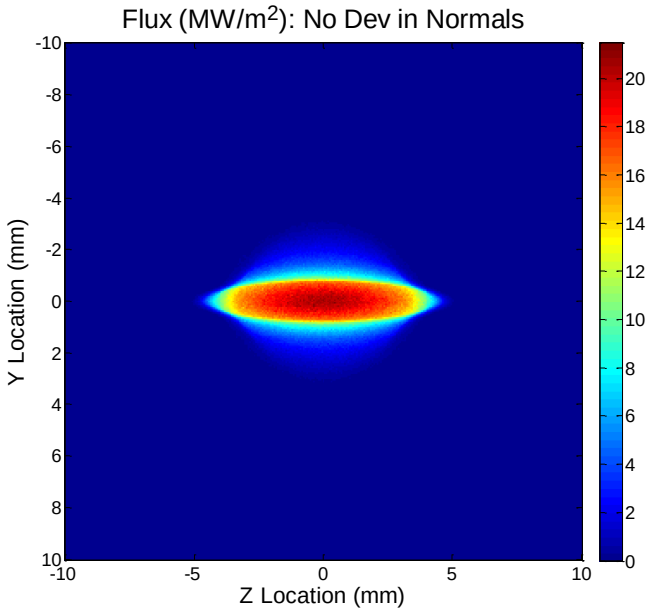


Figure 3.35 **Image of focal plane with no errors in the mirror surfaces, for comparion.**

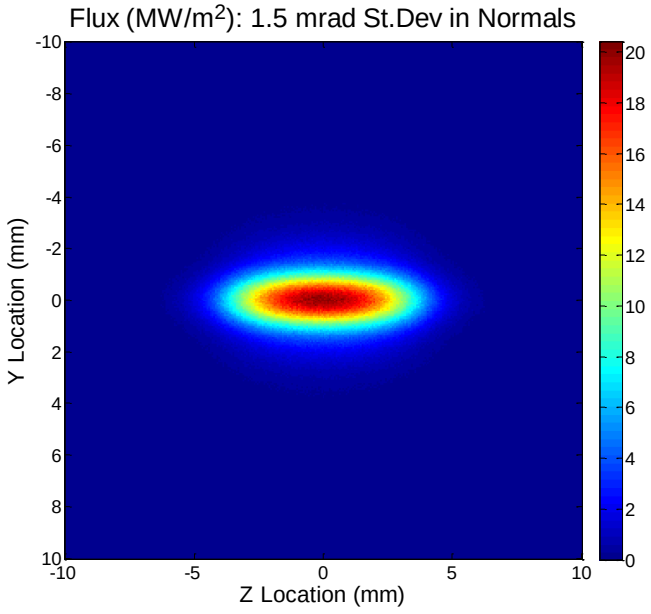


Figure 3.36 **Image of focal plane with a standard deviation of 1.5 miiliradians in mirror surface normals.**

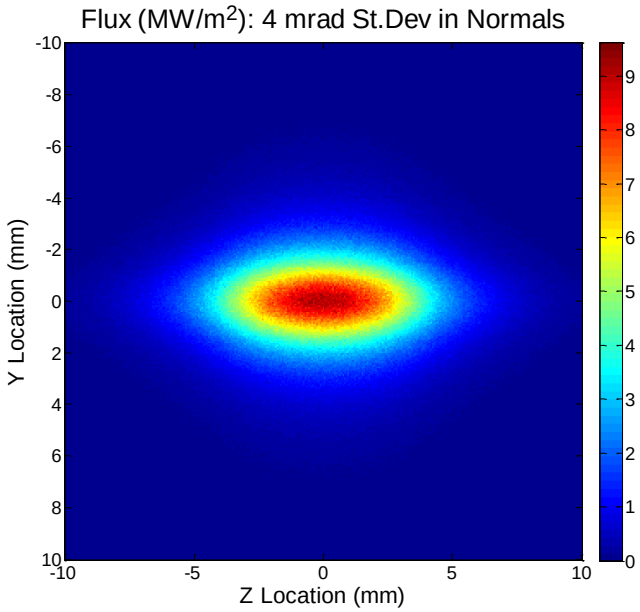


Figure 3.37 Image of focal plane with a standard deviation of 4 miiliradians in mirror surface normals.

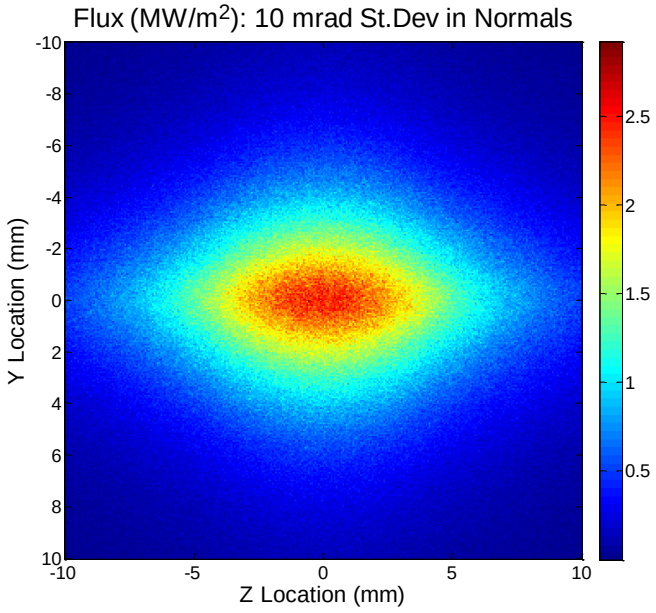


Figure 3.38 Image of focal plane with a standard deviation of 10 miiliradians in mirror surface normals.

As the standard deviation in the surface normal increases the flux in the focal plane becomes less and less concentrated. These results are summarised in Table 3.10 with those most applicable to the experimental data in bold.

Table 3.10 Summary of results for concentration factors and maximum fluxes with varying mirror errors.

St. Dev in Normals (mrad)	Avg Y Pos	Avg Z Pos	St Dev Y	St Dev Z	Area 90% Caustic	CF (90%)	Max Flux
0	0.00380	-0.000975	0.830	1.99	20.4	5480	21.5
1	0.00426	-0.00108	0.959	2.11	26.6	2670	20
1.5	0.00546	-0.000684	1.10	2.24	34.8	**1800**	**20.3**
2	0.00620	-0.000563	1.27	2.41	43.9	1400	17.9
3	0.00980	-0.000176	1.66	2.85	68.3	988	13.3
4	0.0143	-0.000952	2.09	3.36	98.8	**829**	**9.6**
5	0.0221	-0.000779	2.53	3.93	130	764	7.3
10	0.0763	-0.00269	4.86	6.99	238	726	2.9

The standard deviations in y and z of the light rays in the focal plane, now being a confoundment of solar angles and mirror error angles, are no longer directly comparable to experimental data. However, the z values continue to be larger than the y values. Again, this is to be expected given that the parabolic mirror is uniform in z.

The important figures of merit, the concentration factor and maximum flux decline steadily with increasing errors, which is more clearly observed in Figure 3.39.

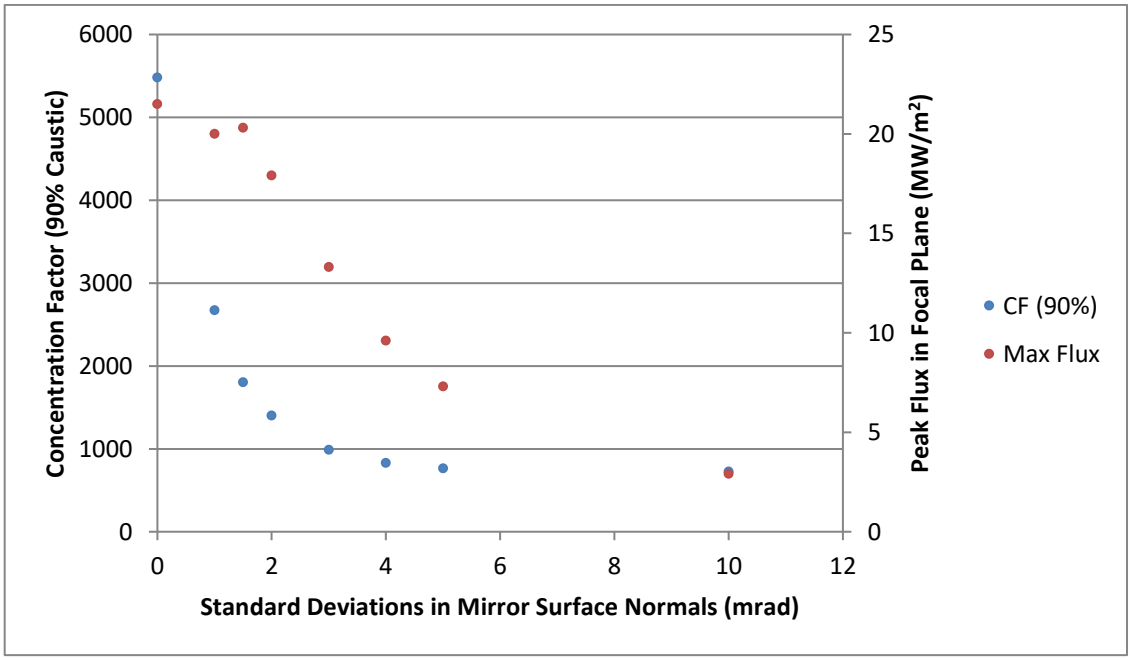


Figure 3.39 Decreases in concnetration factor and maximum flux with increasing surface normal defects.

The theoretical maximum concentration factor for an aperture of the equivalent size of our concentrator is 17700. The value of 5480 for the concentrator without defects should be viewed as a theoretical design maximum of our concentrator, but not to be obtained in practical applications. Nevertheless, for the range of observed errors we can see a drop in concentration factor of 1800 to 829 and a decline in maximum measured flux of 20.3 to 9.6 MW/m^2.

With increasing deviation in mirror surface normals the value of the concentration factor of the concentrator drops off much more quickly than that of the maximum flux measured in the focal plane. In the possible range of errors observed in the experimental data, it can therefore be concluded that these errors could have an effect of halving both the concentration factor and the maximum flux measured. Almost all the input flux is incident on the focal plane in both cases, it is just the concentrations of this flux that differ. In solar cooker applications this reduction in peak flux and maximum concentration may be unimportant as long as total flux to the absorber remains constant. Additionally, this may even be benefical in the sense that peak fluxes will be lower and therefore less likely to exceed material constraints.

However, in applications where high fluxes or temperatures are desired a 100% improvement in both concentration factor and peak flux may be worth the additional cost in reducing the overall system error from an equivalent 4mrad deviation in surface normals to just 1.5 mrad.

3.4.6 Discussion and Implications for Concentrator Design

Given the difference in the standard deviations of laser points in the y and z directions of the experimental data of 0.86mm and 3.2mm respectively, it should be expected that similar magnitude errors will arise from the construction of a solar cooker. That is that the manufacture, assembly and mirror quality will result in similar magnitudes of equivalent

errors. This magnitude of error can as much as half the expected maximum concentration factor of the system.

These errors can be divided into two main areas; those which are dependent on the mirrors and those dependent on the design, manufacture and material of the supporting structure.

3.4.6.1 Implications for Mirror Material Selection

Firstly, in terms of cost, the Alanod mirrors are one of the most expensive items on the concentrator. As part of a future Dytecna prototype the mirrors would represent up to 40-50% of the total system cost at mass production values. In terms of utilising the concentrator design in producing a low-cost solar cooker it is imperative to investigate alternative mirror materials. These materials are likely to consist of thin-membranes, such as aluminised Mylar, or similar materials attached to a supporting sheet for strength. This choice of mirror material and the method of construction are likely to lead to a decrease in the mirror's surface quality. Care will be needed to avoid buckling when the composite structure is bent. Additionally, their bonding to the supporting sheet is likely to lead to surface defects if glue or other adhesives are used.

3.4.6.2 Implications for Concentrator Structure/

It is likely that the accuracy of the tolerances and assembly in the lab prototype would exceed that of a mass production low-cost cooker; the lab prototype being manufactured with the use of both a CNC machine and a laser cutter.

3.5 Conclusion

Using the test rig parallel laser beams were scanned across the surface of the prototype concentrator. The resultant laser points in the focal plane were measured using the CCD sensor of a camera. The statistical analysis of these points, and their deviation from the focal point of the system, indicates that the overall effect of manufacturing, assembly and mirror errors on the concentrator system is in the order of 1.4 to 4mrad equivalent standard

deviation in the mirrors surface normals. The results of the experiment could not be reproduced in terms of rotationally symmetric errors in either of the mirrors surface normal, and the differences in magnitude of errors in the y and z directions of the system are most likely due to a systematic tendency towards z-direction errors within the concentrator system. Firstly, the parabolic mirror is cut from Alanod that was rolled in the same direction as its desired curvature and much better conformity to the structure of the concentrator is observed than for the conical mirror. As the parabolic mirror is uniform in the z-direction it is therefore expected that the overall contribution to errors by the parabolic will be less in the z-direction than for the y-direction. Given the geometry of the parabolic mirror, non-conformity to the concentrator structure will most likely give rise to y-directional errors. Conversely, the conical mirror is more likely to give rise to z-directional errors due to non-conformity to the structure. Additionally, the conical was not able to be cut from Alanod sheet with curvature in the same direction as that desired for the concentrator.

With a conical mirror more likely to give z-directional errors and a parabolic mirror more likely to give y-directional errors the resultant system tendency towards z-direction errors can thus be explained by the difference in path lengths for light rays incident on these mirrors. The path length from the parablic mirror varies from approximately 640mm to 110mm to the focal plane, whilst in the conical mirror it varies from 666mm to 1000mm; depending on where the light is incident. Therefore, it is expected that for the same given error in the mirror's surfaces the conical error will have between 1.04 to 9 times more effect on the resultant position of a given light ray in the focal plane. The standard deviation in experimental results was 3.9 times greater in the z-direction than the y-direction.

The analysis of the mirror's errors is borne out by a visual inspection which confirms more irregularities in the conical mirror surface than in the parabolic mirror surface; see Figures 3.40a & 3.40b for a comparison.



Figure 3.40 (a) Warped conical reflection (b) Regular parabolic reflection.

Given that the overall system errors measured in the prototype, their effect on the performance of the concentrator was modelled using a MATLAB program. Implications for an actual solar concentrator, given the variation in mirror surface normal errors observed experimentally, are a both a drop in maximum flux in the focal plane and in concentration factor of 50% for the largest observed errors of 4mrad compared to the minimum error of 1.5mrad.

Finally a composite image of the test data from the final test run of laser beams provides good agreement with the expected flux profile in the focal plane, see Figure 3.41.

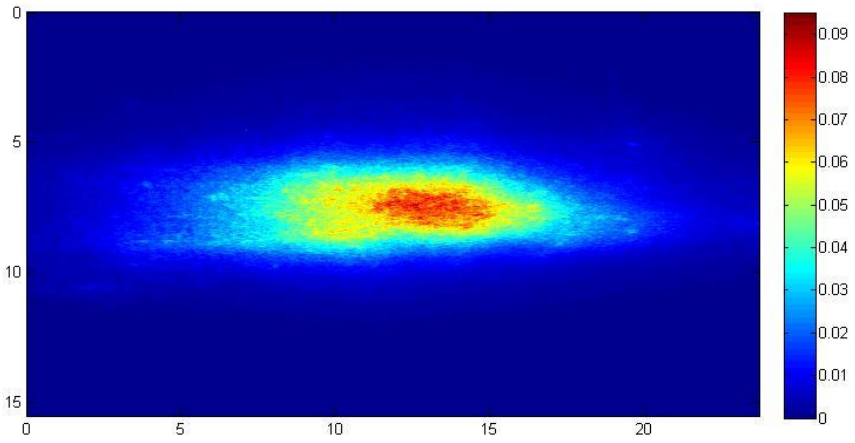


Figure 3.41 Composite image of 135 incident laser beams from the 3rd test run; dimensions of the sensor are 15.5 x 23.7 mm, scale is weighted such that 135 perfectly collinear laser beams equals 1.

4 Oven

An integral part of the development of the solar cooker was research into the oven. During operation the hotplate will receive solar flux from underneath, see Figure 4.1.

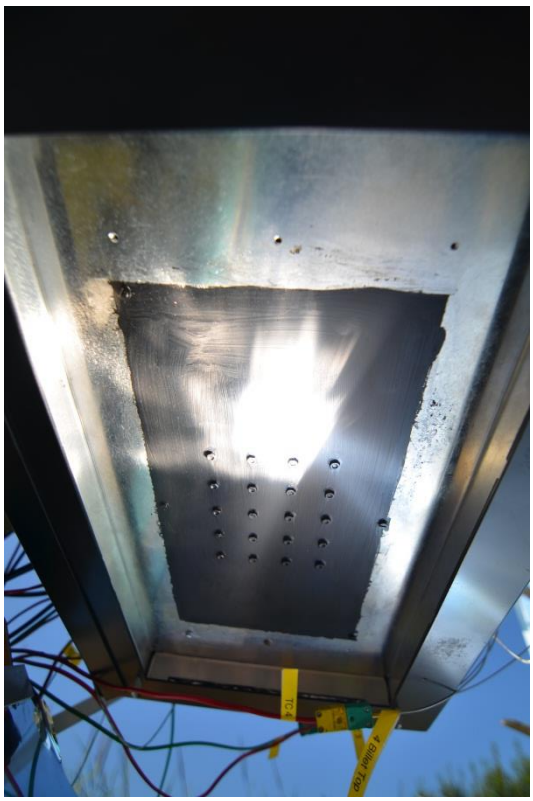


Figure 4.1 Underside of hotplate with incident light, the bright caustic region is only reflecting approximately 5% of the incident light.

Being absorbed by the hotplate, this solar flux will be transformed into heat energy, which will then flow through the oven and its components. The study of these heat flows will be the focus of this chapter.

The performance of the oven will be determined by its ability to heat a thermal load, normally food, placed upon the hotplate for a given solar/thermal input. This performance was investigated through the development of a thermal model of the oven, the testing of the oven with a known thermal input using electrical resistance heating, and finally ex-situ testing of the oven with a measured solar input during field trials in Italy.

4.1 Thermal Model of Oven

A model of the thermal properties of the oven and its components was developed in order to predict its performance.

4.1.1 Description of Heat Flows

The hottest part of the system will be the portion of the hotplate subject to the incident solar flux, which is the only heat input to the oven system. Following the 2nd Law of Thermodynamics heat will flow from this hot region to other cooler components of the oven. Heating of the oven from ambient temperature will be dominated by conductive heat transfer. As the system rises in temperature convective and then radiative heat transfer will become more important.

Firstly, heat will be conducted from the illuminated caustic region of the hotplate towards the edges of the hotplate. A critical heat flow in determining the oven's performance will then be the heat conduction from the hotplate to the cooking load placed thereupon. The conduction of this heat, between two separate bodies, will be dependent on the thermal contact conductance between these bodies. The effect on oven performance of the effective thermal contact conductance is also investigated as part of the model.

The remainder of the energy balance for the hotplate will then be the heat convected and radiated away from the underside of the hotplate to the environment, as well as the heat convected upwards from the hotplate to the interior to the oven. Strictly speaking there will be some heat radiated to the interior of the oven from the hotplate. However, given that the interior surfaces of the oven are low emissivity aluminium, $\varepsilon \approx 0.05$, and that the temperature differences observed inside the oven were of low order, $\Delta T \approx 50K$, the maximum radiative heat transfer would only be of order 1.8 W compared to heat inputs of 300-400 W for the system.

Inside the oven, heat will be convected from the hotter surfaces of the hotplate and cooking load to the inner walls of the oven. Heat is then conducted through the walls before

being convected away from the exterior oven walls. Again, strictly speaking, there will be a radiative balance between the exterior walls of the oven and the environment, but due to small temperature difference and low emissivities it is not significant enough to be addressed in the model. A diagram of the heat flows of the model is shown below in Figure 4.2 with an aluminium billet in place as the thermal load.

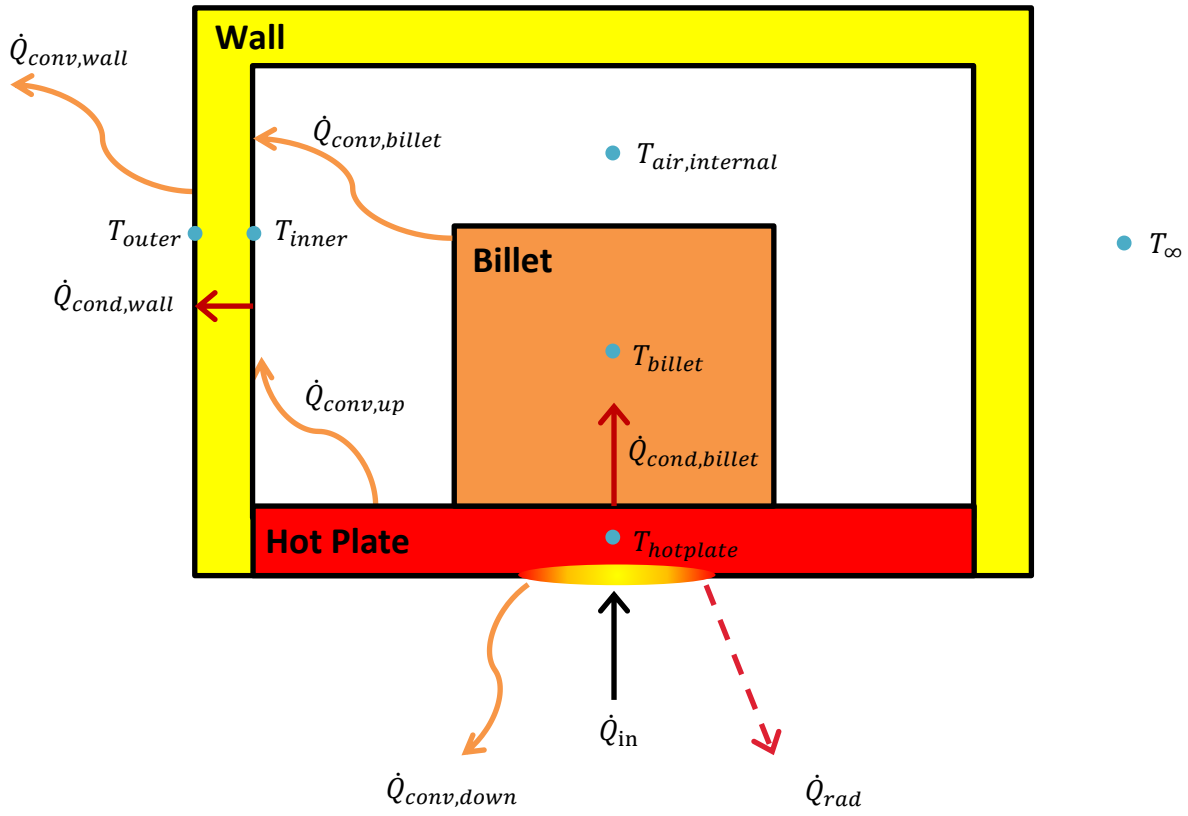


Figure 4.2 Diagram of the dominant modes of heat transfer in the oven model. Heat flows are given as $\dot{Q}$ in Watts.

The heat flows are dependent on the temperatures of the oven's components, which are defined at the positions given in Figure 4.2. Solving for convective heat transfer within the oven requires the thermal properties of the internal air mass to be known, which are somewhat temperature dependent, but will not vary greatly in the temperature ranges observed in the oven. Given that this internal air temperature cannot be solved trivially, the

internal air temperature is therefore taken as the average of the inner wall and hot plate temperatures.

Furthermore, possible internal convection from the hotplate to the billet is not addressed for the following reasons:

- this mode of convection will be minor compared to heat conduction to the billet,
- convection from the hotplate to the wall will dominate any convection to the billet given the temperature differences and geometry of the system
- adequate and relevant equations describing internal natural convection from a horizontal hot surface to a vertical cool wall were not found in the literature.

Equations were then developed to describe the behaviour of the oven given the heat flows and temperature locations described. These equations are functions of the system temperatures but they cannot be solved analytically. To progress through time the model employs a forward Euler method to solve the heat flows explicitly before calculating the subsequent system temperatures.

4.1.2 Mathematical Characterisation of the Oven Model

Dividing the model into three separate thermal masses enables an energy balance to be applied across each mass. The thermal masses are the hotplate, the cooking load and the oven wall. Each separate thermal mass is treated as isothermal.

Equations defining the heat flows in-between the thermal masses of the system and to the environment are applied. These heat flows are dependent on the temperature of the system components and are calculated at each time step. Given these heat flows an energy balance is then applied across each thermal mass, which determines their temperature for the subsequent time step. These new system temperatures then change the calculation of heat flows for the subsequent time step, etc… and the system behaviour may be described through time.

The basic oven model is that of heating of the oven in the lab in still air, i.e. with natural (unforced) convection from the underside of the hotplate and outer oven walls. The cooking load described here is the cylindrical aluminium billet that was used in subsequent testing.

4.1.2.1 Hotplate

Solar flux incident on the hotplate is given by

$$\dot{Q}_{in} = \alpha \cdot \dot{Q}_{solar,incident} \tag{4.1}$$

where α = the absorptance of the hotplate surface for the given spectral flux and orientation

$\dot{Q}_{solar,incident}$ = total incident solar flux after reflection from both mirrors

In the case of simulating the lab results where an electrical resistance heater was used, $\dot{Q}_{\text{in}}$ is simply the calculated electrical heating power. Radiation from the hotplate to ambient will be given by the Stefan-Boltzmann Law

$$\dot{Q}_{rad} = A_{\text{hp}} \cdot \varepsilon \cdot \sigma\left({T_{hotplate}}^4 - {T_\infty}^4\right) \tag{4.2}$$

where A_{hp} = the surface area of the hotplate

ε = the emissivity of the hotplate surface, which is practically temperature independent

σ = the Stefan-Boltzmann constant, 5.67×10^{-8} W·m^{-2}·K^{-4}

The convection from the underside of the hotplate will be natural within the lab. The hotplate is taken as isothermal and as convection is downwards it will be given by

$$\dot{Q}_{conv,down} = A_{\text{hp}} \cdot h_m \left(T_{hotplate} - T_\infty\right) \tag{4.3}$$

$$h_m = \text{Nu}_m \cdot \frac{k}{L_c} \tag{4.4}$$

$$\text{Nu}_m = 0.54\ (\text{Ra})^{1/4}, \quad 10^5 < \text{Ra} < 2\times10^7 \tag{4.5}$$

where h_m = the average heat transfer coefficient, W·m^{-2}·K^{-1}

k = the thermal conductivity of the ambient air, $W \cdot m^{-1} \cdot K^{-1}$

L_c = the critical length of the surface, given as its area divided by its perimeter, m

Ra = the dimensionless Rayleigh number, which describes whether heat transfer within the fluid is primarily driven by conduction or convection

Nu_m = the average Nusselt number, which is the ratio of convective to conductive heat transfer across the hotplate surface

$$\mathrm{Ra} = \mathrm{Gr}_L \cdot \mathrm{Pr} \qquad \mathrm{Pr} = \frac{\nu}{\alpha} \tag{4.6}$$

$$\mathrm{Gr}_L = \frac{g \cdot \beta \left(T_{hotplate} - T_\infty\right) {L_c}^3}{\nu^2} \tag{4.7}$$

where Pr = the dimensionless Prandtl number, which is the ratio of kinematic viscosity to thermal diffusivity

Gr_L = the dimensionless Grashof number, which is the ratio of buoyancy to viscous force acting on a fluid

g = the standard acceleration due to gravity, 9.81 $m \cdot s^{-2}$

β = the volumetric thermal expansion coefficient of the ambient air, temperature dependent

ν = the kinematic viscosity of the air, temperature dependent, $m^2 \cdot s^{-1}$

α = the thermal diffusivity of the air, temperature dependent, $m^2 \cdot s^{-1}$

The convection from the topside of the hotplate into the oven is calculated as free convection in an enclosed space from a lower horizontal hot surface to a horizontal cold surface above. The Nusselt number is therefore given by

$$\mathrm{Nu}_\delta = c \left(\mathrm{Ra}_\delta\right)^n \tag{4.8}$$

$$\mathrm{Ra}_\delta = \mathrm{Gr}_\delta \cdot \mathrm{Pr} = \frac{g \cdot \beta \left(T_{hotplate} - T_{inner,wall}\right) \delta^3}{\nu^2} \cdot \mathrm{Pr} \tag{4.9}$$

where δ = the thickness or height of the fluid layer

Table 4.1 Coefficients for Equation 4.8.

$\mathbf{Ra}_{\delta}$	c	n
$\mathbf{Ra}_{\delta} < 1700$	1	0
$1700 < \mathbf{Ra}_{\delta} < 7\times10^{3}$	0.059	0.4
$7\times10^{3} < \mathbf{Ra}_{\delta} < 3.2\times10^{5}$	0.212	0.25
$3.2\times10^{5} < \mathbf{Ra}_{\delta}$	0.061	0.33

Once the Nusselt number is calculated Equations 4.3 & 4.4 can be used to determine the convective heat flow inside the oven. However, the mechanism for heat transfer in enclosed spaces is complicated to the extent that the correlation of a measured heat transfer with that of the simple derived expression is not expected to be accurate. The derived expression will provide an estimate of the approximate magnitude of the free-convection heat transfer coefficient. The measured heat transfer is also affected by the fact that the oven is not air-tight and the exchange of air mass from inside the oven, around the hotplate, and to the environment is not only possible but was observed during the Italian trials.

The conduction of heat from the hotplate to the billet is dependent on the thermal interface contact conductance between them. This contact conductance is incorporated into the model as a thermal resistance where

$$R_{contact} = \frac{(T_{hotplate} - T_{billet})}{A_{\text{billet}} \cdot \dot{Q}_{cond}} \qquad \textbf{(4.10)}$$

$R_{contact}$ = the thermal contact resistance, $K \cdot m^{-2} \cdot W^{-1}$, which is inverse the conductance

A_{billet} = the contact area between the billet and the hotplate

The thermal contact conductance is dependent on the surface quality and contact pressure between the two bodies. Microscopic surface imperfections limit the effective contact area between two bodies to a finite number of points; this reduction in actual contact area increases resistance to heat flow. Contact pressure is the most important factor in determining contact conductance as contact area will grow with increasing contact pressure.

The effective thermal resistance is calculated by measuring the temperature difference and heat flow across the two bodies. This is done over a large envelope of operation with an average value obtained and then fed back into the thermal model of the oven. The energy balance for the hotplate is therefore given by

$$\frac{m_{\mathrm{hp}} \cdot c_{\mathrm{hp}} \cdot \Delta T}{\Delta t} = \dot{Q}_{in} - \dot{Q}_{cond,billet} - \dot{Q}_{conv,down} - \dot{Q}_{conv,up} - \dot{Q}_{rad} \quad \textbf{(4.11)}$$

$$T_{k+1} = T_k + \frac{\Delta t}{m_{\mathrm{hp}} \cdot c_{\mathrm{hp}}} \left(\dot{Q}_{in} - \dot{Q}_{cond,billet} - \dot{Q}_{conv,down} - \dot{Q}_{conv,up} - \dot{Q}_{rad} \right) \quad \textbf{(4.12)}$$

where m_{hp} = the mass of the hotplate, kg

c_{hp} = the specific heat capacity of the hotplate, $J \cdot kg^{-1} \cdot K^{-1}$

Δt = the step size of the discretisation in time, s

k = the step number of the iterative solution

4.1.2.2 Billet

Heat flows into the billet via conduction from the hotplate. Heat will be convected away from the billet to the walls of the oven. As previously mentioned it is assumed that any convection to the billet from the hotplate is negligible. The energy balance will therefore be given by

$$\frac{m_{\mathrm{b}} \cdot c_{\mathrm{b}} \cdot \Delta T}{\Delta t} = \dot{Q}_{cond,billet} - \dot{Q}_{conv,billet} \quad \textbf{(4.13)}$$

$$T_{k+1} = T_k + \frac{\Delta t}{m_{\mathrm{b}} \cdot c_{\mathrm{b}}} \left(\dot{Q}_{cond,billet} - \dot{Q}_{conv,billet} \right) \quad \textbf{(4.14)}$$

where m_{b} = the mass of the billet, kg, or thermal load

c_{b} = the specific heat capacity of the billet, $J \cdot kg^{-1} \cdot K^{-1}$, or thermal load

The conduction to the billet from the hotplate is given by Equation 4.10. The convection from the billet is a function of the billet temperature, wall temperature, and internal oven air temperature. This convection is treated as two convections; one from the top surface of the billet to the oven lid and one from the sides of the billet to the oven walls

$$\dot{Q}_{conv,billet} = \dot{Q}_{conv,billet\ side} + \dot{Q}_{conv,billet\ top} \quad \textbf{(4.15)}$$

Convection from the top of the billet is modelled as natural convection in an enclosed space from a horizontal hot surface to a cool surface above. Therefore, being analogous to convection from the hotplate to the oven walls, $\dot{Q}_{conv,billet\ top}$ is calculated using Equations 4.3 & 4.4.

However, the convection from the sides of the billet to the oven walls must be calculated as convection from a hot vertical surface to a cool vertical surface. For this case the Nusselt number differs slightly for that defined for the horizontal plate in Equation 4.8 and is now given by

$$\mathrm{Nu}_\delta = c\ (\mathrm{Ra}_\delta)^n \cdot (\frac{\mathrm{H}}{\delta})^m \quad \textbf{(4.16)}$$

where δ = thickness of fluid layer / horizontal distance between the vertical surfaces

H = the height of the fluid layer between the vertical surfaces

Table 4.2 Coefficients for Equation 4.16.

$\mathbf{Ra}_\delta$	c	n	m
$\mathbf{Ra}_\delta < 2000$	1	0	0
$2000 < \mathbf{Ra}_\delta < 2\times10^5$	0.197	0.25	-0.11
$2\times10^5 < \mathbf{Ra}_\delta < 2\times10^7$	0.073	0.33	-0.11

Equation 4.16 is valid for vertical walls or cylindrical annulus but in the model it must be used to describe the square oven walls interacting with the cylindrical aluminium billet. As such the horizontal thickness of the fluid layer is not constant or well defined (varying from 0.16-0.044 m). The fluid layer thickness is therefore given such that it defines an inner wall of an annulus of equal surface area to that of the square oven, δ = 0.13 m. The area required to calculate the convective heat flow is the logarithmic mean area

$$\mathrm{A_m} = \frac{\mathrm{A_o - A_i}}{\log_n(\mathrm{A_o}/\mathrm{A_i})} \quad \textbf{(4.17)}$$

where $\mathrm{A_o}$ = the interior surface area of the oven

A_i = the surface area of the sides of the cylindrical aluminium billet

4.1.2.3 Oven Wall

Heat is convected to the oven walls from the hotplate and the billet and then conducted across the wall before being convected to ambient. The walls themselves have almost negligible thermal mass but this mass is included in the model in order to determine the temperature rise within the walls. As the temperature of the wall is considered at the inner and outer surfaces, the thermal mass of the wall is assumed to be split evenly between these points, i.e.

$$\frac{m_w \cdot c_w \cdot \Delta T_{inner}}{\Delta t} = \dot{Q}_{conv,up} + \dot{Q}_{conv,billet} - \dot{Q}_{cond,wall} \quad \textbf{(4.18)}$$

$$T_{inner_{n+1}} = T_{inner_n} + \frac{\Delta t}{m_w \cdot c_w}\left(\dot{Q}_{conv,up} + \dot{Q}_{conv,billet} - \dot{Q}_{cond,wall}\right) \quad \textbf{(4.19)}$$

and

$$\frac{m_w \cdot c_w \cdot \Delta T_{outer}}{\Delta t} = \dot{Q}_{cond,wall} - \dot{Q}_{conv,wall} \quad \textbf{(4.20)}$$

$$T_{outer_{n+1}} = T_{outer_n} + \frac{\Delta t}{m_w \cdot c_w}\left(\dot{Q}_{cond,wall} - \dot{Q}_{conv,wall}\right) \quad \textbf{(4.21)}$$

where

$$\dot{Q}_{cond,wall} = k \cdot A_w \cdot \frac{(T_{inner} - T_{outer})}{\Delta x} \quad \textbf{(4.22)}$$

k = the thermal conductivity of the wall material Basotect©, $W \cdot m^{-1} \cdot K^{-1}$

m_w = half the mass of the Basotect©, kg

c_w = the specific heat capacity of the Basotect©, $J \cdot kg^{-1} \cdot K^{-1}$

A_w = the surface area of the oven walls, m^2

Δx = the wall thickness, m

Convection from the oven walls to ambient is modelled as unforced convection from a horizontal plate of the same area as the oven walls. $\dot{Q}_{conv,wall}$ is therefore given by appropriate substitution of relevant physical quantities into Equations 4.3 & 4.4.

4.1.2.4 Forced Convection

The basic oven model is also extended to the case that includes forced convection from the underside of the hotplate. This will therefore accommodate modelling of the oven outside of the lab in windy conditions. In the case of forced convection over an isothermal flat plate under laminar flow the average Nusselt number, Nu_m, in Equation. 4.4, is replaced by

$$\mathrm{Nu}_m = 0.664 \cdot {\mathrm{Re}_L}^{1/2} \cdot \mathrm{Pr}^{1/3} \qquad \text{for} \qquad 0.6 < \mathrm{Pr} < 10 \qquad \textbf{(4.23)}$$

$$\mathrm{Re}_L = \frac{u_\infty \cdot \mathrm{L}_c}{\nu} \qquad \textbf{(4.24)}$$

where Re_L = the dimensionless Reynold's number, which describes the ratio of inertial to viscous forces in fluid flow

u_∞ = the free stream velocity of the flow across the hotplate, m·s^{-1}

For the dimensions of the hotplate, low Reynold's numbers ($\mathrm{Re}_L < 10^5$) are anticipated for reasonable wind velocities, therefore laminar flow is assumed in all cases. However, this regular laminar flow is unlikely to reflect real world conditions. Wind flow is unlikely to be laminar and constant across hotplate, especially considering that is somewhat recessed. However, the model will provide valuable information on the sensitivity of the oven to wind.

4.2 Relevant Thermal Properties used in Calculations

Table 4.3 Thermal properties of system elements. Areas are given perpendicular to their respective heat fluxes; lengths are given along the direction of heat flow. The 2nd Aluminium Hot Plate refers to a supplementary hotplate made for the Italian trials with an alternative absorptive coating (see Figure 5.13).

Component	Mass (kg)	Area (m^2)	Length (m)	k (W·m^{-1}·K^{-1})	c (J· kg^{-1}·K^{-1})
Large Aluminium Billet	8.4	0.0181	0.163	170	900
Small Aluminium Billet	1.4	0.0127	0.038	170	900
Aluminium Hot Plate	1.02	0.102		170	900
Copper Hot Plate	4.38	0.102		401	385
2nd Aluminium Hot Plate	1.33	0.102		170	900
Basotect© Insulation		0.505	0.025	0.035	1500
Cast Iron Pot	3.4			55	460
Aluminium Pot	1.10			170	900
Aluminium Heating Element	0.3	0.00935	0.012	170	900

The thermal contact resistance between the thermal load and the hotplate is required to complete the full description of the model, but must be obtained experimentally.

4.3 Measurement of Thermal Contact Resistance

The large aluminium billet used in the lab tests was smooth on one end face, but machined on the other end to increase the surface roughness, see Figures 4.3a & 4.3b. A rough surface, with poor thermal contact with the hotplate, will impede the conductive heat flow between these bodies. Measuring the performance of the system with alternated ends of the billet therefore allowed an investigation and measurement of the effect of thermal contact resistance on oven performance. The key concern of this investigation is that particularly poor thermal contact conductance between the hotplate and user's pots and pans would result in adversely degraded oven performance.



Figure 4.3 The (a) rough and (b) smooth ends of the large aluminium billet; "poor" and "good" contact, respectively.

The billet was heated at 400 W input from the electrical resistance heaters with either one end or the other in contact with the hotplate. The heat flow through the billet was calculated from the increase in measured temperature of the billet, see Figure 4.4. The temperature increase of the billet is taken by averaging the measurements of two thermocouples placed in drilled holes at the base and top of the billet, see Figure 4.3b. Good thermal contact was ensured by coating the thermocouples with mineral oil before placing them in these holes.

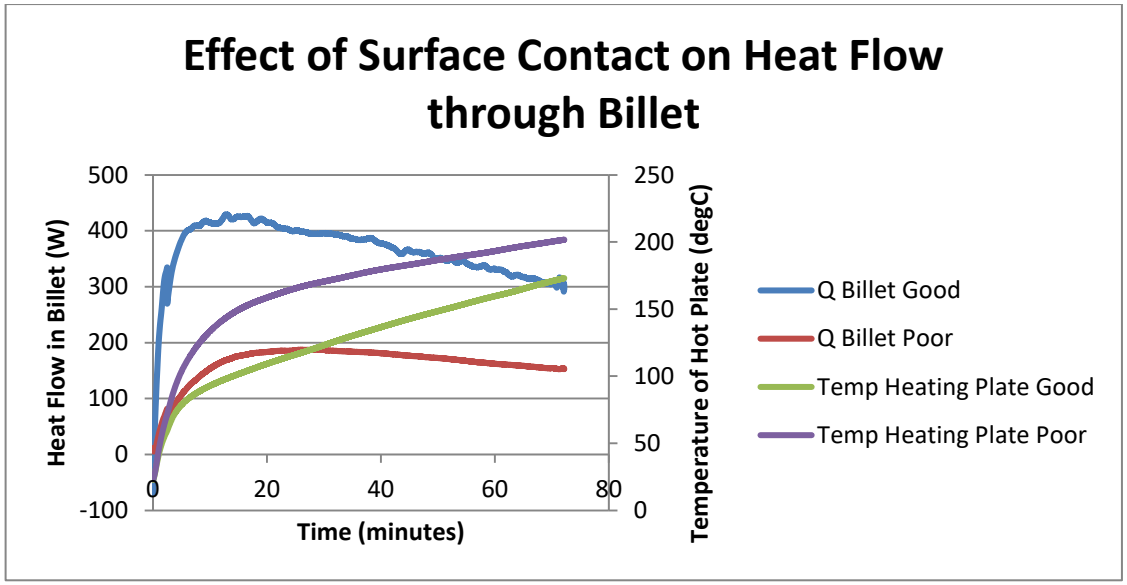


Figure 4.4 Measured effect of surface contact quality on heat flow across hotplate-billet boundary The heat flow into the billet is calculated from its specific heat and the rate of change of the measured billet temperatures. A linear temperature gradient is assumed between the top and bottom of the billet..

Whilst the poor contact results in a lower initial heat flow through the billet, after some time the heat flow is similar in both cases.

Thermocouples placed at the bottom of the billet and in the heating element attached to the hotplate gave the temperature difference across the boundary between the two bodies. This data was used to calculate the effective thermal resistance as per Equation 4.10 and produce Figure 4.5.

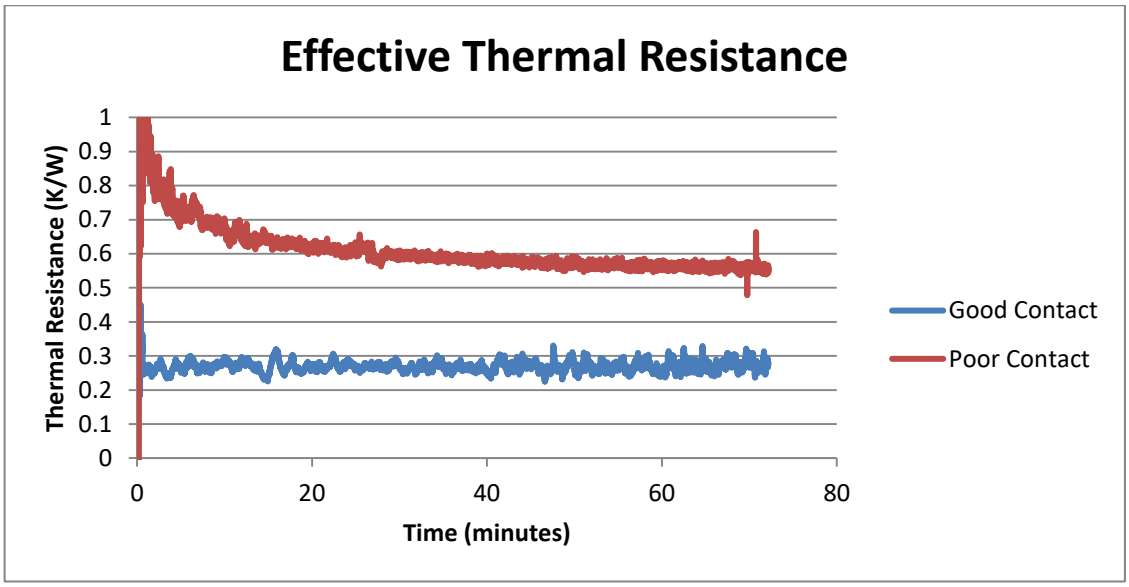


Figure 4.5 Measured effective thermal resistance of the hotplate-billet contact boundary as a function of time.

The drop in the thermal resistance of the poor contact case is interesting. Following Equation 4.11, ΔT was taken by comparing the temperatures measured in the heating element attached underneath the hotplate and in the base of the billet, $\dot{Q}$ is calculated by taking the rate of change in the specific heat of the billet as measured by the average temperature rise. This therefore assumes that there is little to no convection from the billet, which should be a valid assumption close to ambient temperatures.

Not considered in the measurement is the possibility of heat convecting from the hotplate to the billet. If heat is indeed convecting to the billet from the hotplate then there would be a greater $\dot{Q}$ than expected by conduction alone, and the thermal resistance will therefore be calculated lower than anticipated. If this is the case then as system temperatures increase, so will convection, and the thermal resistance will lower with time, as observed. This should only occur for as long as air temperatures inside the oven exceed that of the billet. In Figure 4.6 this is demonstrated to be the case until around 45 minutes into the test, wall temperatures exceed that of the billet until 30 minutes into the test. However, the measured thermal contact resistance continues to decrease monotonically past these limits and therefore internal convection offers a poor explanation for the observed decrease in measured contact resistance.

Furthermore, internal convection is still expected to be minimal on initial heating from ambient and should not change greatly during the first few minutes of operation. Conversely, the greatest change in measured thermal resistance is during the first 10 minutes of heating. Therefore, the explanation for the drop in measured thermal contact resistance cannot be due to internal convection within the oven.

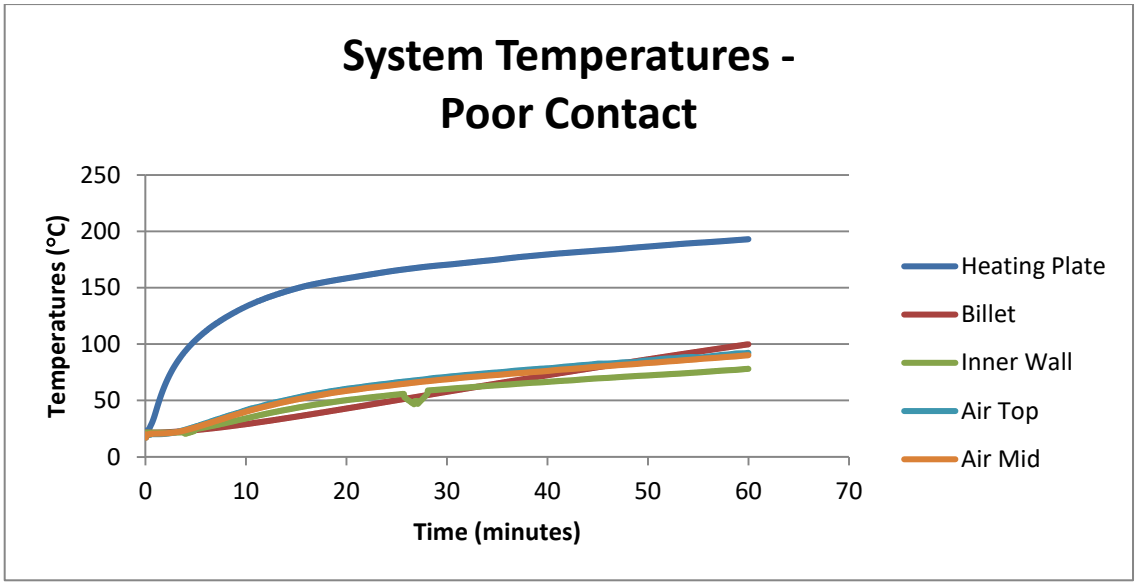


Figure 4.6 **With a poor thermal contact conductance inner wall and air temperatures exceed that of the billet for 30 and 45 minutes respectively. The dip in the inner wall temperature was due to a thermocouple becoming disconnected for a short time. The data was smoothed with a 1 minute rolling average taken.**

Given that the inner wall temperatures unexpectedly exceeded that of the billet until 45 minutes into the test, the behaviour of the billet should only be considered accurate after this time. Therefore, measurements for the thermal contact resistance are taken as the average of observed values after 45 minutes. The average values of the thermal contact resistances are 0.267 $K \cdot W^{-1}$ and 0.679 $K \cdot W^{-1}$ for the good and poor cases respectively, given the system geometry. Few pertinent examples of aluminium-aluminium contact conductances were found at low contact pressures in literature. However, as contact conductance is highly dependent on contact pressure the results obtained are within the expected range for aluminium-aluminium contact. A comparison of the values experimentally obtained to the most relevant one available from literature is given in Table 4.4.

Table 4.4 **Comparison of thermal contact conductances with obtained data.**

	Contact Pressure (kPa)	Contact Conductance ($W \cdot m^{-2} \cdot K^{-1}$)
Aluminium Billet Smooth - Lab	4.7	852
Aluminium Billet Rough - Lab	4.7	187
Aluminium-Aluminium [31]	100-1000	2000-12000

Analogous to the electrical case, the measurement of the effective thermal contact resistance will ultimately be a measure of a parallel resistance, which takes into account both

the thermal contact resistance and thermal resistance of convection to the billet. Values obtained for the relative heat transfer coefficients developed for the model indicate that the contact conductance should be 2 orders of magnitude greater than that for convection anywhere in the oven, see Table 4.4. Therefore the effect of any parallel convection on the value calculated for the contact resistance will be minimal.

Table 4.5 Calculated and measured* values for heat transfer coefficients.

Method of Heat Flow	Range of Heat Transfer Coefficients ($W \cdot m^{-2} \cdot K^{-1}$)
Convection up from Hotplate	0.4 – 3.0
Convection from Billet Top	0.3 – 2.2
Convection from Billet Side	0.0 – 3.1
Convection down from Hotplate	1.1 – 6.0
Contact Conduction*	187 – 852

The best explanation for the observed drop in thermal contact resistance for the poor contact case is in the manner in which $\dot{Q}$ is calculated. Figure 4.5 was calculated with a $\dot{Q}$ that takes the average of the measured temperature from either end of the billet. This assumption is accurate only if the temperature gradient across the billet is linear, which is unlikely to be the case during the initial heating of the billet. By considering the billet temperature to be uniform and equal to the lower thermocouple an overestimate of $\dot{Q}$ and therefore a lower-bound for the thermal contact resistance is developed, see Figure 4.7.

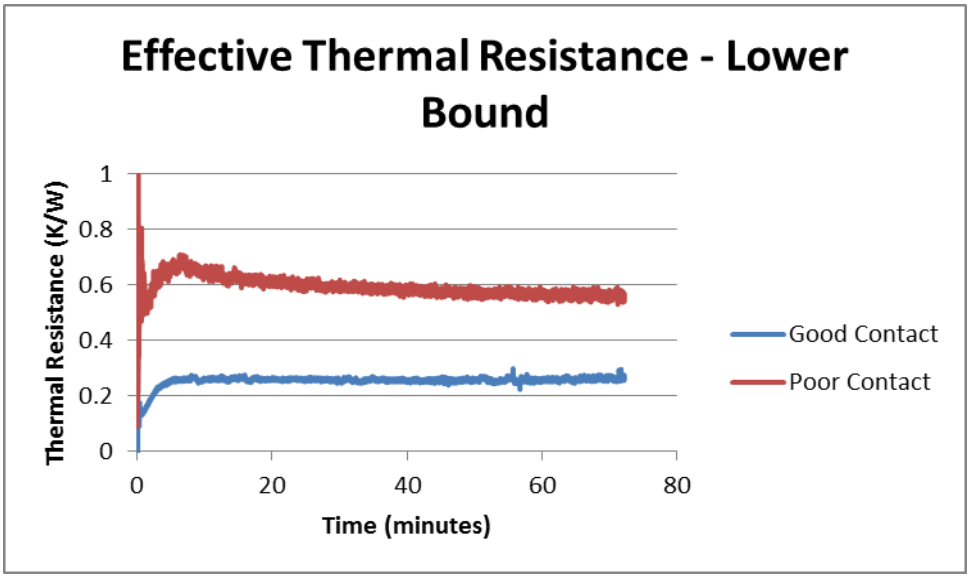


Figure 4.7 Measured lower limit of effective thermal resistance of the hotplate-billet contact boundary as a function of time.

This lower estimate of thermal contact resistance gives initially variable behaviour for both the poor and good contact cases. This would further seem to indicate that the initial calculations of $\dot{Q}$ do not take into account the correct temperature gradients in the system. To investigate the initial behaviour of the system an analytical solution to a simplified oven model was developed.

4.4 Analytical Solution to Initial Temperature Rise

The system of equations which describe the oven model cannot be solved analytically. However, upon consideration of only the conduction between the hotplate and the billet an analytical solution is possible that ignores convection and radiation. This analytical solution can therefore describe the approximate behaviour of the system when radiative and convective losses are small during the initial heating of the system.

The analytical result requires the solution of two coupled non-homogeneous linear ordinary differential equations:

$$\frac{dT_{hotplate}}{dt} = \frac{1}{\mathrm{m{\cdot}c}}\left[Q_{\mathrm{in}} - \frac{(T_{hotplate} - T_{billet})}{R_{\mathrm{contact}}{\cdot}\mathrm{A_{billet}}}\right] \tag{4.25}$$

$$\frac{dT_{billet}}{dt} = \frac{1}{\mathrm{M{\cdot}c}}\left[\frac{(T_{hotplate} - T_{billet})}{R_{\mathrm{contact}}{\cdot}\mathrm{A_{billet}}}\right] \tag{4.26}$$

where M = the mass of the aluminium billet, kg

m = the mass of the hotplate, kg

c = the specific heat capacity of aluminium, $\mathrm{J{\cdot}kg^{-1}{\cdot}K^{-1}}$

The initial conditions are that the hotplate and billet are both at ambient temperature, which yields the following solutions:

$$T_{billet}(t) = \frac{Q_{\mathrm{in}}\mathrm{mM}RA}{(\mathrm{m+M})^2} \cdot \left[e^{-\left(\frac{M+m}{mMcRA}\right)t} - 1\right] + \left(\frac{Q_{\mathrm{in}}}{c(\mathrm{m+M})}\right)t + T_{\infty} \tag{4.27}$$

$$T_{hotplate}(t) = \frac{Q_{\mathrm{in}}\mathrm{M^2RA}}{(\mathrm{m+M})^2} \cdot \left[1 - e^{-\left(\frac{M+m}{mMcRA}\right)t}\right] + \left(\frac{Q_{\mathrm{in}}}{c(\mathrm{m+M})}\right)t + T_{\infty} \tag{4.28}$$

These solutions are plotted for the case of the lab trials given the measured thermal contact resistances, see Figure 4.8.

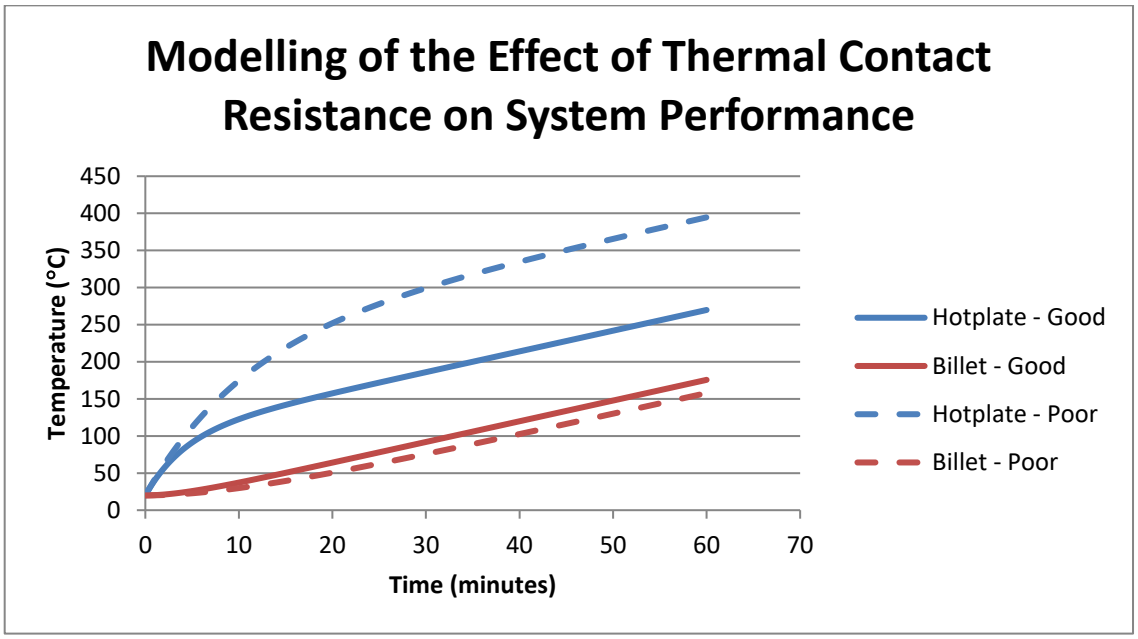


Figure 4.8 Model of only conduction between the hotplate and billet.

As per equations 4.27 & 4.28 the initial system behaviour is dictated by an exponential decay to a linear temperature increase. From these solutions parameters that define the performance of the system, and their dependence on the thermal contact resistance of the system, can be identified:

1) the time delay between when the hotplate reaches a temperature and when the billet then obtains that same temperature,
2) the magnitude of the temperature difference between the billet and hotplate, and
3) the time-constant of the exponential decay to the linear result.

Of great importance to eventual oven performance is the time delay between the temperatures observed in the billet compared to the hotplate. This time delay will result in longer cooking times if the billet temperature lags far behind the hotplate temperature. This time delay is given analytically by:

$$\Delta t = \mathrm{McRA} \tag{4.29}$$

For the measured thermal contact resistances, this time delay will be 34 and 85 minutes respectively for the good and poor cases of thermal contact, i.e. for the case of good thermal contact, once the hotplate reaches 100 °C it will take a further 34 minutes for the billet to reach 100 °C.

The temperature difference between the hotplate and billet will be a factor in determining the ultimate cooking temperature obtainable by the oven. This temperature difference is given by:

$$\Delta T = \frac{Q_{\text{in}}\text{MRA}}{\text{m+M}} \qquad \textbf{(4.30)}$$

For the measured thermal contact resistances, this temperature difference will be 94 and 237 K respectively.

The time-constant describes how long the system takes until the hotplate and billet reach an approximately stable temperature difference. Conduction from the hotplate to the billet and therefore measurements of the thermal contact resistance are dependent on this same temperature difference. The time constant is therefore useful in determining when reliable measurements of the thermal contact resistance can be made, it is given by

$$\tau = \frac{\text{mMcRA}}{\text{m+M}} \qquad \textbf{(4.30)}$$

For the measured thermal contact resistances, the time taken for the exponential decay to reach 63% of its final value is 4.2 and 10.6 minutes respectively for the good and poor cases of thermal contact conductance. These results are summarised in Table 4.6.

Table 4.6 Summary of comparison of conduction only Model and Lab Data.

	Good Thermal Contact		Poor Thermal Contact	
Results Type	Model	Lab Data	Model	Lab Data
Time delay (minutes)	34	47	85	54+
Temperature difference (K)	94	61	237	115
Time constant (minutes)	4.2	3.9	10.6	6

From the comparison to lab data it can be seen that the temperature difference and time-constant are less than predicted by the simple conduction model. However, the time delay in

hotplate-billet temperature was larger than predicted. As per Equation 4.30, this time delay is proportional to the thermal contact resistance.

Strategies to minimise this resistance in-situ depend mostly on counteracting the air-gap that is present under normal conditions between the microstructural surface defects of each surface. This is most easily accomplished with the use of an oil; similar in function to a thermal paste.

Interestingly the time-constant of the exponential decay matches the time period of variable thermal contact resistance measurements, see Figure 4.7. This further supports the idea that the calculated $\dot{Q}$ is erroneous given the non-linear temperature gradients through the system during the initial heating phase. This length of this initial heating phase is determined by the time-constant, which is proportional to the contact resistance as observed in both Figure 4.7 and Table 4.6.

Thus the analytical conduction only solution has given explanation to the anomalies in the measurement of the thermal contact resistance. With the thermal contact resistance measured and the oven model therefore fully described comparisons can therefore be made with lab data.

4.5 Investigation of effect of Thermal Contact Resistance on Oven Performance

The model of the oven system is compared to measured lab data in Figure 4.9 for billet and hotplate temperatures in cases of both good and poor contact thermal contact. The modelled effect of thermal contact conductance seems to have over-estimated hotplate temperatures by around 35 K. Promisingly, billet temperatures agree better and there is excellent agreement for the case of poor contact with the billet. The form of the transient temperature evolution agrees well and it would seem that the higher temperatures expected from the model may be due to an underestimation of real world heat losses.

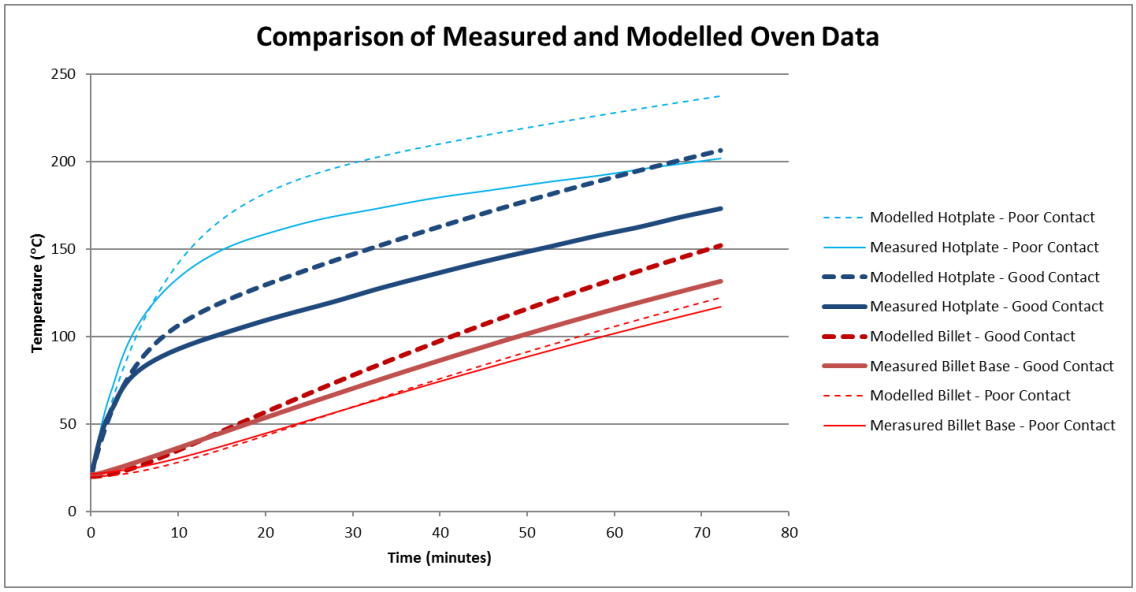


Figure 4.9 Comparison of modelled (dashed line) and measured (solid line) temperatures as a function of thermal contact conductance.

Temperatures for other oven components were obtained from the oven model and are compared with measured data obtained in the lab in Figure 4.10.

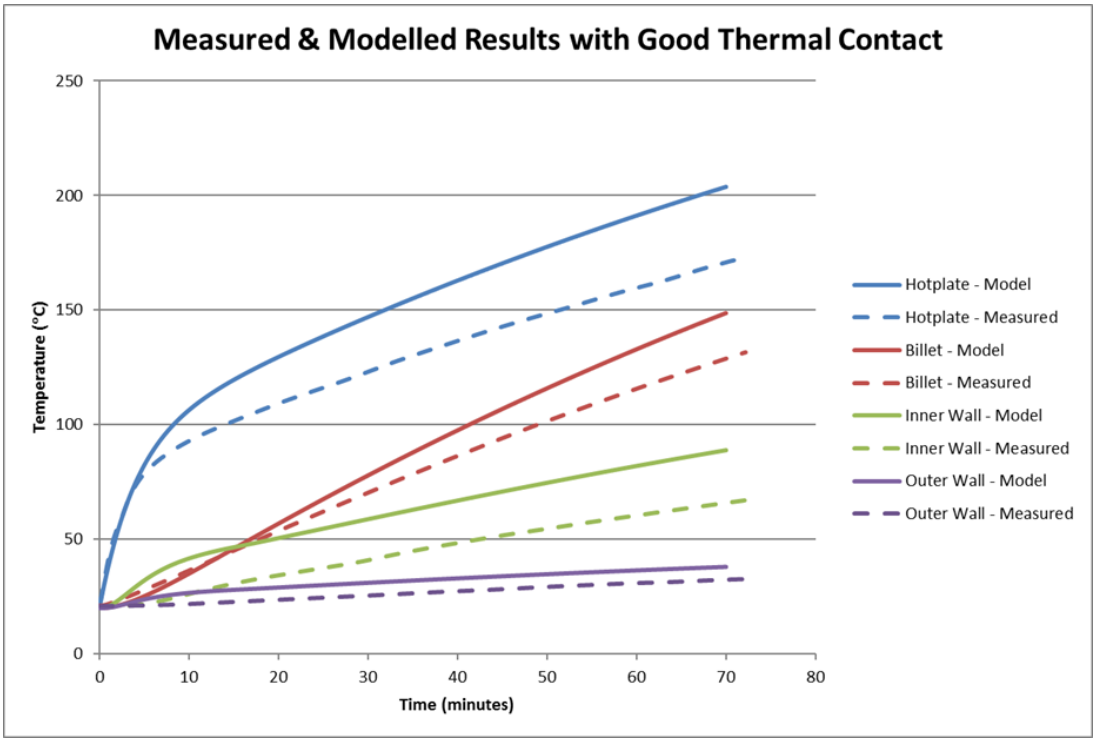


Figure 4.10 Comparison of predicted results for oven performance with measured lab data.

The model gives higher hotplate, billet and inner wall temperatures which would seem to indicate that losses to ambient from the hotplate are underestimated. The model

overestimates hotplate and billet temperatures by approximately 30°C. The larger temperature difference across the wall in the model indicates that conduction through the wall may be overestimated in the model.

In confirmation of the assumption that convection to the billet from the hotplate is negligible the lab results indicate that the billet temperature was at all times higher than air or inner wall temperatures in the oven.

Hotplate losses could be underestimated for several reasons. Firstly, the oven assumes that the convective loss is natural when there is likely to be some wind currents in the lab which could slightly affect the results. Also, the model ignores losses due to heat conductance from the hotplate through its supporting frame to ambient.

The convective losses through the hotplate were multiplied by a factor of 2.5 to investigate the extent to which the model underestimates heat loss, see Figure 4.11.

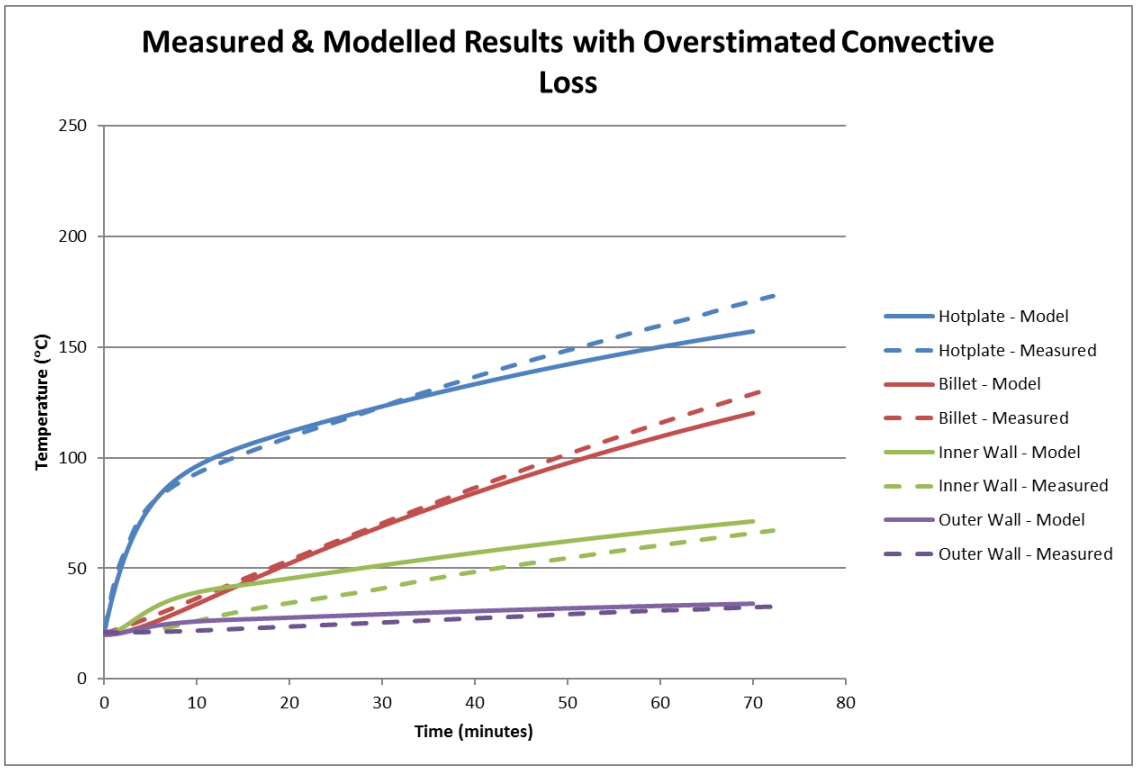


Figure 4.11 Comparison of predicted results for oven performance, including overestimated convective losses from the hotplate, with measured lab data.

Although there is good agreement with the final temperatures, there are still a few discrepancies between the data and the model, especially with the hotplate temperatures. The model is limited to assuming an isothermal hotplate, whilst in reality there will exist a temperature gradient across the hotplate. There will be a hot spot at the centre of the hotplate where the electric resistance heater is attached and where the thermocouples are placed, whilst temperatures towards the edges of the hotplate will be lower.

A summary of the recorded system temperatures for the models and lab tests is given in Table 4.7.

Table 4.7 Summary of system temperatures after 60 minutes of heating. *The hot plate temperature measured in Italy was significantly lower than anticipated due to convective losses from the hotplate where the thermocouple was placed.

Temperatures at 60 minutes	Hot Plate (°C)	Billet (°C)	Inner Wall (°C)	Outer Wall (°C)
Model – Good Contact	191	133	82	36
Lab Test – Good Contact	159	111	60	31
Model - 2.5x Convective Losses	150	109	67	33
Analytical Solution (no losses)	247	177	-	-
Model – Good Contact - 315 W	134	97	60	31
Italy – Good Contact – 315 W	94*	95	61	32

4.6 Sensitivity Analysis of the Oven Model

Given the relatively good agreement between the model and data a sensitivity analysis was undertaken in order to further test the model and also predict oven behaviour.

4.6.1 Effect of Oven Wall Insulation on Oven Performance

The thickness of the Basotect© insulation in the oven is 20mm. The thickness of this insulation was varied between 2mm and 200mm in the analysis, see Figure 4.12.

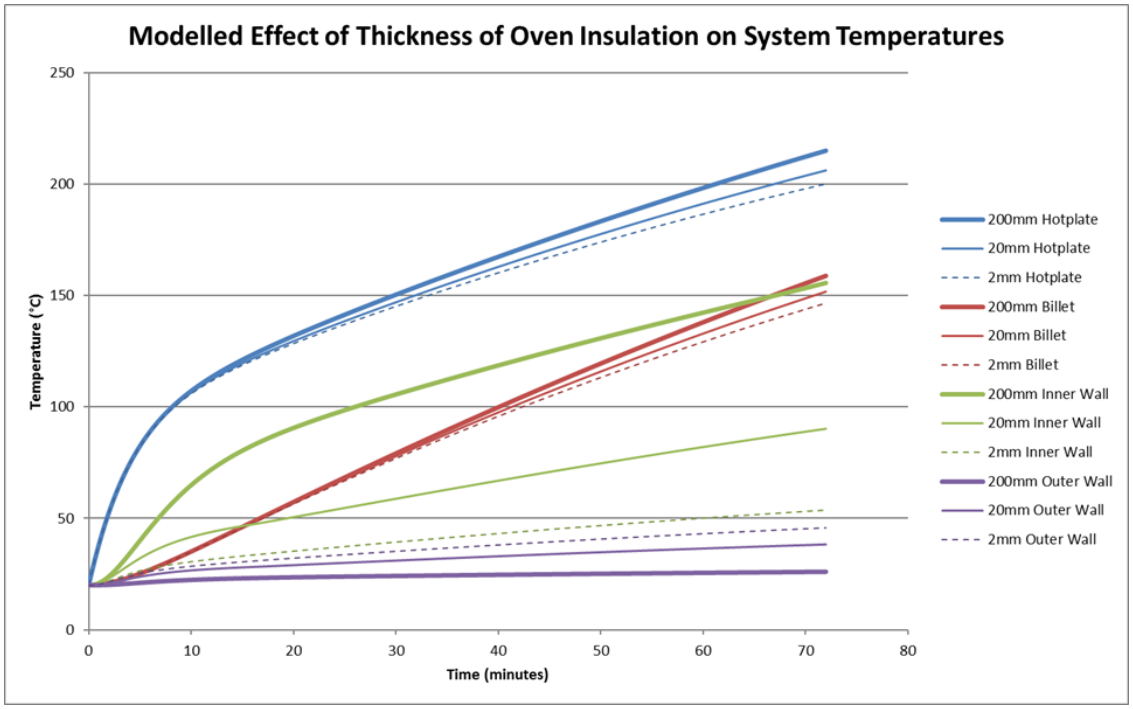


Figure 4.12 Modelling the effects oven wall insulation thickness of 200mm, 20mm, and 2mm on system temperatures.

The thickness of Basotect© in the oven wall has a minor effect on either hotplate or billet temperatures. However, it will have a large effect on the inner wall temperature of the oven and the heat flow through the oven walls, see Figure 4.13.

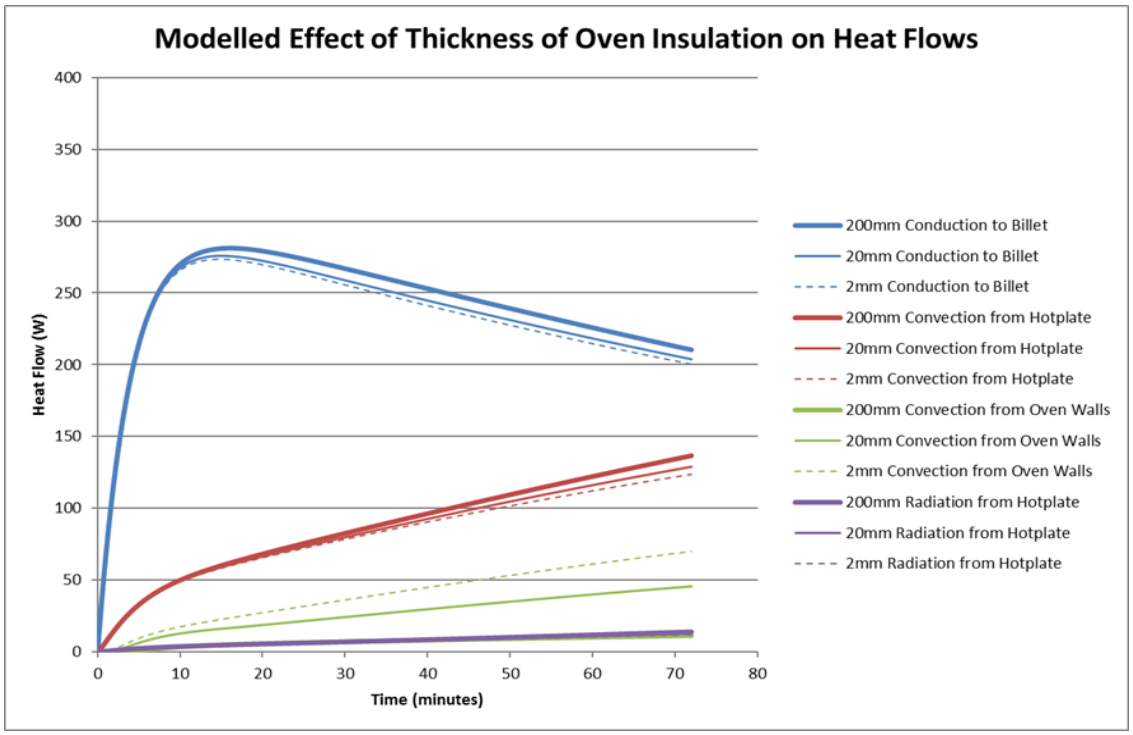


Figure 4.13 Modelling the effects oven wall insulation thickness of 200mm, 20mm, and 2mm on system heat flows.

The extra insulation in the oven wall can reduce heat flow through the oven walls from 50 W to 5 W. However, this results in only a slightly higher conduction to the billet, with a slightly higher convection from the hotplate also predicted.

4.6.2 Effect of Convective Losses from the Hotplate on Oven Performance

Convective losses for the standard model were compared to those with double, and triple these losses by doubling and tripling the heat transfer coefficient calculated for downwards convection from the hotplate. For the case of forced convection this corresponds to, respectively, four and nine times the original wind speed as per Equations 4.23 & 4.24, see Figures 4.14 & 4.15.

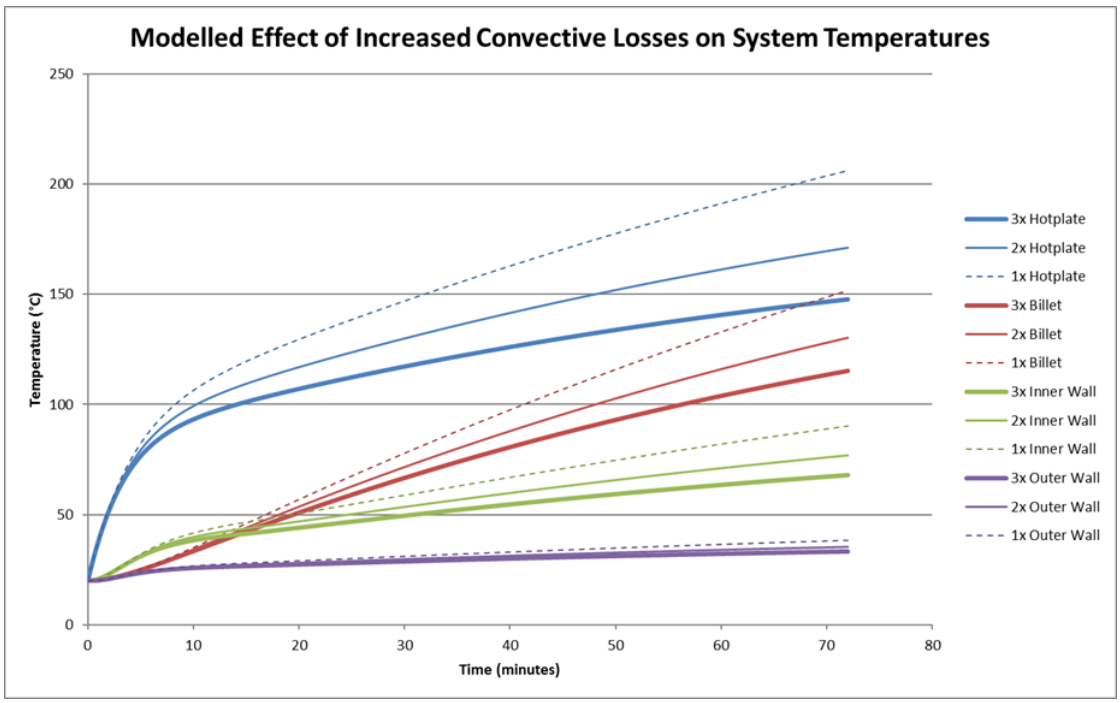


Figure 4.14 Predicted system temperatures for 1x, 2x, and 3x the expected downwards convection from the hotplate.

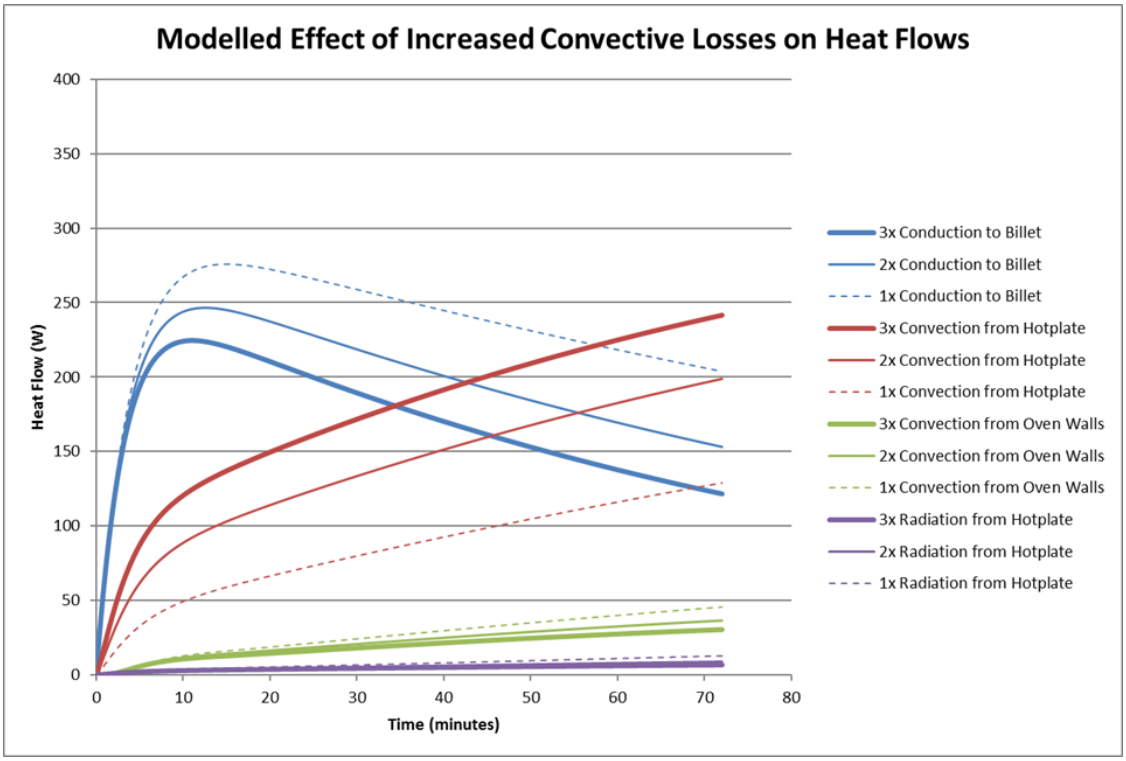


Figure 4.15 Predicted system heat flows for 1x, 2x, and 3x the expected downwards convection from the hotplate.

Increasing the amount of convection from the underside of the hotplate affects all expected temperatures in the system; less heat will remain in the hotplate and therefore less heat will conduct to the billet and then convect to the walls. Doubling convective losses lowered expected billet temperatures by approximately 15 K, whilst tripling these convective losses lowered expected billet temperatures by a further 15 K.

4.6.3 Effect of Contact Conductance on Oven Performance

The effect of contact conductance between the billet and hotplate on the performance of the system is further investigated for thermal contact resistances outside the range of those measured in the lab. The ratio of contact resistances measured in the system, based on the rough and smooth ends of the aluminium billet, was 2.54. The range of resistances modelled was extended past those measured by this same ratio, such that $R_{contact,lower}$ = 0.10 K·W^{-1} and $R_{contact,upper}$ = 1.73 K·W^{-1}, see Figures 4.16 & 4.17.

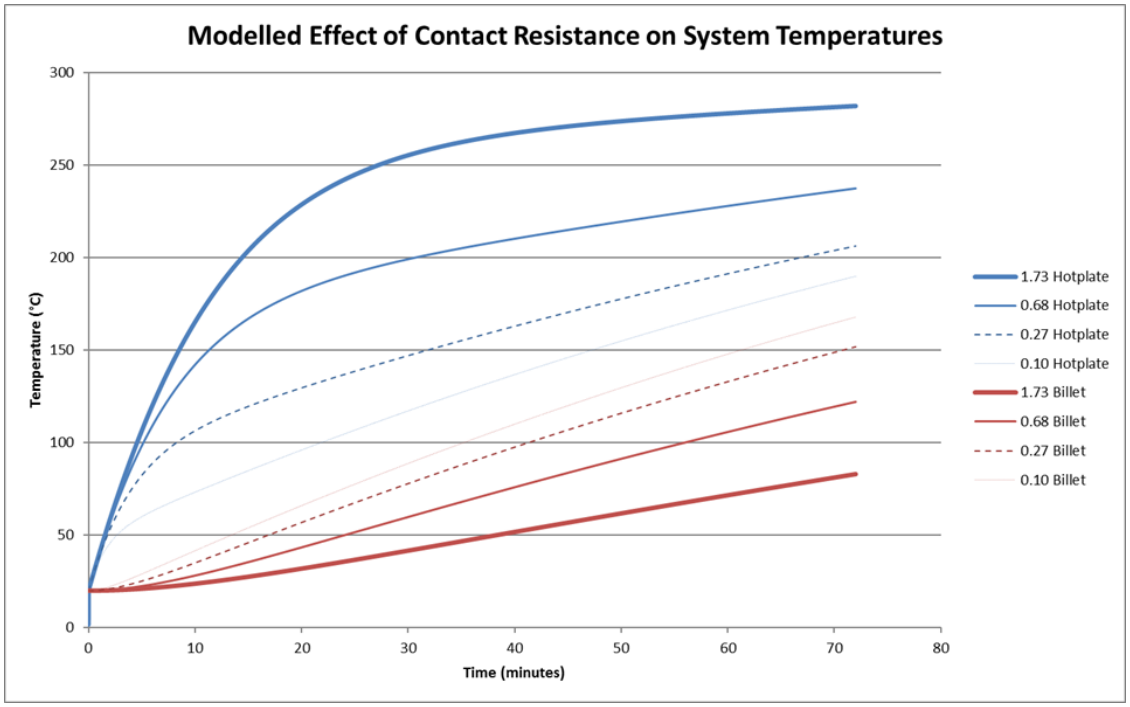


Figure 4.16 Predicted system temperatures for contact resistances of 0.10, 0.27, 0.68 and 1.73 K·W^{-1} between the hotplate and billet.

.

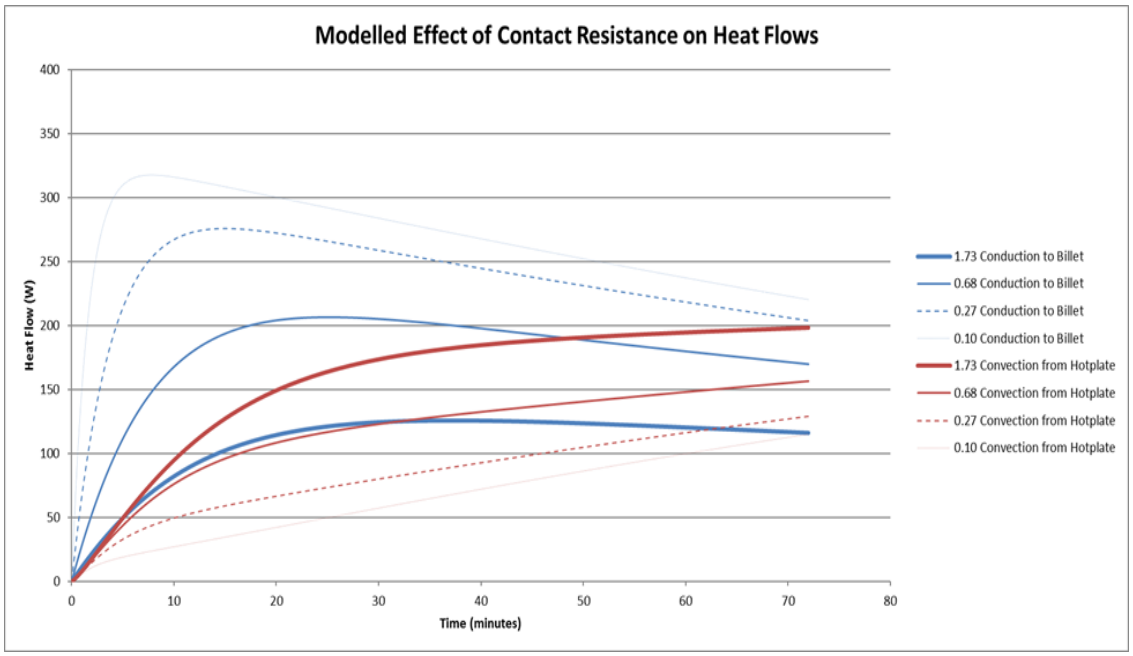


Figure 4.17 Predicted system heat flows for contact resistances of 0.10, 0.27, 0.68 and 1.73 K·W^{-1} between the hotplate and billet.

The pattern across all scenarios is that increases in thermal contact resistance will raise the hotplate temperature whilst lowering the billet temperature. This will increase convective losses and increase the heating time for the billet to reach a given temperature. Changing the

contact resistance had little effect on oven wall temperatures or convection from the oven walls.

4.6.4 Summary of Sensitivity Analysis

Thickening or thinning the layer of insulation in the oven walls has little effect on the overall system performance in terms of temperatures obtained in the billet and hotplate. However, the presence of an oven will reduce convective losses significantly, particularly in windy conditions.

If convective losses through the underside of the hotplate increase, both hotplate and billet temperatures will be reduced. However, the rise in billet temperatures remains approximately linear in these cases and will generally closely follow the hotplate temperature. The greatest impact to the rate in temperature increase of the billet will come from the thermal contact resistance between the hotplate and the billet. As this resistance rises the temperature difference between the hotplate and billet required to drive thermal conduction increases. As the system is currently designed elevated hotplate temperatures will result in increasing convective losses from underneath the hotplate, limiting oven performance. Not only will billet temperatures remain low but the time taken to reach a given billet temperature will also increase.

However, caution should be taken when applying poor thermal contact conductances as the model does not consider convection to the billet from elevated oven air temperatures. In this regard the model presents a worst case scenario for heat flow to the billet. Additionally, the range of thermal contact resistances investigated here is likely to be much larger than would reasonably be expected from general oven use.

4.7 Comparison of Model with Experimental Data

Baseline performance of the oven was established using an electrical resistance heater attached to the underside of the receiver to simulate incident light. The heater was set to

400W output in order to simulate a larger family-sized cooker, compared to the 236W expected from the prototype after reflective and absorptive losses. The contact area of the electrical resistance heater with the hotplate is 10-25% larger than the anticipated caustic region from earlier optical modelling, but this would not have a significant effect on performance. The results from these experiments were used to produce a dynamic thermal model of the oven and receiver. This model showed good agreement with results despite its simplicity, see Table 4.8.

Table 4.8 Temperatures of various system elements after 60 minutes of heating; model values compared to lab data with calibrated heat input in the lab. An aluminium billet was used as a thermal load for the oven.

Cooking Mode	Hot Plate (°C)	Billet (°C)	Inner Wall (°C)	Outer Wall (°C)
Lab Test – 400 W	159	111	60	31
Model – 400 W	150	109	67	33

4.8 Estimation of Heat Losses

This model includes estimates for the main mechanisms of heat loss in the system, in decreasing order of importance; forced convection from the underside of the receiver, radiation from the receiver and conduction through the oven walls. For the thermal properties of the oven, the ranges of heat transfer coefficients for these mechanisms are listed in Table 4.9.

Table 4.9 Relevant data for calculation of baseline data using a thermal model of the oven system.

Method of Heat Flow	Range of Heat Transfer Coefficients ($W \cdot m^{-2} \cdot K^{-1}$)
Natural Convection up from Hotplate	0.4 – 3.0
Forced Convection down from Hotplate[1]	1.1 – 31.91
Conduction to Billet/Thermal Load[2]	187 – 852
Radiation from Hotplate[3]	

[1]These values are given for a wind speed up to 5 m/s.
[2]These values are dependent on the thermal contact resistance between the thermal load and the hotplate; the values given here were found experimentally.
[3]Radiative heat loss from the hot plate is minimal; for an emissivity of 0.35 the radiative heat loss is only 18.9 W at 100°C, compared to convective losses of 135 W. Although radiative heat losses will grow by approximately the fourth power of the temperature of the hotplate, at observed temperatures for the system, they will always be inferior to convective heat losses.

Convective losses will clearly dominate the system if the hotplate behaves similarly to a flat plate under forced convection. The estimates for convective losses are more than twice that of conductive losses through the oven walls at a modest wind speed of only 0.5m/s. The

choice of finish for the underside of the hotplate becomes important with regards to radiative losses. The difference between the performance of the solar paint (ε = 0.05) and enamel paint (ε = 0.32) is approximately equivalent to the conductive losses of the system, see Figure 4.18.

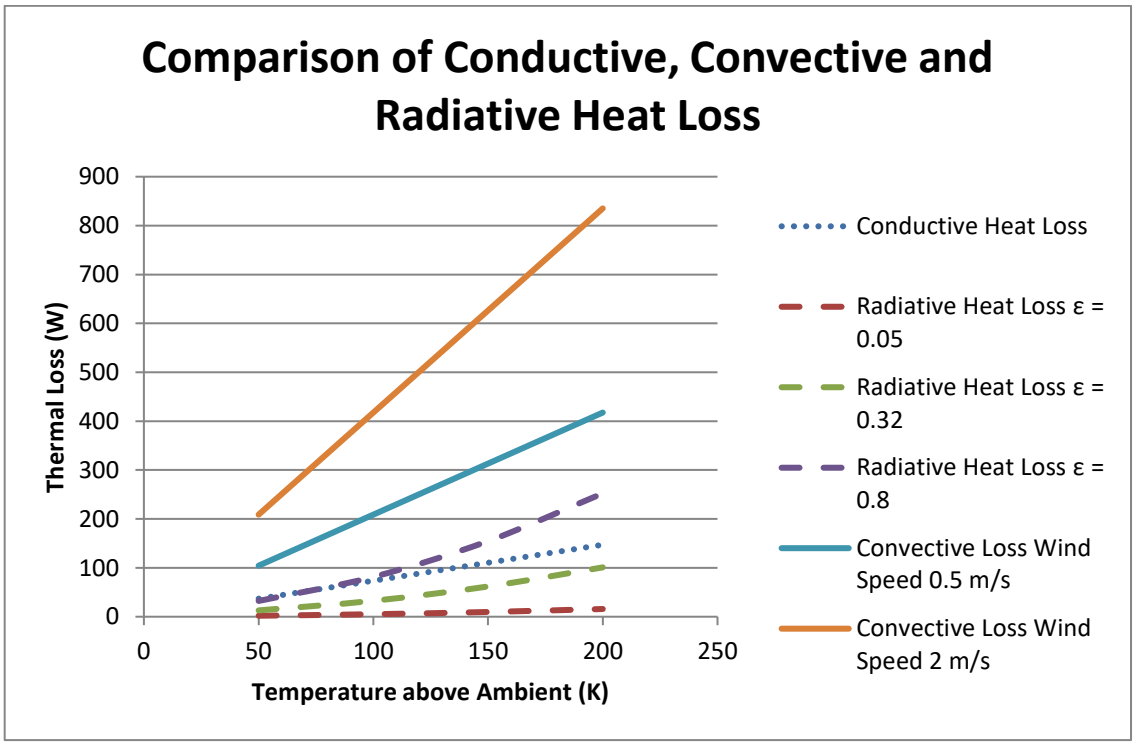


Figure 4.18 Comparison of thermal losses from the oven system, the convective losses shown assume a laminar boundary layer.

When further considering the way in which the system behaves in the field the convective losses will still likely dominate. This is due to the fact that the heat flow inside the oven will be limited by both natural convection and radiative balance between aluminium surfaces that have low emissivities. Heat will most easily be conducted through the hotplate (and the thermal mass inside the oven), where there is the potential for it to be convected away.

However, if food is being cooked inside the oven the high water content will tend to limit the temperatures in the oven to around 100°C. This in turn will help to limit thermal losses in the system.

5 Dytecna Prototype

Over several brainstorming sessions the design for a solar cooker was developed with our industrial partners Dytecna. This solar cooker was based off the geometry of the lab prototype, but was large enough to provide adequate power for cooking, estimated at 300W after reflective and absorptive losses, see Figure 5.1.



Figure 5.1 Prototype solar cooker as supplied by Dytecna.

During the design sessions Steve Harrison and Richard Kennedy from Dytecna were present along with Prof. Nick Jelley and myself. Over the course of these meetings the requirements were set out for the Dytecna prototype cooker and the details of many design elements were finalised. My experience in assembling the prototype was critical for the design of the attachments to secure the mirrors, and to ensure that they conformed to the desired geometry. Additionally, the mirror geometries were developed independently by both Prof Nick Jelley and myself before being supplied to Dytecna. The tracking mechanism and absorber dimensions were also developed following my experience with determining the

optical performance of the system for off-axis scenarios. With the critical design elements finalised during these meetings Dytecna were then able to develop the remainder of the system, i.e. the work table and base support, before manufacturing the prototype themselves. In anticipation of a field trial in Italy the prototype solar cooker developed by Dytecna was received in the cryogenics lab in the Engineering Department.

5.1 Design Features

The primary goal of the Dytecna prototype was to establish the Oxford reflex concentrator design as an effective solar cooker. To this end the mirrors were enlarged in order to guarantee sufficient power to provide adequate cooking times. The lab prototype was scaled at a power of 236 W incident flux on the receiver, whilst the Dytecna prototype was scaled at a power of 300 W; assuming mirror reflectivities of 90%. The scaling of the mirrors at 300W was deemed adequate for cooking whilst ensuring that two pairs of mirrors could be cut from a single sheet of the supplied Alanod with minimal wastage. A summary of the changes in mirror dimensions is available in Table 5.1.

Table 5.1 Summary of changes to mirror variables for the Dytecna prototype.

Variable	Lab Prototype	Dytecna Prototype	Units
r_1	666	710	mm
r_2	1000	1100	mm
α	60	60	degrees
gap	20.0	20	mm
y_1	557	595	mm
s	0.958	0.85	(ratio)
d	208	306	mm
h	99.5	130	mm

Several key features related to the unique properties of the Oxford reflex concentrator are evident in the design of the prototype solar cooker. The beam-up configuration of the mirrors ensures that the receiver/hotplate is relatively high from the ground. However, in contrast to parabolic dish system where the receiver is placed in the aperture, the receiver area for the Dytecna prototype is easily accessible. The extra space permits the placement of a surface for

cooking preparation next to the hotplate. This surface is placed conveniently at standard work table height.

Another design feature is the extra wide hotplate which allows for the simultaneous heating of two pots. Additionally, the wide hotplate allows for generous tolerances in tracking errors, which enables the user to wait up to 15-20 minutes between tracking adjustments whilst still capturing most of the solar flux on the underside of the hotplate.

As shown in Figure 5.1, tracking of the system can be performed from the standing position next to the hotplate and food preparation surface. This is performed using the handles placed next to the top of the parabolic mirror.

Finally, a hole can be seen in the centre of the food preparation surface. This is situated so that an upright umbrella/parasol can be placed here to shade the user. Due to the unique geometry of the system this can be managed such that an umbrella of small diameter will not shade the mirrors. If the angle of the umbrella is matched to that of the conical/optical axis of the system shading of the mirrors will be avoided.

In combination the design features are intended to allow a user to cook from a single standing position where they can prepare food, look after the pots, and adjust the mirrors, all whilst standing in the shade. Despite featuring several parts made from bent sheet metal and scaffold tubing the Dytecna prototype was able to be flat-packed in a relatively small profile of ~14cm. In addition to the parts supplied by Dytecna an oven was constructed for the cooker by Prof. Nick Jelley and myself. Additionally, I designed a small sundial which would attach to the mirror assembly and aid in tracking of the system. The sundial was designed to be parallel with the optical axis of the system such that no shadow would be cast when the system was correctly aligned with the sun.

Lastly, there was some concern over the rigidity of the mirror support assembly, which featured slotted joints and 6mm thick plywood. I suggested adding some further supports

including some triangulation to the design in order to increase rigidity, these were added for the Italian trial.

5.1.1 Lab Verification of Optics

The mirror geometry of the Dytecna prototype was verified by placing the concentrator in the testing rig which had been constructed to accommodate the lab prototype. However, the increased dimensions of the Dytecna prototype required the testing rig to be enlarged. It became apparent upon preliminary testing that two support ribs in the mirror's structural assembly had not been manufactured to the correct dimensions. These were redesigned by myself using SolidWorks before being remade using the router in the Engineering Science Department.

The increased dimensions of the concentrator resulted in significantly longer optical paths for the testing laser beams, and a greater spread in the resultant laser points in the focal plane. Additionally, the tolerances in the predominantly wooden mirror structure (which featured slotted joints) contributed increased errors in the optical performance of the system. Therefore, it was not possible to position the sensor of the Nikon D50 camera at the focal point of the system. Instead, a sheet of grided paper on the underside of a glass surface would be placed at the focal plane of the system. The camera would then be used, with a lens, to take pictures of the laser points incident on this paper.

These measurements were used not to determine exact optical performance, as per the tests for the lab prototype, but to ensure that the system was focusing light correctly. Configured as a solar cooker the Dytecna prototype had a large enough receiver to absorb almost all light from the conical mirror given tracking errors of ±2.5°, or equivalently ±10 minutes of solar movement. The exact distribution of this flux on the receiver is not crucial for calculations of heat flow into the system.

The results taken confirmed that, with the replacement ribs, the system was focusing correctly, see Figure 5.2.

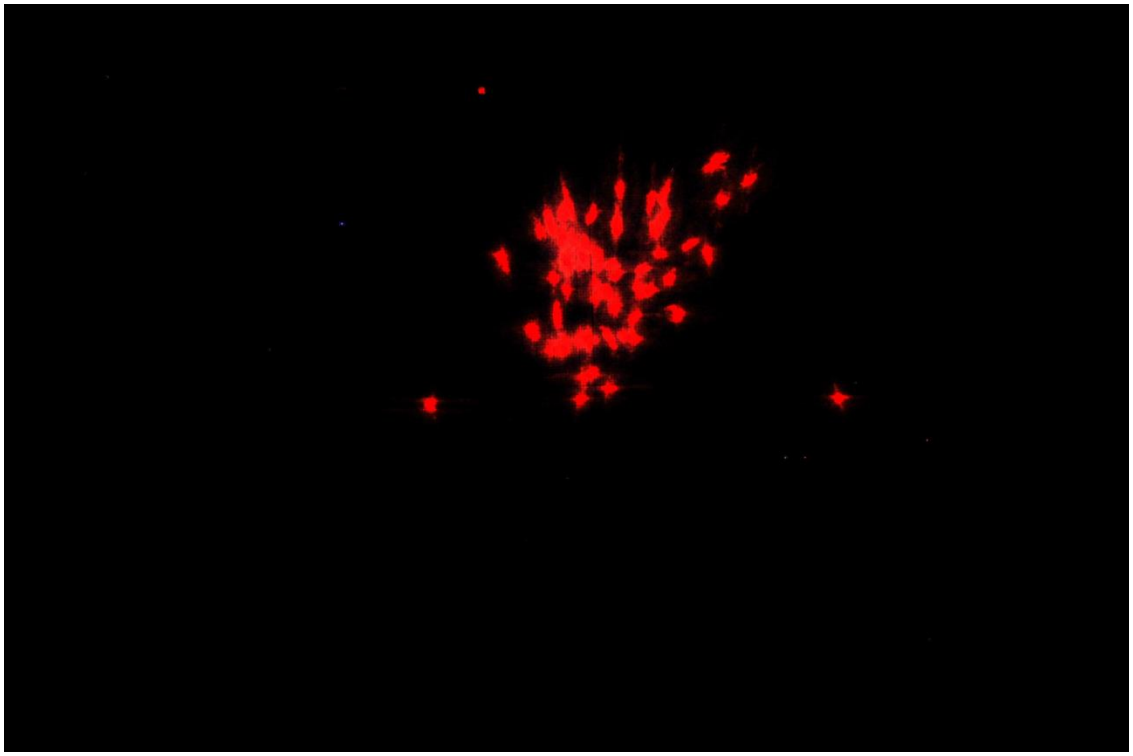


Figure 5.2 Composite image of approximately 50 laser beams incident in on the focal plane. Dimensions are 18cm by 28cm.

5.1.2 Construction of Lightmeter

During the field trials in Italy it would be necessary to measure the direct normal irradiance of the sun, in order to determine the flux incident on the receiver. Pyroheliometers proved to be prohibitively expensive, and none were available to the group. Instead it was decided to construct a small lightmeter, using Kingbright™ KPS-5130PD7C photodiodes, in order to give an approximate measurement of direct solar irradiance. These photodiodes would be placed inside a collimator, to ensure that only direct sunlight from the solar disk was measured. The collimator was constructed such that the photodiodes could see a 2.5° radius of the sky.

The lightmeter would be powered with two 9 V batteries supplying ±9V rails to 3 operational amplifiers. The Kingbright KPS-5130PD7C is a 3-channel/1 Chip (R,G,B) Si Photodiode, such that 3 operational amplifiers were required. The photodiodes, and the circuit board holding the operational amplifiers and other components are all housed in a black box, which can be seen in Figure 5.3 , the brass collimator is attached. The peak

sensitivity wavelengths for the red, green and blue channels are 620, 550 and 470nm respectively.

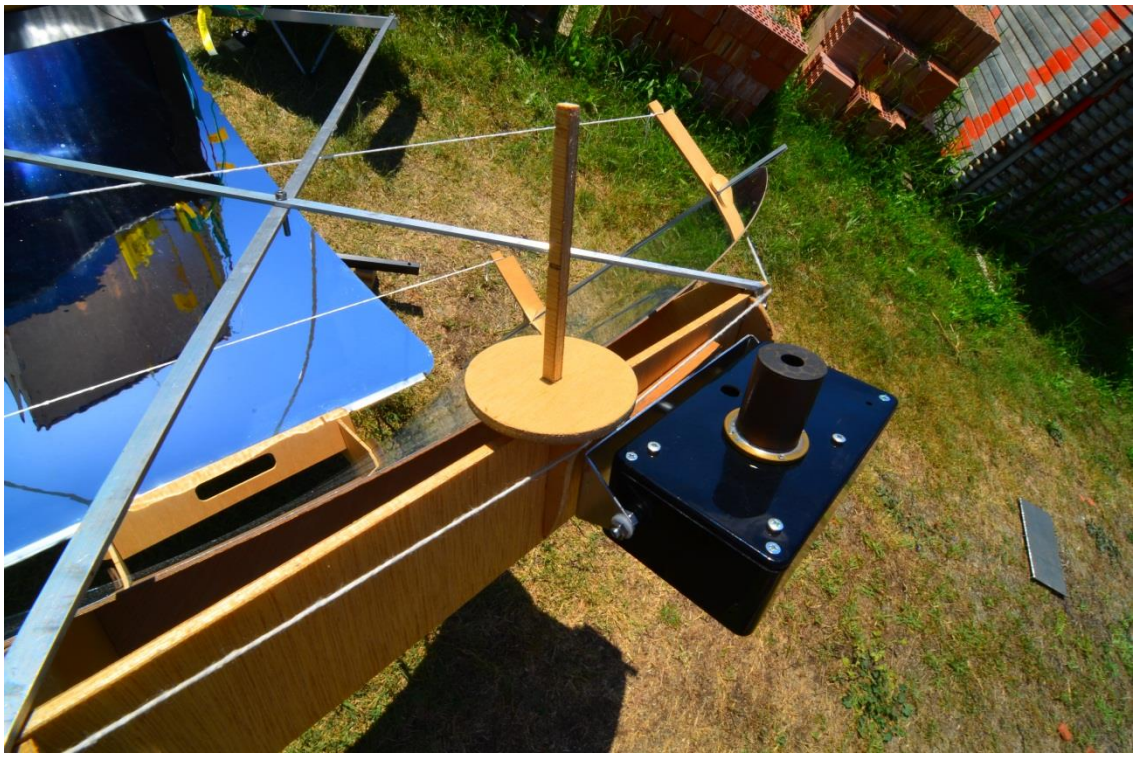


Figure 5.3 Lightmeter attached to the upper edge of the conical mirror support. Also observable is the sundial used to track the concentrator; the central pole is collinear with the optical axis of the concentrator.

The lightmeter gives 3 voltage signals which vary linearly dependent on the solar flux incident in each of the photodiodes of its three colour channels. These voltage signals needed to be calibrated before any measurements of solar flux could be determined.

5.1.3 Calibration of the Lightmeter

The calibration of the light meter was performed with the use of a solar simulator operated by the Perovskite PV group in Physics. Additionally, several absorber surfaces were heated with the use of the solar simulator in order to determine their relative absorptivities. The solar simulator used is an ABET Class AAB Sun 2000 Solar Simulator with a 150W Xenon bulb. Light is emitted downwards from the simulator onto the staging area, as in Figure 5.4.

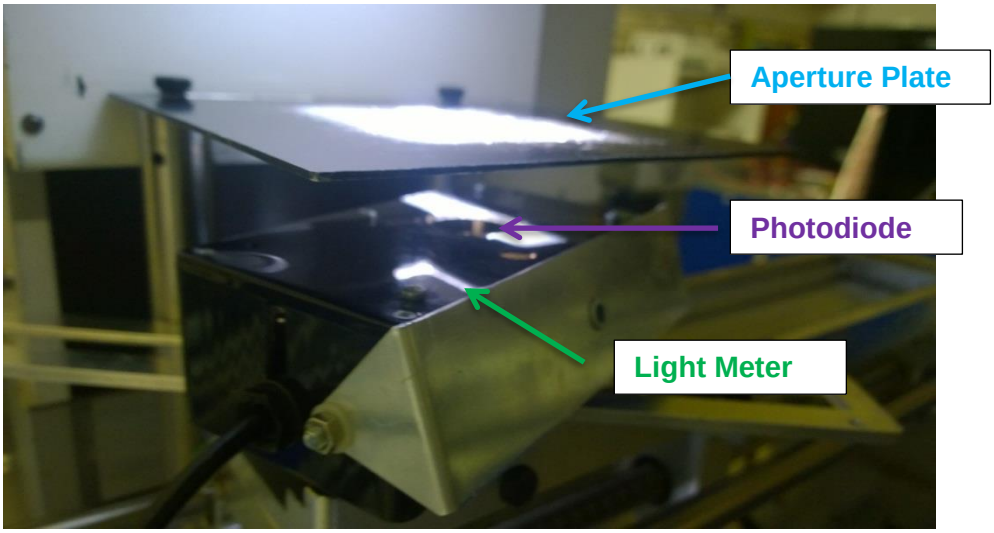


Figure 5.4 **Light from the solar simulator illuminating both an aperture and the light meter below.**

Once warmed up the Xenon Lamp is calibrated for an output of 1 Sun, 1000W/m^2, using a PV cell of known efficiency. This calibration was performed with an aperture in place above the test cell, as seen Figures 5.5a & 5.5b.

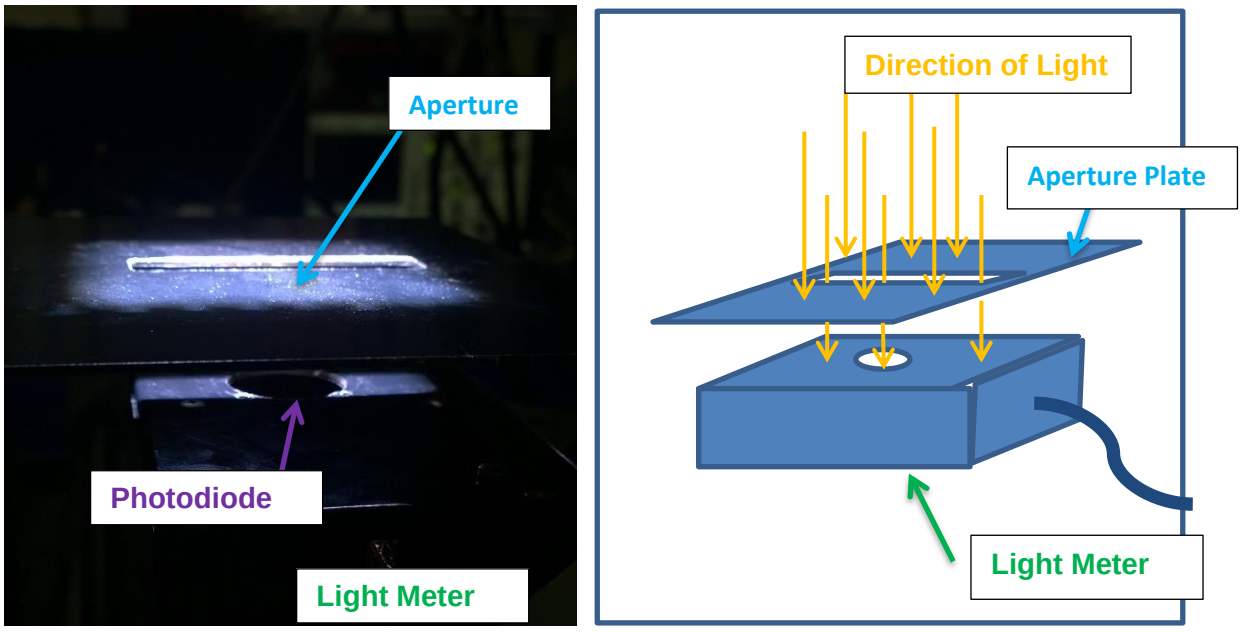


Figure 5.5 **(a) Low-exposure photo of light incident on the aperture from above with (b) graphic representation of the direction of the incident light.**

It became apparent during the testing the flux from the lamp was not uniformly distributed and the peak intensity measured depended on the location and distance of the photodiodes with respect to the lamp. Measurements were therefore taken with the photodiodes positioned in the same location as the PV cell was during calibration. The voltages measured

in each channel of the light meter are adjusted to account for the spectral response of the Kingbright™ KPS-5130PD7C photodiodes, given in Figure 5.6.

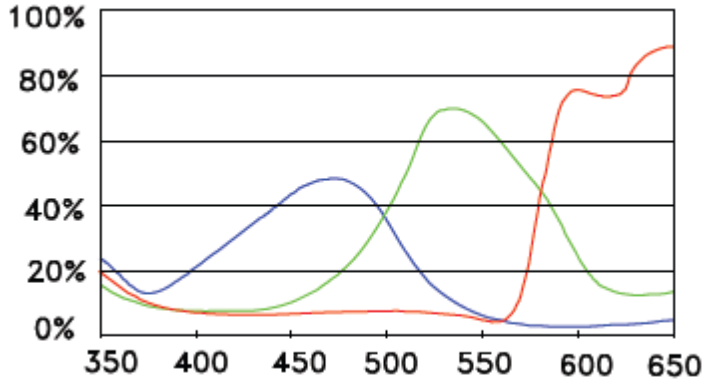


Figure 5.6 Spectral response curves of the KPS-5130PD7C photodiodes.

The spectral response for each of the three photodiode channels is expressed as photosensitivity and is given in units of Amperes per Watt (of incident light). The current generated in each photodiode is directly proportional to the measured voltage for each channel. Therefore, the output voltages measured must be scaled by the photosensitivity of each colour area, as per Table 5.2.

Table 5.2 Peak sensitivity wavelengths and signal scaling applied to results.

Colour	Peak Sensitivity Wavelength (nm)	Photosensitivity of single colour areas (A/W)	Signal Scaling (ratio)
Red	620	0.33	1
Green	550	0.25	1.32
Blue	470	0.18	1.83

The 0.85mm^2 area of each colour element under 1000W/m^2 would therefore result in 2.805x10^{-4}A in the red channel. Each photodiode channel is connected in a transimpedance amplifier circuit, where the gain of the amplifier is set by the value of the feedback resistor chosen, as per Equation 5.1

$$-I_p R_f = V_{out} \quad \textbf{(5.1)}$$

The 20kΩ resistor used would therefore result in an expected voltage of 5.61V if all the flux was received at the peak sensitivity wavelength of 620nm. Given the spectral response of the

red photodiode, see Figure 5.6, the measured voltage will be approximately one quarter of this value. This agrees with the maximum voltages observed during testing of approximately 1.4V for the red channel. Lower values for the blue and green channels were also observed, given their lower photosensitivity.

Once scaled these measured voltages can now be referenced against the output spectrum of the solar simulator, the values are given at the peak sensitivity wavelength for each channel, see Figure 5.7.

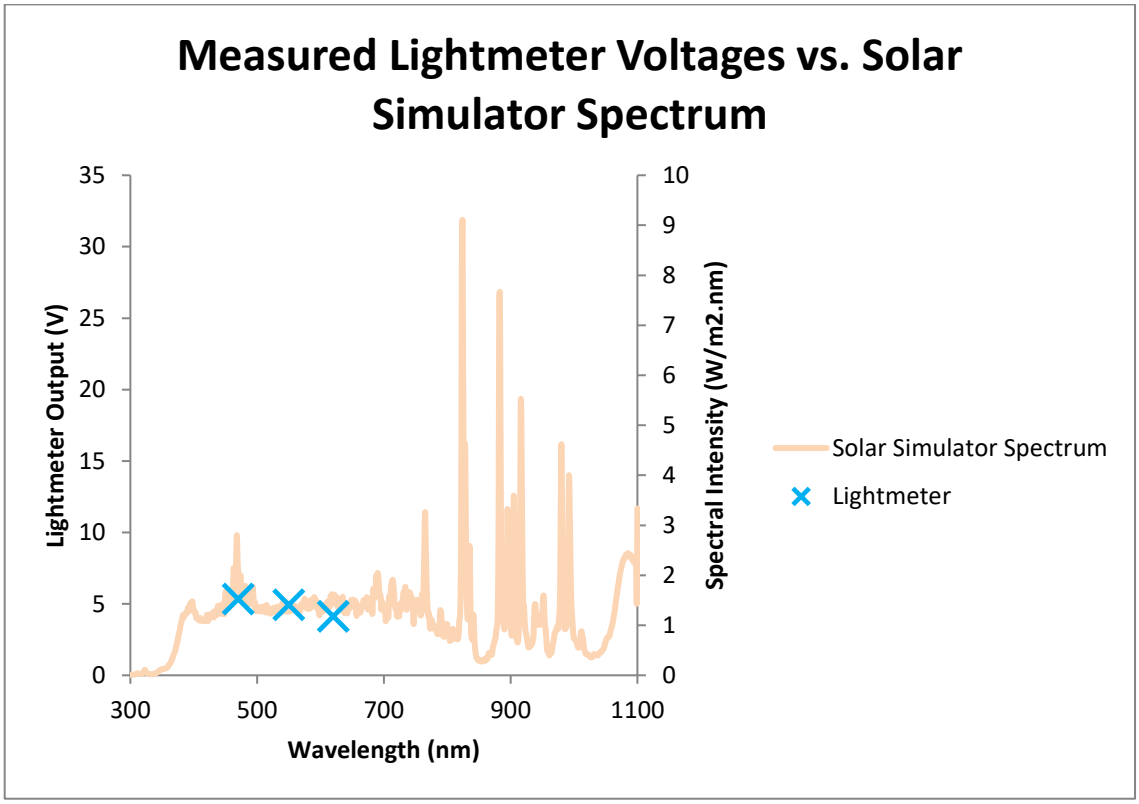


Figure 5.7 Measured voltages for light meter output (plotted at peak sensitivity wavelengths) vs. the previously measured output spectrum of the solar simulator.

The scaled data obtained from the lightmeter agrees well with the measured output from the Solar Simulator. The blue channel at 470nm gives the highest value in agreement with the spike in output flux from the solar simulator near this wavelength. The response for a given channel is the weighting of its spectral response with the measured spectrum. Given that the spectral response of each individual channel is constant, a difference in the ratio of measured values in the channels therefore indicates a difference in the measured spectra.

5.1.3.1 Spectral Response of the Lightmeter

Standardised solar spectra are defined for varying degrees of atmospheric thickness and were used for the calibration of the light meter. Atmospheric thickness is defined with 1AM corresponding to the sun being directly overhead and sunlight traversing through 1 thickness of atmosphere; standardised solar spectra for direct sunlight are published for 1AM, 1.5AM and 2AM.

During the Italian trials the zenith angle of the sun throughout the day of the 27th of August, when testing was scheduled to begin, would result in an atmospheric thickness of between 1.2 at solar noon and 1.6 at 4pm. Therefore the 1.5AM spectrum is used in the calibration of the light meter, see Figure 5.8. Generally, it is standard practice to use the 1.5AM solar spectrum in solar applications.

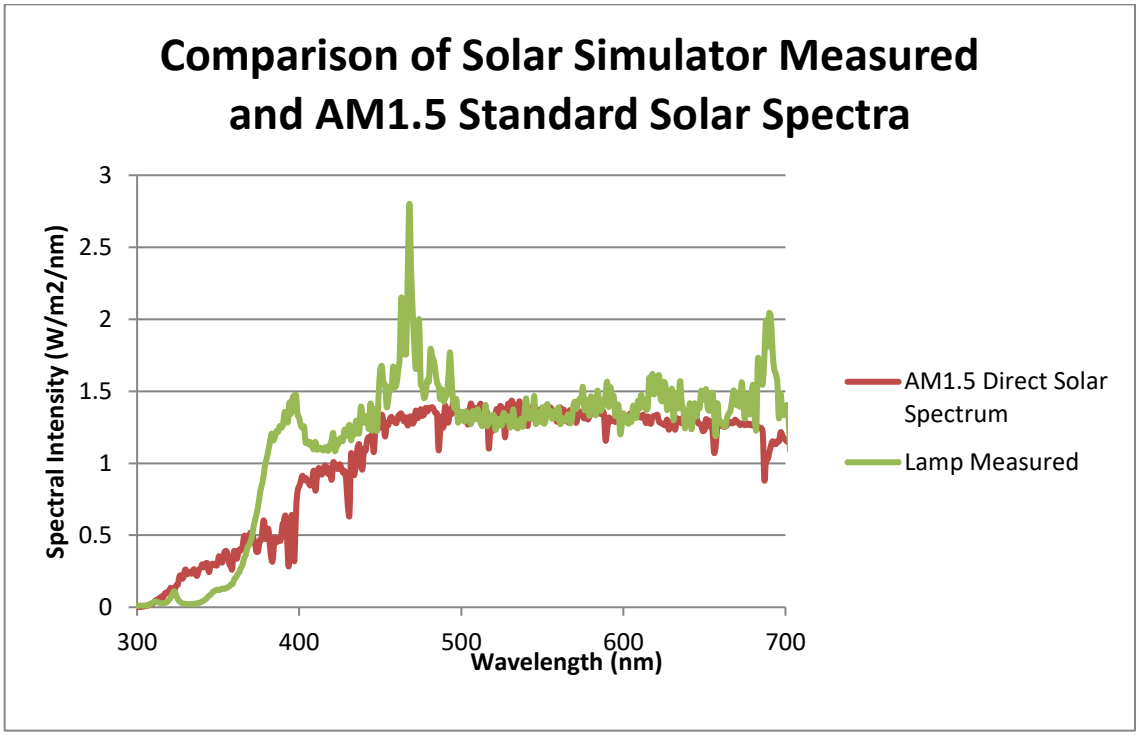


Figure 5.8 Standard solar spectrum for 1.5AM compared to measured spectrum for the solar simulator over visible wavelengths.

The comparison of the measured spectrum of the solar simulator with that of the standard solar spectra gives good agreement over the visible range of light. However, there are slight

differences in the spectra around the peak sensitivity wavelengths of both the blue (470nm) and red (620nm) channels. There is excellent agreement between the two spectra round the peak sensitivity of the green wavelength (550nm).

The standard solar spectrum used for comparison here is for direct and circumsolar light and does not include diffuse light. The Solar Simulator is calibrated to reproduce a standard 1 Sun output of 1000W/m^2 which includes diffuse light. The portion of this standard output that is direct sunlight is 939.5W/m^2. This scaling is applied to the results as the Light Meter does not accept diffuse light.

Given the excellent agreement between the spectra at the peak sensitivity wavelength of the green channel the calibration for the light meter is given for the voltage measured in the green channel. At an output of 1000W/m^2, of which 939W/m^2 is direct flux, this resulted in a measured output voltage of 1.23V from the Light Meter, see Table 5.3.

Table 5.3 Calibration of Solar Simulator.

	Total Irradiance (W/m^2)	Direct Irradiance (W/m^2)	Light Meter Output (V)
Lab	1000	939	1.23

Uncertainties in this calibration value include variations in the measured output voltage of up to 2.2% due to either electronic noise or the non-uniformity of flux profile from the Solar Simulator. The supplied calibration for the Solar Simulator was performed with the previous bulb, before it was replaced in 2014. However, this calibration data should be accurate to within a couple of percent, a conservative estimate of the total error would then be 5%. Therefore, for direct sunlight:

$$1.31V = 1000W/m^2 \pm 5\% \quad \textbf{(5.2)}$$

The response of the photodiodes to light is expected to be linear and not a source of error, this was investigated by placing neutral density filters above the light meter.

5.1.3.2 Linearity of Photodiodes Response - Filters

Neutral density filters were placed over the photodiodes in order to verify that the response of the light meter was indeed linear with respect to irradiance. The filters were all pieces cut from the same sheet of 1-stop (50% transmittance) neutral density filter. The output voltage for the three colour channels was measured, whilst keeping the light meter in the same position, with:

- no filter in place (300-358 seconds),
- a 1-stop neutral density filter (360-412 seconds),
- two 1-stop filters (425-474 seconds), and
- three 1-stop filters (493-583 seconds).

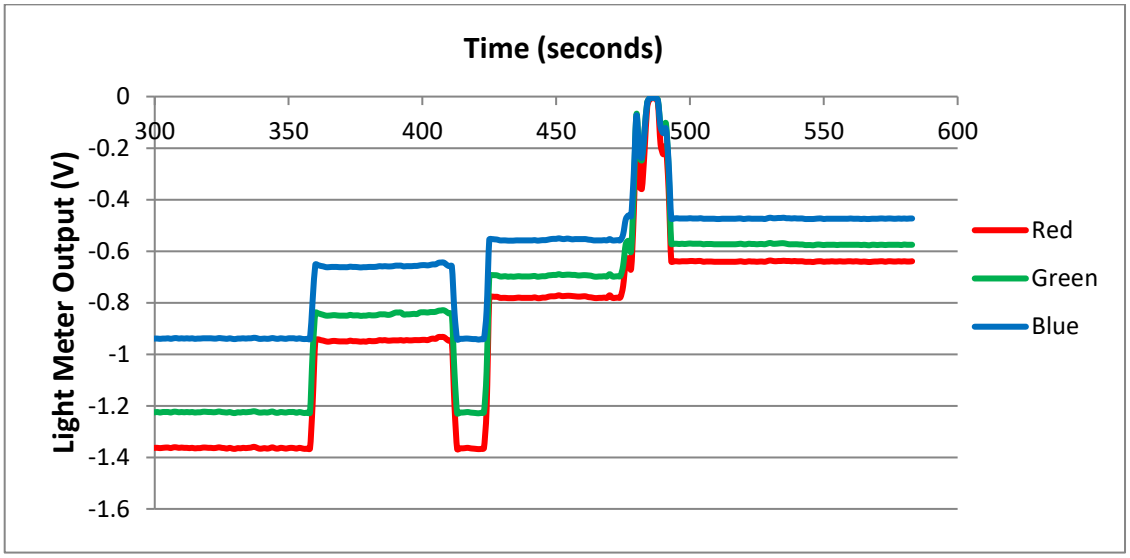


Figure 5.9 Light meter response to increasing number of neutral density filters.

If the response of the photodiodes is linear with respect to incident irradiance then it is expected that the measured voltage for each colour channel will drop by half with each additional filter applied. The drops in measured voltage are shown in Table 5.4.

Table 5.4 Transmittance at each application of a 1-stop neutral density filter.

Channel	1st Filter	2nd Filter	3rd Filter
Red	0.69	0.82	0.82
Green	0.69	0.82	0.83
Blue	0.70	0.84	0.85

Clearly the measured voltages are not falling by half with each subsequent application of a 1-stop neutral density filter. The reason why the transmittance is higher than expected was because the filters used act primarily over the visible spectrum, 390-700nm and not in the infrared. In order to simulate the solar spectrum, the xenon bulb emits strongly in the near-infrared (>700nm); 58.3% of the xenon bulb's emitted irradiance being at wavelengths longer than 700nm. Therefore, a filter acting on only the visible range of light would act on only 41.7% of the xenon bulb's emitted irradiance. In this case, a 1-stop filter would result in 0.79 transmittance instead of the anticipated 0.5, which is similar to the results obtained.

Further applications of this filter will continue to only filter the visible wavelengths and therefore the effectiveness of the filter will fall with subsequent applications, which is observed in the results. Unfortunately, data could not be obtained to indicate the performance of the LEE Filter no. 209 in the near-infrared to infrared range. However, this filter lacks any form of metallic film which would indicate high transmittance throughout these wavelengths. However, without this data an exact indication of the linearity of the photodiodes' response is not possible and a quick experiment was conducted to test this further.

5.1.3.3 Linearity of Photodiodes Response - Inverse Square Law

To verify the linearity of the photodiodes' response to incident flux a test was performed using the lightmeter and an incandescent bulb. The lightmeter was placed at varying distances away from the bulb and the resultant output of the lightmeter was measured, see Figure 5.10.

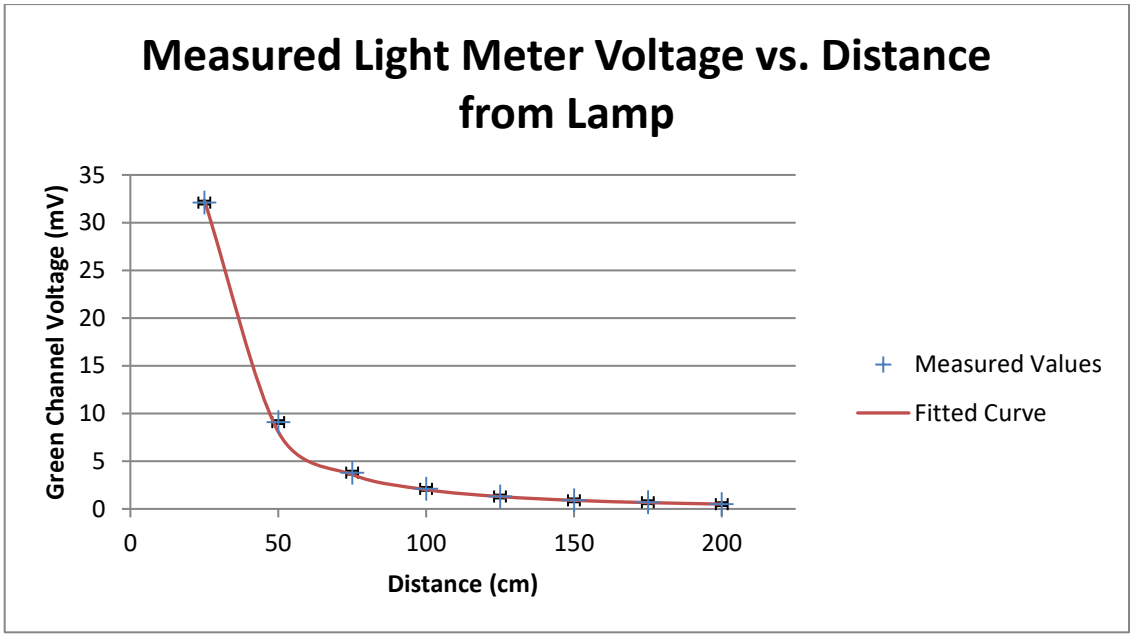


Figure 5.10 Measured Light Meter voltage at varying distances from incandescent bulb; plotted with best-fit curve.

The data from the green channel of the light meter was fitted to match the inverse square law with an r-squared value of 0.99. Given the agreement of the results the behaviour of the photodiodes is indeed linear with respect to incident flux. This becomes more evident when the natural log of the data is plotted, the best-fit power function fitted to the curve has an exponent of -2.01, close to the -2 expected with the inverse square law, see Figure 5.11.

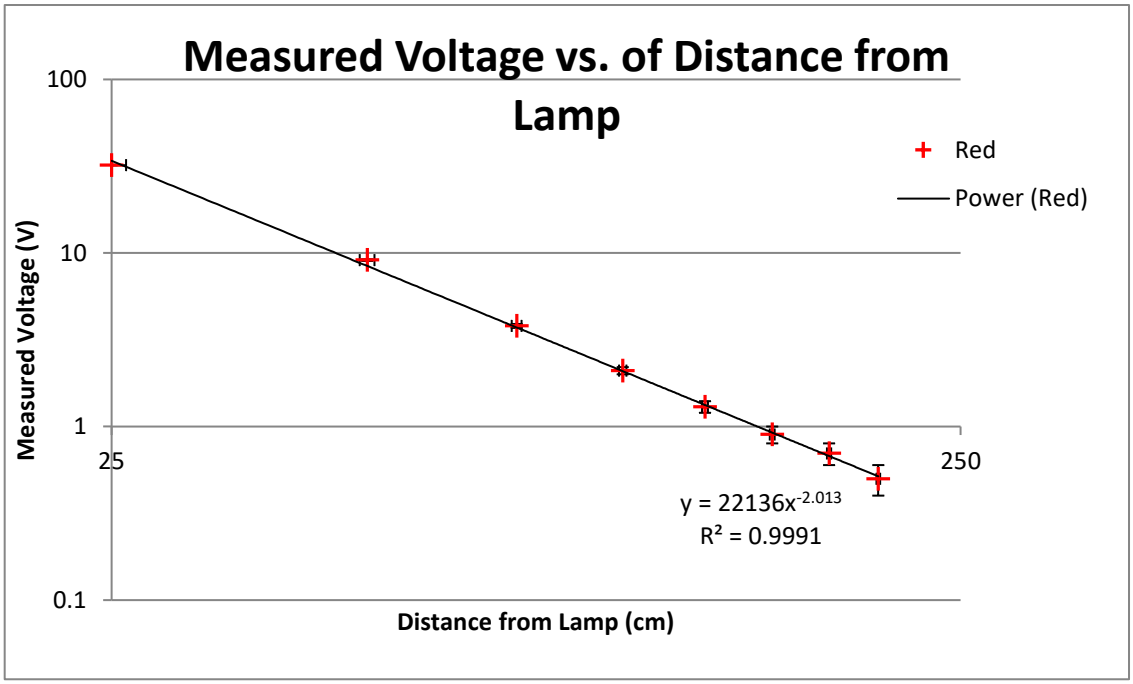


Figure 5.11 **Measured lightmeter voltage at varying distances from the incandescent bulb; plotted with best-fit curve.**

5.1.4 Data Acquisition System

The data acquisition system consisted of 8 thermocouple channels, 3 light-meter channels and 2 battery voltage level channels. The 8 thermocouple channels were amplified by a factor of 1000 to get a response in V/K as opposed to mV/K. This amplification was performed using a custom built thermocouple amplifier from cryogenics; this amplifier was powered on the 9V rails supplied by the lightmeter. The thermocouples and the amplifier are accurate to within 1K. All channels were fed into a National Instruments 16-Channel USB-6210 Data Acquisition system. The DAQ took 200 measurements per second, which were recorded as averages over 100 measurements, resulting in all channels being recorded at half second intervals. This arrangement enabled all devices to be powered by either USB ports or the two 9V batteries of the lightmeter.

5.2 Italian Field Trials

The field trial was conducted in Pisa, Italy, during August of 2014. Italy promised the combination of cloud-free skies and strong sunlight unavailable in the UK.



Figure 5.12 Map of average annual sum of direct normal irradiance for Italy (DNI).

5.2.1 Preparation for the Trials

Prior to the trial several adjustments were made to the concentrator. Metal beams were added in an effort to increase the rigidity of the mirror support structure. Two lever arms were attached to flex the mirror into place and ensure good conformity with the conical ribs.

In addition to applying matte black enamel paint to the current hotplate, two more hotplate/receivers were constructed, see Figures 5.13a, 5.13b & 5.13c. One was an aluminium sheet with a layer of SolarSelect© paint applied underneath whilst the other employed the use of a special selective receiver from Alanod. This selective absorber was supplied on a thin copper sheet and was therefore bonded to a copper plate.



Figure 5.13 (a) Aluminium Plate with Enamel Paint, (b) Aluminium Plate with HI/SORB-II™ Paint, (c) Copper Plate with Solar Select©.

5.2.2 Calibration of Solar Irradiance in Italy

The previously established calibration for the lightmeter was used to determine the insolation in Italy. At the location of the field trial in Pisa, a peak DNI of 757 ± 25 W/m^2 was measured at solar noon, see Figure 5.14.

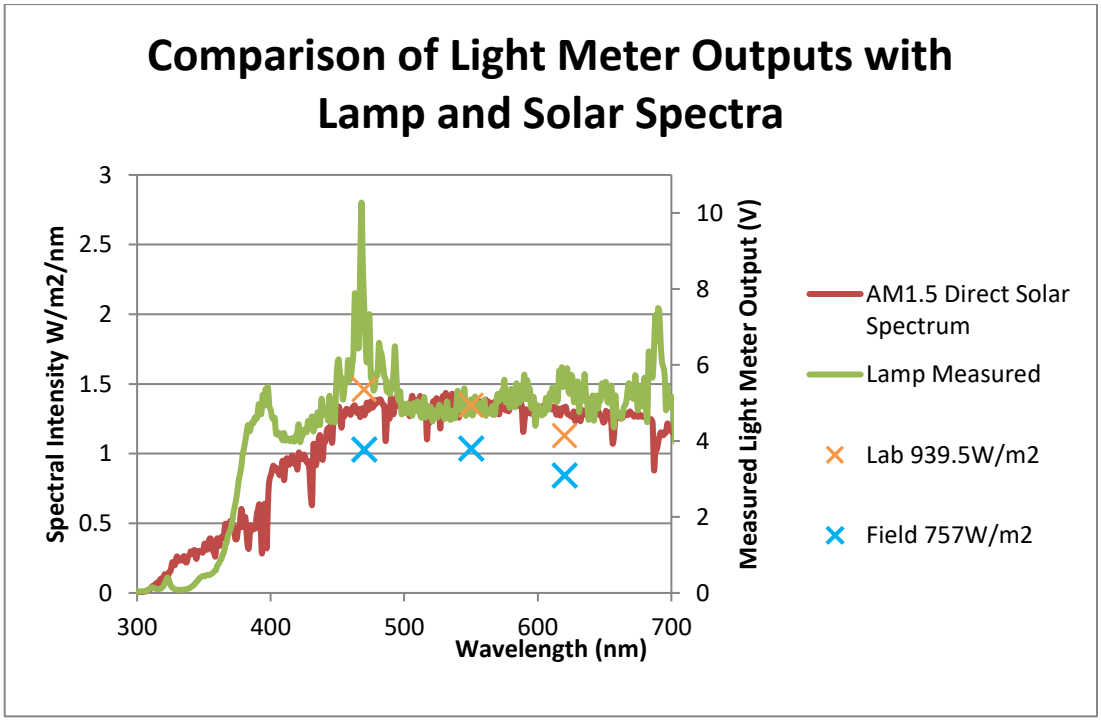


Figure 5.14 Comparison of lab-measured spectra and standard AM1.5 direct solar spectra. Measured lightmeter outputs are shown for the peak sensitivity wavelengths of each colour channel for both the lab results and field trial; these particular values correspond to DNIs of 939.5 W/m² for the lab and 722 W/m² for the field trial in Italy.

Given the results obtained with the use of the Solar Simulator the green channel of the light meter was then calibrated according to Table 5.5.

Table 5.5 Calibration of Solar Simulator and Italian results.

	Total Irradiance (W/m²)	Direct Irradiance (W/m²)	Light Meter Output (V)
Lab	1000	939	1.23
Italy (max)	806	757	0.99

The maximum direct and circumsolar solar flux measured in Italy was 757 W/m². The calibration applied to the results from the Italian trial is given by:

$$1V = 760.8 \pm 23.4 W/m^2 \quad \textbf{(5.2)}$$

The error is a combination of the observed fluctuation in the measured light meter voltages of both the Italian trial and the lab calibration. That is the error accounts for small observed variations in the measured voltage of the light meter under steady flux.

5.2.2.1 Comparison of Spectral Data for Italian, Standard and Solar Simulator Results

The exact spectra of the sunlight during the Italian trials were not measureable. However, comparisons can be made with the relative voltages of the light meter outputs. The voltage measured in any given channel of the light meter will be a function of that channels spectral response weighted with the spectra of the incident light. The equation for the spectral response for each colour channel was obtained by tracing curves from the supplied data on each photodiode's spectral response in Figure 5.6. The weighting of the spectral response of the green photodiode channel with 1) the measured Solar Simulator spectra and 2) the standard solar spectra are shown in Figures 5.15 and 5.16 respectively.

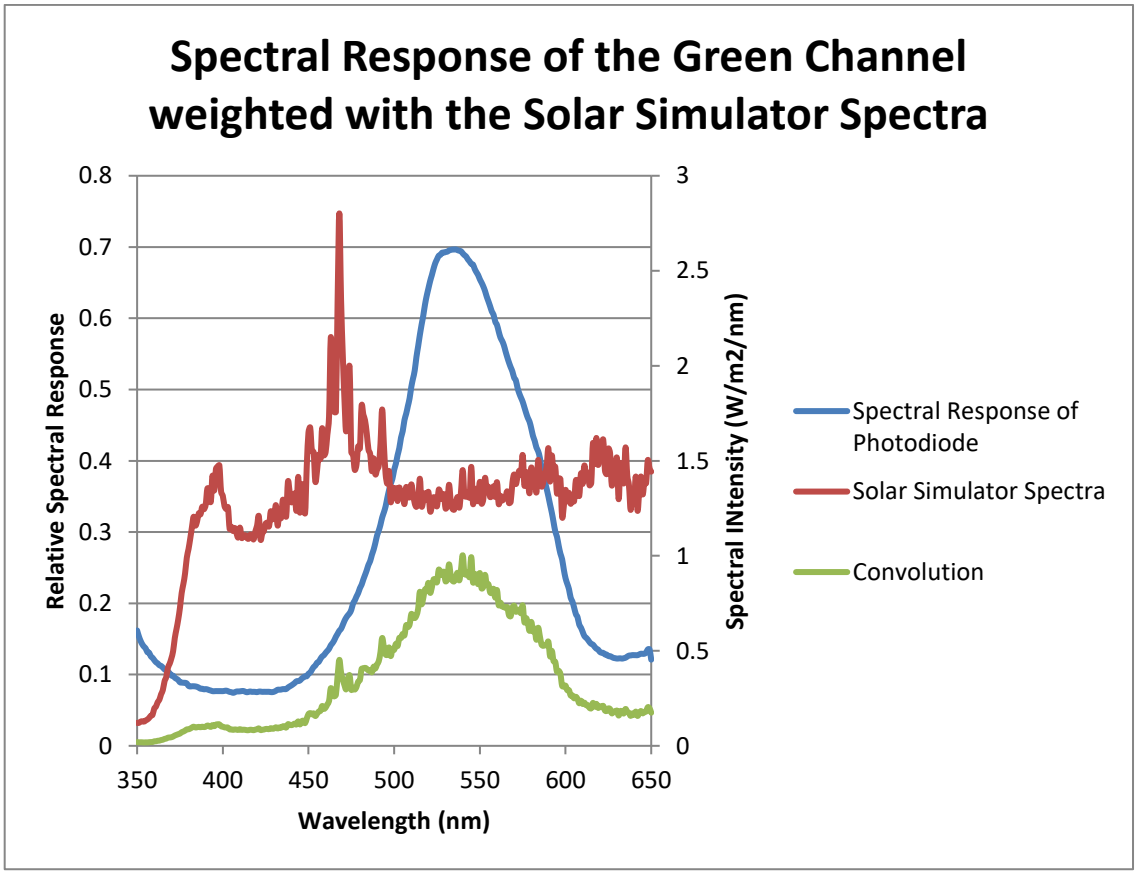


Figure 5.15 **Green photodiode spectral response weighted with the Solar Simulator spectra**.

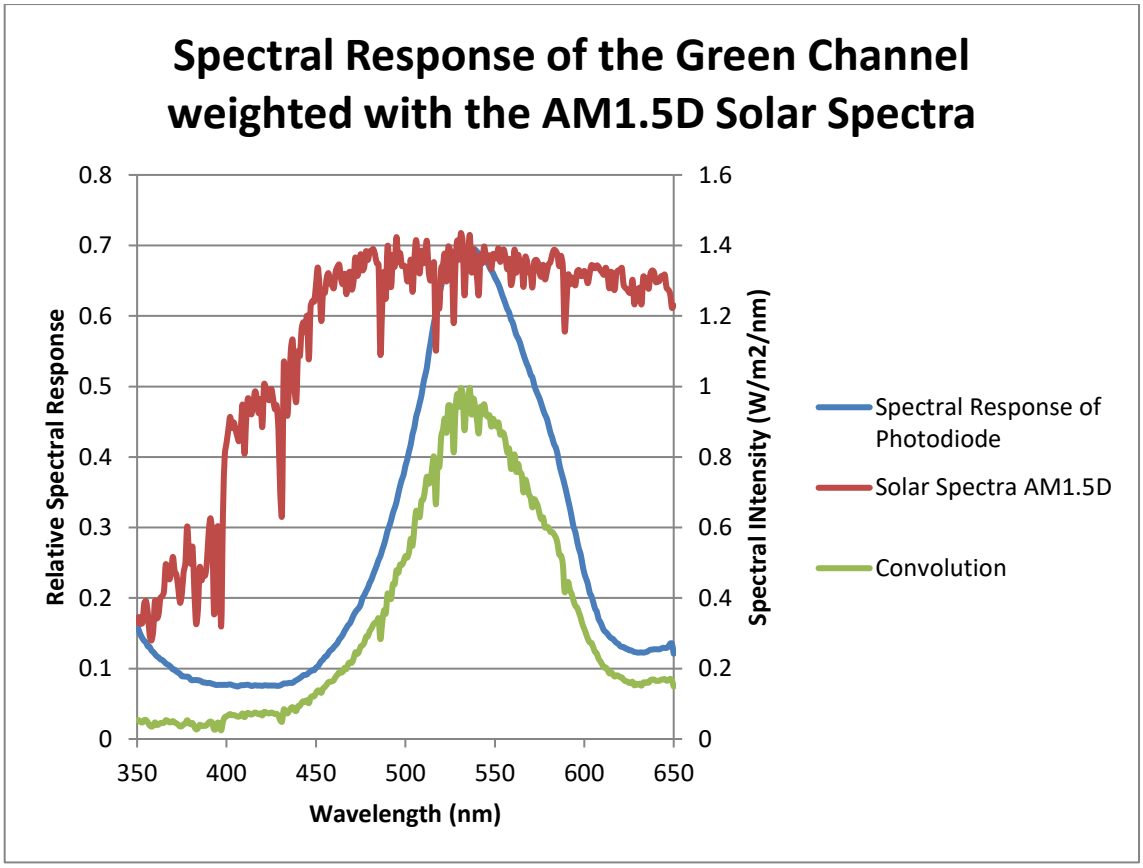


Figure 5.16 Weighting of the green photodiode spectral response with the AM1.5D solar spectra.

All three colour channels' spectral responses were weighted with both the standard solar spectra and Solar Simulator spectra. The integral of these weighted functions will be proportional to the measured voltage in each colour channel for the given incident spectra. To correct for any differences in total incident flux the relative values of these voltages are measured to give information on the spectra measured. These values are calculated for the lab-measured and standard spectra, see Table 5.6.

Table 5.6 Expected ratios of measured voltages of red/green/blue channels given the weighting of known solar spectra with the photodiodes' spectral response over the visible range.

	Red/Green	Green/Blue
Solar Simulator Measured Spectra	1.10	1.24
AM1.5D Standard Solar Spectra	1.14	1.37

The expected ratios of measured voltages in the colour channels can therefore be compared to the ratios actually measured in Italy and the lab, see Table 5.7.

Table 5.7 Expected ratios of measured voltages of red/green/blue channels given the weighting of known solar spectra with the photodiodes' spectral response over the visible range.

	Red/Green	Green/Blue
Solar Simulator Measured Light Meter Voltages	1.11	1.28
Italian Trial Measured Light Meter Voltages	1.08	1.39

The observed voltage ratios agree very well with the expected values, all within 5% or less. It can therefore be reasonably concluded that the spectra of the measured Italian sunlight is very well predicted by the AM1.5 standard solar spectra.

To note is that these results do not agree with the ratios observed for the photosensitivity of the coloured areas of the photodiodes, which are given only for peak sensitivity wavelengths. As data for the spectral response of the photodiodes is only supplied over the 350-650nm range, the ratios of measured voltages should only strictly apply to these wavelengths. Light absorbed in the infrared is unlikely to produce exactly the same proportional voltage responses in the light meter. Given that the majority of light is incident in the near-infrared and infrared this would explain small discrepancies in these observed ratios comparing Tables 5.6 & 5.7.

5.2.3 Key Results from the Italian Field Trial

Temperature measurements were taken using thermocouples placed within relevant thermal masses, see Figures 5.17a & 5.17b.

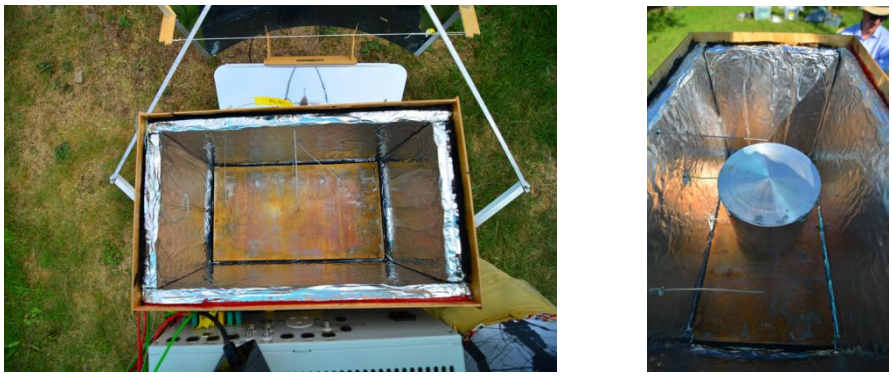


Figure 5.17 Thermocouples in (a) empty oven, (b) aluminium billet.

5.2.3.1 High-Temperature Results

Figure 5.18 shows that the empty oven was able to achieve temperatures of 140°C on the hotplate in only 17 minutes of full sun. Ultimately a maximum temperature of 190°C was measured on the top side of the copper plate after 65 minutes of operation. These results were achieved without an aperture or transparent window to mitigate convective losses from the underside of the receiver, which dominated the thermal losses.

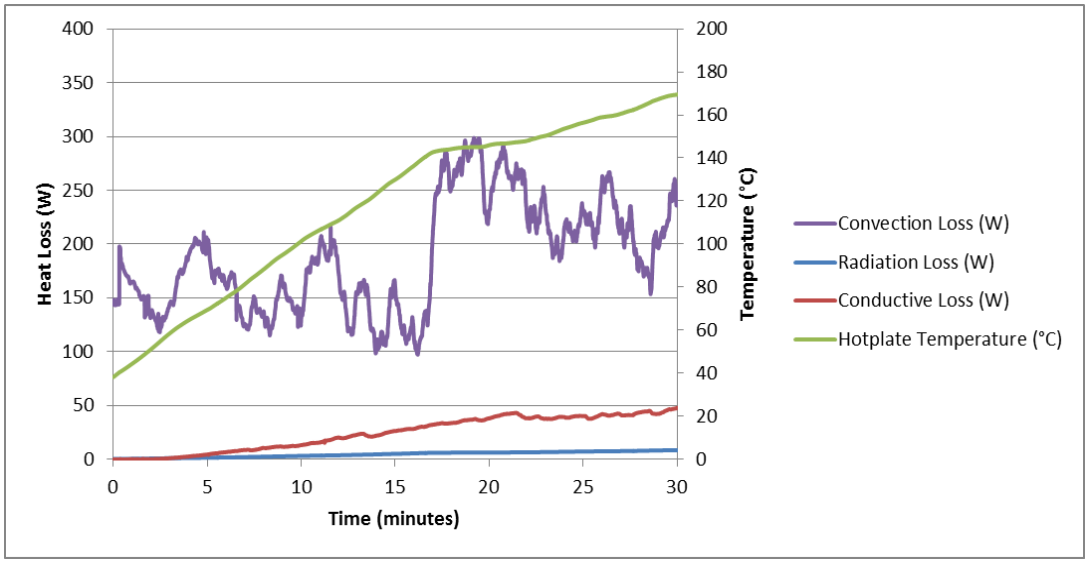


Figure 5.18 Rates of heat loss from the system with respect to hotplate temperature. The convective losses dominate the results but are highly variable due to gusts of wind driving forced convection from the hotplate.

The high temperatures achieved in the hotplate allow the grilling and frying of many foods. In particular, roti, a staple of Indian cuisine must be cooked at temperatures of at least 150°C to achieve satisfactory results. Given the insulated walls of the oven, and the low emissivity of the receiver material at relevant temperatures, convective losses expectedly dominate from the large flat copper hotplate. The effect of wind gusting on the slightly recessed hotplate is visible in the large changes in the rate of convective loss during the test.

5.2.3.2 Boiling Water Results

Cooking often requires the boiling of water or the heating of food with high water content. Tests were conducted to gauge the performance of the cooker under these cooking regimes by measuring system temperatures as a pot of water was brought to boil, see Figure 5.19, and then measuring the amount of water evaporated during a given time period.

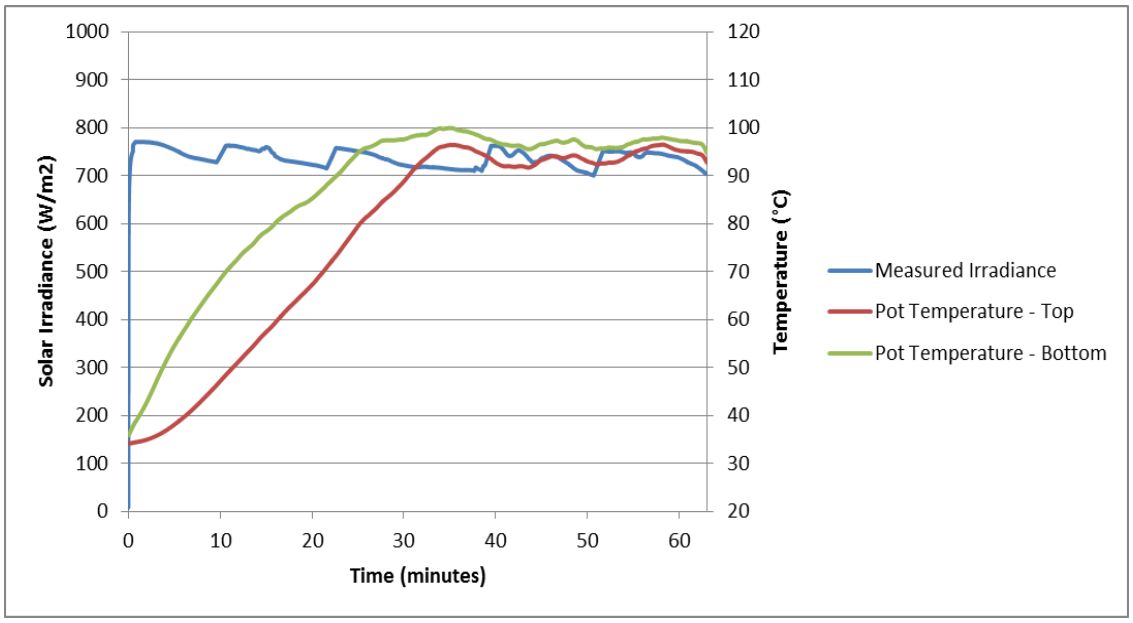


Figure 5.19 Temperature of the bottom and top of a pot holding 0.75L of water over 63 minutes of heating. The water started boiling at approximately 33 minutes. The measured irradiance is given; the oscillatory nature is due to the manual tracking performed approximately every 10 minutes.

The amount of evaporated water was measured as the weight difference upon heating. The large latent heat of vaporization of water kept system temperatures near 100°C and subsequently kept convective losses relatively low. Despite some intermittent cloud cover, high cooking efficiency results were obtained for both the heating and evaporation phases, as per Table 5.8.

Table 5.8 Boiling water test results from the trial. Cooking efficiency is defined as the proportion of heat flow into the water as a percentage of that into the receiver.

Cooking Mode	Heating	Boiling
Time (minutes)	33	30
Average Cooking Rate (W)	203	187
Cooking Efficiency	0.61	0.57

The volume of water heated to boiling in these tests was 0.75 L in a 1.1 kg aluminum pot. After the test the water was used to cook 1.5 cups of basmati rice within another 20 minutes of cooking time.

5.2.3.3 Aluminium Billet Results

The 8.4kg aluminum billet was placed in the prototype to determine the heating power of the oven as temperatures increased above 100°C. This heating power declines as convection and radiative losses from the underside of the receiver increase with receiver temperature. For the first hour of heating an average solar input of 309 W resulted in an average of 144 W being available for cooking with the billet reaching a temperature of 95°C.

Table 5.9 Comparison of Italian data to the thermal model of the system after 60 minutes of heating.

Cooking Mode	Hot Plate (°C)	Billet (°C)	Inner Wall (°C)	Outer Wall (°C)
Model – 315 W	134	97	60	31
Italy – 315 W (Average)	94*	95	61	32

* The hot plate temperature measured in Italy was significantly lower than anticipated due to convective losses from the hotplate directly under where the thermocouple was placed. The thermocouple could only be attached towards the edge of the hotplate on its underside. Overall hotplate temperatures observed towards the centre of the hotplate, and on its top surface, were generally much higher..

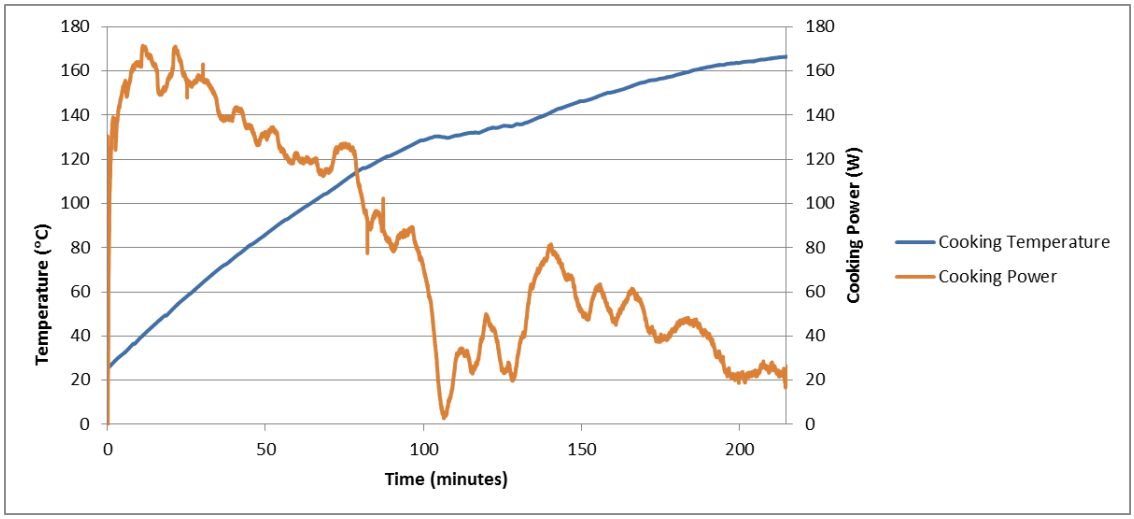


Figure 5.20 Temperature and heat flow into the aluminum billet over 3.5 hours of heating, the drop in cooking power from around 100 to 140 minutes into the test is due to intermittent cloud cover.

In Figure 5.20 as the aluminum billet reaches 165°C the cooking rate drops to 20W and the rate of increase in billet temperature slows to 0.25 K/minute. The performance of the oven is

comparable to moderate oven temperatures used in cooking. Higher temperature would be possible by negating some of the convective loss from the hotplate with an aperture or pane of glass.

5.2.3.4 Conclusion

The results from the Italian trial demonstrated that the prototype cooker can meet the requirements of various modes of cooking, including high temperature grilling and baking. The solar cooker's ability to reach high temperatures can make otherwise unavailable methods of not only cooking but latent heat storage practical. The prototype's novel geometry and developable mirror surfaces allow this high performance without expensive formed mirrors.

5.2.4 Feedback from Trial

The solar cooker used in Italy, see Figure 5.21, performed all tasks admirably. However, during the week several design deficiencies became apparent.



Figure 5.21 Solar cooker prototypes in Italy, visible are, the laptop and thermocouple amplifier used for data acquisition, which are shaded by the umbrella without blocking the mirrors.

The field trials conducted in Italy provided a wealth of data. As to be expected from the current flat plate absorber, convective losses were significant and wind conditions had a

significant effect on the stagnation temperature of the oven. Despite these losses the oven still performed well.

5.3 Measurement of Receiver Absorptivities

Three different surfaces were used on the absorber during the Italian trials; an aluminium absorber coated with a matt-black enamel paint, an aluminium absorber coated with a paint designed specifically for solar applications and a copper plate bonded to a thin sheet of Solar Select™ absorber from Alanod. Solar Select™ is a thin sheet of copper with a surface treatment which increases solar absorbance to 0.95±0.02 with an emissivity of only 0.05±0.02 at 100°C. The optical properties of the paints are dependent on the surface to which they are applied and the method of application.

To measure the absorbance of these surfaces several aluminium discs were prepared. To control for inconsistencies in applying the paint and bonding the Solar Select, 2 of each surface type were prepared. In addition two control discs of plain aluminium without surface treatment were used; one with a machined surface and one with a rough surface, see Figure 5.22. All aluminium discs are 38mm in diameter, approximately 5mm thick and weigh 15g after holes were drilled to attach thermocouples.

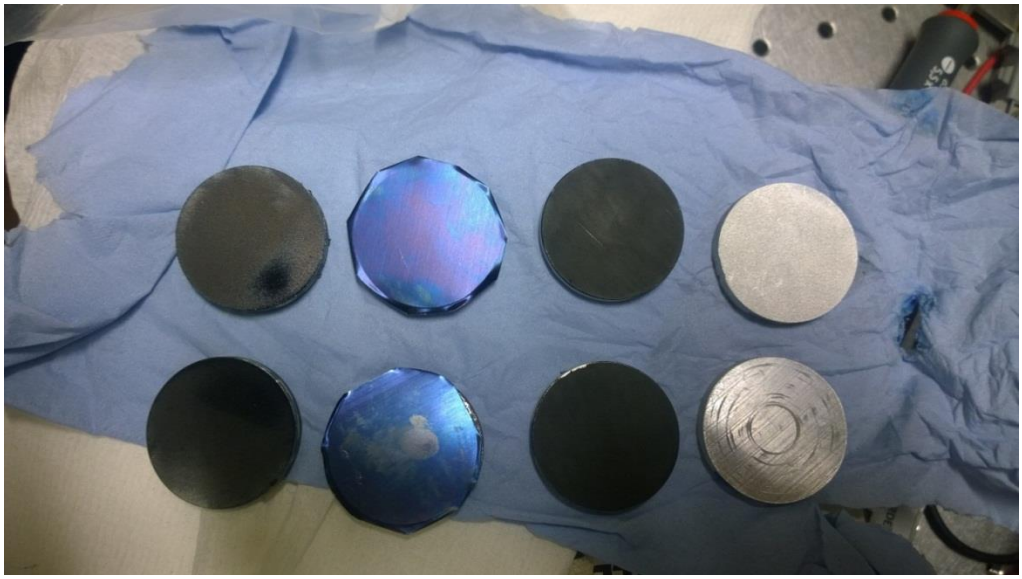


Figure 5.22 Absorbance testing samples, from left to right: Solar Paint, Solar Select, Enamel Paint, no treatment rough (above) and no treatment machined (below).

Although all the aluminium discs are of the same weight, the additional thermal mass of the Solar Select™ was also taken into consideration. The samples were placed underneath the Xenon lamp solar simulator whilst their temperature was recorded with a thermocouple placed inside the aluminium disc. The samples were placed in a piece of Basotect™ to reduce conductive heat loss during the testing. The samples were recessed from the top of the Basotect to help minimise convective losses, see Figure 5.23.

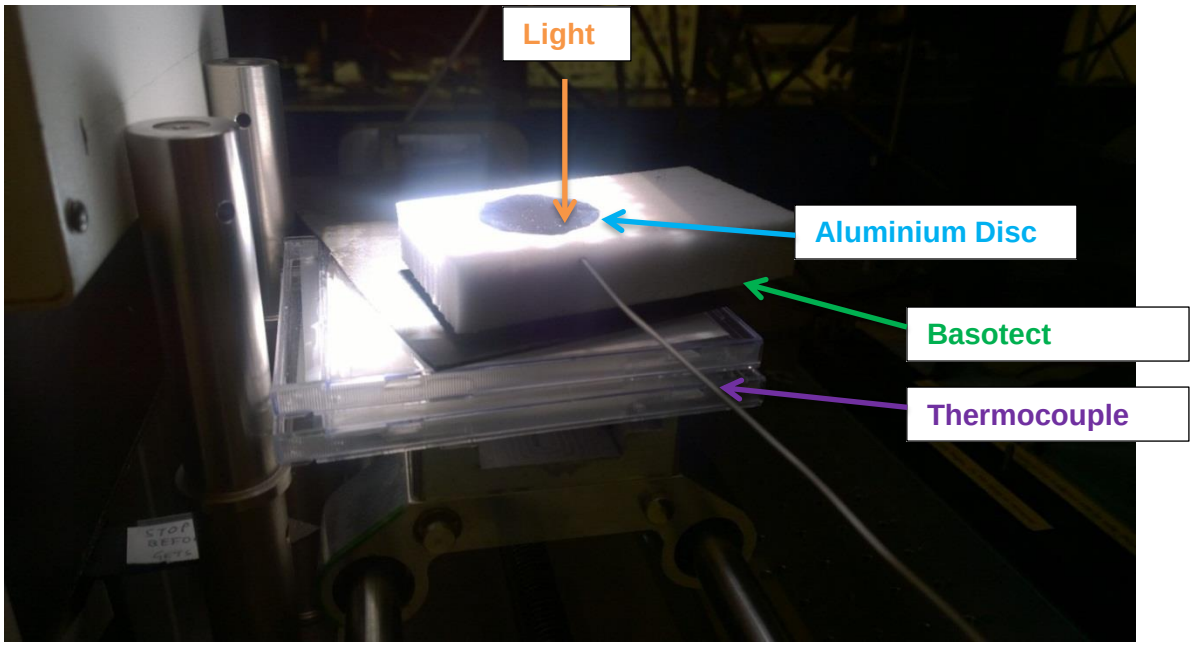


Figure 5.23 Basotect© base holding a sample underneath the Xenon Lamp with thermocouple attached.

The samples were heated via the xenon lamp for approximately 10 minutes. Differing absorptivities between the samples resulted in different rates of temperature rise and different stagnation temperatures. Convective losses were measured by switching off the Xenon lamp and recording data whilst the samples cooled.

It was not possible to directly determine the energy flows through the sample using the known output of the Xenon Lamp. The xenon lamp does not have a uniform flux distribution and the samples were much larger than the aperture size that was used during calibration. The data obtained was therefore used to gauge relative performance between the samples. Lastly, it was also not possible to take into consideration varying the angle of

incidence of the lamp's flux. Therefore all results are for a normal, or near normal, flux with respect to the absorbing surface.

5.3.1 Experimental Results

Heating curves were obtained for each sample; these curves were fit to an exponential rise of the form of:

$$T(t) = T_{initial} + A(1 - e^{-Bt}) \quad \textbf{(5.3)}$$

There was some noise to the data, see Figure 5.24, but equations were fit to all data with R-squared values always > 0.99.

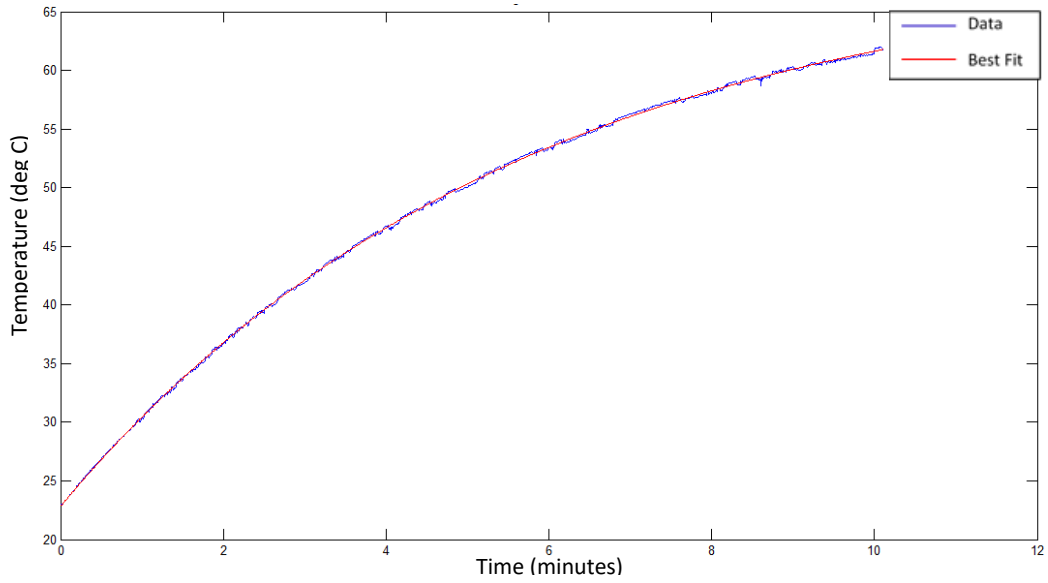


Figure 5.24 Heating curve for the 1st Enamel sample.

Ambient temperature was measured throughout the testing and did not vary by more than 2°C. A summary of the results obtained is found below in Table 5.10.

Table 5.10 Summary or equation fitting for absorbance results.

		Heating		
Test		Initial	A	B
1	Enamel 1	22.83	46.74	0.18
2	Enamel 2	23.65	44.94	0.19
3	Solar Select 1	22.11	47.11	0.17
4	Solar Select 2	24.02	49.38	0.16
5	Solar Paint 1	22.50	47.13	0.18
6	Solar Paint 2	24.05	45.60	0.18
7	Rough	23.57	25.22	0.17
8	Smooth	22.68	20.57	0.14

5.3.1.1 Results from Immediate Temperature Rise

To measure the relative solar absorptions of the samples, the time derivative of their temperature is calculated at t=0. The immediate temperature rise in each sample will be independent of convective and radiative heat losses. Using the fitted equations obtained from the data these derivatives are considered below in Table 5.11.

Table 5.11 Relative solar absorbances given initial temperature rises.

	dT/dt (degC/s)	dQ/dt (W)	Relative Absorbance
Enamel	8.37	112.43	0.97
Solar Select	7.86	109.87	0.95
Solar Paint	8.43	113.30	0.98
Al - Rough	4.34	58.33	0.50
Al - Smooth	2.81	37.73	0.33

Given the initial temperature rise there is little to distinguish the three treated surfaces. From the fitted equations it is not until several more minutes into the test that the Solar Select™ begins to outperform the two painted surfaces. These results give an indication of solar absorbance for the plain aluminium surface that agree reasonably with literature; 0.4-0.6 for rough surfaces and much lower for smooth surfaces dependent on surface quality.

During the Italian trials the enamel surface which was subjected to the highest fluxes at the centre of the caustic region suffered some degradation that gave it a burnt or charred appearance. Similarly the solar painted surface seemed to give off a small amount of fumes which may have just been solvent evaporating. Lastly, a small portion of the Solar Select™ surface seemed to have detached from the hotplate under intense flux.

5.3.1.2 Results from Stagnation Temperatures

Given the relative stagnation temperature of the surfaces it is possible to infer differences in their thermal properties. At stagnation temperature the energy absorbed by the surface will be balanced by convective losses and radiative losses, assuming that conductive losses are small into the highly insulating Basotect™ support. Given the very similar absorbances of the

surfaces a higher emissivity will affect the radiative balance and result in a lower stagnation temperature, see Table 5.12.

Table 5.12 Solar absorptions obtained from data near stagnation temperatures.

Finish	Stagnation Temp (degC)	Estimated Emissivity	Estimated Radiative Loss (W)
Enamel	69.08	0.80	0.33
Solar Select	71.31	0.05	0.02
Solar Paint	69.64	0.32	0.13
Al - Rough	48.80	0.07	0.02
Al - Machined	43.25	0.05	0.01

The slightly higher stagnation temperature of the Solar Select surface could be due to its much lower emissivity. Despite having very low emissivity, the unfinished aluminium surfaces perform poorly as they have low absorbances. In regards to the oven performance, the radiative losses will still be small with respect to convective losses. However, it seems that the solar select paint offers a reasonable performance at a much lower price than the solar select material.

5.4 Summary of Dytecna Prototype

The Dytecna prototype succeeded in its aim of demonstrating the inherent potential of a solar cooker based on the Oxford reflex concentrator. The results from the Italian trial indicate that temperatures as high as 190°C could be obtained and that at boiling temperatures the thermal efficiency of the cooker was as high as 0.57. Work done supporting the trial developed a low-cost lightmeter and subsequently identified the solar select paint as the best candidate for absorber surfaces going forward.

Unfortunately Dytecna went in to administration after a major client of theirs defaulted on a large contract. Dytecna were therefore no longer able to assist with the project.

6 Tanzanian Field Trials

6.1 Design Changes for the Tanzanian Prototype

Preparation for the Tanzanian field trials began almost as soon as the Italian trials had ended. Lessons that were learnt from Italy were applied to new iteration of the solar cooker design.

6.1.1 Revised Oven

Modelling work before the Italian trial had indicated that the thickness of the insulation on the oven walls was not an important factor in determining oven performance. The experience of the Italian trials, supported by modelling, was that convective losses from the underside of the hotplate would dominate system performance. Therefore the revised thermal model for the oven was used to predict the performance of the oven without insulation in the walls, i.e. bare plywood.

The mirrors were slightly enlarged to a nominal power rating of 400W. This design change was prompted by the requirement that the stove be able to cook two pots simultaneously, and to ensure that ample power could be provided over an extended trial in the event of mirror degradation. Solar irradiance in Tanzania would be similar to Italy and therefore an enlargement of the mirrors was required, which had to be accommodated with more structural support, including a tripod-like design, see Figures 6.1a & 6.1b.

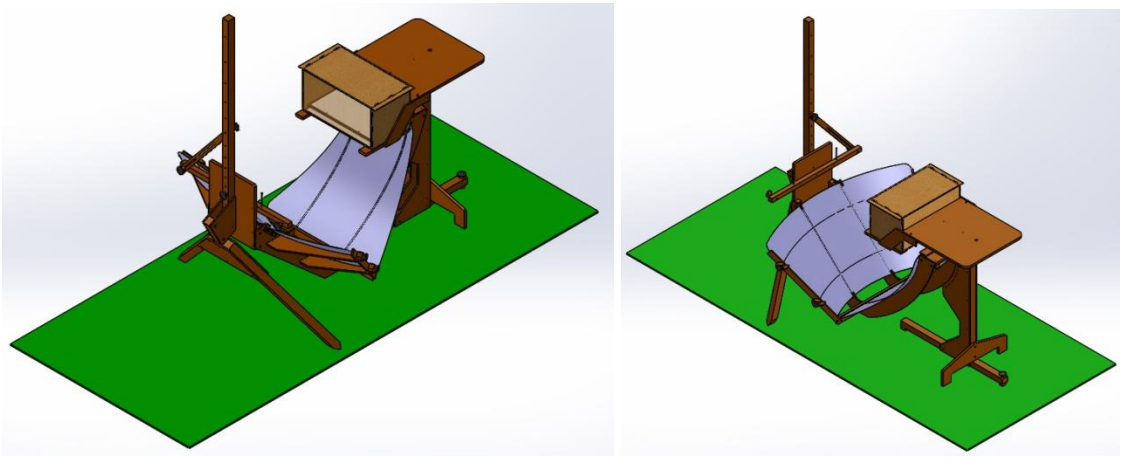


Figure 6.1 (a) (b) Redesigned solar cooker with tripod support for the mirror structure.

The addition of the tripod meant that the tracking of the oven would now be performed from the far end, away from the oven. However, the tracking would be able to be performed with much greater precision and sturdiness. The Dytecna was prone to slippage and required a lot of strength to overcome the friction.

In addition to this major change, the construction of the Dytecna prototype was deemed too expensive; estimates from colleagues at Dytecna put the unit price at around £100 only upon very large production volumes. Therefore it was decided that the majority of construction would be done in wood. This has the added advantage of decreasing the difficulty of manufacturing overseas.

6.1.2 Redesign of Hotplate

Given the emissivity data for the solar select paint and its low cost compared to other absorber materials it was identified as the best choice for the oven. At the same time it was decided to redesign the hotplate to reduce the cost of construction by cutting it from a flat plate.

6.2 Preparation for the Field Trial

In contrast to the Italian trials the Tanzanian trials would be much more difficult to coordinate. Spare parts and equipment would prove hard to come by and it was the intention to ship all 10 new prototype ovens with a complete toolset required for their construction. Much time was spent assembling the 10 ovens into their boxes for shipment to Tanzania. The system could flat-pack down to 12cm, however this required careful placement of the parts inside.

6.3 Notes on the Field Trial

The weather conditions in Tanzania were mixed. The testing location in the coastal city Dar es Salaam was plagued by cloud cover. Much better conditions were not experienced until reaching the arid interior at Dodoma, which is separated from the coast by a mountain range.

Although we had arrived at the end of the dry season in Dar es Salaam the cloud cover was perhaps unseasonal, as attested by the locals. In general the cloud cover was not enough to stop testing, just enough to ensure that results would be sporadic and difficult to interpret.

The road conditions were quite bad in some locations and for any future project shipment of solar cookers will pose a challenge. It took an entire day of driving each time the 450km trip was made to and from Dodoma.

The bureaucracy in Tanzania is perhaps no less onerous than that in other countries, but perhaps moves at a slower pace. Almost an entire week was lost whilst waiting for the ovens to clear customs.

Although some parts of Tanzania are quite wealthy, shopping for specific items can be at times quite difficult. When items were available they were generally cheap but sometimes of poor quality, the microfiber cloths being a prime example. For any commercial product in Tanzania it would need to be supplied with everything included.

The field trial, let alone navigating the maze of local customs, would have been impossible without the invaluable assistance of Dr. Joseph Matiko of the Dar es Salaam Institute of Technology.

6.4 Technical Results

6.4.1 Calibrating Solar Irradiance Measurements

The available solar resource in any given location is ultimately dependent on atmospheric conditions. The driving factors in the determination of this resource are the altitude of the solar collector, the relative thickness of atmosphere given solar movements and the often changing composition of the atmosphere. The accurate prediction of solar resource is not only important for commercialization of the solar oven, but also for the validation of the solar intensities measured with the light meter.

6.4.1.1 Determining Solar Resource

The most important factor in determining instantaneous solar resource is the relative thickness of the earth's atmosphere that sunlight must traverse to reach the collector; which is described by the air mass (AM). The air mass coefficient is defined as the optical path length that sunlight traverses relative to when the sun is directly overhead; an air mass of 1 is defined with the sun directly overhead, the air mass is otherwise given by Equation 6.1.

$$AM \approx \frac{1}{\cos z} \tag{6.1}$$

Where *AM* is the relative air mass
z is the solar zenith angle in degrees

The solar zenith angle and relative air mass vary with latitude, season and time of day. The relative air mass can then be used to determine the solar intensity, given by Equation 6.2 [32].

$$I = 1.1 \times I_o \times 0.7^{AM^{0.678}} \tag{6.2}$$

Where *I* is the solar intensity for the given air mass
I_o is the solar intensity measured outside the Earth's atmosphere, i.e. 1367W/m^2.

The air mass thickness will also determine the spectral composition of the incident light. Standard results from literature are available for an air mass of 1.5, to which the light meter has been calibrated.

Once differences in relative air mass are accounted for, further discrepancies in measured solar intensity with the lightmeter will indicate variations in altitude and atmospheric composition.

6.4.1.2 Tanzanian Solar Resource

Tanzania has excellent solar resource given its location just south of the equator. However, this resource is not evenly spread across the country. The mountain range running north-

south through Morogoro and most of the country tends to divide the climate into an arid interior and a more temperate coastal region, see Figure 6.2.

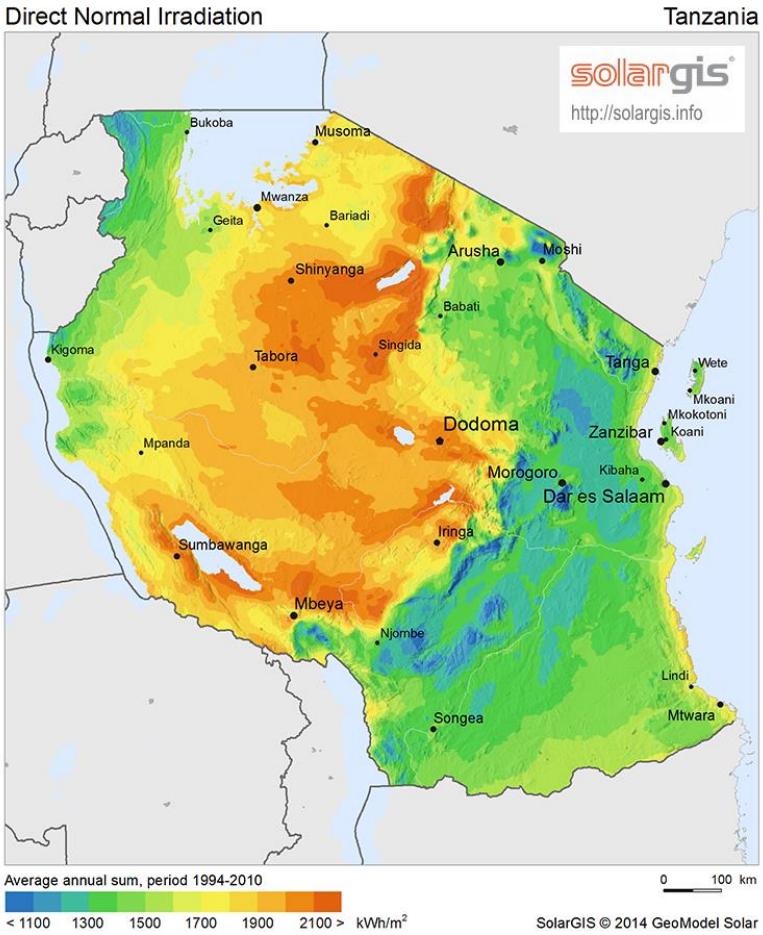


Figure 6.2 Average annual sum of direct normal irradiance across Tanzania, kWh/m².

This difference in climate was of particular relevance to the Tanzanian field trial and the choice of Dar es Salaam and Dodoma as locations for testing. However, these climatic differences are borne out by subtle differences in cloud cover and are most noticeable in annual averages. Given the relative geographical proximity of Dodoma to Dar es Salaam it should be expected that for clear sunny days, similar solar intensities should be measured. Dodoma and Dar es Salaam are approximately 400km from each other, see Table 6.1.

Table 6.1 Coordinates of Dodoma and Dar es Salaam.

	Dodoma	Dar es Salaam
Latitude	6.2° S	6.8° S
Longitude	35.7° E	39.3° E

Given the geographical proximity of Dodoma and Dar es Salaam there is very little difference in the observed daily solar movement between the sites. In fact, the greatest difference in diurnal solar movements was due to seasonal movement of the sun over the month-long trial, see Table 6.2.

Table 6.2 Changes in noontime solar elevation between Dodoma and Dar es Salaam.

	Dodoma: 26th-28th August	Dar es Salaam: 12th-19th August
Min. Solar Elevation (Noon)	73.4°	68.2°
Max. Solar Elevation (Noon)	74.1°	70.4°

The maximum difference in relative air mass observed at solar noon between Dodoma and Dar es Salaam is therefore given as 1.07 AM vs. 1.04 AM. However, this difference in relative air mass would only explain a difference in observed peak solar intensity of 9.2 W/m^2, which is less than the margin of error for measurements from the lightmeter. Therefore, large divergences in measured solar intensities between Dodoma and Dar es Salaam are due to either altitudinal or atmospheric effects.

6.4.1.3 Effect of Altitude on Solar Resource

Whilst coastal Dar es Salaam is at sea level, the testing at Dodoma was conducted at a much higher altitude, see Table 6.3.

Table 6.3 Altitude of Dodoma and Dar es Salaam.

	Dodoma	Dar es Salaam
Altitude	1135m	60m

The expected effect of altitude on measured total solar irradiance is $8\% \pm 2\%$ per 1000m [33]. This altitude effect is stronger at shorter wavelengths but for CSP applications this will not alter calculations for total irradiance values. It is therefore to be expected that with similar conditions that relative irradiance values at Dodoma will be $8.6\% \pm 2\%$ higher than those measured at Dar es Salaam. Alternatively, this relationship is given via Equation 6.3.

$$I = 1.1 \times I_o \times \left[\left(1 - \frac{h}{7.1}\right) 0.7^{AM^{0.678}} + \frac{h}{7.1}\right] \quad \textbf{(6.3)}$$

Where h is the altitude in km above sea level of the collector.

Substituting values of relative air mass observed at Dodoma and Dar es Salaam results in a calculated 6% difference in expected peak irradiance measured. However, the effect of altitude cannot explain daily variations at the same site which must be due to changing atmospheric composition.

6.4.1.4 Effect of Particulates on Solar Resource

The effect of atmospheric conditions will have a substantial effect on observed solar irradiances. This may occur due to both natural (dust, water vapour) and man-made (smoke, smog) aerial particulates. The nature of the atmospheric pollution varied greatly between Dodoma and Dar es Salaam. The dry, arid conditions in Dodoma led to large amounts of airborne dust which not only collected on the mirrors but also hung in the lower atmosphere, see Figure 6.3.



Figure 6.3 A dusty sunset highlights the atmospheric conditions in arid Dodoma.

In contrast to this the vast urban metropolis of Dar es Salaam suffered much more severely from smoke and smog. Man-made emissions were particularly bad during the somewhat frequent black-outs when many small generators were turned on in the city centre to power small businesses. Additionally the more temperate conditions near the cost meant there was less airborne dust but far more humidity in the air, see Figure 6.4.

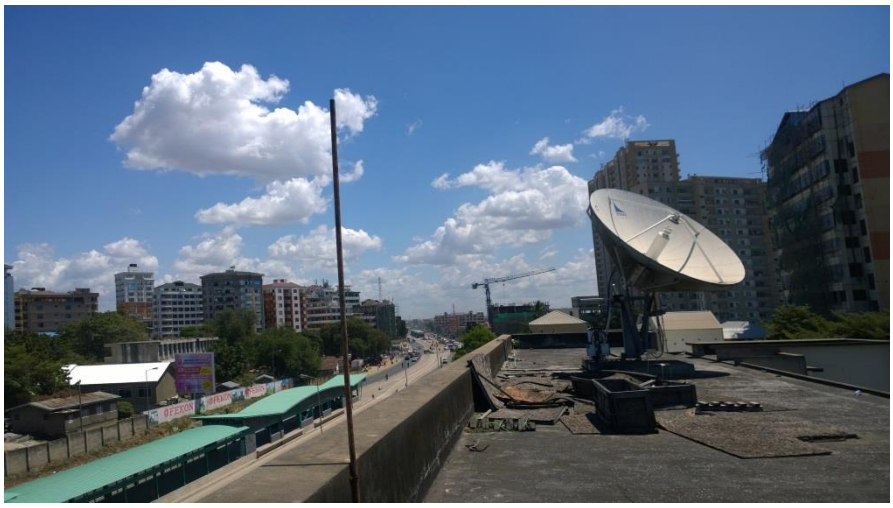


Figure 6.4 View from the rooftop test-site illustrating the far more humid conditions in Dar es Salaam.

The effect of air pollution on measured solar intensity varies dependent on the air mass the sunlight passes through and are given as per Table 6.4.

Table 6.4 Possibly effect of air pollution on measured solar intensity.

AM	1	1.5	2
Change in Solar Intensity	-15%	-21%	-27%

The effect of air pollution on measured results should be noticeable on a day-to-day basis at each testing site.

6.4.1.5 Dodoma Results over Subsequent Days

The measured output of the light meter is given across three different days of testing in Dodoma, see Figure 6.5.

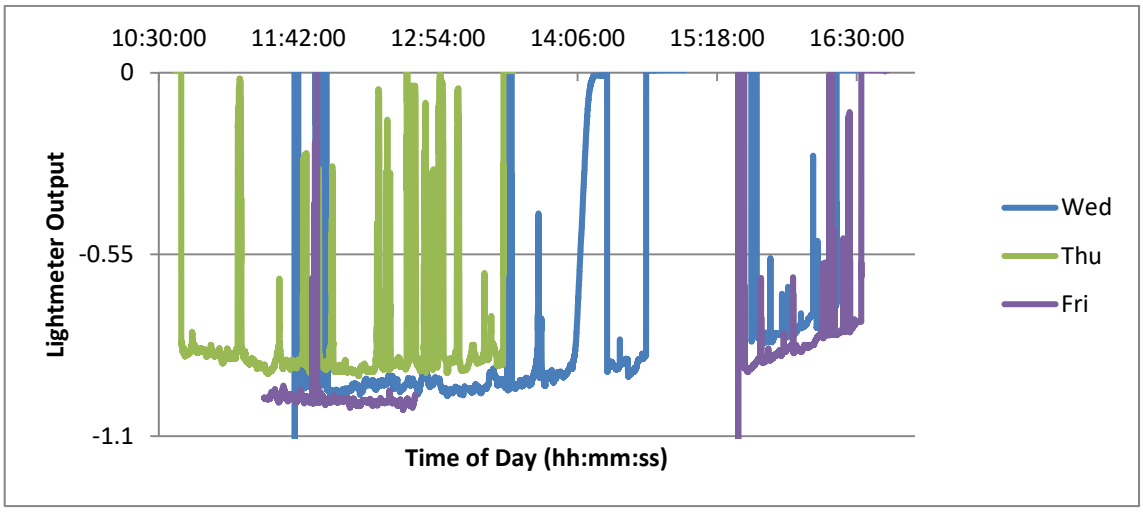


Figure 6.5 Lightmeter output as a function of time over three days of testing in Dodoma.

A variation of 14% between the maximum measured solar intensities on Thursday and Friday is due to differences in levels of atmospheric dust. This agrees well with an expected maximum change in solar intensity due to pollution of 15% as per table 4. The change in measured solar intensity due to an increasing air mass as the sun approaches the horizon is clearly visible in across all days. Maximum solar intensities were measured close to solar noon (12:38) on all days.

The peak measured solar intensity at Dodoma was 785 W/m^2 near solar noon on Friday, which is the within errors of the maximum measured in Italy, 773 W/m^2. The peak measurement in Dar es Salaam was 803 W/m^2.

6.4.1.6 Comparison of Spectral Data between Italy and Tanzania

The ratios of the measured values in each colour channel compare very well between Italy and Tanzania. This would seem to indicate that a very similar solar spectrum is being measured, which would further indicate that our calibrations from Italy remain valid.

Indeed the slight difference in solar zenith angle of 20 in Tanzania compared to 25 in Italy during the trials adequately explains the slight difference in observed maximum irradiances. A summary of these results is in Table 6.5.

Table 6.5 Ratios of measured colour channel ratios from Italy.

	R/G	G/B	R/B
Italy	1.08313	1.386845	1.502128
Tanzania	1.075231	1.419723	1.526162

6.4.2 Boiling Water Test – Saturday the 15th

The test conducted on Saturday the 15th of August to heat 1 kg of water has been taken as the standard case for Tanzania, to which the other tests will be compared. This test was chosen because it occurred with almost full continuous sunlight over a period of 2.25 hours.

6.4.2.1 Test Details

The test was conducted on the roof of DIT in Dar es Salaam. 1kg of Water was heated and then kept on the boil. This water was placed in a thin Aluminium pot with a lid. The lid was kept slightly ajar owing to the placement of thermocouples in the water. The test was performed with both the aperture and hotplate in place below the pot. The oven was placed over the pot and hotplate for the entirety of the test. After 2.25 hours of heating the pot was removed from the oven and weighed to determine the mass of water lost to evaporation.

6.4.2.2 Key Results

The 1kg of water was brought to the boil in just over 25 minutes. The average rate of heat flow into the water during the heating phase was 206 W. The average rate of heat flow into evaporating water once at boiling point was 226W.

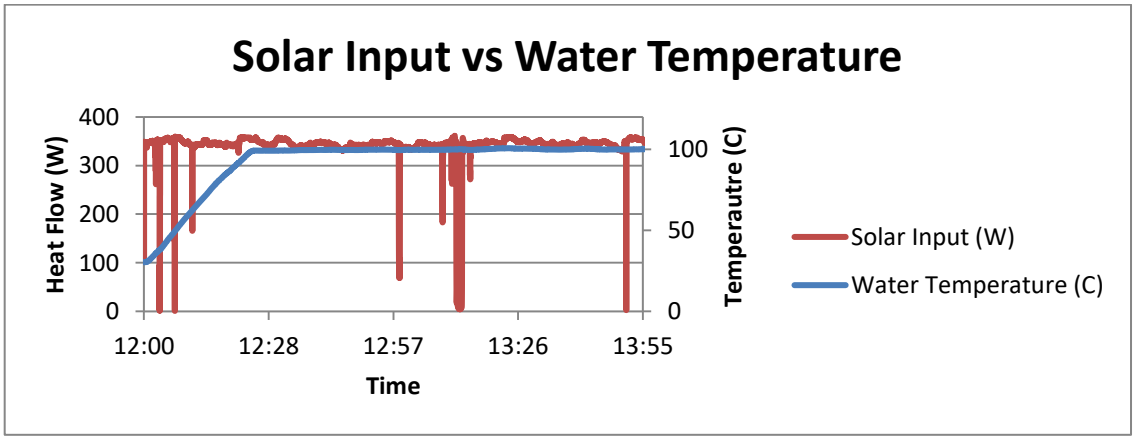


Figure 6.6 Solar Input compared to water temperature whilst bring 1kg of water to boil.

The rate of heat flow into the water during the heating phase is indeed lower than during the boiling phase. During the heating phase some heat is flowing to warm up the oven components, whilst when at boiling these components will have a constant temperature.

6.4.2.3 Hot Plate Results

During the initial heating phase the average heat flow into the hotplate was 246W; from this 40 W was stored as latent heat in the hot plate, whilst 206 W was conducted to the pot. Caustic temperatures measured with the infrared probe were as high as 212 C compared to 150 C measured in the most central thermocouple, see Figure 6.7.

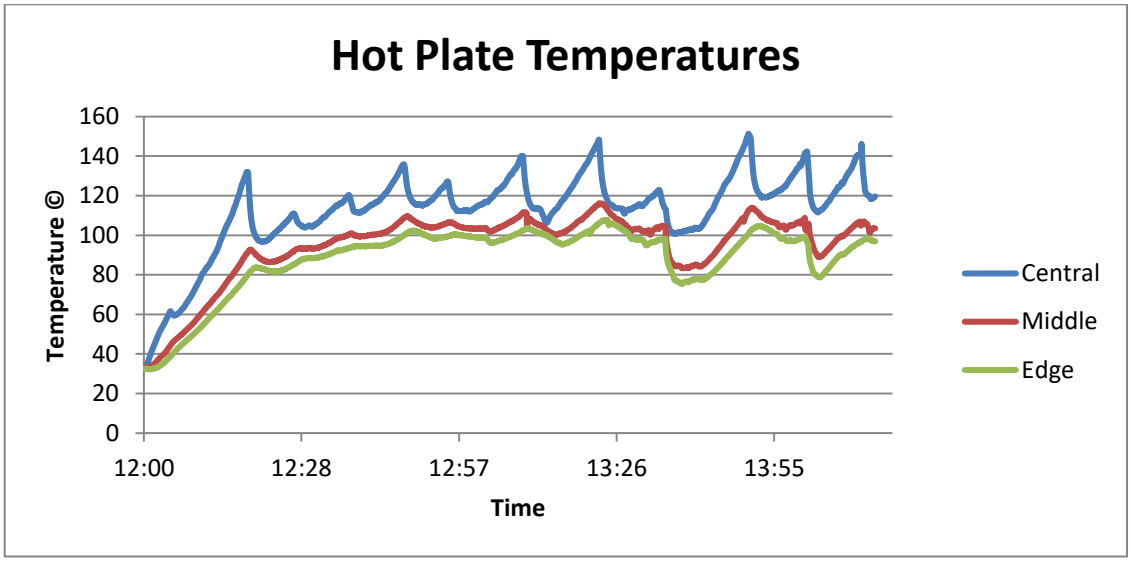


Figure 6.7 Hot plate temperatures during a boiling water test.

Thermocouples were placed 1mm deep into the 1.4mm thick aluminium hot plate. As such the measured temperatures were closer to that of the surface receiving solar flux than the interior hot plate / oven temperature. The periodic oscillations in the measured temperatures are due to the adjustments made to the tracking of the concentrator. During each tracking cycle the caustic would slowly travel over the surface of the receiver as the sun moved through the sky. Given the proximity of the thermocouple to the receiving surface the increase and decrease in temperatures was observed as a function of the position of the caustic. The periodicity of this oscillation coincided exactly with the tracking adjustments made to the concentrator.

The larger dip in temperature at 13:35 was due to a combination of wind gusts up to 15.5 km/h and a slight bumping of the oven which resulted in a small amount of water spilling onto the hotplate (for which a faint hissing sound was noted).

6.4.2.4 Overall Performance

Heat flows of 246W during heating and 226W during boiling were obtained. Average heat losses of 100 W during heating and 114 W during boiling were deduced; these flows correspond to efficiencies of 72 and 66% respectively, see Figure 6.8.

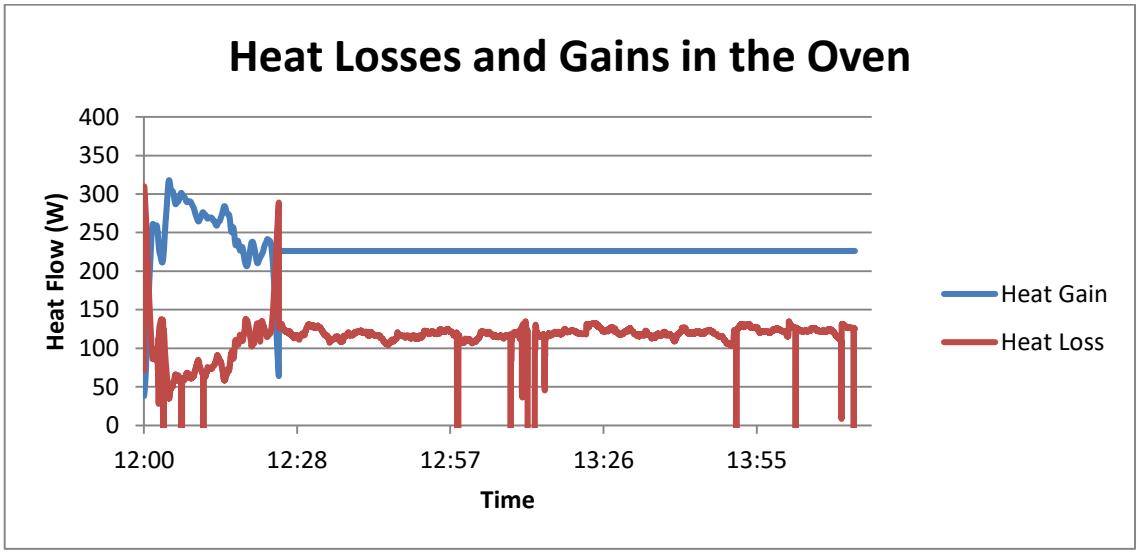


Figure 6.8 Heat losses (convection from the hotplate) vs heat gain by the water, a constant boiling rate is assumed.

The heat loss curve should rise steadily with temperature until it reaches a stable maximum once the water is boiling, where it remains more or less constant. This maximum is much more stable here as the rate of evaporation is taken as constant throughout the boiling phase. The above curve also assumes that evaporation only commences at 12:25 once the water temperature reaches 100C.

6.4.2.5 Wind

The location of the test was on top of the roof of a 4 storey building in DIT. The height of this building meant that wind gusts on the roof were often substantial. The perimeter of the roof

was a solid concrete wall of approximately the same height as the bottom of the oven. This wall resulted in wind speeds being lower nearer to the roof and possibly lower wind speeds near the bottom of the oven than otherwise measured.

For this particular test wind speeds as high as 15.5 km/h were measured during brief gusts. Wind speeds were generally closer to 5 km/h and there were often periods of calm that lasted up to 5 minutes. These wind gusts would drive forced convection from the hotplate which is not reflected in this limited case.

6.4.3 Testing of Vinyl vs. Alanod Mirrors

The test conducted on Thursday the 27th of August to heat 1 kg of water using the Aluminised Vinyl mirror surfaces whilst simultaneously a second concentrator heated 1 kg of water using Alanod mirrors.

6.4.3.1 Test Details

The test was conducted in the family compound in Dodoma. 1kg of Water was heated and then kept on the boil in both concentrators. The water was placed in a thin Aluminium pot with a lid. The lid was kept slightly ajar owing to the placement of thermocouples in the water. The test was performed with the hotplate in place below the pot, apertures were not used. The oven was placed over the pot and hotplate for the entirety of the test. After just over an hour the pot was removed from the oven with the Aluminium mirrors so that the family could use the oven. The oven with the vinyl mirrors was run for an additional 1 hour and 45 minutes. In both cases when the pot was removed from the oven, it was weighed to determine the mass of water lost to evaporation.

6.4.3.2 Dodoma Baseline

The Vinyl mirrors brought 1kg of water to the boil in approximately 47 minutes, whilst the Aluminium mirrors brought 1kg of water to the boil in approximately 29 minutes. The average

rate of heat flow into the water during the heating phase was 123 W and 278 for the Vinyl and Alanod mirrors respectively. The average rate of heat flow into the water during the boiling phase was 86 W for the Vinyl mirrors and 203 W for the Alanod mirrors.

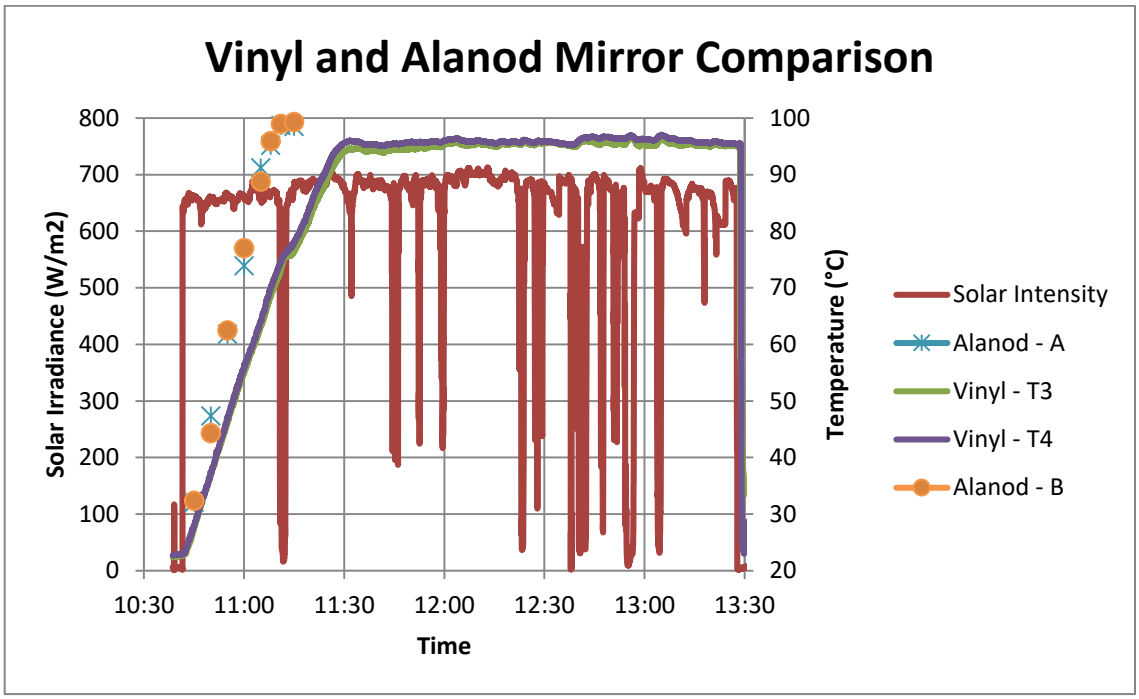


Figure 6.9 Comparison between the Vinyl and the Alanod Mirrors.

The overall effectiveness of the Vinyl Mirrors was approximately 42-44% of the Alanod Mirrors, in terms of delivering heat to the water. The pots used varied slightly in weight but were otherwise identical in size and shape. With the help of Dr. Matiko, tracking was performed for both the ovens in unison. The performance of the Alanod Oven was slightly poorer than the best tests from Dar es Salaam.

6.4.3.3 Hot Plate Results

During the initial heating phase the average heat flow into the hotplate was 146 W for the Vinyl mirrors and 321 W for the Alanod Mirrors. On average for the Vinyl Mirrors, of the heat flow into the hotplate 26 W was stored as latent heat in the hot plate, whilst 123 W was conducted to the pot. On Average for the Alanod Mirrors, of the heat flow into the hotplate 43 W was stored as latent heat in the hot plate, whilst 278 W was conducted to the pot.

Caustic temperatures measured on the underside of the hotplate with the infrared probe were sometimes over 200 C for the Aluminium mirrors compared to a maximum of 115 C measured for the Vinyl mirrors, see Figure 6.10.

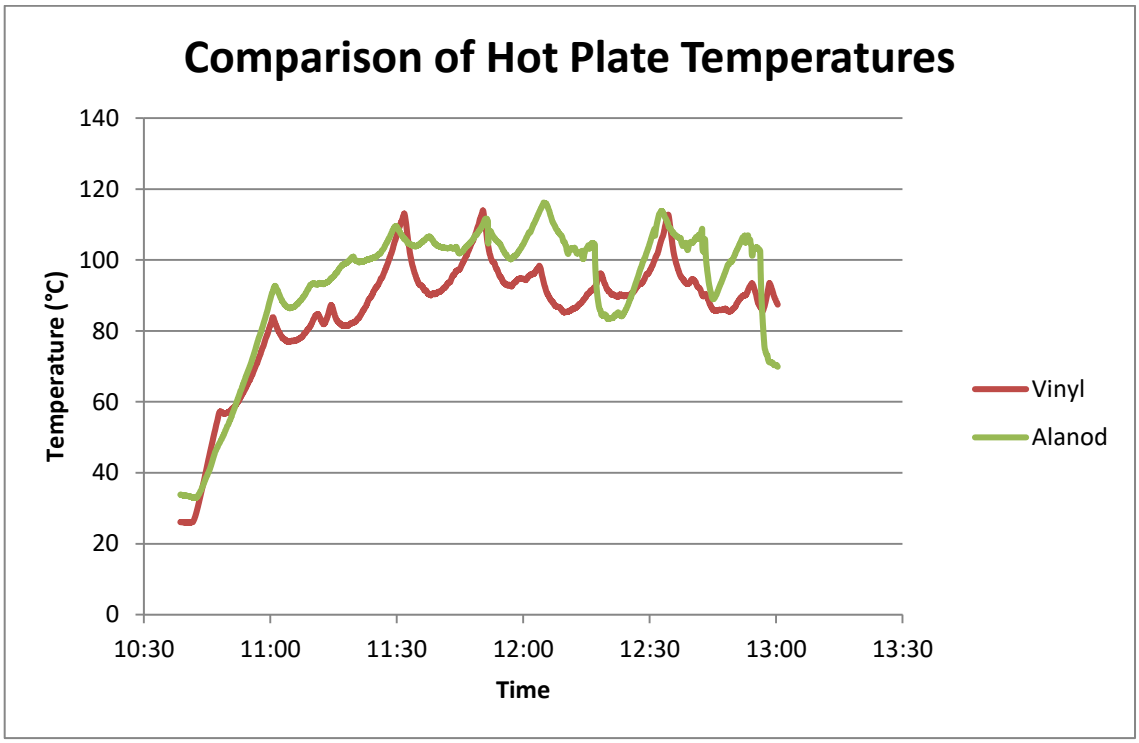


Figure 6.10 Comparison of hotplate temperatures for vinly and alanod mirrors.

The hotplate temperatures measured for the Alanod oven reached higher temperatures slightly more quickly than for the Vinyl oven. However, there was only a slight difference in these times. During the initial heating phase hot plate temperatures must rise to a sufficient degree to provide the temperature gradient needed for increased heat flow to the pot. The pots used had flat bases to minimise the contact resistance between the pots and the hot plates. The thermal mass of the pot and water was about 5 times that of the hotplate in both cases.

The Alanod mirror hot plate temperatures were more stable near their stagnation temperatures than those observed for the vinyl mirrors. However, there was little difference in these stagnation temperatures. It is therefore a reasonable assumption that, with similar hot plate temperatures, similar convective losses would take place in both the Alanod and

Vinyl ovens. The greater heat flow into the hotplate of the Alanod oven meant that hotplate temperatures recovered more quickly to their stagnation temperatures after wind gusts.

6.4.3.4 Overall Comparison

Table 6.6 Effective efficiencies of the Alanod and vinyl mirror systems.

	Vinyl	Alanod
Thermal Efficiency	0.38	0.59
Optical Efficiency	0.59	0.90
System Efficiency	0.22	0.51

6.4.3.5 Thermal Efficiency

The thermal efficiency of the Vinyl and Alanod ovens was calculated by determining the heat flow into the hotplate compared to the heat flow in the pot and water. The heat losses from the system are predominantly convective from the hotplate. Given the similar hotplate temperatures these were assumed to be identical.

A possible explanation for the superior thermal efficiency of the Alanod system is the solar flux distribution on the hotplate. For the Vinyl case was this flux is much more dispersed owing to the poorer mirror confinement and the poorer quality of the reflective surface of the Vinyl. In the Alanod case a highly concentrated caustic resulted in higher measured caustic temperatures, which drives heat flow across the hotplate / pot boundary.

The natural warp of the plywood backing has a greater effect on mirror conformity for the non-rigid Vinyl as opposed to the Alanod. Careful selection and manufacture of these mirrors may help improve solar flux concentrations on the hotplate.

6.4.3.6 Optical Efficiency

The optical efficiency of the Vinyl mirror's surface was calculated as 0.77; for a total value of 0.59 for the two reflections. A concentrator utilising vinyl mirrors would have to be sized just over 50% larger than an equivalent Alanod system to achieve the same solar flux onto the hot

plate. Focusing this greater mirror area onto the same-sized receiver would pose further challenges.

However, a further issue with the Vinyl is that electrostatic attraction to dust particles with result in a much faster degradation in reflectivity than for Alanod mirrors. Regular cleaning may help resolve this but still poses a challenge.

6.4.3.7 System Efficiency

The total system efficiency incorporates the reflectivity of the mirrors, thermal efficiency of the hotplate and the absorber efficiency. It represents the heat delivered to the pot and water compared to the total solar flux intercepted by the system. The Alanod system is more than twice as efficient as the Vinyl system.

6.4.3.8 Wind

The location of the test was in a compound in the outskirts of Dodoma. Wind gusts were not a major factor in thermal losses from the ovens. The hotplates were positioned well below the walls of the compound. However, wind gusts are likely to have played a role in reducing expected solar irradiances.

The wind stirred up a lot of dust in the dry arid conditions of Dodoma. Much of this dust was deposited on the mirror surfaces. However, much of it remained airborne and contributed to reduced direct solar radiation.

6.4.4 Billet Tests

The heating of the same 8.4 kg aluminium billet previously used in the lab tests of the oven and the Italian field trials provided a good comparison between results. The relatively large thermal mass of the aluminium billet reduces the effects of small transients in the data, such

as wind gusts, and therefore provides good estimates of longer term results. Furthermore, as opposed to water tests, the ability to heat the billet above 100°C will give a better understanding of the thermal losses in the system.

6.4.4.1 Tanzanian Billet Tests

There were three opportunities to heat the aluminium billet whilst in Tanzania during August, all in Dar es Salaam. A summary of these tests is given in Table 6.7.

Table 6.7 Summary of aluminium billet tests run in Dar es Salaam, August 2015.

Date of Test	Duration of Test	Maximum Billet Temperature
Wednesday 12th	77 minutes	60°C
Thursday 13th	90 minutes	50°C
Monday 17th	105 minutes	126°C

The first two tests gave mixed results as the maximum temperatures achieved in the aluminium billet were relatively low. These tests were run for short periods in the late afternoon with weakening irradiance , they were also subject to intermittent cloud cover. The final test on Monday the 17th was run for approximately 105 minutes, with clear skies, and temperatures up to 126°C were recorded in the aluminium billet.

6.4.4.2 Modified Thermal Model of Oven

The model of the oven was originally calculated based on the hotplate used in the lab tests and also the Italian trials. However, a slightly different hotplate was used during the Tanzanian trials. In addition to the thermal properties of the new hotplate, the thermal contact conductance of the hotplate and aluminium billet is also expected to change. The calculation of this change in thermal contact conductance can only be obtained from experimental results and must therefore be calculated from the results; see Table 6.8 for a summary of the changes to the thermal model of the system.

Table 6.8 Summary of changes to thermal model of the oven system.

Changes to Thermal Model of Oven	
Known	Mass of hotplate
	Emissivity of hotplate
	Thickness of oven walls
Unknown	Thermal contact conductance of billet & hotplate

It is expected that the properties affecting convective heat transfer from the hotplate remain unchanged given its highly similar geometry to the previous model. However, differences in the thermal properties of the hotplate will introduce some uncertainty into the model. Given the higher degree of planarity of the new hotplate compared to the one used in the lab and Italy it is expected that the thermal contact conductance between the billet and the hotplate will increase.

The insulating Basotect© material was removed from the oven walls to reduce cost and complexity of the design. However, to reduce the work load in redesigning the model this insulating layer was kept in the model, albeit at a greatly reduced thickness of 0.15mm, as the wood was not otherwise modelled. It is calculated that this will have very little impact on the balance of heat flows through the system, as the insulation is sufficiently thin for the inner and outer walls to be effectively isothermal, see Figures 6.11 & 6.12.

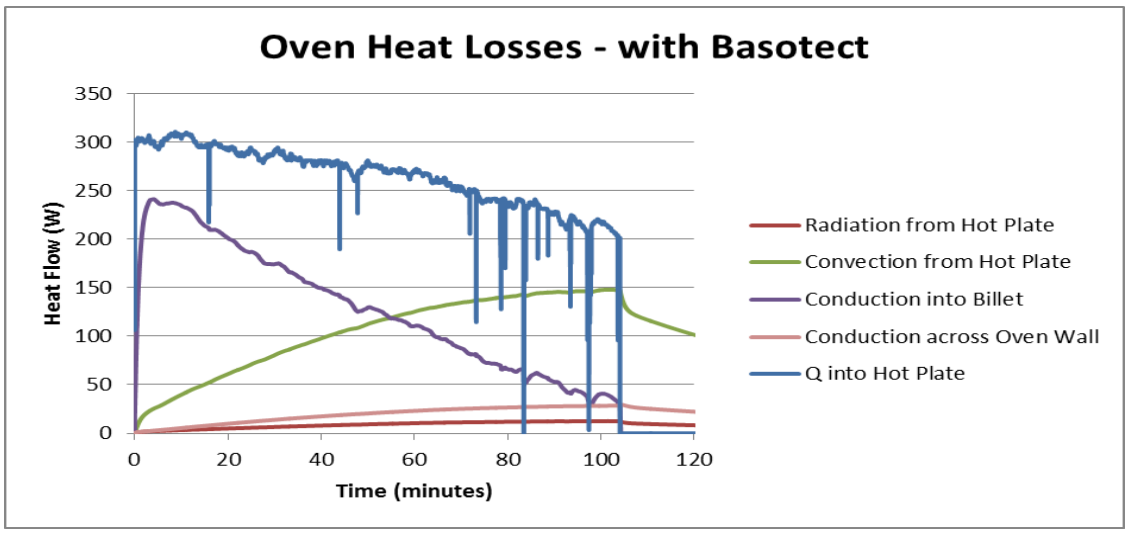


Figure 6.11 Modelled oven heat losses with the Basotect© insulation in place.

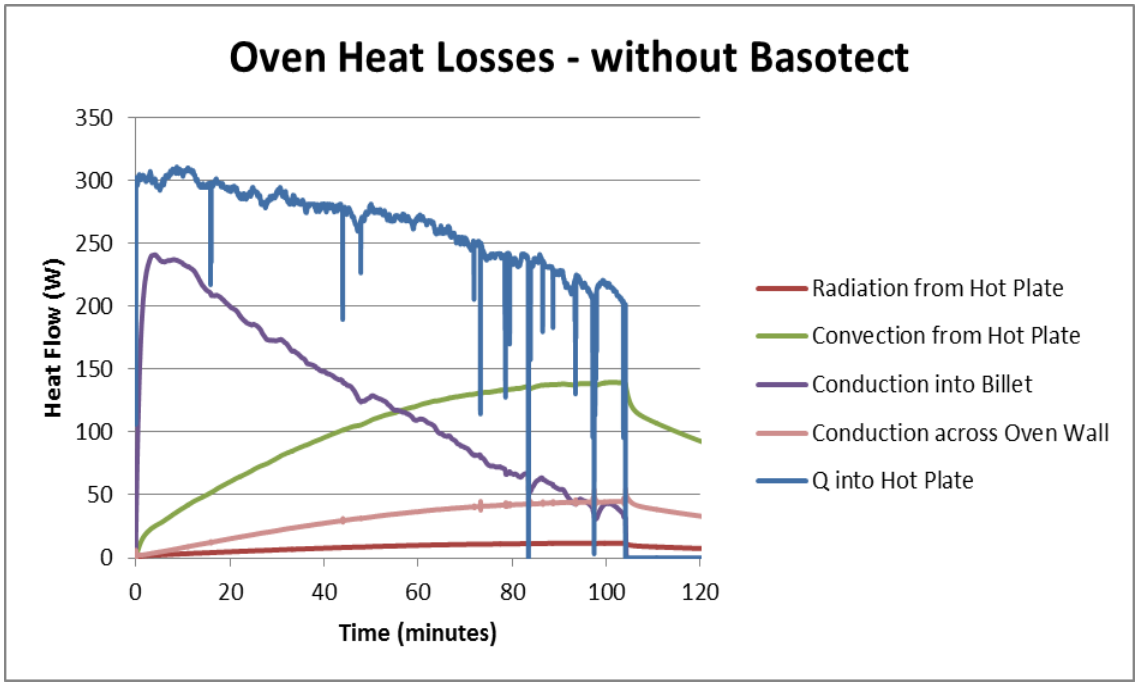


Figure 6.12 Modelled oven heat losses without the Basotect© insulation in place.

It can be seen from the models that by redefining the Basotect© insulation at a thickness of 0.15mm that the model predicts there will be negligible effect on the billet temperatures, and only a slight increase in conduction across the oven walls. The effect can be summarised as shifting a small heat flow from convection across the hotplate, to convection across the oven walls, summarised below in Table 6.9.

Table 6.9 Modelled rates of heat loss for a billet temperature of 125 °C.

Heat Flow @ 125°C Billet Temperature	With Basotect©	Without Basotect©
Convection from Hotplate	150 W	140 W
Conduction across Oven Wall	35 W	50 W
Radiation from Hotplate	10 W	10 W

The model predicts that by removing the Basotect© insulation the conduction through the oven walls will increase by a factor of approximately 1.6, with a negligible impact on the rate of heat flow into the billet. To a first order approximation the plywood which makes up the oven sides will have similarly poor thermal properties to a layer of 0.015 mm thick Basotect©. This is taken as a good approximation given that the other modes of heat flow; conduction through the billet, and radiation and convection from the hotplate, are from thermally more

conductive metallic surfaces. Indeed the treatment of the model here is borne out by experimental results, see Figure 6.17 in the result section.

6.4.4.3 Estimating the Thermal Contact Conductance

The results from Monday the 17th of August were without cloud cover and therefore used in order to determine the value for the thermal contact conductance. In order to estimate the thermal contact conductance a few assumptions were made. Firstly, it was assumed that convective losses from the underside of the hotplate would be similar to those measured in the Italian trials. Wind measurements were taken using a handheld anemometer to identify gusty periods which were noted in the logbook. Average wind speeds were recorded and the same calibration factor for convection was used; that the coefficient of heat transfer was 2.5 times that predicted by a simple case of natural convection downwards from a flat plate. Additionally, a 1.5 times factor is used to predict the coefficient of heat transfer due to natural convection from the oven walls in a similar fashion.

The estimation of the coefficient of heat transfer as 2.5 times the case for natural convection downwards is equivalent to the case of forced convection from the underside of the same plate with a wind speed of 1m/s. Given the complex nature of convection from the underside of the recessed hotplate these measures are used interchangeably. There will be a slight discrepancy in these values as the temperature dependence for forced convection is closer to $(\Delta T)^{1.25}$ instead of ΔT, yet this difference will be smaller than uncertainties elsewhere in the model, in particular the wind speed itself.

Given assumptions that the convection case will be similar to Italy, the thermal contact conductance between the new hotplate and the billet can be estimated. Using the model the value calculated is approximately 3.5 times that of the smooth billet end with the previously used hotplate, see Figure 6.13 to see how this estimation compares with results from Dar es Salaam.

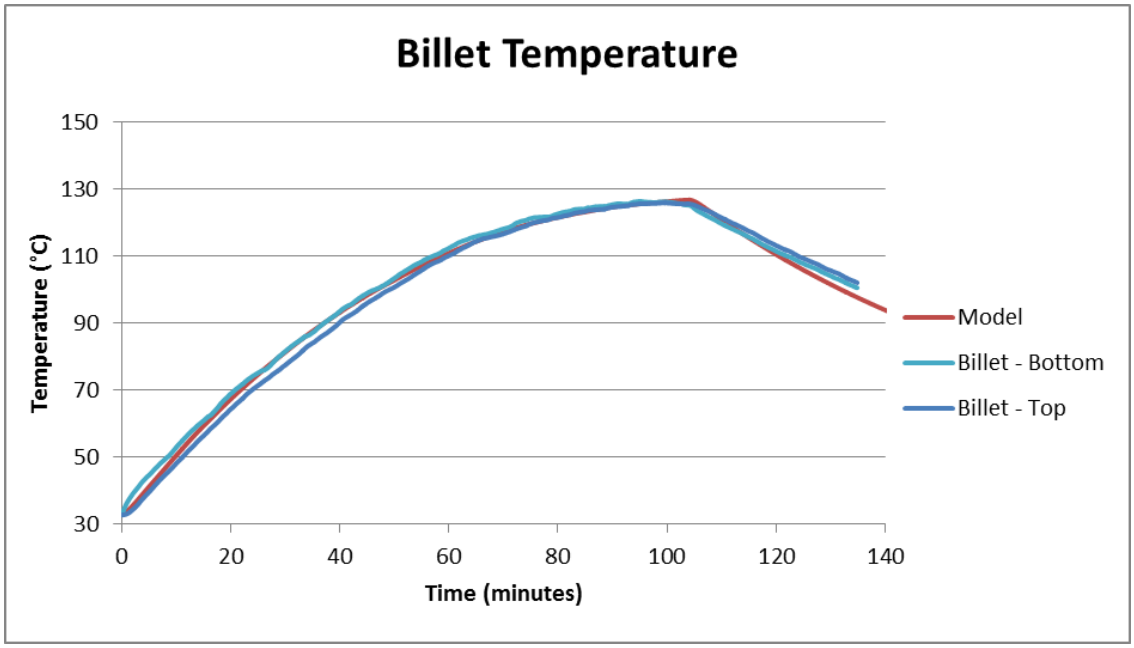


Figure 6.13 Comparison of modelled data, using a thermal contact conductance of 3.5 times the previous value, with the measured data from Monday the 17th, Dar es Salaam.

There is good agreement with model and the data. However, the model is not very sensitive to the figure entered for the thermal contact conductance and values between 2.5 and 4.5 produced acceptable results. Using a value of 3.5 the thermal contact conduction between the new hotplate and the smooth end of the aluminium billet is 3238 $W \cdot m^{-2} \cdot K^{-1}$. Previous results for the old hotplate were 852 and 187 $W \cdot m^{-2} \cdot K^{-1}$ for the smooth and rough end of the billet respectively.

These results make sense given the increased planarity of the hotplate used in the Tanzanian trials, which was cut from a machined-flat sheet of Aluminium. Previously, in the Italian trials, the hotplate had been pressed from a flat sheet of aluminium in order to provide supporting edges. The bending of this aluminium plate resulted in residual stress in the hotplate and a slight curvature to the surfaces.

Lastly in the above test there is some divergence in the results after the hotplate ceases to be heated at around 105 minutes. The model predicts a sharper decline in billet temperature than occurs. However, the good agreement of the model and data during the heating phase is acceptable given the simplicity of the model.

6.4.4.4 Thursday 13th August – Billet Results

Using this updated model it was possible to validate results taken on days with less reliable sunshine. On Thursday the 13th a relatively good agreement with the model and data can be obtained considering that there was relatively little sunshine, see Figure 6.14.

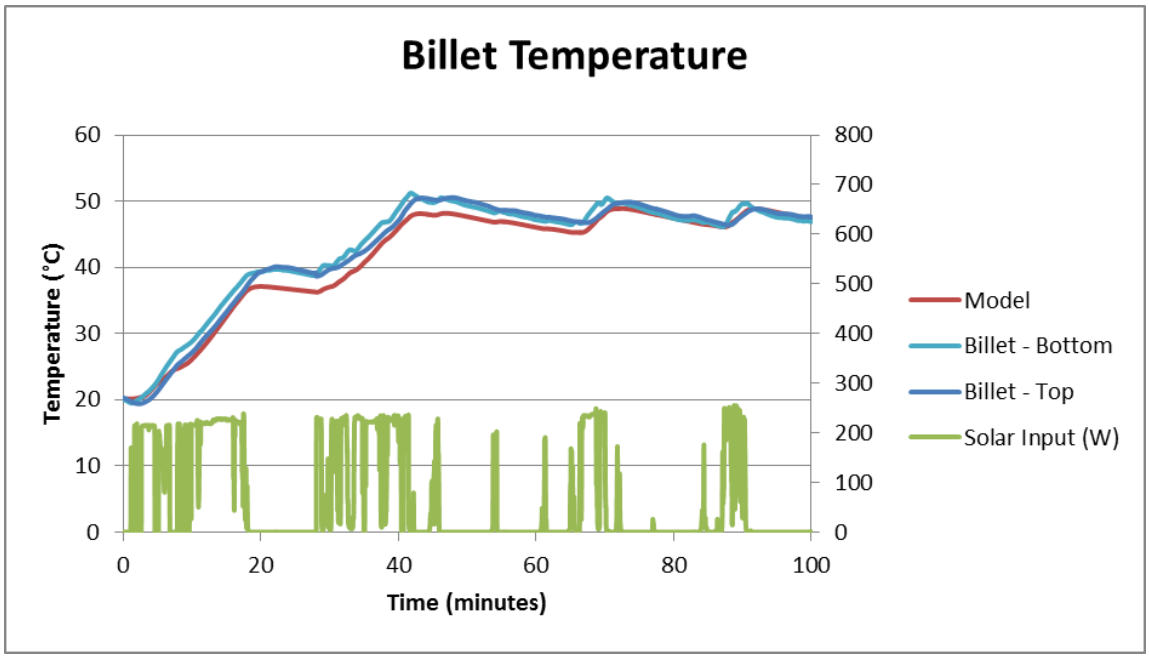


Figure 6.14 Comparison of model and measured data for Thursday the 13th.

There is some slight disagreement with measured data and the model during the first few heating cycles. However, the long term results agree well. This discrepancy may be due to latency in heat flows that are not built into the model which acts more or less instantaneously. Previous calculations indicated that in laboratory conditions there may be a delay of up to 8 minutes for a thermal wave to propagate the length of the billet. However, in practice a smaller delay was measured, and temperature differences across the ends of the billet were lower than expected.

It is therefore unlikely that these discrepancies are due to any latency in the heat flows. Given that the greatest temperature differences observed in Figure 6.14 are only of the

order of 2-3 K they could more simply be attributed to errors in thermocouple measurements. Small differences to the locations of the thermocouples and errors in their measurements.

6.4.4.5 Wednesday 12th August – Billet Results

The data from Wednesday was also used to validate the calculated variables for the updated oven model. However, using the same calibration for convective losses from the underside of the hotplate leads to less good agreement with the model, see Figure 6.15.

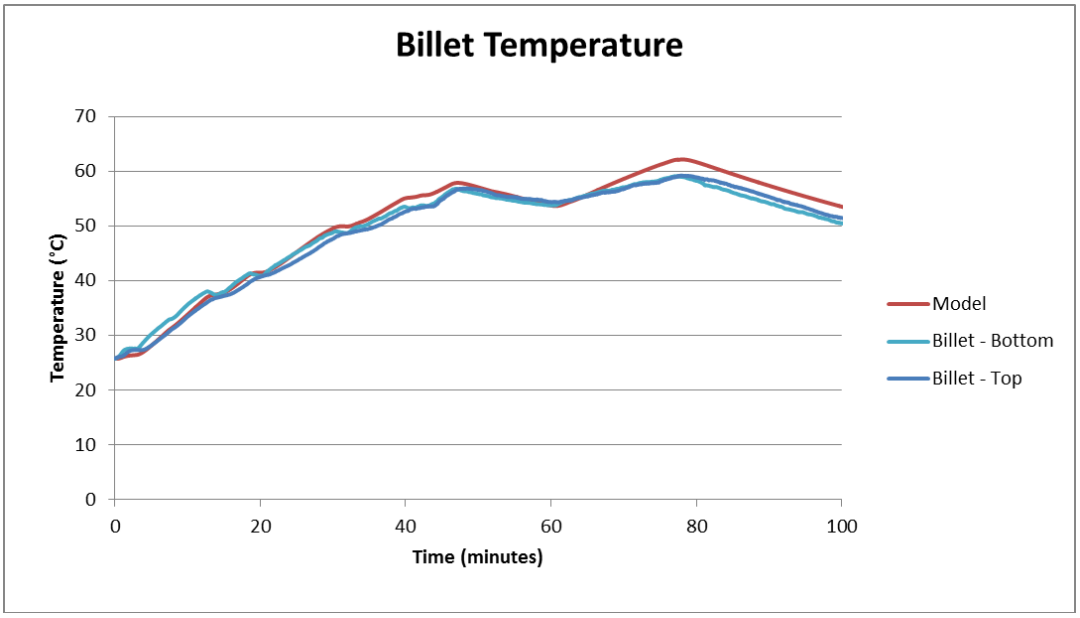


Figure 6.15 Model and data for Wednesday with a 2.5 times calibration for convective losses from the hotplate.

Logbook records indicate that, generally, Wednesday 12th and Monday 17th had similar wind conditions. However, a very slight increase in the average wind recorded, up to a 2.9 times factor for the coefficient of convective heat transfer, gives much better agreement between data and model, see Figure 6.16.

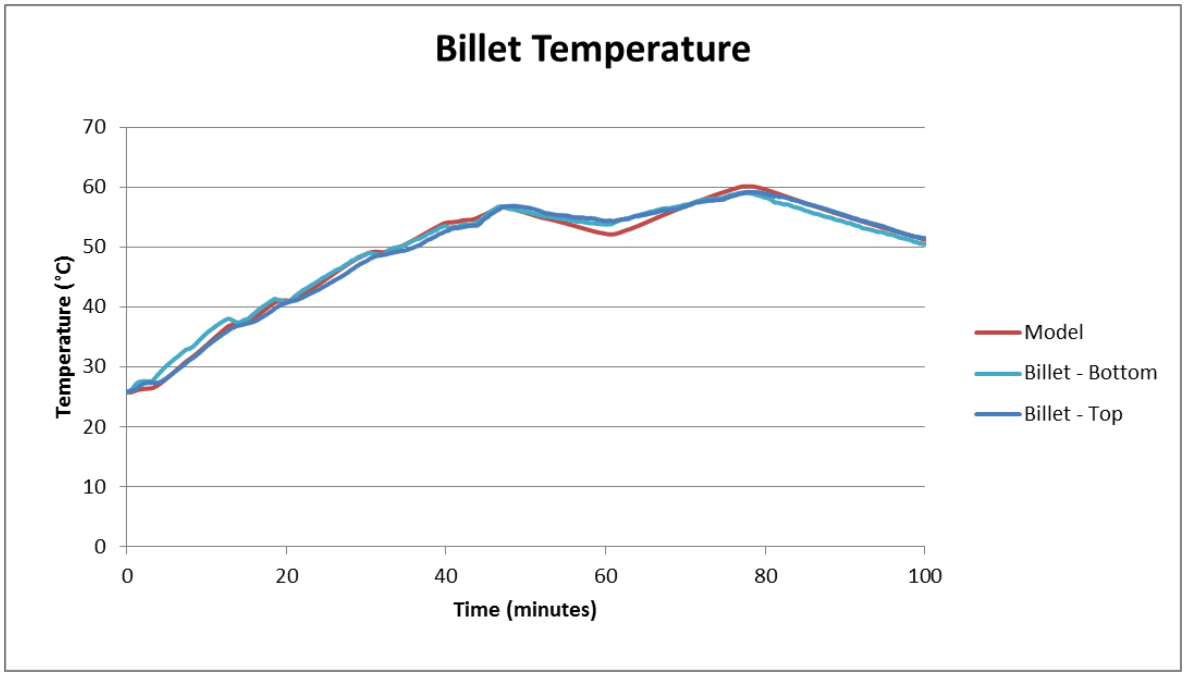


Figure 6.16 Results for the Wednesday 12th trial compared with the model with a 2.9 times factor for the coefficient of heat transfer.

The increase in estimate of heat transfer coefficient is equivalent to an increase in average wind speed from 1m/s to 1.35m/s. This would not have been remarked upon in the logbooks as generally only measurements of gusts were taken. There does not seem to be a large increase in the incidence of these gusts on Wednesday 12th.

Additionally, the model tends to overestimate the peaks and troughs at around 60 and 80 minutes. (The temperature measurements from the thermocouples presented here were taken at 1 second intervals). Again, this is unlikely to be due to any latency in heat flows as the direction of thermal conduction reverses in the billet during the overcast periods. These small discrepancies in the results might be due to instrument error.

6.4.4.6 Wall Temperatures

The wall temperatures show good agreement in almost all cases, see Figures 6.17 and 6.18.

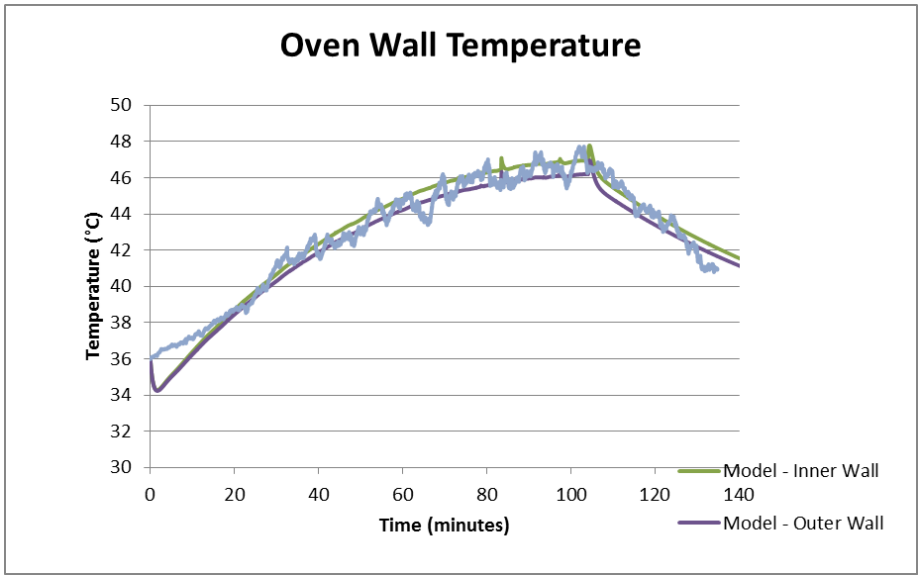


Figure 6.17 Modelled and measured data for wall temperatures from the Monday 17th data.

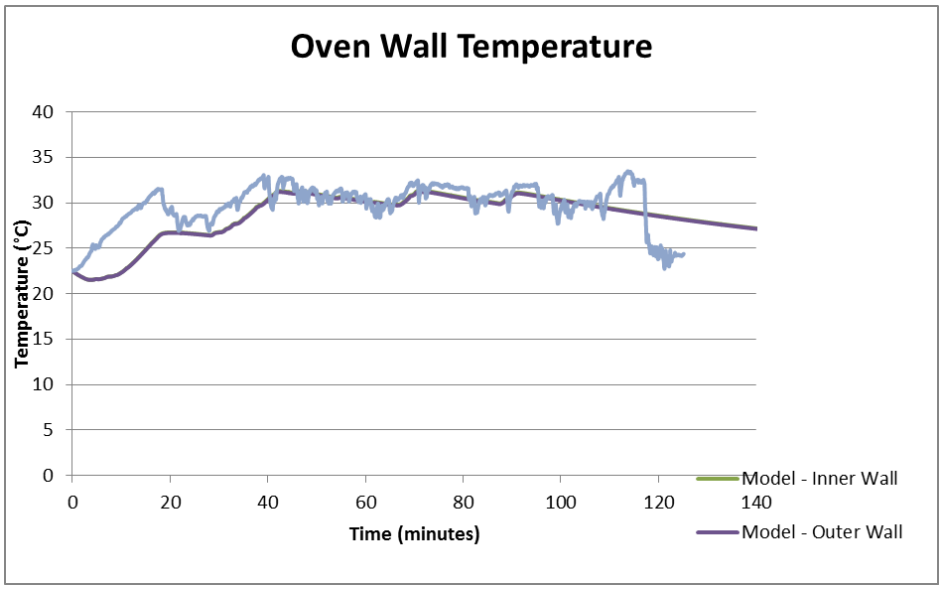


Figure 6.18 Modelled and measured data for wall temperatures from the Thursday 13th data.

The modelled data includes estimates of both the inner and outer wall temperatures, including the minimal thickness of Basotect© included in the results. The data for Wednesday 12th is not included as there was only an increase of a few degrees above ambient measured in the wall owing to the very limited heating of the billet. These results bear out the assumption that the plywood oven can be approximated as a 0.15 mmm thick layer of Basotect© insulation for the purpose of modelling and inner wall temperatures and convection from the oven walls.

6.4.4.7 Hot Plate Results

The key results for the hotplate data, the test from Monday the 17th of August, shows good agreement with the model, given the limitations inherent in the model, see Figures 6.19 & 6.20. The model treats the hotplate as isothermal and cannot include effects of having a highly concentrated hotspot due to the caustic region. Despite this general trends can be observed and sensible limits imposed.

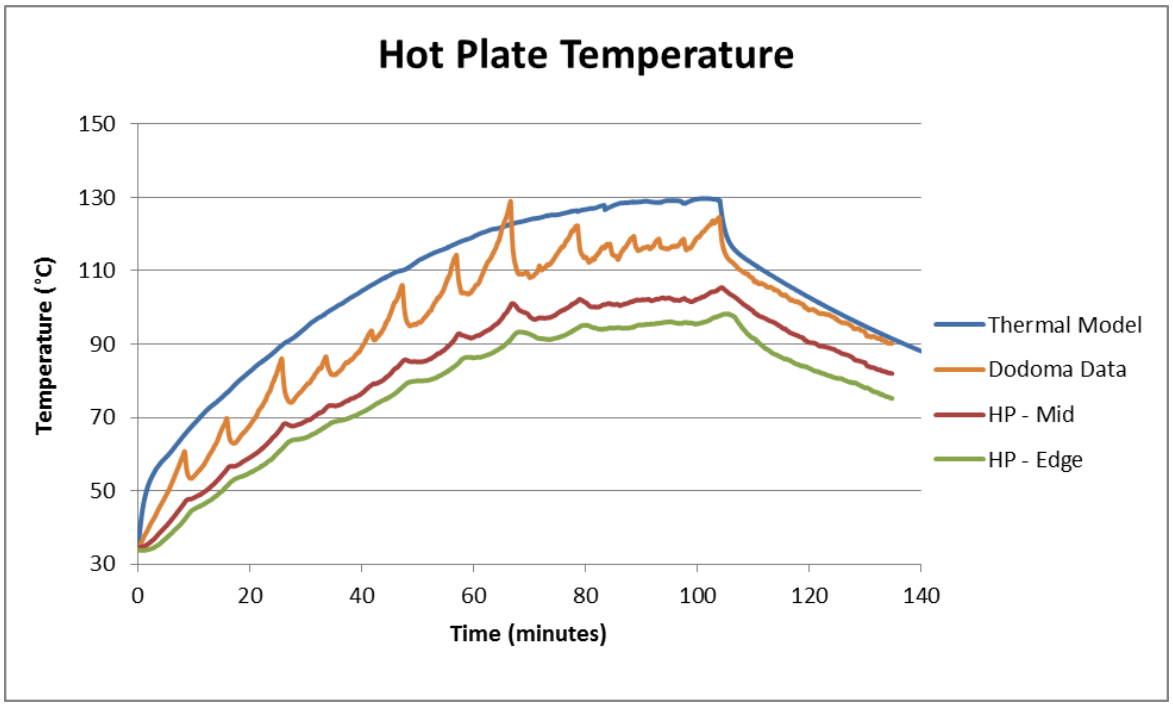


Figure 6.19 Modelled and measured data for hotplate temperatures from the Monday 17th data.

The three measurements for the hotplate temperatures are taken from the edge of the billet going outwards towards the edge of the hotplate, as per Figure 6.20. The variation in the central 'Dodoma Data' thermocouple is due to the caustic region moving across the hotplate as the sun moves in the sky and the mirrors remain stationary. The oscillations are therefore periodic with the adjustment of the mirrors to track the sun.

Treating the hotplate as isothermal will mean that the model will tend to overestimate convective losses whilst underestimating radiative losses. However, radiative losses are unlikely to be high and the convective losses can only be approximated given the complex nature of the downwards convection compared to the simple case in the model.

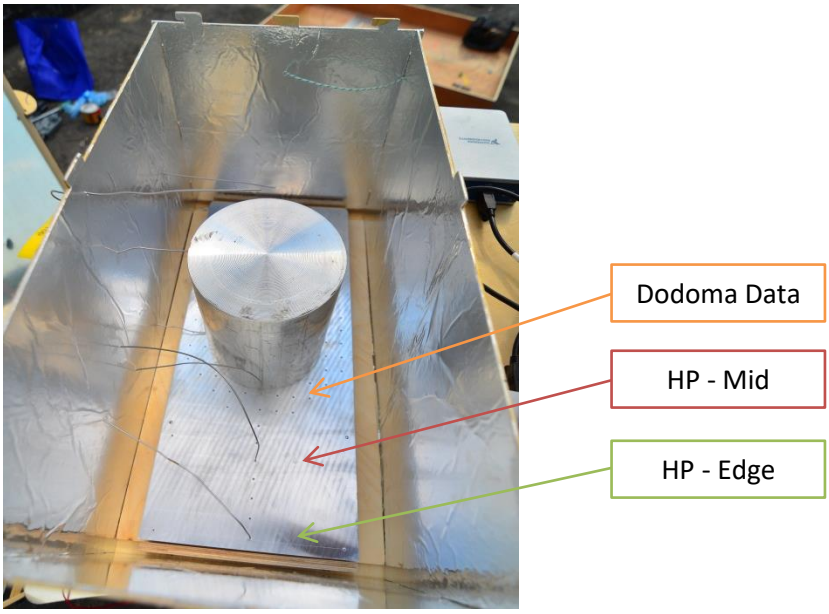


Figure 6.20 Locations of thermocouples in the hotplate with regards to the billet. The billet as seen here is placed centrally on the hotplate with its smooth side down.

The data for Thursday 13th August is more complex given the intermittent cloud cover present that day. However, the model still roughly predicts the behaviour of the most central thermocouple whilst acting as an upper bound limit, see Figure 6.21.

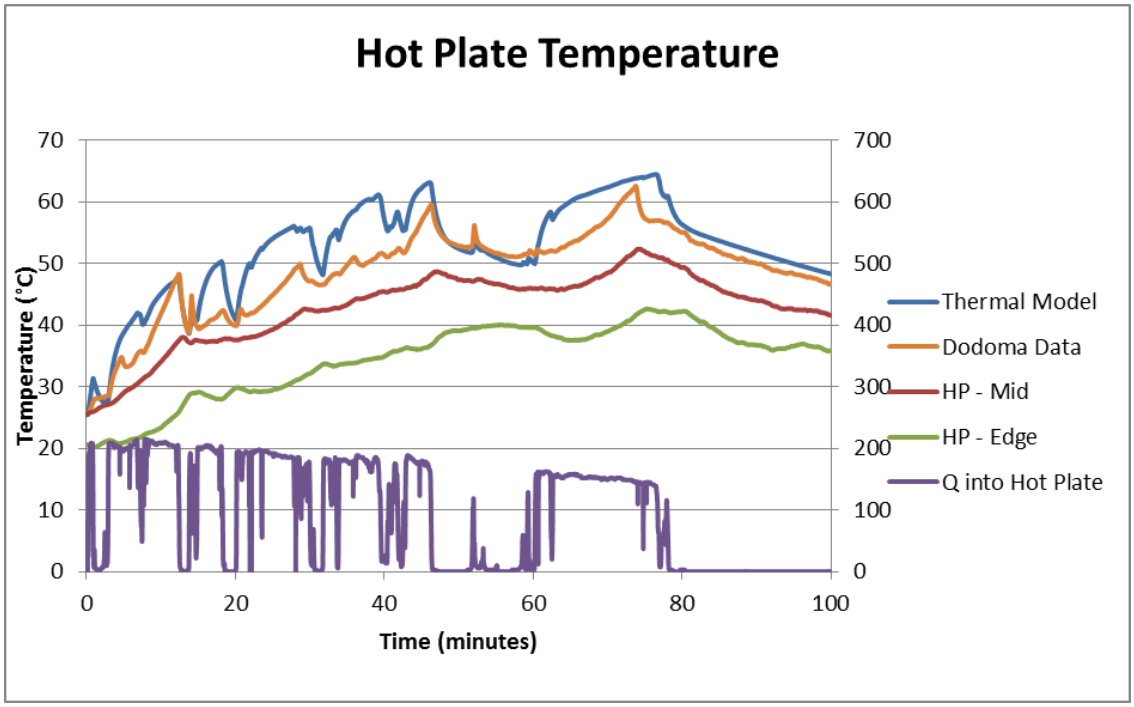


Figure 6.21 Modelled and measured data for hotplate temperatures from the Thursday 13th August, including incident solar flux on the hotplate.

The model predicts higher temperatures as it must predict the centrally located maximum required to drive thermal conduction to the billet. Therefore the model is likely to overestimate convective losses from the hotplate, as the temperatures towards its edges are cooler than those observed centrally. Conversely the model will likely underestimate radiative losses due to the higher temperature of the caustic region and the T^4 radiative dependence.

Results for the hotplate temperature observed on Wednesday 12th August are included, although the limited temperature range observed limits their utility in describing the model in greater detail, see Figure 6.22. Despite this limitation there is still good agreement between the data and the model.

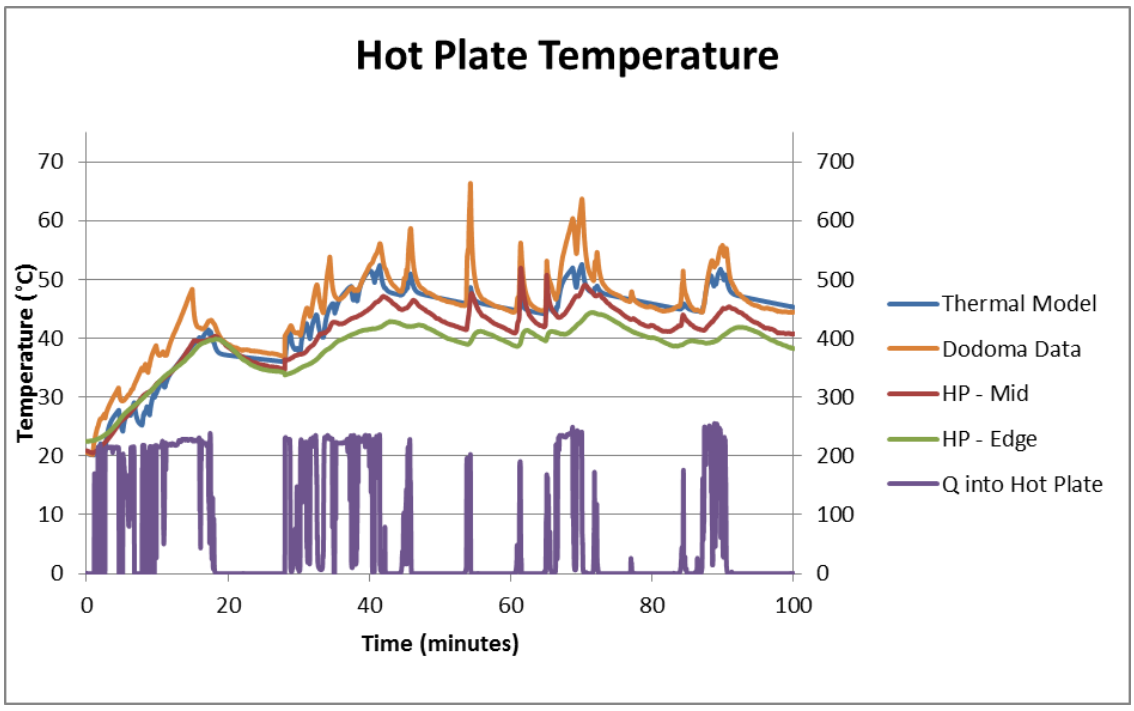


Figure 6.22 Wednesday 12th August results were taken with large amounts of passing cloud, as indicated in the fluctuating value of Q into the hotplate.

6.4.4.8 Summary of Billet Results

Overall the results measured in Tanzania for tests run with the billet compare well with the thermal model developed. Convective losses from the underside of the hotplate are similar to those measured in Italy, whilst the removal of the Basotect© insulation from the oven walls

has had a negligible effect on the system. The improved thermal contact conductance between the billet and the hotplate ensured good heat flow even at low ΔT.

6.5 Technical Feedback

The design feedback that has come from the trials has been divided according to its nature and source. The principal distinction is whether the feedback concerns technical issues with the cooker (pertaining to its performance, construction, durability and other tangible measures) or whether the feedback concerns the usability or user-friendliness of the cooker. Beyond these distinctions the feedback can be further categorised by its source, from the users or from our own working group. Most of the technical feedback is from ourselves, whilst much of the usability feedback is from Tanzanian families.

As the trials are currently ongoing and analysis of technical data has only just begun, it is expected that any concerns listed here will be expanded upon in both number and content in the future.

6.5.1 Performance of Vinyl Mirror Surface

The vinyl mirror surface currently suffers from some major issues including its tendency to 'bubble' despite correct application. The application of the vinyl itself is quite difficult and the self-adhesive is not particularly strong. If the vinyl is applied incorrectly, lifting it up to reapply the vinyl is often not possible as the glue will have already lost its tackiness. Applying the vinyl is quite difficult, a multiple person operation, which can be foiled very easily: the vinyl must be stretched taut whilst applying to avoid bubbles forming on its underside, however, this leads to problems if the vinyl is not stretched uniformly in direction. Quite often stretching the vinyl in one direction will lead to bubbles forming in the other orientation. Another issue with the vinyl mirrors is that they provide no structural rigidity to the mirror; therefore, any natural bend or warp in the backing ply will not be corrected for.

6.5.2 Manufacturing Tolerances

A lot of difficulty was experienced slotting many of the ribs together. This was not due to the varnish applied as the concentrators were assembled during the application of the varnish. Without sandpaper and files the assembly of many of the concentrators in the field would have proven impossible. Additionally, the rib with the slot for the bottom of the parabolic mirror was positioned too low. Router tolerances must be better incorporated into the design. Another problem was that the top of the parabolic was incorrectly toleranced and the backing plate extended past the leading spine edge in almost all concentrators. This meant that instead of sitting flush on the spine, with correct geometry, the top of the parabolic would be pushed past this edge.

6.5.3 Conformity of Mirror Geometry

Provided the mirror structure was flat it could be relatively easy to position the mirrors and achieve a good conformity to geometry. However, further consideration must be given to visual feedback that enables users to position the conical and parabolic mirrors both centrally and symmetrically. The screws used to hold down both the parabolic and conical mirrors can and have slackened off over the course of a day or two. With the thinner Alanod there was a noticeable increase in apparent warp in the mirrors due to the play and an associated increase in the difficulty of achieving good mirror conformity. One pair of mirrors had to be replaced as the originally supplied pair was so poor.

6.5.4 Stability

With an umbrella attached to the structure the table can become very unstable in wind. This resulted in a broken phone and damaged laptop during the trials. If umbrellas are to be used as shade the whole stability of the structure needs to be improved. Additionally there is currently very little adjustment that can be done if the ground underneath the cooker is not flat. Some of the more wealthy families had underground water tanks with flat tops that

proved perfect for placing the cooker. However, not every family will have these available to them.

6.5.5 Condensation

With the current oven design condensation during cooking will accumulate towards the bottom of the oven where it can drip onto the parabolic mirror below. This results in a heightened need of cleaning the mirrors; see next point.

6.5.6 Mirror Surface Finish

There are in general two types of mirror cleaning that need to be performed. The first is a light dusting, whilst the second is to remove stains. These stains occur when condensation on the mirror combines with the dust and then dries. These stains are very difficult to clean off and require water and significant pressure applied to the front of the mirrors. Cleaning the mirrors in the latter fashion demands that the mirror structure has enough strength to apply a not insignificant pressure on the front. There seemed to a marked difference in the accumulation of dust on the mirrors between the vinyl and Alanod mirror surface, possibly due to electrostatic attraction. A final consideration the choice of mirror surface will be that any form of cleaning will be hampered by a mirror surface that is not perfectly flat; the crease in the vinyl mirror surface made it's cleaning very difficult. The surface finish of the mirror can be almost as important as its reflectivity.

6.5.7 Oven Support Material

The current oven supports are wooden and prone to burning if the concentrator is misaligned. These have been covered in aluminium foil in the current generation of cookers but the choice of material here will need to be reviewed going forward. Even with the protective film still in place on the mirrors they managed to burn the wooden underside of the oven. We failed to be able to stop this completely despite our intimate knowledge of the cooker and awareness of the problem.

6.6 User Feedback

6.6.1 General Feedback

Most people seemed enthusiastic when receiving their ovens. Unfortunately, many people were unable to immediately use their ovens due to cloud cover and without seeing the ovens working first hand some of this initial enthusiasm was dulled. Most people seemed to pick up the adjustments required for daily tracking, although many did not seem to be adjusting the ovens at frequent enough intervals.

6.6.2 Ease of Assembly

The best assembly time Dr. Matiko and I achieved was approximately 40 minutes. Given our intimate knowledge of the cookers this would be markedly larger for other users. Whatever the final design is there is a lot of complexity that must be removed from the assembly phase if we hope to have people building concentrators themselves. The small screwdrivers supplied with the ovens can do the job required, but they need much more effort and concentration to use than the large ones.

Worth consideration is the sad fact that, despite Tanzania's great progress in recent decades, many of the intended users will be without any formal education past primary school. In particular, female users of the ovens are still far less likely to attend high school than their male siblings.

No families offered to help during the assembly of their ovens, most likely owing to the complexity of the process.

6.6.3 Ease of 'Track-ability'

Most people had little to no trouble in tracking the sun, at least daily movement, once they were shown how. Even the more advanced concept of rotating the concentrator through a large daily angle, in order to verify that both the latitude and the north-south orientation of

the oven are set correctly, was picked up on by some families. Indeed, the 2nd Dodoma family was able to perform these adjustments without our supervision.

Despite the knowledge of this process, many families did not seem to be adjusting their ovens at frequent enough intervals. By just looking at the sun-dial screws one cannot gauge how good or poor the caustic is on the bottom of the hotplate. It may help to provide an aiming circle around these screws to indicate the maximum distance the sun should be allowed to travel before further adjustment is required. One factor in the infrequent adjustment of the cookers may be cultural, in that Tanzanians seem to keep a less precise concept of time.

6.6.4 Ergonomic considerations

The 'standard table height' of the oven is perhaps set a little high for the comfort of some Tanzanian users, who don't seem to be very tall (on average). The issue is not so much the table height but perhaps more so the height of the oven walls, which must be reached and looked over in order to cook. With dual screw sun-dials at least one is normally below eye level for even the shortest users.

6.6.5 Mobility

Currently most families seem to have adequately secure compounds that won't require them to bring the cooker inside each night. However, if this is needed (which is the case for at least one family) then disassembling the concentrator into the table, mirror assembly, and rear bipod was the only workable solution. It remains unclear if this can be performed easily alone. An inescapable drawback here is that the concentrator must be realigned for both north-south orientation and latitude after this disassembly.

6.6.6 Safety – Glare

Most of the cooking during the trial was performed with the hotplate in place so the principal issue regarding glare was people hurting their eyes when looking at the caustic on the receiver. However, very few of the families seemed curious as to what the underside of the

cooker looked like during operation. Additionally, none of the families had their own sunglasses with which to look at the receiver. Those that did take a quick peek underneath the receiver were wary of staring too long and this may even serve to highlight the dangers of looking into or touching the caustic spot.

The few instances where families cooked without the hotplate were performed under our supervision. Our own experience of cooking without a hotplate gave us a few indications on how to responsibly cook. Firstly, greater attention should be paid to closely tracking the sun. Furthermore, cooking at the very start or end of the day where the solar angles.

6.6.7 Ease of Cleaning

The aluminium hotplate is easy enough to clean yet the soft surface may scratch. The biggest issue remains in the cleaning of the mirrors. In the absence of moisture it is rather trivial to dust off the mirrors to ensure they remain clean. However, the always present dust in Tanzania, when combined with condensation dripping from the oven results in stains on the mirror surfaces that require much more effort to remove. This dried dust requires both water and a lot of pressure on the mirror surface in order to clean adequately. This is even more of an issue for the vinyl mirrors. An appropriate mirror cloth will have to be supplied with each concentrator.

6.6.8 Initial Orientation

Orientating the oven in the correct north or south position was performed by us and not the families. To note is that many people may not be familiar with the use of a compass.

6.6.9 Switching between cooking modes

The aluminium box section currently used to support either the hotplate or a pot directly above the solar flux needs some further design work. Currently, 4 locating screws extend only a few millimetres past the bottom of the assembly, which must then be located in small holes in the oven supports below. Such is the difficulty in doing so that none of the families were

able to do so satisfactorily. The principal issue here is that with these screws not located in their holes the whole oven assembly including the hotplate can be bumped off the concentrator.

6.6.10 Latitudinal Adjustments

We explained how to perform the latitudinal adjustments of the concentrator but were not able to visit families after a long enough period to require making these adjustments. We await further feedback from the trial.

6.6.11 Hemisphere Adjustments

The twice yearly adjustment of the cooker to follow the movement of the sun between north and south hemispheres was explained to all families. Again, much more time needs to pass before this adjustment is required.

6.6.12 Physical Exertion

All of the screw type fasteners for the mirrors require significant levels of strength in order to conform the mirrors properly. It may be worth considering larger diameter handles for better leverage. The daily tracking of the oven did not seem overly strenuous for most people to perform. However the latitudinal adjustments require a level of strength and coordination that may challenge some elderly or infirm users.

6.6.13 Affordability

A woman in Dodoma initially commented that she would be happy to pay approximately 60 pounds for an oven. However, this comment was made before the oven was used. More feedback will become available as the trial continues.

6.6.14 Safety – Fire Hazard

Despite our intimate knowledge of the oven, we even had trouble ensuring that the mirrors were stowed in a safe position at all times. This lead to the burning of the underside supports

of the oven. One family experienced a similar event and decided it best not to use the oven until the vulnerable supports were covered in aluminium. A thick cloth to drape over the mirrors when not is use may be a desirable safety feature.

6.6.15 Performance

The few families that used the oven in our time in Tanzania seemed pleased with the performance of the oven. However, it did take longer than cooking with charcoal. For rice and stews, which we witnessed the cooking of, the oven performed well enough to keep the families very happy. Ugali, a staple of Tanzania, may prove too difficult to cook with our oven. Ugali is made by mixing flour into water whilst stirring over a flame. Not only does this require the heating of a very large quantity of water but the cooking process must be done without any lids which would otherwise prevent heat loss.

6.7 Summary of Field Trials

The Tanzanian field trials were conducted during August 2015 in both Dar es Salaam and Dodoma, Tanzania. Initially there were multiple setbacks for the trial, including long and complicated delays with customs. The purchasing of pots for cooking and matte black enamel paint to coat their undersides was made difficult by the relatively poor selection of paints available. Eventually the concentrators were delivered and the testing commenced. However, the weather was highly variable and the intermittent cloud cover at Dar es Salaam proved difficult to work with.

After a week of sporadic testing, including the delivery of several ovens to families based in the Dar es Salaam region, it was decided to travel inland to Dodoma. The remaining concentrators would be taken to Dodoma, which is inland in a much more arid region, with less humidity and less cloud cover. This decision paid dividends as the tests at Dodoma proved

invaluable to the field trials, with 3 days of continuous sunshine providing many excellent results and large improvements over Italian data. However, the aridness of the region resulted in large amounts of dust circulating in the air which led to investigations into its effect on the expected solar irradiance. An investigation into this effect showed noticeable declines in the measured irradiances, including a small red colouration in the relative measured intensities of sunlight.

From a technical perspective, the results from the trials validated several design choices made previously and were generally very positive. The majority of these results have been analysed and the thermal model of the system has been further refined. Brief tests with aluminised vinyl mirrors highlighted several severe drawbacks to this alternative, despite its low cost; the electrostatic attraction of dust was of foremost concern. The experience of using an oven in its intended conditions provided many insights which have been included into suggestions for further design improvements. The analysis of the Tanzanian results is eventually intended to be the topic of a paper, see proposed future activities.

The concentrator used in the African field trials was redesigned such that it could be constructed in wood wherever possible. This was done first to reduce cost, but also to ensure that the concentrator could eventually be built in Tanzania. The change of the design to wood resulted in many differences to the design previously used in Italy, including a separate bipod which was added to stabilise the previously unsupported and cantilevered end of the mirror structure. The insulation was removed from the oven walls after modelling predicted that the removal of the Basotect© insulation hardly alter the balance of heat losses. Lastly the hotplate was made from flat aluminium sheet rather than it being pressed into form. This hotplate could be removed and a pot could be placed at the focal point in its place.

In contrast to Italy, where we had the luxury of sending a large crate of equipment and supplies, the 10 prototypes supplied for the Tanzanian trial were envisioned to be stand-alone

units. Other design constraints for the concentrator were that it was to be flat packable in a box of limited dimensions, to ensure transportability in the back of a car and to reduce overall freight costs. The careful design of the concentrator ensured there was very little empty space in the flat-packs. In fact there were very few ways in which the entire concentrator could be placed in their boxes. To aid in further shipment of these concentrators the ideal placement for all the parts were traced into the boxes and their lids.

In addition to the 9 concentrators that would be distributed to Tanzanian families there was one concentrator which was reserved for testing at the Dar es Salaam Institute of Technology. This concentrator was packed with several additional items including; testing equipment, alternative mirrors, and hotplates with holes machined for thermocouples. The preparation of these concentrators into their boxes and then pallets took some time and effort.

From a user's perspective the Tanzanian field trials provided invaluable feedback into the concentrator's design. In the time at Dodoma two of the families cooked several dishes using the concentrators and feedback was generally positive. However, many of the families in Dar es Salaam were unable to use their ovens effectively with the sporadic weather as the wet season approached. A document was produced summarising the general and specific feedback towards the design during the weeks we were in Tanzania. This feedback encompasses both the use of the oven and also expected challenges in having them manufactured in Tanzania.

6.8 Reflectivity Measurements of Proposed Mirror Materials

The reflectivity of the chosen mirror materials will be of the utmost importance to the final design for the solar cooker. As a dual mirror system, any reflective losses will be squared over the two reflections. For a desired power the reflectivity of the mirrors will determine the required mirror surface area and therefore the exact geometry of the design. The price per square metre of these mirror surfaces is also very important. The ratio of the price per m^2 to the reflectivity squared of each material could be an important figure of merit.

However, the dimensions in which each mirror surface is supplied could also have a significant impact on the amount of off-cuts and hence the overall price per system. Additionally, there are limitations to the size of the mirrors if user-friendliness is to be maintained. The durability of each surface must also be considered in the context of the environment in which they are used.

6.8.1 Proposed Mirror Materials

All proposed mirror surfaces are aluminium, which generally reflects well over the entire solar spectrum. Aluminium will tend to have a small dip in reflectance in the 700-900nm range; whilst the solar spectrum's peak intensity is approximately at 500nm, depending on the atmospheric conditions. The proposed mirror materials are as per Table 6.10:

Table 6.10 The nominal reflectances are given as a) solar-weighted reflectance quoted from manufacture's data sheet, b) reflectance over unspecified wavelengths from online store [34]**, c) reflectance over unspecified wavelengths from manufacturer's website** [35]**.**

Mirror Material	Nominal Reflectivity	Nominal Price
Alanod	90%[a]	30€/m^2
MarsRock	84-98%[b]	10$/$m^2$
Vinyl	86%[c]	12$/$m^2$

Pure uncoated aluminium has poor environmental and mechanical properties and simple protective surface coatings are applied to all proposed mirror materials. These surface coatings can reduce reflectivity. However, the two quarter wavelength layers applied to the Alanod material are claimed by the manufacturer to both enhance durability and maintain high reflectivity. The MarsRock material also has protective layers but the manufacturer does not state over what spectral range the quoted 84-98% reflectance was for, or if it was solar-weighted. The vinyl mirror surface was noticeably less reflective than the other two surfaces upon visual inspection.

6.8.2 Spectrophotometer

To measure the reflectivity of the mirror samples a PerkinElmer Lambda 1050 Spectrophotometer in the Physics Department was used. The Lambda 1050 is a UV/Vis/NIR Spectrophotometer that can measure across the entire range of 175nm to 3300nm, which more than adequately covers the solar spectrum.

However, in order to save time, measurements were only taken over the range from 300nm to 1800nm as very little of the total energy of the solar spectrum is above 1800nm or below 300nm. In fact, this measurement range represents 95.6% of the total energy of the direct component of the solar spectrum.

The angle of incidence for samples placed in the spectrophotometer is 12°. However, there was some difficulty in ensuring that the placed sample was correctly aligned in the instrument. If the samples were not completely flat or placed horizontally in the instrument then this led to errors in the measurements. A summary of these errors is given in Figures 6.23, 6.24 & 6.25.

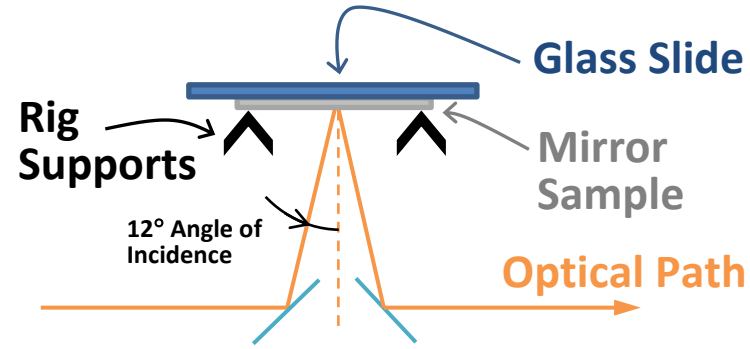


Figure 6.23 Diagram of planar mirror sample placed correctly in spectrophotometer.

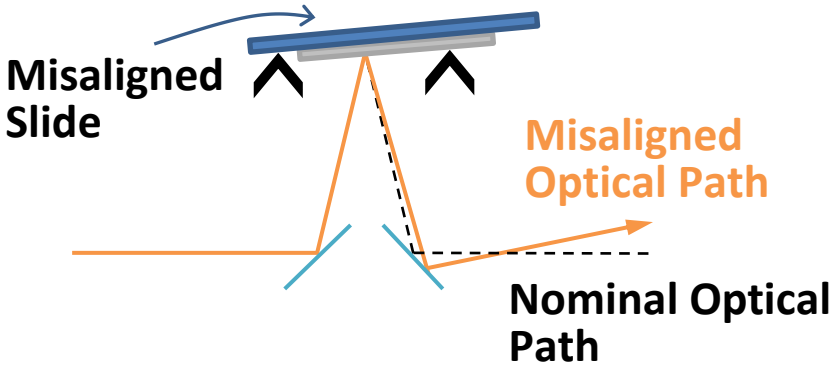


Figure 6.24 Diagram of planar mirror sample placed incorrectly in spectrophotometer.

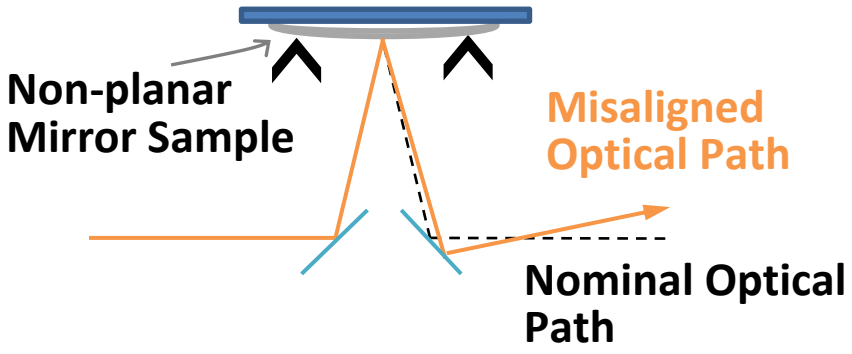


Figure 6.25 Diagram of non-planar mirror sample placed in spectrophotometer.

The non-planarity of the sample, or its incorrect placement in the instrument, always produced erroneous results. This was most noticeable when the Spectrophotometer switches between bulb types, see Figure 6.26.

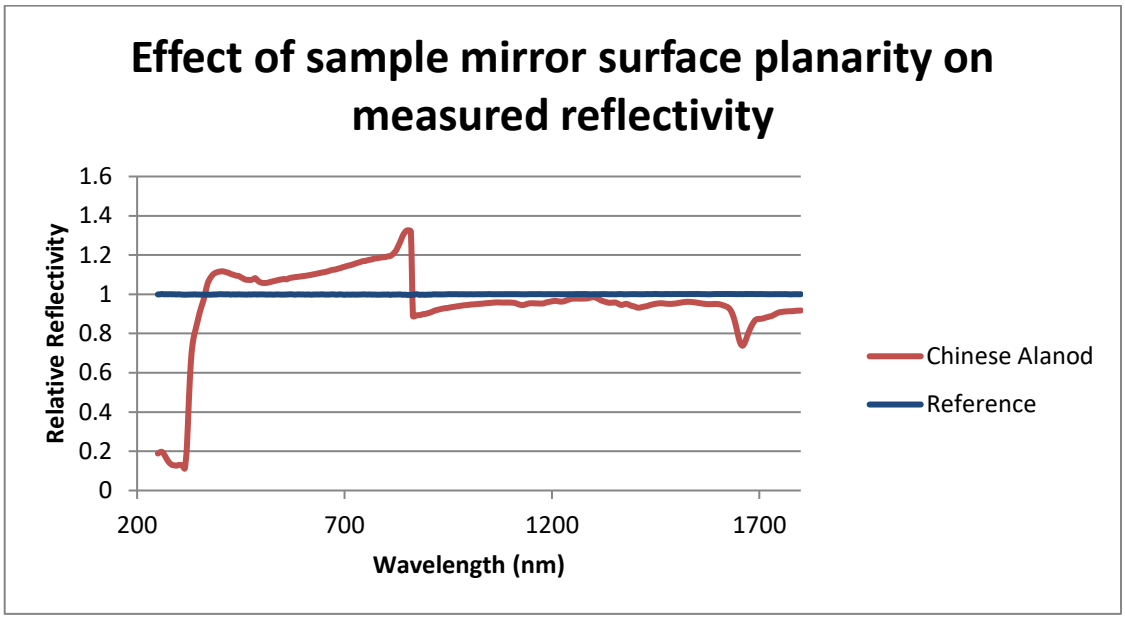


Figure 6.26 The step-change in measured reflectivity at 870nm is due to a bulb change in the spectrophotometer. Note that the planar reference mirror does not experience the same step-change at 870nm.

In Figure 6.26, the MarsRock data actually measures a peak absolute reflectivity just below 870nm before undergoing a discontinuity as the bulb in the spectrophotometer swaps at 870nm. In contrast, the planar reference mirror measures an almost constant relative reflectivity of 1 ± 2% when calibrated against itself, regardless of bulb changes.

The non-planarity of the samples is highlighted during the spectrophotometer bulb changes as these bulbs are unlikely to emit light in exactly the same manner. Any differences in emission profiles are unlikely to be noticed when reflected off a planar surface but would be more likely to do so off a non-planar surface.

The first set of data was rejected due to discontinuities in reflectance data obtained for the samples, as per Figure 6.26. Care was subsequently taken to ensure that not only were the samples as planar as possible but that they were placed horizontally in the instrument. In

contrast to some of the samples, the reference mirrors used are planar to a very high degree of accuracy and gave consistently good results.

The Thorlabs reference mirror has a thick base of aluminium and is planar to a high degree of accuracy. Therefore, errors are only expected from the non-planarity of the samples used. Whilst the 0.5mm thick Alanod material has good mechanical properties, the Vinyl and the 0.15mm thick MarsRock material lacked rigidity and needed to be attached to glass sample slides to ensure relatively planar surfaces, see Figure 6.27.

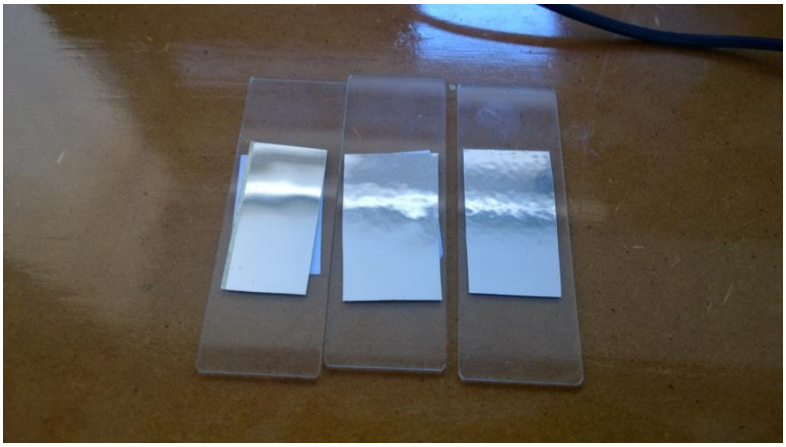


Figure 6.27 **Left - 0.15mm thick MarsRock material attached to glass sample slides. Middle and Right – Vinyl mirror surface attached to glass sample slides.**

6.8.3 Calibration of the Spectrophotometer

With planar samples aligned correctly in the instrument, the remaining factor in obtaining accurate results from the spectrophotometer is its calibration. The spectrophotometer gives results as relative reflectance compared to a first-run, calibrated sample. To correctly calibrate the results of the spectrophotometer the reflectivity of this first run-sample must be known accurately. The mirror used for this calibration was a Thorlabs Aluminum Mirror with Protective Coating.

The reflectance of the Thorlabs Aluminium Mirror was obtained in an excel file from the manufacturer's website. This reflectance is given in Figure 6.28.

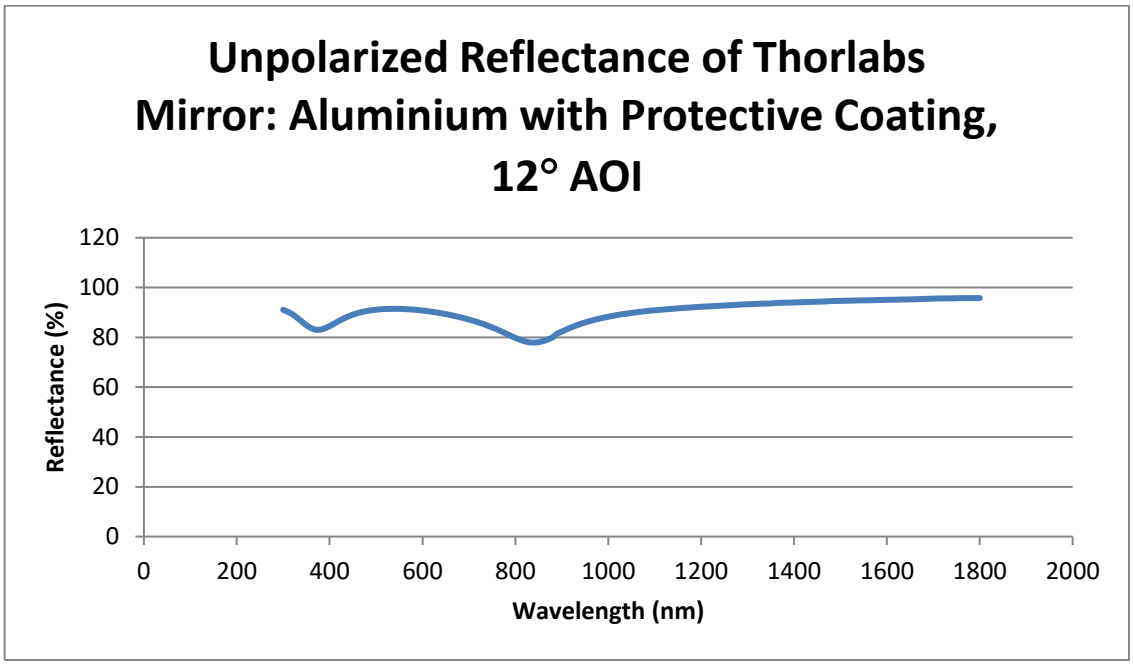


Figure 6.28 Reflectance of the Thorlabs mirror over the 300nm – 1800nm range.

The reflectance below 300nm was not supplied by the manufacturer; therefore results below this wavelength cannot be calibrated with this mirror. However, all sample mirrors have a dip in reflectivity just below 300nm and there is very little direct solar energy in this range. The 300-1800nm range represents 95.6% of the total energy from the direct and circumsolar spectrum.

6.8.4 Expected Reflectance Results

Detailed reflectivity data was only available for the Alanod mirror surface, see Figure 6.29. The surface coating on this mirror results in deviations from the smooth reflectance curves of the reference mirrors.

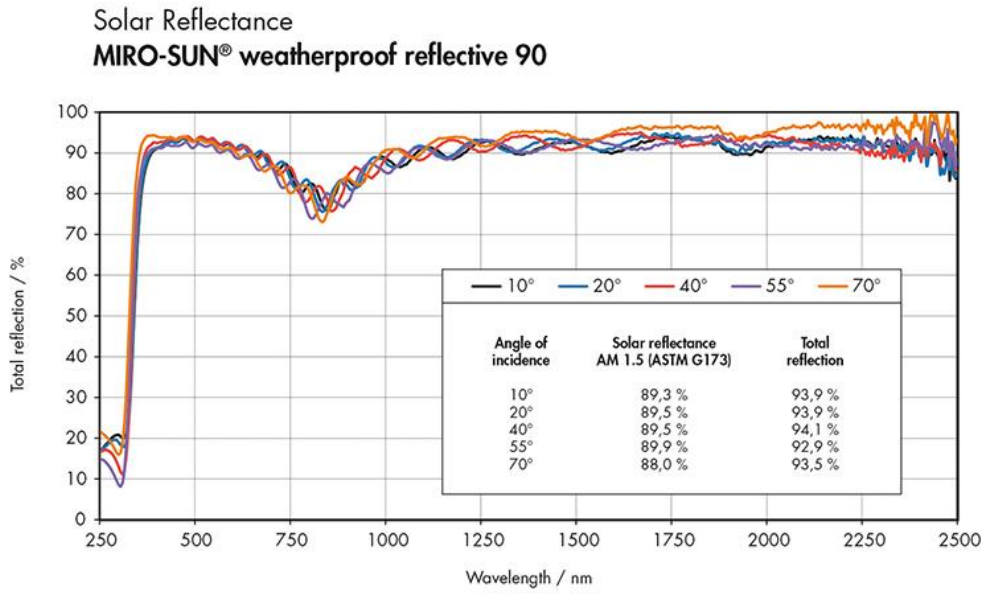


Figure 6.29 Reflectance of Alanod Miro-Sun© weatherproof reflective 90.

A plot of reflectance as a function of wavelength was not obtainable for the samples of the MarsRock material. The quoted reflectivity given was 84-98% but is unclear whether these values are the average for the visible range, the solar spectrum, or if it is solar-weighted and even if it indeed allowed for the protective coating applied. The reflectivity of the aluminised Vinyl is expected to be of the order of ~85%. Upon visual inspection it was the least reflective of the three mirror samples.

6.8.5 Reflectance Results

6.8.5.1 Alanod

The first results were to verify the reflectance curve quoted by the manufacturer of the Alanod mirror. These results were calibrated with the Thorlabs reference mirror. Generally, the measured reflectance compares quite well with the overall shape of the expected reflectance curve. However, the measured reflectance was lower than expected at all wavelengths, see Figure 6.30.

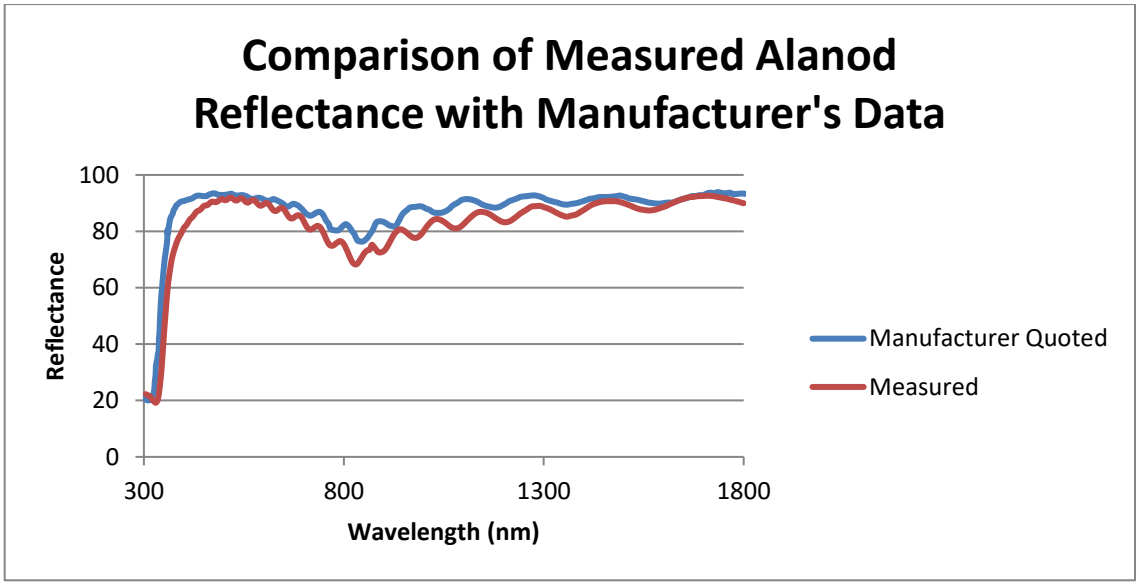


Figure 6.30 **Comparison of measured and quoted reflectance of the Alanod mirrors.**

6.8.5.2 Vinyl and MarsRock

The second set of results measured the reflectance of both the MarsRock material and the Vinyl mirror surfaces with the Thorlabs Mirror for calibration. Without manufacturer's data for comparison they are plotted against the reflectivity of the Thorlabs Optic, see Figure 6.31.

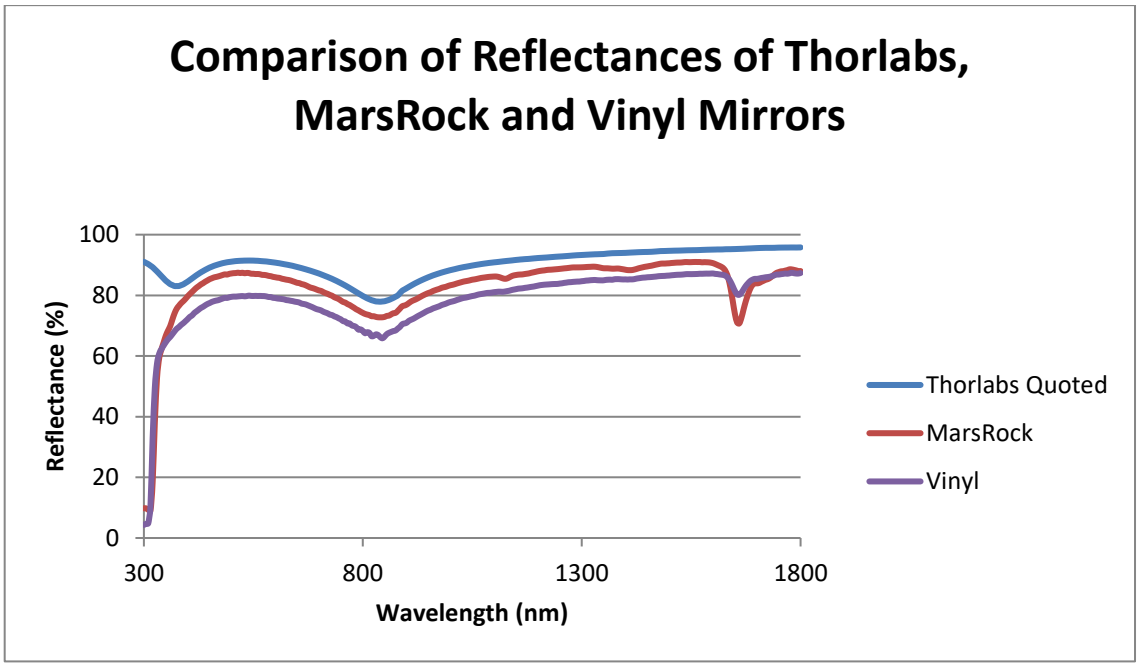


Figure 6.31 **Comparison of Reflectance of MarsRock and vinyl Samples to Thorlabs Optical Mirror.**

In comparison to the reference mirror, there is a clear drop in reflectance for the MarsRock material and again for the Vinyl mirror due to their optically inferior protective surfaces. There is a noticeable dip in reflectance at 1650nm in both the MarsRock and Vinyl samples, which is not observed in the reference mirror.

6.8.5.3 Overall Comparison

In general the Alanod performed better than the other two potential mirror surfaces, especially in the visible range. However, all the mirror surfaces follow the expected curve for reflection from an aluminium surface, see Figure 6.32.

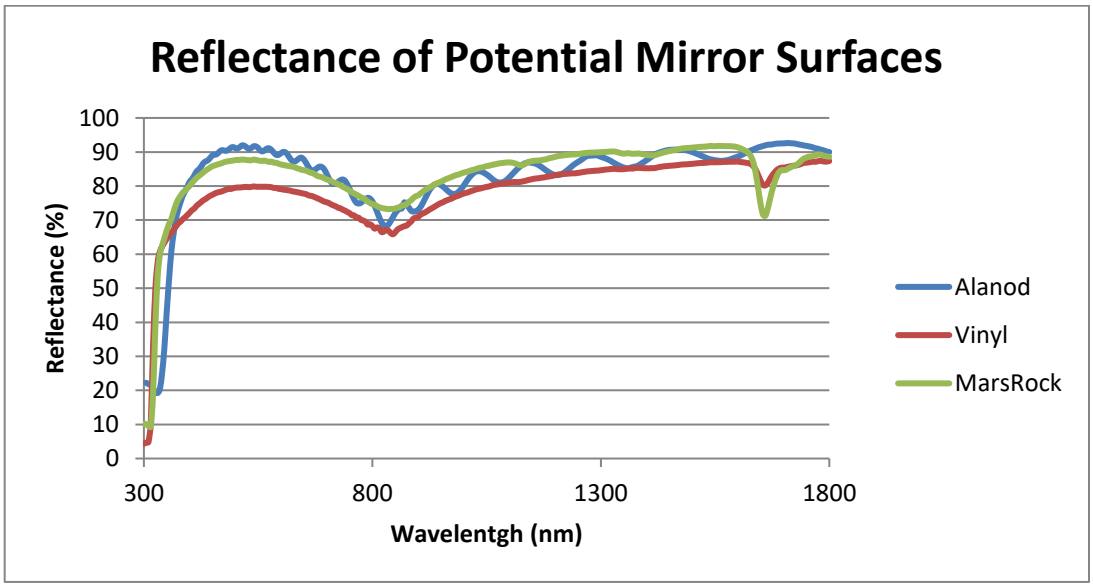


Figure 6.32 Representative comparison of the reflectance all three potential mirror surfaces.

Figure 6.32 is representative of the performance of each potential mirror surface but the results plotted are only for a single sample run per material. The final reflectance results were calculated using the average reflectance over several sample runs, which was then solar-weighted.

6.8.6 Solar-Weighting

For mirror applications involving thermal solar power the solar-weighted reflectance will be more important in determining performance than the absolute reflectance. The solar-weighted reflectance takes into the account the greater weighting of visible and near infrared light in the solar spectrum. The calculation of this performance is the multiplication of the reflectance spectra and the solar intensity spectra. The result is the solar-weighted total energy reflectance. The solar spectra for an atmospheric thickness of 1.5AM is given in Figure 6.33.

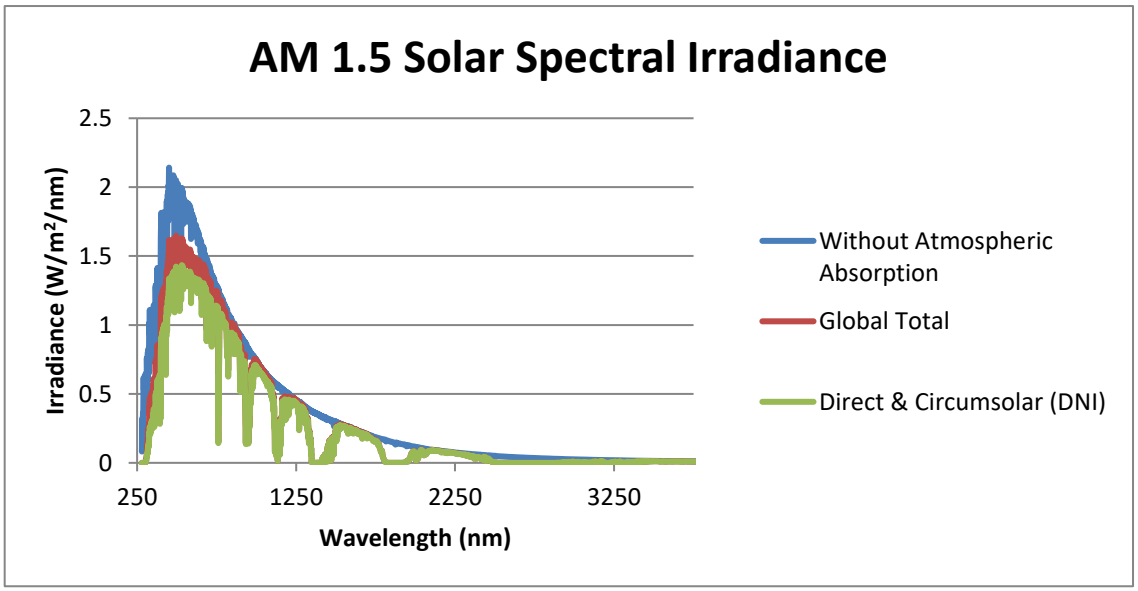


Figure 6.33 Solar Spectrum for an atmospheric thickness of 1.5, which is equivalent to a tilt of 37°.

The solar spectrum used for calculating weighted reflectances is the direct and circumsolar spectrum, which is otherwise known as direct normal irradiance (DNI). This spectrum represents solar irradiance from the solar disk and the solar aureole; which is defined as the irradiance within a half angle of 2.5° from the centre of the solar disk. This spectrum therefore ignores solar irradiance due to atmospheric refraction, which is not applicable to concentrating systems. The weighting of the reflectance data obtained from the PerkinElmer

Lambda 1050 with the solar spectrum was used to calculate the solar-weighted reflectances in Table 6.11.

Table 6.11 Direct and circumsolar-weighted reflectances for proposed mirror materials.

Mirror Material	Average Solar Weighted Reflectance
Alanod	84.7
MarsRock	82.9
Vinyl	75.7

The calculation of this solar-weighted reflectance is only over the 300-1800nm range and therefore ignores 4.4% of the direct and circumsolar spectrum that lies above 1800nm; there is negligible direct or circumsolar energy below 300nm present in the solar spectrum after atmospheric interaction. The Alanod material has a marginally higher reflectance than the MarsRock material but both outperform the Vinyl material.

Almost all design work on the solar concentrator has been done using the Alanod material for its mirrors. The assumed reflectance of the Alanod material has therefore directly led to calculations regarding the mirror size and power of the concentrator. For a solar concentrator utilising the MarsRock or the Vinyl surfaces larger mirror sizes are required to maintain the same power output; or alternatively using the same mirror sizes will result in a lower power output. These results are summarised in Table 6.12.

Table 6.12 Relative design considerations compared to Alanod mirrors.

	Relative Mirror Size	Relative Power
MarsRock	+4%	96%
Vinyl	+25%	80%

However, the difference in relative mirror size is reduced when considering that the increase in linear dimensions for a mirror surface will be the root of these results, see Table 6.13.

Table 6.13 Relative design considerations compared to Alanod mirrors.

	Relative Mirror Size	Relative Linear Dimension Increase
MarsRock	+4%	+2%
Vinyl	+25%	+12%

6.8.6.1 Considerations for Power Requirements of Solar Cookers

In contrast to mirror area requirements, the reduction in relative power will have greater implications for the performance of a solar cooker. When boiling, or cooking food with high water content, parts of the system tend to equilibrate around 100°C, and thermal losses become relatively constant regardless of input power. That is, as long as there is enough energy input to maintain a system temperature of 100°C then thermal losses are relatively constant regardless of input power. Based on results from the field trials in Tanzania, Table 6.14 was produced, under the assumption that for an input power of 220W from Alanod mirrors, thermal losses were constant at 106W whilst boiling water.

Table 6.14 Relative cooking power compared to Alanod mirrors.

	Relative Input Power	Relative Cooking Power
MarsRock	96%	92%
Vinyl	80%	61%

The implications here are that a small reduction in reflectance of the mirrors can produce a proportionally greater reduction in effective cooker power. Therefore to maintain cooking power it would be most prudent to increase mirror surface area to compensate for lower reflectances.

6.8.7 Errors

The errors associated with the calculation of the results can be categorised into three main areas; calibration errors, errors from the Spectrophotometer, and errors in aligning the samples correctly in the instrument. However, uncertainty in the calibration is expected to be relatively low. The manufacturer's data for the reflectance of the Thorlabs mirror was to better than 7 significant figures, which will be much smaller than other errors accounted for in the results. Furthermore, errors in the calibration of the results will affect the absolute reflectances given, but not how the results compare relative to one another.

6.8.7.1 Spectrophotometer Errors

Errors from the use of the Spectrophotometer will relate to the stability of the bulbs and therefore the consistency of the results taken over the course of testing. The best example of these errors came from comparing the Thorlabs reference mirror to itself over the course of 5 samples runs during approximately an hour of testing, see Figure 6.34.

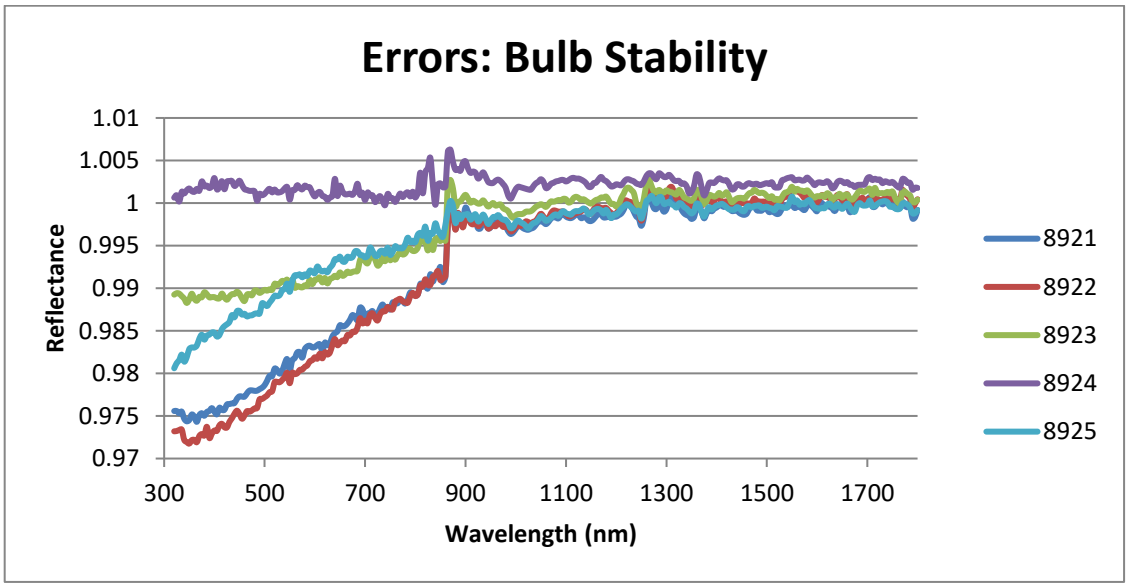


Figure 6.34 Relative reflectance of the Thorlabs mirror calibrated against itself over 5 sample runs.

The stability of the bulb used above 870nm is clearly superior to the bulb used below 870nm. Above 870nm there is approximately less than 0.5% difference is measured reflectance between all 5 sample runs. Below 870nm there is clearly greater divergence in the measured reflectances, up to 2.5% between sample runs at wavelengths near 300nm. However, overall the errors are relatively low and once the differences in these reflectances are solar-weighted these errors are only 1.2%.

Conservatively, the compound effect of bulb stability and calibration errors of the Thorlabs reference mirror are expected to be at most 2%.

6.8.7.2 Sample Misalignment Errors

The errors arising from the inability to accurately position the samples within the instrument were affected primarily by the sample material. More rigid sample materials, such as the Alanod and the MarsRock produced results that were less variant than the Vinyl mirror material, see Table 6.15.

Table 6.15 Comparisons of variance amongst sample materials in solar-weighted reflectance.

	Alanod	**MarsRock**	**Vinyl**
Variance in Solar-Weighted Reflectance	1.0	0.10	1.6

In particular, the MarsRock samples showed very little variance between sample runs. Unexpectedly the variance of the results for the Alanod samples was higher than those for the MarsRock. The Alanod sample is expected to be more planar given its 0.5mm thick layer of Aluminium in comparison to the 0.15mm layer in the MarsRock material. The higher variance amongst the Alanod sample results is peculiar given that it was the same sample of Alanod used in every measurement.

This increased variance in measured reflectance may be due to less precise location in the spectrometer. Indeed, the manufacturer's data, see Figure 6.29, indicates that the measured reflectance will vary strongly with the angle of incidence. However, it is also clear that there is an oscillation in the measured reflectance which is wavelength dependent, see Figure 6.35. It is therefore likely that a complex interaction between the angle of incidence, wavelength of incident light and the surface coatings of the Alanod make precise measurements difficult.

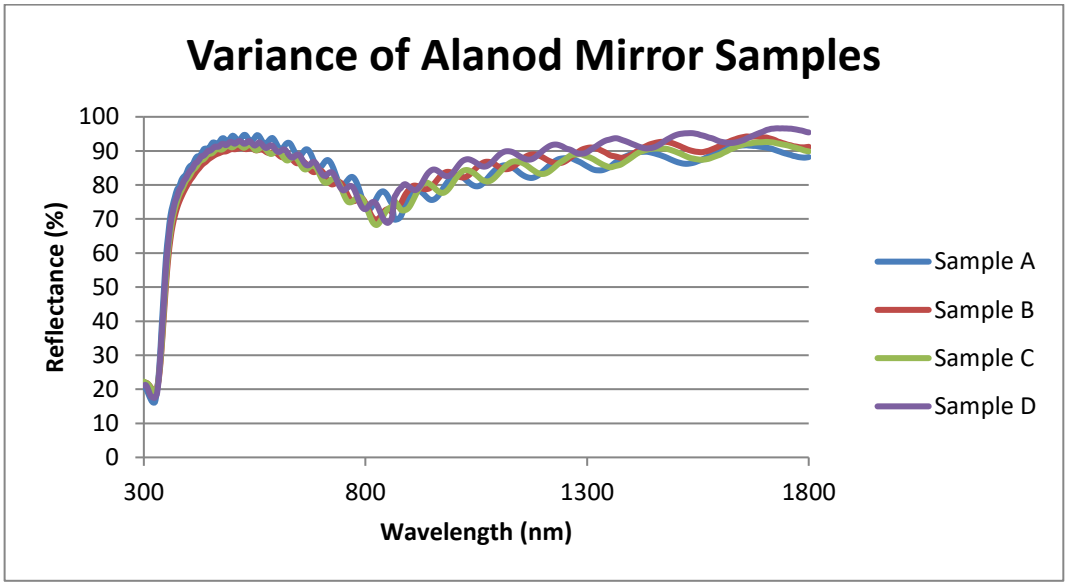


Figure 6.35 Variation in reflectance between four sample runs of the Alanod mirror.

The oscillations in the measured reflectance of the Alanod sample will clearly increase the variance between sample runs, even when these oscillations appear to be around approximately the same average reflectance. However, the variance across the 4 sample runs of the solar-weighted reflectivity was only 1%.This solar-weighting of the results hides some of the discrepancies in the results at particular wavelengths. The solar-weighted reflectances for the four sample runs are summarised in Table 6.16.

Table 6.16 Solar-weighted reflectance of the same Alanod sample over 4 sample runs.

Sample Run	A	B	C	D
Solar-weighted Reflectance	85.4	84.1	83.7	85.8

To put these results in context, the manufacturer of Alanod quotes an overall solar-weighted reflectance of 89.3% for an angle of incidence of 10°. The best result obtained from the experimental run of 4 trials was a solar-weighted reflectance of 85.8%, whilst the average solar-weighted reflectance for Alanod over the 4 trials was 84.7%. There is a clear discrepancy with the manufacturer's quoted reflectance, which is 4.6% above the average obtained and outside of generous error ranges.

The error for misalignment of the samples is excepted to be of the order of less than 1% for the MarsRock samples, and as much as 3-4% for the Alanod and vinyl samples. Overall the total errors are therefore expected to be of the order of 3% for the MarsRock material, 5% for the Alanod material and 6% for the Vinyl. The Spectrophotometer itself gives accurate results, yet the variance introduced with the misalignment of the samples means that these results are not very precise. While there may be uncertainty in the precise reflectances of the proposed materials, what is clear is that the relatively small error in the measurements will be insignificant against the large cost differentials between the Alanod material and its alternatives.

6.8.7 Other Considerations in Mirror Selection

Whilst the reflectance of a chosen mirror material will be a great concern to the overall design and function of a solar cooker, other factors affecting the mirrors cannot be ignored. These include, but are not limited to: the materials electrostatic attraction of dust, the mirror materials resistance to abrasion, the mirror materials resistance to erosion, the mirror materials structural durability, the mirror materials resistance to corrosion and water damage, manufacturing costs of the entire mirror assembly and the material cost of the mirror itself.

The Alanod material which was chosen for both the Italian and Tanzanian trials has a proven commercial record of offering excellent reflectance, low dust attraction and good

environmental properties, albeit at a relatively high price point. Limited use of the vinyl material in Tanzania exposed dual weakness of high electrostatic attraction of dust and poor resistance to abrasion. This made cleaning of the mirrors very difficult. Although, the vinyl material is much cheaper than the Alanod its weakness in these areas are unlikely to yield a favourable outcome.

At first glance the MarsRock material appears to offer a good compromise between the Alanod and Vinyl mirror materials. It offers comparable reflectance to the Alanod at the price point of the Vinyl material. According to the manufacturer's website the material includes an anti-static layer which should prevent the build-up of dust. What remains to be seen is the environmental performance of the MarsRock material, including its resistance to abrasion, corrosion and water damage.

All proposed mirror materials were attached to supporting structures and any final design decision must take this into consideration. In particular, the ease of applying thin films onto structural backing materials will impact manufacturing costs. Additionally, the quality of the reflective surface may be influenced by irregularities in the backing material or glue. Finally, transportation and customs issues should not be ignored as the Tanzanian trials proved that these can be both costly and time-consuming.

7 Conclusions and Future Work

7.1 Conclusions

The Oxford reflex concentrator is a promising and novel solar concentrator design. A vector proof was demonstrated which defined the concentrators unique geometry with 5 key variables. Using design tools developed from the vector proof, a prototype geometry of the reflex concentrator was optimised to ensure a narrow cone of vertical light would be incident on the underside of a receiver.

This geometry was then validated using Monte-Carlo based ray tracing techniques. This modelling established a theoretical maximum concentration factor of 5,400 for the prototype. The performance of the prototype was then compared to that of an equivalent parabolic dish, subtending the same solid angle. Under direct solar alignment the peak flux and concentrations factors of these two systems were highly similar. Modelling demonstrated that the reflex concentrator does not achieve peak irradiances as high as an equivalent parabolic dish when misaligned. However, it was demonstrated that the caustic region of the reflex concentrator is subject to an asymmetric displacement when misaligned that may prove beneficial. In real world applications the difference in theoretical peak irradiances are unlikely to be borne out. However, the reflex concentrator will retain its price and tracking advantage over parabolic dishes.

A lab-scale concentrator prototype was constructed based on the previously optimised geometry. Optical testing in the lab confirmed its performance. Specific attention was made during these tests to establish limits to which errors in the mirror surfaces would affect the concentration of the system. Standard deviations amongst measurements taken whilst scanning the mirrors with a laser pointer indicated that mirror errors contributed to a standard deviation of 0.87 mm and 3.2 mm in the positioning of the focal point in the y and z

directions of the concentrator respectively. Using the ray tracing code, these deviations were shown to correspond to a standard deviation in mirror surface normals of between 1.4 and 4 mrad. Experimental results and data confirmed that the system is more sensitive to mirror surface errors in the conical mirror.

A detailed thermal model of the oven was developed in order to establish performance indices and benchmark results for future field trials. Experimental work in the lab in support of this thermal model established that the thermal contact conductance between the hotplate and a thermal load placed on top could significantly alter the performance of the system. A low thermal contact conductance would result in slower cooking times and more heat being lost to convection from the hotplate. Experimental values for the thermal contact conductance between an aluminium billet and the hotplate were measured, in order to supply reference data for future trials. The importance of the oven to limit convective losses was demonstrated, whilst showing that the thickness of any insulation had little effect on thermal losses.

A large scale field prototype was developed in conjunction with an industrial partner, Dytecna, which involved numerous design sessions. This Dytecna prototype was supplied to the group in advance of an upcoming Italian field trial. During testing in the lab with laser pointers several deficiencies in the design were made apparent. Replacement support ribs were modelled in SolidWorks and manufactured to correct improper mirror geometry in the system. Simultaneously, improvements were made to enhance the rigidity of the mirror's supports. In support of the trial a 3 channel RGB light meter was constructed in order to measure direct normal irradiance during the trial. This light meter was calibrated using a solar simulator in the Physics Department.

The Italian trials of the modified Dytecna prototype demonstrated that the design concept functioned well. However, convective losses from the underside of the hotplate exceed estimates established with the model and lab testing, but could be qualitatively

understood as arising from increased convective losses arising from wind. Nevertheless, the concentrator met several design objectives including a stagnation temperature of 190°C in the hotplate, which guarantees frying as a method of cooking. Additionally, at boiling temperatures an efficiency of 57% useful heat to a pot was achieved compared to heat flow into the hotplate. Lastly, 0.75 litres of water were brought to boil in 33 minutes and a dish of rice was prepared large enough feed 3-4 people.

Following the successes of the Italian trials many design revisions were made to the concentrator, in anticipation of a large scale trial of many solar cookers in Tanzania. Design changes included larger mirrors to increase the power of the system. However, this necessitated supports for the mirror structure which had already been lacking in rigidity during the Italian trials. The hotplate was redesigned to be cut from aluminium sheet whilst the remainder of the concentrator structure was to be constructed in wood. Italian data was fed back into the thermal model of the system in order to refine estimates of heat loss. These results illustrated that the insulation in the oven walls was not required. Apertures were constructed for the Tanzanian trials to reduce convective losses from the hotplates and various paints for their absorber surfaces were tested.

The Tanzania trials brought further challenges above and beyond those conducted in Italy. Communication barriers and bureaucratic hurdles would have proved insurmountable without help from our Tanzanian colleagues. Despite less than ideal weather 8 solar cookers were distributed to families in Tanzania. Experimental results were mixed however, until the decision was made to travel to the arid interior near Dodoma. Two of the three families in Dodoma made great use of the ovens during the trials. Several meals were partly cooked using the ovens and a stew was cooked entirely using our oven during one lunch. However, the third family in Dodoma struggled to operate the oven without supervision, highlighting the challenges that remain in making the oven as user friendly and intuitive as possible. Aluminised vinyl mirrors were tested, however these proved to attract far too much dust in

the arid environment of Dodoma. The ovens remain with their families in Tanzania awaiting further feedback.

An analysis of the Tanzanian data showed improvement over the Italian trials. A spot temperature of just over 300°C was measured in the centre of the hotplate. Previous modelling was confirmed when the removal of insulating material in the oven walls was demonstrated to not affect results. Although the results varied somewhat with local conditions, a boiling efficiency of 66% was measured, an 8% improvement over the Italian trials.

Further work in Oxford on analysis of mirror materials has highlighted the great potential of a cheap Chinese-made alternative to Alanod. This MarsRock material was determined to have a solar-weighted reflectivity of 83%, which compares favourably with the 85% measured solar-weighted reflectivity of the Alanod. However, the measured reflectivity for the Alanod is significantly below the 90% value quoted by the manufacturer.

Whilst the commercialisation of a solar cooker may take several more months or years there has been solid progress in support of this in many areas. The research contributions towards solar cookers include: material analysis and modelling of mirror and absorber materials, development of a low-cost solar irradiance measurement device, development of thermal and optical modelling tools, a functional oven design, and many practical design improvements. The ongoing trials in Tanzania will be certain to further inform this progress.

7.2 Future Work

The initial work on determining solar-weighted reflectivities for potential mirror surfaces highlighted the great potential of the MarsRock material. However, work needs to be done establishing its performance in the field. The electrostatic attraction of dust was a large factor in the poor performance of the aluminised vinyl mirrors in the Tanzanian trials. Any successful

mirror surface will have to remain reflective for several years or be easily replaced; corrosion resistance and durability to scratching must be proven in these materials.

The Tanzanian trials are still ongoing and once the dry season returns to Tanzania the families are expected to return to using their cookers. Although initial feedback has proven a wealth of information, long-term feedback is also required to guarantee success. Some improvements to the ovens have already been made in the field and these will need to be applied to future models; in particular, the covering of wooden surfaces which can be exposed to large solar fluxes on the underside of the oven.

The economic viability of any commercialisation of the project will depend heavily on the low labour costs of Tanzania or other countries. Work will need to be done establishing proper production facilities in these countries.

The potential of the Oxford reflex concentrator as a solar cooker has been demonstrated over the course of much theoretical and practical work as well as two successful field trials. However, as a general concentrating system there may still be potential in pursuing the designs for other applications. Currently, there is great worldwide need for water purification and desalination, both of which generally require large energy inputs. A feasibility study should be conducted in adapting the reflex concentrator to these needs. Simple calculations would seem to indicate that with an intelligently designed counter-flow heat exchanger, efficiencies may be attained that would allow the purification of many litres of water per day. The use of thermal stores for evening cooking or for running thermoelectric generators is also a future possibility.

A tracking system for the concentrator was initially deemed unnecessary, given the optimisation for lax tracking requirements. However, some user feedback from Tanzania and the possible use of the system as a water purifier would necessitate a tracking system. The

current design may be able to incorporate a simple gravity driven system. However, the cost of small high-torque DC motors may not be cost-prohibitive and should be investigated further. The tracking system for diurnal solar movements has proved intuitive, yet it remains to be seen if the same is true for the latitudinal/seasonal adjustments currently required.

Whilst the unique design of the Oxford reflex concentrator holds great potential, the success of a future solar cooker will depend highly on making a product which fully incorporates the wishes and requirements of the 3 billion people that cook every day with wood. Whilst technical advancements will be necessary for the project, perhaps one of the most integral components of future success is keeping in mind the potential user.

Bibliography

[1] "solarreserve.com," [Online]. Available: http://www.solarreserve.com/en/global-projects/csp/crescent-dunes/gallery/over-the-30-year-operating-life-the-plant-will-expend-more-than-10m-per-year-in-salaries-and-operating-costs-much-of-this-spent-in-the-region.jpg/@@images/image/large. [Accessed 20 April 2016].

[2] REN21, "Renewables 2015 Global Status Report," REN21 Secretariat, Paris, 2015.

[3] F. Mauthner, W. Weiss and M. Spörk-Dür, "Solar Heat Worldwide: Markets and Contribution to the Energy Supply 2013," AEE - Institute for Sustianable Technologies, Gleisdorf, Austria, 2015.

[4] "David Learns Chinese," [Online]. Available: http://www.davidlearnschinese.com/. [Accessed 13 April 2016].

[5] World Health Organization, "Household air pollution and health; Fact sheet N°292," WHO, [Online]. Available: http://www.who.int/mediacentre/factsheets/fs292/en/. [Accessed 03 April 2016].

[6] H. M. Toonen, "Adapting to an innovation: solar cooking in the urban households of Ouagadougou (Burkina Faso)," *Physical and Chemistry of the Earth,* vol. 34, pp. 65-71, 2009.

[7] T. Stocker, D. Qin, G.-K. Plattner, M. Tignor, S. Allen, J. Boschung, A. Nauels, Y. Xia, V. Bex, P. Midgley and (eds.), "Climate Change 2013: The Physical Science Basis. Contribution of Working Group 1 to the Fifth Assessment Report of the Intergovernmental Panel on Climate Change," Cambridge University Press, Cambridge, United Kingdom and New York, NY, USA, 2013.

[8] "http://www.forumbiodiversity.com/showthread.php/42243-Dominican-Rep-plans-to-built-wall-on-its-border-with-Haiti," [Online]. Available: http://i.imgur.com/u3DrV.jpg. [Accessed 14 April 2016].

[9] E. Rehfuess and World Health Organization, "Fuel for Life: Household Energy and Health," World Health Organization (WHO), Geneva, 2006.

[10] W. Akpalu, I. Dasmani and P. B. Aglobitse, "Demand for cooking fuels in a developing country—to what extent do taste and preferences matter?," *Energy Policy,* vol. 39, pp. 6525-6531, 2011.

[11] MNES, "Annual Report: 1993-1994," Ministry of Non-Conventional Energy Sources (MNES), Government of India, New Delhi, 1994.

[12] Census of India, "www.censusindia.gov.in," Ministry of Home Affairs, Government of India, [Online]. Available: www.censusindia.gov.in/Census_And_You/availability_of_eminities_and_assets.aspx. [Accessed 18 01 2016].

[13] TERI, "Bioenergy in India. A background paper prepared for the International Institute for Environment and Development (IIED) for an international ESPA workshop on biomass energy.," The Energy and Resources Institute (TERI), New Delhi, 2010.

[14] N. Gronewold, "One-quarter of world's population lacks electricity," Scientific American, 2009. [Online]. Available: http://www.scientificamerican.com/article/electricity-gap-developing-countries-energy-wood-charcoal/. [Accessed 4 09 2014].

[15] R. Muthusivagami, R. Velraj and R. Sethumadhavan, "Solar cookers with and without thermal storage: a review," *Renewable and Sustainable Energy Review,* vol. 14, pp. 691-701, 2010.

[16] N. Nahar, “Performance and testing of a hot box storage solar cooker,” *Energy Conversion and Management,* vol. 44, pp. 1323-1331, 2003.

[17] “3tier,” Vaisala, 2014. [Online]. Available: http://www.3tier.com/static/ttcms/us/images/support/maps/3tier_solar_irradiance.jpg. [Accessed 12 04 2016].

[18] B. Halacy and C. Halacy, Cooking with the sun, Lafayette, CA: Jack Howell, 1992.

[19] Ministry of Non-conventional Energy Sources, “Annual Report 2011,” Government of India, New Delhi, 2011.

[20] O. Ekechukwu and N. Ugwuoke, “Design and measured performance of a plane refelctor augmented box-type solar-energy cooker,” *Renewable Energy,* vol. 28, pp. 1935-1952, 2003.

[21] M. A. Jibril, “IRIN News,” IRIN, 7 November 2014. [Online]. Available: http://www.irinnews.org/report/100805/soaring-charcoal-prices-hit-livelihoods-somaliland. [Accessed 2 April 2016].

[22] A. Wickramasinghe, “Energy access and transition to cleaner cooking fuels and technologies in Sri Lanka: issues and policy limitations,” *Energy policy,* vol. 39, no. 12, pp. 7567-7574, 2011.

[23] R. K. Agrawal and S. P. Singh, “Energy allocations for cooking in UP households (India),” *Energy Conversion and Management,* vol. 42, pp. 2139-2154, 2001.

[24] M. Bansal, R. P. Saini and D. K. Khatod, “Development of cooking sector in rural areas in India-A review,” *Renewable and Sustainable Energy Reviews,* vol. 17, pp. 44-53, 2013.

[25] S. A. Quadir, S. S. Mathur and T. C. Kandpal, “Barriers to dissemination of renewable energy technologies for cooking,” *Energy Conversion and Management,* vol. 36, no. 12, pp. 1129-1132, 1995.

[26] E. Biermann and e. al, “Solar Cooker Acceptance in South Africa: Results of a Comparative Field-Test,” *Solar Energy,* vol. 66, no. 6, pp. 401-407, 1999.

[27] EPRI, “Performance of the Vanguard Solar Dish-Stirling Engine Module,” Electric Power Research Institute, AP 4608, 1986.

[28] Sandia, “Sandia, Stirling Energy Systems set new world record for solar-to-grid conversion efficiency,” 12 February 2008. [Online]. Available: https://share.sandia.gov/news/resources/releases/2008/solargrid.html. [Accessed 09 November 2014].

[29] D. Buie, A. G. Monger and C. J. Dey, “Sunshape distributions for terrestrial solar simulations,” *Solar Energy,* vol. 74, no. 2, pp. 113-122, 2003.

[30] “Wikipedia,” [Online]. Available: http://en.wikipedia.org/wiki/Bayer_filter. [Accessed 19 April 2016].

[31] L. J. Salerno and P. Kittel, “Thermal Contact Conductance,” NASA Technial Memorandum, Ames Research Centre, 1997.

[32] A. Meinel and M. Meinel, “Applied Solar Energy,” Wesley Publishing Co., 1976.

[33] M. Blumthaler, W. Ambach and R. Ellinger, “Increase in Solar UV Radiation with Altitude,” *Journal of Photochemisty and Biology,* vol. 39, pp. 130-134, 1997.

[34] “MarsRock,” [Online]. Available: http://www.marsrock.com.cn/product/805471943-215122379/0_15mm_Thickness_Mirror_Reflector.html. [Accessed 20 April 2016].

[35] “Solarcooker at Cantina West,” [Online]. Available: http://www.solarcooker-at-cantinawest.com/vinyl_reflective_material_self_adhesive.html. [Accessed 20 April 2016].

[36] P. Balachandra, “Dynamics of rural energy access in India: An assessment,” *Energy,* vol. 36, no. 9, pp. 5556-5567, 2011.

[37] E. Rehfuess, S. Mehta and A. Prüss-Üstün, “Assessing household solid fuel use: multiple implications for the Millennium Development Goals,” *Environmental health perspectives,* vol. 114, no. 3, pp. 373-378, 2005.

[38] D. Buie, A. G. Monger and C. J. Dey, “Sunshape distributions for terrestrial solar simulations,” *Solar Energy,* vol. 74, pp. 113-122, 2003.

[39] W. H. Organization, “Burden of disease from household air pollution for 2012,” 2014.